IMPERIAL

Reconfigurable Intelligent Surfaces:
Beamforming, Modulation, and Channel Shaping

Yang Zhao

Supervisor: Prof. Bruno Clerckx

Department of Electrical and Electronic Engineering
Imperial College London

This dissertation is submitted for the degree of
Doctor of Philosophy

Declaration

The contents presented in this dissertation are original and have been carried out by myself under the guidance of my supervisor Prof. Bruno Clerckx. Any work from other researchers, scholars, or sources have been properly cited and acknowledged. Figures, tables, and results presented in this dissertation are generated by myself, unless otherwise stated. I would like to acknowledge the use of large language models for assistance in improving the clarity and readability of this thesis. The contents have not been submitted in whole or in part for consideration of any other degree or qualification in any academic institution. I am aware of the ethical standards and academic integrity policies of Imperial College London, and I have adhered to these principles throughout the course of study. In signing this declaration, I affirm my commitment to academic honesty, intellectual integrity, and the pursuit of knowledge in the service of truth and understanding.

Any comments, suggestions, or corrections are greatly acknowledged and can be sent to `i@snowztail.com`. The source code of all simulation results in this dissertation are publicly available at `https://github.com/snowztail/`. Finally, I would like to appreciate Bruno, my colleagues, and whoever is reading this dissertation.

Yang Zhao
May 2024

Abstract

Reconfigurable Intelligent Surface (RIS) is one of the most promising physical-layer technology for 6G. It adopts numerous low-power scattering elements to customize the propagation environment for improved network performance, unlocking a new potential of *channel design* as never before. In this dissertation, we first provide an overview of its physical structure, characteristics, applications, and scattering models, then discuss how it addresses the key issues in Simultaneous Wireless Information and Power Transfer (SWIPT) and compare it with Backscatter Communication (BackCom) in terms of functionalities and preferences. The work chapters investigate three typical use cases of RIS: Joint design with transceiver for a specific performance measure (beamforming); ride its own information over legacy networks (modulation); and manipulate the inherent properties of the wireless environment as a stand-alone device (channel shaping). In particular, we address the following topics:

- *RIS-aided SWIPT:* We introduce RIS into multi-antenna, multi-carrier SWIPT systems, investigating joint waveform and beamforming design. Rate-Energy (R-E) region of practical receivers are characterized under non-linear harvester and frequency-flat RIS models.

- *RIScatter:* This novel scatter protocol integrates RIS and BackCom from an input distribution perspective. The reflection pattern is exploited simultaneously for beamforming of the primary link and modulation of the backscatter link. We propose a practical cooperative receiver and characterize the achievable rate region.

- *Multiple-Input Multiple-Output (MIMO) channel shaping:* We exploit an advanced Beyond-Diagonal (BD)-RIS architecture for singular value redistribution in Point-to-point Channel (PC) and leakage interference minimization in Interference Channel (IC). Their implications on joint RIS-transceiver designs are also discussed. We also propose an efficient and universal BD-RIS design framework.

Table of contents

List of figures

List of tables

Abbreviations

AF   Amplify-and-Forward
AI   Artificial Intelligence
AM   Arithmetic Mean
AmBC   Ambient Backscatter Communication
AO   Alternating Optimization
AP   Access Point
AWGN   Additive White Gaussian Noise

BackCom   Backscatter Communication
BBC   Bistatic Backscatter Communication
BCD   Block Coordinate Descent
BD   Beyond-Diagonal
BLE   Bluetooth Low Energy

CLT   Central Limit Theorem
CP   Canonical Polyadic
CR   Cognitive Radio
CSCG   Circularly Symmetric Complex Gaussian
CSI   Channel State Information
CSIT   Channel State Information at the Transmitter
CSS   Chirp Spread Spectrum
CW   Continuous Waveform

DC   Direct Current
DF   Decode-and-Forward
DMMAC   Discrete Memoryless Multiple Access Channel
DMTC   Discrete Memoryless Thresholding Channel
DoF   Degree of Freedom

DP	Dynamic Programming
DSSS	Direct-Sequence Spread Spectrum
EIRP	Effective Isotropic Radiated Power
FPGA	Field-Programmable Gate Array
FS	Frequency-Selective
FSK	Frequency-Shift Keying
GM	Geomtric Mean
GP	Geometric Programming
i.i.d.	independent and identically distributed
IC	Interference Channel
IoE	Internet of Everything
IoT	Internet of Things
KKT	Karush-Kuhn-Tucker
LC	Low-Complexity
LEH	Linear Energy Harvester
LoRa	Long Range
LoRaWAN	Long Range Wide Area Network
LoS	Line-of-Sight
M2M	Machine-to-Machine
MBC	Monostatic Backscatter Communication
MIMO	Multiple-Input Multiple-Output
MISO	Multiple-Input Single-Output
ML	Maximum-Likelihood
MMSE	Minimum Mean-Square-Error
MRC	Maximal Ratio Combining
MRT	Maximum Ratio Transmission
MSE	Mean-Square Error

NLoS   Non-Line-of-Sight
NOMA   Non-Orthogonal Multiple Access
NRZ   Non-Return-to-Zero

OFDM   Orthogonal Frequency-Division Multiplexing

PAE   Power-Added Efficiency
PAPR   Peak-to-Average Power Ratio
PC   Point-to-point Channel
PDF   Probability Density Function
PGA   Projected Gradient Ascent
PIN   Positive Intrinsic Negative
PS   Power Splitting
PSK   Phase Shift Keying

QAM   Quadrature Amplitude Modulation
QoS   Quality of Service

R-E   Rate-Energy
RCG   Riemannian Conjugate Gradient
RF   Radio-Frequency
RFID   Radio-Frequency Identification
RIS   Reconfigurable Intelligent Surface
RSMA   Rate-Splitting Multiple Access
RZ   Return-to-Zero

SCA   Successive Convex Approximation
SDP   Semi-Definite Programming
SDR   Semi-Definite Relaxation
SIC   Successive Interference Cancellation
SISO   Single-Input Single-Output
SMAWK   Shor-Moran-Aggarwal-Wilber-Klawe
SMF   Scaled Matched Filter
SNR   Signal-to-Noise Ratio
SR   Symbiotic Radio
STAR   Simultaneous Transmission and Reflection

SVD   Singular Value Decomposition
SWIPT   Simultaneous Wireless Information and Power Transfer

TS   Time Switching

UE   User Equipment

WF   Water-Filling
WIT   Wireless Information Transfer
WPCN   Wireless Powered Communication Network
WPT   Wireless Power Transfer
WSN   Wireless Sensor Network
WSR   Weighted Sum-Rate

Notation

Constants

e	Euler's number $\simeq 2.71828\ldots$
$\jmath$	Imaginary unit $= \sqrt{-1}$
π	Archimedes' constant $\simeq 3.14159\ldots$

Objects

a, A	Scalar
$\mathbf{a}$	Column vector
$\mathbf{A}$	Matrix
$\mathcal{A}$	Finite set
$\mathbf{0}$	All-zero matrix
$\mathbf{1}$	All-one matrix
$\mathbf{I}$	Identity matrix

Sets

$\mathbb{N}$	Natural numbers (excluding 0)
$\mathbb{R}$	Real numbers
$\mathbb{R}_+$	Real nonnegative numbers
$\mathbb{C}$	Complex numbers
$\mathbb{I}$	Probability domain $[0, 1]$
$\mathbb{H}_+^{n \times n}$	Positive semi-definite matrices of dimension $n \times n$
$\mathbb{U}^{n \times n}$	Unitary matrices of dimension $n \times n$

Operations

$(\cdot)^*$	Complex conjugate
$(\cdot)^\mathsf{T}$	Transpose
$(\cdot)^\mathsf{H}$	Hermitian (conjugate transpose)

$(\cdot)^\dagger$	Moore-Penrose inverse
$(\cdot)^+$	Ramp function $\max(0, \cdot)$
$\lvert\cdot\rvert$	Absolute value of a complex number
$\lVert\cdot\rVert$	Euclidean norm of a vector
$\lVert\cdot\rVert_\mathrm{F}$	Frobenius norm of a matrix
$\arg(\cdot)$	Argument of a complex number
$\mathrm{card}(\cdot)$	Cardinality of a finite set
$\log(\cdot)$	Natural logarithm of a real number
$\exp(\cdot)$	Exponential of a scalar or square matrix
$\mathrm{tr}(\cdot)$	Trace of a square matrix
$\det(\cdot)$	Determinant of a square matrix
$\mathrm{sv}(\cdot)$	Singular values sorted from largest to smallest
$\mathrm{diag}(\cdot)$	Constructs a square matrix with inputs on the main diagonal
$\mathrm{diag}^{-1}(\cdot)$	Retrieves the main diagonal of a square matrix
$\Re(\cdot)$	Retrieves the real part of a complex number
$\Im(\cdot)$	Retrieves the imaginary part of a complex number
$\mathbb{E}(\cdot)$	Expectation operator
$\mathbb{A}(\cdot)$	Extracts the direct current component of a signal
$\odot$	Hadamard product
$\otimes$	Kronecker product
$(\cdot)_{[x:y]}$	Shortcut for $(\cdot)_x, (\cdot)_{x+1}, \ldots, (\cdot)_y$

Distributions

$\sim$	Follows a distribution
$\mathcal{CN}(\mathbf{0}, \boldsymbol{\Sigma})$	Multivariate circularly symmetric complex Gaussian with covariance $\boldsymbol{\Sigma}$

Subscripts

$(\cdot)_\mathrm{D}$	Direct
$(\cdot)_\mathrm{F}$	Forward
$(\cdot)_\mathrm{B}$	Backward
$(\cdot)_\mathrm{I}$	Information
$(\cdot)_\mathrm{P}$	Power
$(\cdot)_\mathrm{T}$	Transmit
$(\cdot)_\mathrm{S}$	Scatter
$(\cdot)_\mathrm{R}$	Receive

Superscripts

$(\cdot)^{(r)}$ r-th iterated value

$(\cdot)^{\star}$ Stationary point

$(\cdot)^{[kj]}$ Associated with transmitter j and receiver k

Chapter 1

Introduction

1.1 Motivation

The quest for better wireless connectivity has been long-standing since Marconi's illuminating radio in 1895. Great successes have been made at the transmitter and receiver sides over the past century, and the communications society is unprecedentedly close to the Shannon limit [5]. By 2025, global mobile data traffic is expected to reach 607 exabytes (1 exabyte is 10^{18} bytes) per year [6] while the number of connected devices may exceed 75 billion (almost 10 per person on average) [7]. At the same time, wireless applications are also evolving in various forms to address world-changing incidents like COVID-19, climate change, geopolitical tensions, and Artificial Intelligence (AI) revolution. An initial attempt was made in 5G where the network prioritizes among high-throughput, ubiquitous-coverage, high-reliability, low-latency, massive-connectivity, and energy-efficient services [8]. However, the desire of human and machine for better communication shows no signs of slowing down. Emerging applications such as smart cities, autonomous driving, telemedicine, extended reality, federated learning, and generative intelligence are calling for a stronger and smarter wireless infrastructure. It is envisioned that 6G will be designed to meet the following requirements [9–11]:

- *Throughput:* The network would be able to provide a peak data rate of 1 Tbps and an average data rate of 100 Gbps per user.

- *Latency:* Sub-millisecond end-to-end latency would be achieved for low-latency applications like autonomous driving and remote surgery.

- *Reliability:* A success rate of 99.9999% would be guaranteed for ultra-reliable applications like industrial automation and cooperative robotics.

- *Connectivity:* The number of connected devices per kilometer square would be increased to 10 million for supporting Internet of Everything (IoE).

- *Mobility:* Commercial airlines with a maximal velocity of 1000 km/h would be the target application scenario.

- *Energy efficiency:* Power consumption has been a major criticism for 5G. It is expected that energy per bit would be reduced by over 90% in 6G to reduce carbon footprints.

- *Positioning accuracy:* Thanks to THz base stations, a 3D positioning accuracy of centimeter level may be achieved for indoor and outdoor environments.

- *Coverage:* Poor coverage has been another bottleneck for 5G. A terrestrial-satellite-aerial integrated network would provide a ubiquitous and uniform coverage for urban, rural, and remote areas.

- *Security and privacy:* Physical-layer security can be improved with narrower beams at higher frequencies and destructive scattering at the environment. Privacy can be enhanced with federated learning and homomorphic encryption.

Beyond the statistical requirements above, the next-generation wireless network is desired to integrate human, machine, environment, and AI seamlessly for a harmonic ecosphere. This paradigm shift from *connectivity* to *intelligence* is fueled by the latest advances in machine learning (theory) and programmable metamaterials (hardware). The former enables the network to understand the environment while the latter evolves the environment from a chaotic medium to a conscious agent that can serve on demand. Together, they form a symbiotic relationship with the potential to revolutionize how the world energize, sense, communicate, and interact.

One promising candidate within this 6G vision is Reconfigurable Intelligent Surface (RIS), a programmable metasurface that recycles and redistributes the electromagnetic waves in the air for improved wireless performance. It could be incorporated into the transmitter and receiver for *beamforming*, employed as a free-rider information source for *modulation*, or simply placed in space as a standalone device for *channel shaping*. These applications have distinctive requirements and trade-offs, but the operation principles are the same and those roles are not mutually exclusive. Imagine a future where everything can be "smartened" by coating with a metamaterial layer and attaching a microcontroller tag. Only a few active radiating sources (like the sun) are needed, while most objects (like the universe) can exploit the surrounding waves to energize themselves, sense the environment, communicate with others, and help those in need when idle. This vision motivates three research questions to be addressed in this thesis:

- *How does RIS impact different wireless applications such as communication and far-field power transfer?*

- *Is it possible to integrate RIS with other scattering applications into a versatile tool that blurs the boundary between the network and environment?*

- *What is the ultimate limit of channel reshaping through passive RIS and what are the implications on transceiver designs?*

Before delving into these questions, we first provide a short overview of RIS and introduce some potential applications. A detailed literature review and technical discussion on RIS and other technologies will be reserved for the following chapters.

1.2 Overview on Reconfigurable Intelligent Surface (RIS)

1.2.1 Concept

RIS is commonly known as a planar surface involving numerous wave scattering elements (a.k.a. unit cells, reflective patches), whose amplitude and phase responses can be engineered in real-time to achieve a desired radiation pattern. It behaves like a delicate Radio-Frequency (RF) mirror with adjustable curvature and orientation, which allows the incident signals to be focused and redirected in a particular direction. As shown in Fig. 1.1, its typical architecture consists of three stacked layers and a controller [1]. The top layer is a two-dimensional array of scattering elements printed on a dielectric substrate. The elements directly interact with the impinging waves, which are usually fabricated from metamaterial or patch/dipole antennas with sub-wavelength dimension and spacing. The middle layer is a copper ground plate that provides voltage reference and avoids signal leakage. The bottom later is a circuit board that associate each element with adjustable components, such as varactor and Positive Intrinsic Negative (PIN) diodes [12]. It also hosts a Field-Programmable Gate Array (FPGA) controller that controls the circuit and coordinate with transceivers in the network. By adjusting the scatter response of all elements, the RIS can effectively manipulate the wavefront for a constructive or destructive superposition and thus improve the ambient wireless environment.

1.2.2 Characteristics

The key characteristics of RIS are summarized as follows:
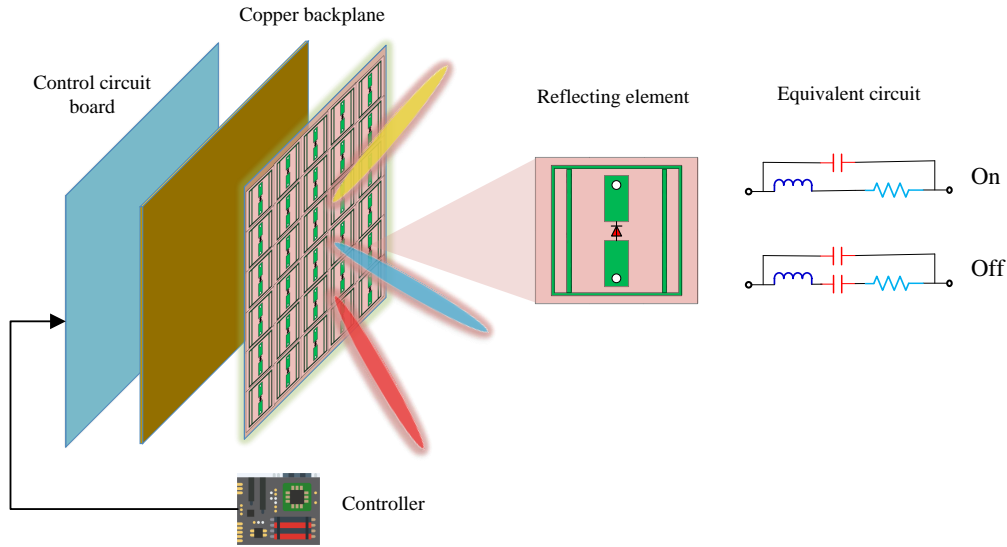
Fig. 1.1 A typical architecture of RIS. Source: modified from [1].

- *Low-power with negligible noise:* RIS reflects the incident waves in a passive manner and does not require dedicated RF chains.[1] This is different from Amplify-and-Forward (AF) relays that require power-hungry oscillators and introduces considerable thermal noise.

- *Programmable in real-time:* It provides a software configurable environment that can be adapted for different applications and scenarios. This is different from conventional reflectarray [13] and frequency selective surfaces [14] with predefined radiation patterns and frequency response.

- *Full-duplex without self-interference and delay:* This physical-layer solution can simultaneously support communication, sensing, and power transfer without self-interference. The optimal downlink and uplink configurations coincide with each other thanks to channel reciprocity [15]. This is different from Decode-and-Forward (DF) relays that are designed for a specific transmission and suffers from packet delays.

- *Low-cost and conformal:* It can be manufactured from low-cost materials and deployed in various forms (e.g., walls, windows, ceilings) to provide seamless coverage and powerful customization for indoor and outdoor environments. This is different from conventional Multiple-Input Multiple-Output (MIMO) systems that features complex hardware and bulky structures.

---

[1]The controller may be implemented with low-power components and powered by ambient energy.

- *Non-resonant and sub-wavelength:* Instead of relying on the resonance effect at a specific frequency, RIS ideally functions as a universal scatterer serving a wide range of frequency bands with independent response control. Miniature elements with sub-wavelength dimension and spacing further reduces mutual coupling and improves spatial resolution. However, they pose a great challenge on the design and optimization of the circuit components and matching network.

1.2.3   Applications

The channel manipulation capability of RIS unlocks a wide range of applications, such as signal enhancement [16], interference suppression [17], blockage bypassing [18], coverage extension [19], and security control [20]. It also has the potential to convey additional information [21], compensate for the Doppler effect [22], transform frequency-selective channels into frequency-flat [23], improve the spatial diversity for multi-antenna systems [24], and create artificial time diversity for multi-user orthogonal [25] and non-orthogonal [26] multiple accesses.

Those fancy characteristics and applications of RIS have also attracted significant attention from the industry. The first public testing attempt was made in 2018 by NTT Docomo and Metawave, who demonstrated a metasurface-based reflectarray in the FR2 band of 5G can boost a downlink data rate from $60\,\mathrm{Mbps}$ to $560\,\mathrm{Mbps}$ [27]. Later in 2020, NTT Docomo developed a transparent dynamic RIS that can allows 28GHz signals to reflect or pass through with negligible power loss. "RIS alliance" was formed in 2021 by Chinese companies and institutes including ZTE, China Mobile, and CAICT, which soon released a white paper [28] to promote the technology and standardization. In December 2022, ITU-R drafted a recommendation report for IMT-2030 (6G) [29] that marks RIS as a key technology to enhance the radio interface for multiple physical dimension transmission. These developments showcase the rapid progress of RIS from theoretical concept to practical implementation, paving the way for its integration into the next-generation network.

1.3   Publications

- Y. Zhao, B. Clerckx, and Z. Feng, "IRS-aided SWIPT: Joint waveform, active and passive beamforming design under nonlinear harvester model," *IEEE Transactions on Communications*, vol. 70, pp. 1345–1359, 2022

- Y. Zhao and B. Clerckx, *RIS in Wireless Information and Power Transfer*. Hoboken, NJ, USA: Wiley, 2023, pp. 271–295

- ——, "RIScatter: Unifying backscatter communication and reconfigurable intelligent surface," *IEEE Journal on Selected Areas in Communications*, pp. 1–1, Dec 2024

- Y. Zhao, H. Li, M. Franceschetti, and B. Clerckx, "Channel shaping using reconfigurable intelligent surfaces: From diagonal model to beyond," *To be submitted to IEEE Transactions on Wireless Communications*

Chapter 2

Background

This chapter provides essential background for topics covered in the thesis. A detailed literature review will be presented within each research chapter.

2.1 Reconfigurable Intelligent Surface (RIS)

2.1.1 Programmable Metamaterials

Metamaterials refer to artificial structures engineered for unusual properties that may not be found in nature. The concept was initially proposed by Victor Veselago in 1967, who conjectured the existence of mediums with negative dielectric constant $\epsilon < 0$ and negative permeability $\mu < 0$ [34]. Such metamaterials are known as "negative-index" because the refraction index is defined as the *negative* square root $n = -\sqrt{\epsilon\mu} < 0$, in order to be consistent with Maxwell's equations. It was not until 1999 that their feasibility was experimentally demonstrated by John Pendry at Imperial College using split-ring resonators [35]. Since then, metamaterials have attracted significant interests due to their counterintuitive properties, to name a few:

- *Negative refraction:* As shown in Fig. 2.1a, the incident and refracted rays stay at the same side of the normal axis [34]. This phenomenon is in contrast to the usual refraction but can still be predicted from Snell's law

$$\frac{\sin\theta_1}{\sin\theta_2} = n.\tag{2.1}$$

It is worth mentioning that a generalized law of refraction and refraction has been proposed in [36], which has become a standard reference for the design and analysis of metamaterials.

(a) Negative-index material (b) Positive-index material
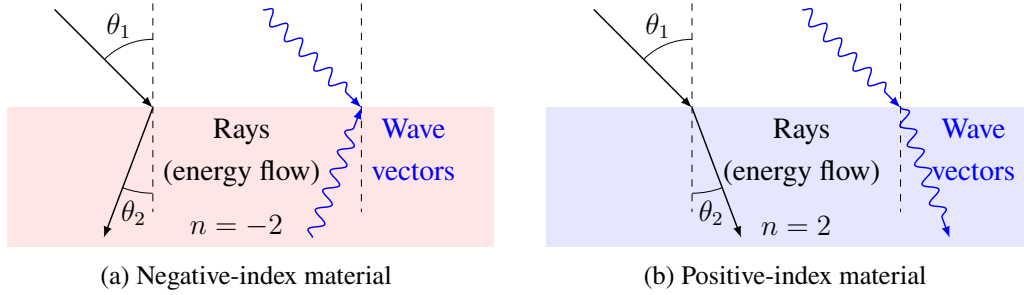
Fig. 2.1 Refraction in negative and positive-index materials. Incident and refracted rays stay at the same side of the normal axis in a negative-index material.

- *Opposite wave direction:* As shown in Fig. 2.2a, the wave vector and energy flow (indicated by the Poynting vector) are opposite to each other in a negative-index material [37]. This can be inferred from the electric field equation

$$\vec{E} = \vec{E}_0 \exp(\jmath k z - \jmath \omega t) \tag{2.2}$$

where $k = k_0 n < 0$ is the wavenumber, $\vec{E}_0$ and k_0 are the free-space electric field and wavenumber reference, z is the propagation distance, ω is the angular frequency, and t is the time. Negative-index materials are thus also called "left-hand" because the propagation direction of the electric and magnetic fields can be determined by a left-hand rule.

(a) Negative-index material (b) Positive-index material
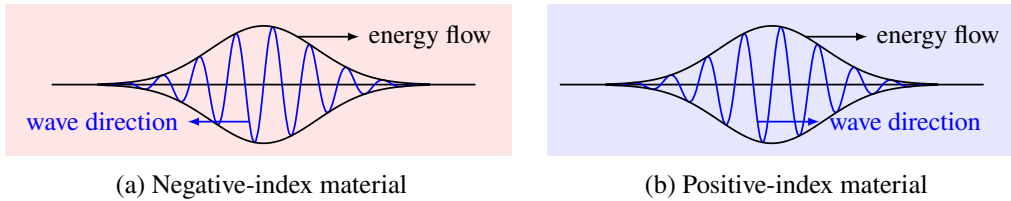
Fig. 2.2 Wave and energy have opposite directions in a negative-index material.

Conventional metamaterials have fixed properties that depend on the geometry and arrangement of their constituent elements. Once fabricated, these properties cannot be easily changed unless the structure is physically altered. This limits their early usage to military, with applications such as invisibility cloaks and optical illusions. In 2014, the concept of "coding" and "programmable" metamaterials was validated by researchers at Southeast University [38], who realized digital control of radar cross-section using biased diodes and FPGA. With a proper model of the target properties and external citation, the metamaterial can be

reconfigured in real-time for desired behaviors. For example, a self-adaptive metasurface equipped with motion and light sensors have been developed in [39] for single- and multi-beam steering.

Next, we discuss the principles of electromagnetic wave redirection via refraction and reflection:

- *Refraction:* As shown in Fig. 2.3(a), the negative-index material can re-focus the beams diverging from a point source to another point behind the material [40]. This could be helpful for wireless applications where the transmitter and receiver are at different sides of the obstacle.

- *Reflection:* As shown in Fig. 2.4(b), the scattering elements cooperatively alter the phase of the incident wave for a constructive (or destructive) superposition of the reflected waves in the target direction [41]. This could be helpful to concentrate ambient electromagnetic energy within a specific area.

$n = -2/3$ $n = 2$

(a) Negative-index material   (b) Positive-index material
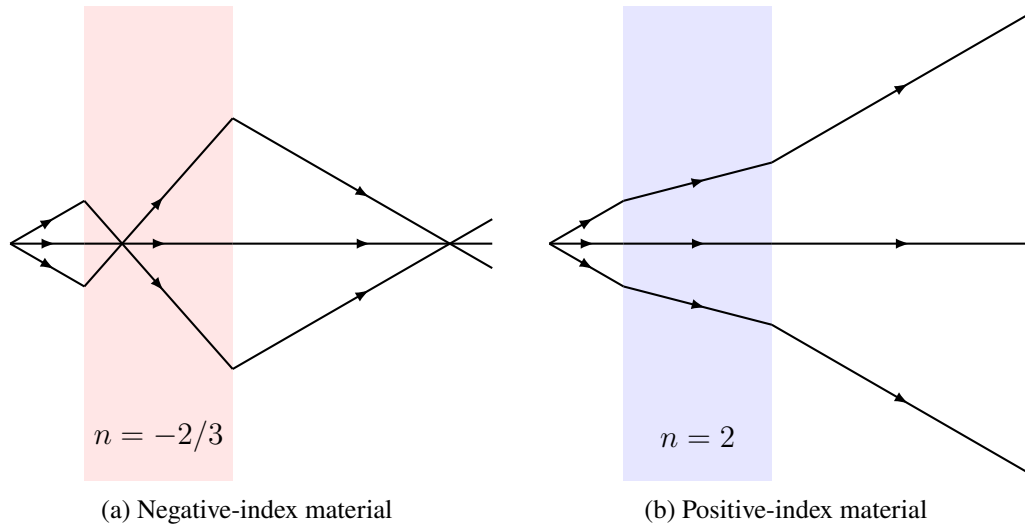
Fig. 2.3 Refraction through metamaterials. For negative-index material, beams diverging from a point source is set in reverse and converges back to another point behind the material.

(a) Incident wave   (b) Reflected wave
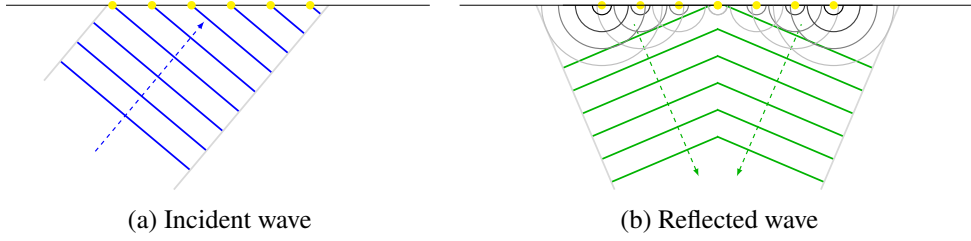
Fig. 2.4 Reflection through metamaterials. Yellow dots represent scattering elements. Solid and dashed lines denote wavefronts and rays, respectively. The scattering elements work together to manipulate the phases of incident waves, resulting in a focused beam steered in the intended direction.

It is worth noticing that refraction and reflection are different forms of wave scattering where the signal amplitude and phase are altered by the metamaterial. Their contributions can be jointly modeled within the scattering matrix $\boldsymbol{\Theta}$, which corresponds to the S-parameters in microwave engineering and the channel matrix in wireless communications. In the next subsection, we will introduce some typical RIS scattering models and their physical architecture.

2.1.2 Wave Scattering Models

2.1.2.1 Principles

RF wave can be manipulated by scattering elements made from *programmable metamaterials* or *passive antennas* [42]. As discussed above, the former refracts or reflects the incident signals at the air-cell boundary and mainly applies a phase shift. In contrast, the latter allows the wave to feed into the antenna port such that some energy can be absorbed by the circuit and the rest is reradiated to the space. An interesting observation is that when excited by an external wave, a scattering element can simultaneously function as an object and a radiator. The corresponding scattered field is [43]

$$\vec{E}_{\text{scatter}}(Z_{\text{L}}) = \underbrace{\vec{E}_{\text{structural}}}_{\text{structural component}} + \underbrace{\Gamma I_{\text{M}} \vec{E}_{\text{antenna}}}_{\text{antenna component}}, \tag{2.3}$$

where Z_{L} is the load impedance, $\vec{E}_{\text{structural}}$ is the residual field under perfect matching (i.e., modelling as an object), $\vec{E}_{\text{antenna}}$ is the radiated field with unit current at the terminal and no external excitation (i.e., modelling as a radiator), I_{M} is the current under perfect matching,

and Γ is the reflection coefficient

$$\Gamma = \frac{Z_{\mathrm{L}} - Z_0^*}{Z_{\mathrm{L}} + Z_0},\tag{2.4}$$

and Z_0 is the characteristic impedance for programmable metamaterials or the input impedance for passive antennas. Specifically,

- *Structural component:* Depends on the geometry and material of the scatterer. It is usually modeled as part of the environment multipath [44, 45] or a baseband Direct Current (DC) offset when the impinging signal is Continuous Waveform (CW) [46].

- *Antenna component:* Depends on the reflection coefficient and load impedance. This is widely exploited for various scattering applications, such as backscatter modulation in Backscatter Communication (BackCom) and passive beamforming in RIS [32].

We then introduce two canonical RIS models that will be adopted in the work chapters. Advanced models based on field equations (e.g., [47, 48]) and parametric fitting (e.g., [49]) are also available in the literature for accurate and practical analysis.

2.1.2.2 Diagonal Phase Shift Model

A straightforward way to model the RIS scattering effect is to consider independent scattering elements with purely reactive load impedance [50]. The reflection coefficient of the n-th element is thus

$$\theta_n = \frac{\jmath X_n - Z^*}{\jmath X_n + Z} = \exp(\jmath \phi_n),\tag{2.5}$$

where X_n is the reactance and ϕ_n is the phase shift on the scattered wave. For a total of N_{S} elements, the RIS scattering matrix is *diagonal with complex unit-magnitude entries*

$$\boldsymbol{\Theta} = \mathrm{diag}(\theta_1, \ldots, \theta_{N_{\mathrm{S}}}) = \begin{bmatrix} \theta_1 & 0 & \cdots & 0 \\ 0 & \theta_2 & \cdots & 0 \\ \vdots & \vdots & \ddots & \vdots \\ 0 & 0 & \cdots & \theta_{N_{\mathrm{S}}} \end{bmatrix}.\tag{2.6}$$

Despite the strong assumptions, this diagonal phase shift model is widely used for the analysis of RIS systems due to its simplicity and analytical tractability.

2.1.2.3 Beyond-Diagonal (BD) Model

How to model the RIS response if the passive scattering elements can cooperate with neighbors via physical connections? This question has been answered by [2] through a

Beyond-Diagonal (BD) model. From a network theory perspective [51], a general BD-RIS can be modeled as an N_S-port network that divides into G individual groups, each containing $L \triangleq N_S/G$ elements interconnected by real-time reconfigurable components. It allows wave impinging on any element to propagate within the circuit and depart partially from other elements in the same group, such that both amplitude and phase of the scattered wave can be redistributed with zero power loss. Fig. 2.5 illustrates an 8-element BD-RIS with group size 2 (left) and 4 (right).
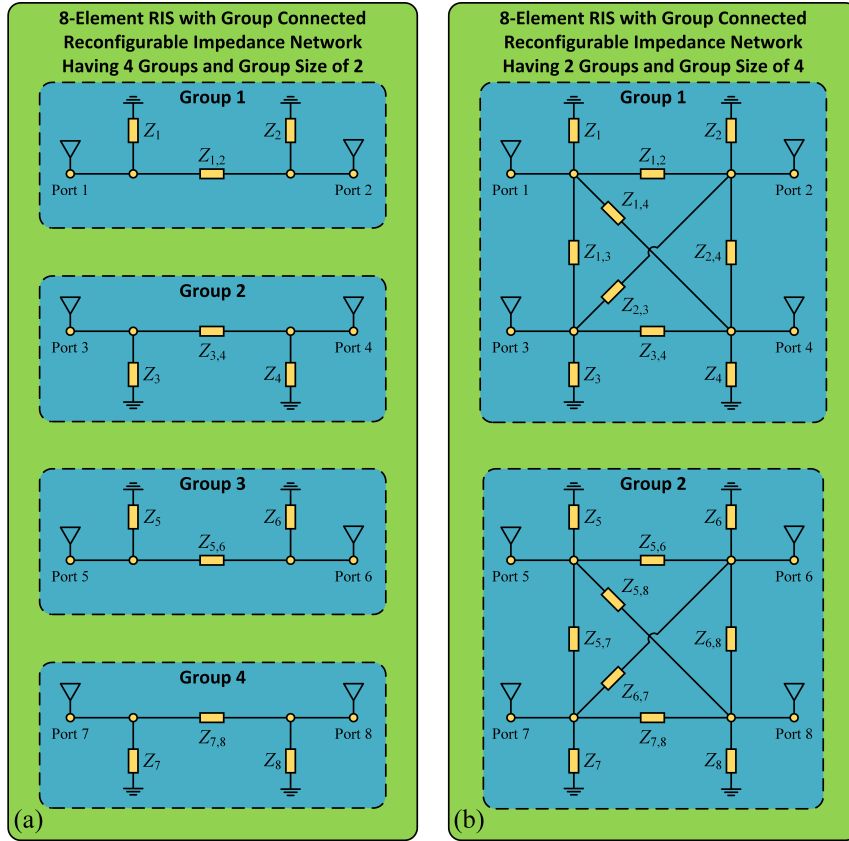
Fig. 2.5 Network model of an 8-element RIS with group-wise cooperative scattering of group size (a) 2 and (b) 4. The group size is a design parameter to balance the circuit complexity and scattering performance. Source: modified from [2].

Using passive symmetric components (e.g., capacitors and inductors), the scattering matrix of group $g \in \mathcal{G} \triangleq \{1, \ldots, G\}$ is [2]

$$\mathbf{\Theta}_g = (\jmath \mathbf{X}_g + Z_0 \mathbf{I})^{-1} (\jmath \mathbf{X}_g - Z_0 \mathbf{I}), \tag{2.7}$$

which satisfies both *symmetric* and *unitary* properties

$$\mathbf{\Theta}_g = \mathbf{\Theta}_g^\mathsf{T}, \tag{2.8a}$$

$$\mathbf{\Theta}_g^\mathsf{H}\mathbf{\Theta}_g = \mathbf{I}. \tag{2.8b}$$

On the other hand, lossless networks may also be built over asymmetric passive components (e.g., ring hybrids and branch-line hybrids) such that the symmetric constraint (2.8a) can be relaxed. A 4-port ring hybrid is illustrated in Fig. 2.6.
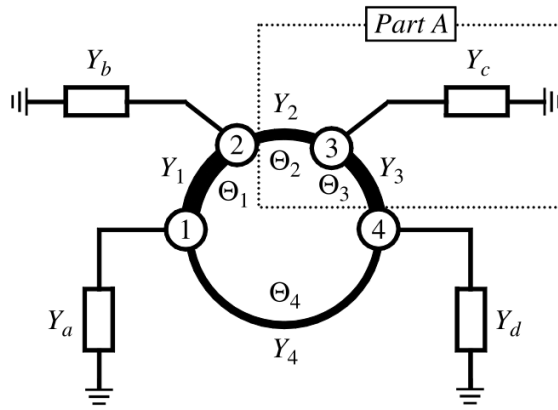
Fig. 2.6 A 4-port asymmetric ring hybrid. Here the arc length between ports are $\Theta_1 = \Theta_2 = \Theta_3 = \lambda/4$ and $\Theta_4 = 3\lambda/4$ where λ is the wavelength. The termination admittances Y_a to Y_d are arbitrary and the characteristic admittances of transmission-line sections are not necessarily the same, such that the scattering parameters can be asymmetric. Source: modified from [3].

By reconfiguring passive asymmetric components, we end up with the ultimate passive model where energy conservation (2.8b) is the only constraint for each group, as has been widely adopted in quantum physics. The overall scattering matrix of asymmetric BD-RIS is thus *block-diagonal with unitary diagonal blocks*

$$\mathbf{\Theta} = \mathrm{diag}(\mathbf{\Theta}_1, \ldots, \mathbf{\Theta}_G) = \begin{bmatrix} \mathbf{\Theta}_1 & \mathbf{0} & \cdots & \mathbf{0} \\ \mathbf{0} & \mathbf{\Theta}_2 & \cdots & \mathbf{0} \\ \vdots & \vdots & \ddots & \vdots \\ \mathbf{0} & \mathbf{0} & \cdots & \mathbf{\Theta}_G \end{bmatrix}, \tag{2.9}$$

where (2.8b) is equivalently denoted as $\mathbf{\Theta}_g \in \mathbb{U}^{L \times L}$. The group size L is a design parameter to balance the circuit complexity and scattering performance. Diagonal (single-connected) and unitary (fully-connected) RIS can be viewed as extreme cases with group size $L = 1$ and $L = N_\mathrm{S}$, respectively. Therefore, the BD model (2.9) is envisioned to be the next-generation

theoretical foundation for passive RIS, which grants more design freedom and stronger signal processing capability.

It is also worth mentioning that each group can be abstracted as a mathematical graph with L vertices and a variable number of edges [52]. Two elements are in the same group if and only if there is at least one path (via edges) between them. It implies that instead of connecting every pair of elements, the practical circuit can be designed to have a sparse graph with only a few connections, which is beneficial for reducing the circuit complexity and power loss from non-ideal components. Antenna directivity and radiation pattern should also be modeled in the scattering matrix, especially when the locations of users or RIS are not fixed. This has motivated the concept of Simultaneous Transmission and Reflection (STAR)-RIS [53, 54] and multi-sector RIS [55] where incident wave is partially steered to various directions for different users.

2.2 Wireless Power Transfer (WPT)

2.2.1 Introduction

Wireless devices are becoming smarter as well as more energy-efficient and eco-friendly. Koomey's law [56] predicts the computing efficiency roughly doubles every 19 months and the amount of power needed for the same operation decreases to 1% in a decade. Over the past 15 years, the rise of low-power technologies like Wireless Sensor Network (WSN) and Internet of Things (IoT) have hatched life-changing applications including smart homes, digital healthcare, and industrial automation. Today, Radio-Frequency Identification (RFID) tags and basic sensors (e.g., thermometer and proximeter) can operate on microwatts of power [57, 58], while communication protocols like Bluetooth Low Energy (BLE) and Long Range Wide Area Network (LoRaWAN) only consume tens of milliwatts [59]. This low-power trend together with the upsurge of mobile devices is calling for a *truly wireless* energy solution that eliminates the need for periodic cable plugging or battery replacement. While great successes have been witnessed for candidates like solar and piezoelectric, their prospects in wireless systems remain unclear due to the bulky converter, unpredictable source, and limited operation range. One promising solution on the horizon is Wireless Power Transfer (WPT) through electromagnetic waves. It can be classified into two categories based on the operation principle [60]:

- *Non-radiative near-field:* Power is transferred over a short distance (typically a few centimeters) by inductive coupling between coils or capacitive coupling between electrodes in a field-to-field manner. The former has been widely standardized (e.g., Qi

2.0) and commercialized (e.g., wireless charging pads), while the latter is still in the research stage.

- *Radiative far-field:* Power is transferred over a long distance (typically a few meters) by directional microwave or laser beams between antennas in a point-to-point manner. It shares many similarities with RF communication (e.g., infrastructure and wireless environment) but suffers from lower energy efficiency than non-radiative WPT due to pathloss.

Radiative WPT[1] brings numerous opportunities to future wireless networks. First, it completely eliminates wired connections and can be integrated into existing wireless systems with minimum modifications. Those properties translate to simple deployment, high scalability, and low maintenance cost. Second, the power can be simultaneously radiated to multiple devices on demand in a predictable, sustainable and reliable manner. This fits in our initial vision and differs from other unstable energy sources. Third and most importantly, radio waves carries power and information simultaneously. WPT can therefore be jointly designed with Wireless Information Transfer (WIT) to make the most of radiation, spectrum and infrastructures. However, energy efficiency and safety concerns have been two major obstacles that limit the practical development of WPT. In Section 2.3, we will discuss how RIS can help address these issues.

2.2.2 Modules and Coupling Effect
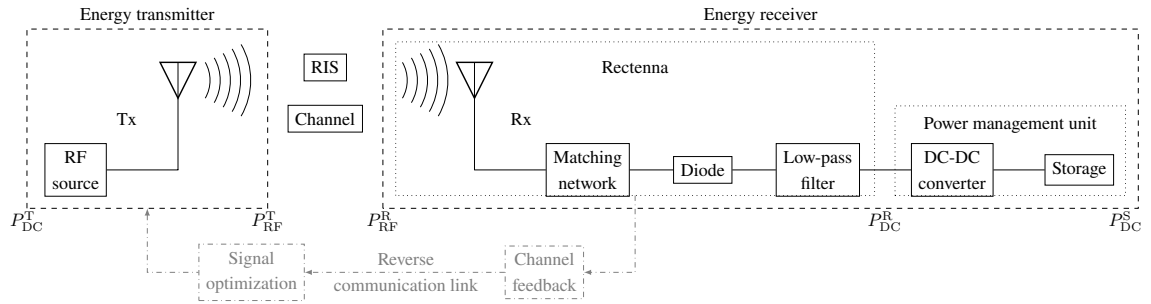
Fig. 2.7 Block diagram of a closed-loop RIS-aided WPT.

The block diagram of a closed-loop RIS-aided WPT system is illustrated in Fig. 2.7. The RF signal is generated and radiated by the energy transmitter, propagated through a wireless channel in the presence of a RIS, captured by the antenna(s) at the receiver, converted to DC power by rectifier(s), then passed to the power management unit. Upon successful harvesting,

---

[1]In the following part of the thesis, WPT refers to radiative WPT.

the DC power is either delivered directly to the device or stored in a battery/super capacitor for future operations. When a feedback link is available, one can acquire Channel State Information (CSI) at the energy transmitter and exploit it for signal optimization. Such a closed-loop RIS-aided WPT system can provide a complete control of transmitter, channel, and receiver, which is essential for maximizing the end-to-end power transfer efficiency

$$\eta = \frac{P_{\mathrm{DC}}^{\mathrm{S}}}{P_{\mathrm{DC}}^{\mathrm{T}}} = \underbrace{\frac{P_{\mathrm{RF}}^{\mathrm{T}}}{P_{\mathrm{DC}}^{\mathrm{T}}}}_{\eta_1} \underbrace{\frac{P_{\mathrm{RF}}^{\mathrm{R}}}{P_{\mathrm{RF}}^{\mathrm{T}}}}_{\eta_2} \underbrace{\frac{P_{\mathrm{DC}}^{\mathrm{R}}}{P_{\mathrm{RF}}^{\mathrm{R}}}}_{\eta_3} \underbrace{\frac{P_{\mathrm{DC}}^{\mathrm{S}}}{P_{\mathrm{DC}}^{\mathrm{R}}}}_{\eta_4}, \tag{2.10}$$

where $P_{\mathrm{DC}}^{\mathrm{T}}$ is the transmitted DC power, $P_{\mathrm{RF}}^{\mathrm{T}}$ is the transmitted RF power, $P_{\mathrm{RF}}^{\mathrm{R}}$ is the received RF power, $P_{\mathrm{DC}}^{\mathrm{R}}$ is the received DC power, and $P_{\mathrm{DC}}^{\mathrm{S}}$ is the stored DC power. The power conversion efficiencies are specified below:

- η_1: Transmitter DC-to-RF conversion efficiency[2] that depends on the RF power amplifier and transmit antenna. It is also called "drain efficiency" and state-of-the-art designs can achieve $\eta_1 \geq 70\%$ [62].

- η_2: Channel RF-to-RF conversion efficiency that depends on the wireless environment and RIS configuration. This is the major bottleneck of WPT since the radiated power is inversely proportional to the propagation distance squared.

- η_3: Receiver RF-to-DC conversion efficiency that depends on the impedance matching and rectifier design. We will discuss its behavior and modelling in the next subsection.

- η_4: Storage DC-to-DC conversion efficiency that depends on the converter circuit and battery characteristics. Modern power management units can achieve a charging efficiency $\eta_4 \geq 90\%$ [63].

It is worth mentioning that η_1 and η_3 also depend on the signal characteristics such as power level, carrier frequency, and Peak-to-Average Power Ratio (PAPR) [64]. Extensive efforts have been contributed from RF, wireless communications, and power electronic communities to improve the conversion efficiency of individual modules. However, it is often overlooked in the literature that a practical WPT system is highly *non-linear* since the amplifier and rectifier are very sensitive to the input waveform. This non-linear behavior can lead to a coupling effect between the modules, such that optimizing η_1 to η_4 independently does not necessarily maximize the end-to-end power efficiency η [64]. Besides, the system modeling

---

[2]This is different from Power-Added Efficiency (PAE) used in amplifier rating, which takes into account both DC power and input waveform power [61].

and analysis are subject to practical constraints like diode threshold and reverse-breakdown voltages, device parasitics, impedance mismatch, and harmonic generation [65].

2.2.3 Non-Linear Harvester Behavior

2.2.3.1 Equivalent Circuits

(a) Rectenna   (b) Half-wave rectifier
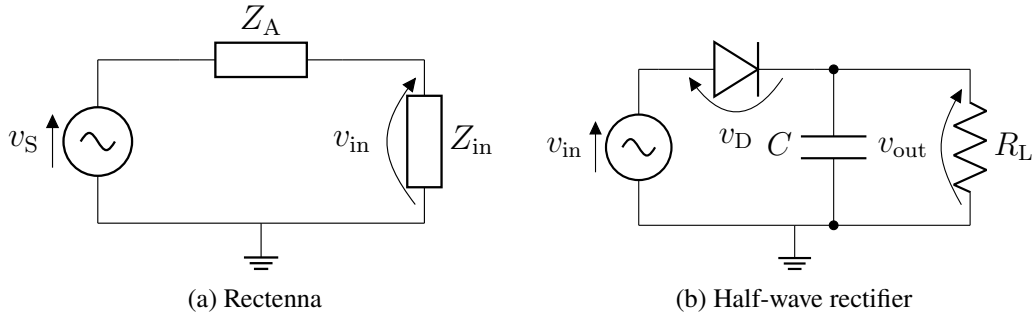
Fig. 2.8 Equivalent circuit of (a) rectenna and (b) single-diode half-wave rectifier.

The rectifier is a nonlinear circuit that converts the RF signal to DC power by rectifying and filtering the input signal. Fig. 2.8 illustrates the equivalent circuits of a rectenna (antenna and rectifier) and a single-diode half-wave rectifier, where v_{S} is the source voltage on the receive antenna, $Z_{\mathrm{A}} = R_{\mathrm{A}} + \jmath X_{\mathrm{A}}$ is the antenna impedance, $Z_{\mathrm{in}} = R_{\mathrm{in}} + \jmath X_{\mathrm{in}}$ is the total impedance of the matching network and rectifier, v_{in} is input voltage on the matching network and rectifier, v_{D} is the diode voltage, C is the buffer capacitance, R_{L} is the rectifier load resistance, and v_{out} is the output voltage. It is worth mentioning that the half-wave rectifier is the most popular choice in WPT literature due to its simple layout and low cost. Other rectifier topologies like full-wave, bridge, and voltage doubler can potentially improve the RF-to-DC conversion efficiency [66], but their modeling and analysis are much more complicated.

2.2.3.2 Operation Regions and Signal Models

The diode is the key non-linear component that determines to the harvested energy. Roughly speaking, the behavior of any rectenna can be separated into three operation regions [64]:

- *Linear region:* When the input power level is relatively low, the output power is proportional to the input and the RF-to-DC conversion efficiency η_3 is a constant. Most early WPT research (especially from communications society) assume the rectenna works in this region. For a received signal $y(t)$, the harvested DC power in this region can be modeled as

$$P_{\mathrm{DC}}^{\mathrm{R}} = \eta_3 P_{\mathrm{RF}}^{\mathrm{R}} = \eta_3 \mathbb{A}\big\{|y(t)|^2\big\}, \tag{2.11}$$

which suggests that maximizing the received RF signal power is sufficient to maximize the harvested DC power.

- *Non-linear (transition) region:* When the input power level is moderate, the output power increases *exponentially* with the input and η_3 is significantly higher than the linear region. This is the most interesting region that can be exploited to improve the overall power efficiency. For a tractable model, consider a perfectly matched $(Z_{\text{in}} = Z_{\text{A}}^*)$ half-wave rectifier in Fig. 2.8(b) and assume the voltage across the matching network is negligible. The received RF power is totally transferred to the rectifier input $P_{\text{RF}}^{\text{R}} = \mathbb{E}\big\{|y(t)|^2\big\} = \mathbb{E}\big\{|v_{\text{in}}(t)|^2/R_{\text{in}}\big\} = \mathbb{E}\big\{|v_{\text{in}}(t)|^2/R_{\text{A}}\big\}$ such that the voltage sources can be expressed in terms of the received signal [64]

$$v_{\text{in}}(t) = y(t)\sqrt{R_{\text{A}}}, \quad v_{\text{S}}(t) = 2y(t)\sqrt{R_{\text{A}}}. \tag{2.12}$$

The current passing through the diode is given by the characteristic equation $i_{\text{D}}(t) = I_{\text{S}}\big(\exp(v_{\text{D}}(t)/nv_{\text{T}}) - 1\big)$, where I_{S} is the reverse bias saturation current, v_{T} is the thermal voltage, and n is the ideality factor. Its Taylor expansion around the steady point $-v_{\text{out}}$ is [64]

$$i_{\text{D}}(t) = \sum_{i=0}^{\infty} k_i\big(v_{\text{D}}(t) + v_{\text{out}}\big)^i = \sum_{i=0}^{\infty} k_i v_{\text{in}}^i(t) = \sum_{i=0}^{\infty} k_i R_{\text{A}}^{i/2} y^i(t), \tag{2.13}$$

where $k_0 = I_{\text{S}}\big(\exp(-v_{\text{out}}/nv_{\text{T}}) - 1\big)$, $k_i = I_{\text{S}}\frac{\exp(-v_{\text{out}}/nv_{\text{T}})}{i!(nv_{\text{T}})^i}$ for $k \in \mathbb{N}$. The rectifier output DC current can be written as a function of the received signal

$$i_{\text{out}} = \sum_{i=0}^{\infty} k_i R_{\text{A}}^{i/2} \mathbb{A}\big\{y^i(t)\big\} = \sum_{i=0,\text{even}}^{\infty} k_i R_{\text{A}}^{i/2} \mathbb{A}\big\{y^i(t)\big\} \tag{2.14}$$

where the second equality is because $\mathbb{A}\big\{y^i(t)\big\} = 0$ for odd i. Note that the dependency of k_i on $-v_{\text{out}} = -i_{\text{out}}R_{\text{L}}$ makes it nontrivial to formulate a closed-form expression for the harvested DC power. Fortunately, it is shown in [64] that maximizing the harvested DC power is equivalent to maximizing the quantity

$$z \triangleq \sum_{i=2,\text{even}}^{n_0} \beta_i \mathbb{A}\big\{y^i(t)\big\}, \tag{2.15}$$

where $\beta_i = I_{\text{S}}\frac{R_{\text{A}}^{i/2}}{i!(nv_{\text{T}})^i}$ is a constant and n_0 is the truncation order. Selecting $n_0 = 2$ yields the same result as (2.11), which suggests that the linear model is a special case

of the more accurate non-linear model. For a moderate excitation, the contribution of higher-order terms is significant and should be modeled in the harvested DC power.

- *Saturation region:* When the input power level is too high, the diode works in the reverse breakdown region, the rectifier is saturated, and the output power is a constant. This is the region where the η_3 significantly drops and should be avoided by circuit design. For a fixed rectenna with Gaussian input signal, a parametric model was proposed in [67]

$$P_{\mathrm{DC}}^{\mathrm{R}} = \frac{\Psi_{\mathrm{DC}} - P_{\mathrm{sat}}\Omega}{1 - \Omega}, \quad \Psi_{\mathrm{DC}} = \frac{P_{\mathrm{sat}}}{1 + \exp\big(-a(P_{\mathrm{RF}}^{\mathrm{R}} - b)\big)}, \quad \Omega = \frac{1}{1 + \exp(ab)}, \tag{2.16}$$

where the constant P_{sat} denotes the maximum harvested power when the rectifier is saturated, and the constants a and b model the nonlinear charging rate with respect to input power and the minimum turn-on voltage of the rectifier, respectively. Parameters P_{sat}, a, and b can be obtained by curve fitting over measurement results.

The exact boundaries between those regions depend on the rectifier circuit and input waveform [68]. Signals with a higher PAPR usually exhibit the nonlinear and saturation effects at lower input power levels. For example, the nonlinear region is typically $[-20, 0]$ dBm for a CW and $[-30, -10]$ dBm for a multisine [69]. This not only motivates adaptive multi-carrier waveform designs [64, 68, 70, 71] but also calls for a joint optimization of the transmitter, channel (via RIS), and receiver to improve the end-to-end power efficiency.

2.3 Simultaneous Wireless Information and Power Transfer (SWIPT)

2.3.1 Introduction

WIT and WPT have been treated separately over the past century and have made significant progress in their respective fields. Interestingly, electromagnetic waves carry information and energy simultaneously and the same signal can be used for communication and power transfer. The idea of Simultaneous Wireless Information and Power Transfer (SWIPT) was first proposed in 2008 [72] and has since attracted significant attention from both academia and industry. It is a promising solution to connect and energize trillions of low-power mobile devices, providing power at microwatt level and coverage up to tens of meters in a unified manner [73]. SWIPT can also smoothly shift between the two extreme cases to fully exploit the RF spectrum and network infrastructure. It is envisioned that future network providers

will be able to offer a complete wireless solution including data and power services, which is essential for the upcoming intelligent era.

One of the most important issues in SWIPT is that the energy harvester requires a much higher received signal power (several orders of magnitude) than the information decoder [74]. Since the channel RF-to-RF efficiency η_2 is the primary constraint on the overall power efficiency, how to combat the pathloss and fading effects has been recognized as a crucial research topic for WPT and SWIPT. Fortunately, this issue can be effectively mitigated by introducing a RIS to the environment. By carefully tuning the scatter response of the RIS elements, one can potentially achieve the following benefits:

- *Energy focusing:* The scattered waves can be steered towards the receivers or focused on a dedicated "hotspot zone" to increase the harvester input power level. This is also helpful to extend the coverage and improve the reliability of the energy link.

- *Beam splitting:* Instead of transmitting one strong beam towards each user, the energy signal can be split into multiple weaker beams rerouted by the RIS to even out the spatial power distribution. This is useful to bypass physical obstacles (especially in high-frequency and large-scale networks) and reduce the health risk of radiation.

RIS can also be used to assist the information link by Signal-to-Noise Ratio (SNR) enhancement and interference suppression, as mentioned in subsection 1.2.3.

2.3.2 Rate-Energy (R-E) Trade-off

Despite WIT and WPT share many similarities, their difference in design objectives, system architectures, and practical constraints make a joint implementation of SWIPT particularly challenging. Some preference of WIT and WPT are inherently conflicting, for example:

- *Waveform and modulation:* Under an average power constraint, WIT favors Gaussian signaling with maximum entropy distribution [75] while WPT prefers deterministic (unmodulated) multisine with higher PAPR [76].

- *Channel:* In a MIMO scenario, WIT favors full-rank Non-Line-of-Sight (NLoS) with high spatial diversity at high SNR while WPT prefers rank-deficient Line-of-Sight (LoS) with high spatial correlation [77].

- *Receiver:* The power sensitivity is usually in the range of -40 to -80 dBm for information receivers and -10 to -30 dBm for energy harvesters [78].

Those disparities translate to a fundamental trade-off between information and power transfer in SWIPT systems, which is often quantified by a *Rate-Energy (R-E) region*.

$$\mathcal{C}_{\text{R}-\text{E}}(P) \triangleq \Big\{ (r, e) : 0 \le r \le \log(1 + \gamma), \ 0 \le e \le z \Big\}, \tag{2.17}$$

where P is the average transmit power, γ is the SNR at the information decoder, and z in (2.15) relates to the harvested DC power. Each point in this region corresponds to a *rate-energy pair* achieved by a particular *resource allocation scheme*. It is worth mentioning that different transceive strategies (e.g., waveform and receiver design) can lead to totally different R-E regions instead of different points in the same region, which motivates a joint optimization of the transmitter, channel, and receiver.

2.3.3 Modules and Operation Modes

2.3.3.1 Information and Energy Flows

In SWIPT, the information and energy are always transmitted from the same source while their receivers can be either co-located or separated, as shown in Figs. 2.9(a) and 2.9(b). This is different from BackCom where the energy is delivered in the downlink and the information is sent in the uplink, as shown in Figs. 2.9(c) and 2.9(d).
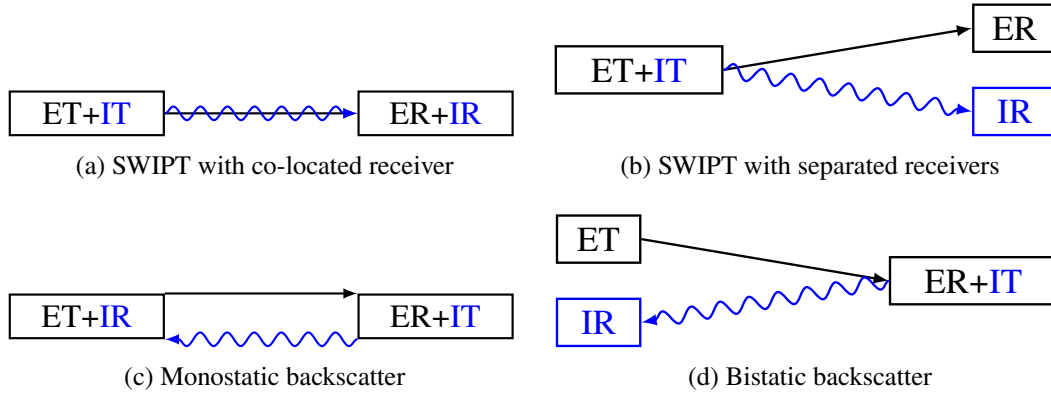
Fig. 2.9 Information and energy flows in SWIPT and BackCom systems. The blue and black parts denote information and power subsystems, respectively.

From a design perspective, co-located SWIPT receiver is a more general model since it can exploit the received signal for either purpose or a mixture in between. We thus focus on this model in the following context.

2.3.3.2 Receiver Architectures

Figure 2.10 illustrates four potential architectures for a co-located SWIPT receiver [79]:

(a) Ideal receiver   (b) Time switching receiver

(c) Power splitting receiver   (d) Integrated receiver
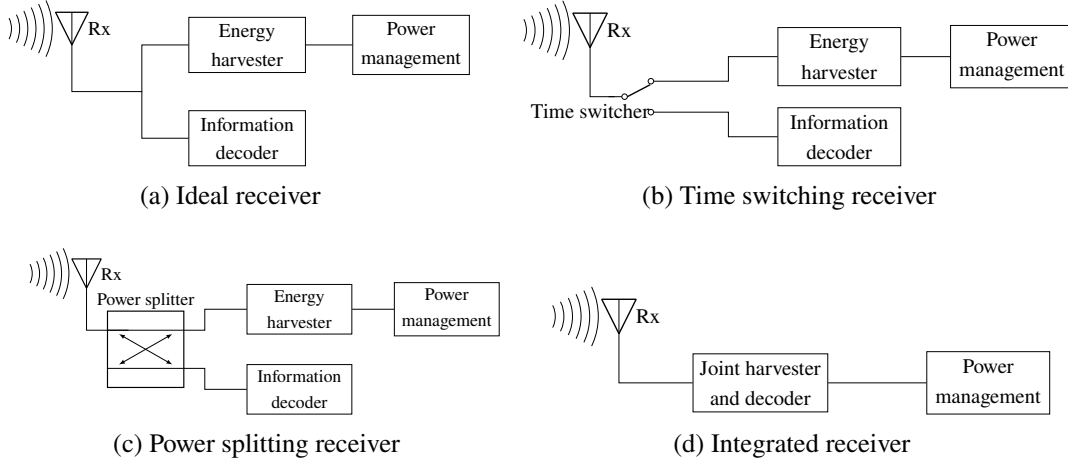
Fig. 2.10 Architectures of a co-located SWIPT receiver.

- *Ideal receiver:* The received signal is used for both information decoding and energy harvesting. This is theoretically the most efficient design with a rectangle R-E region but is unimplementable in practice due to hardware constraints.

- *Time Switching (TS) receiver:* Each time block is divided into individual WIT and WPT phases, where the receiver switches between information decoder and energy harvester, respectively. The transmitted waveform and RIS response are optimized independently for each phase, and the resulting R-E region is a triangle with two vertices corresponding to WIT-only and WPT-only.

- *Power Splitting (PS) receiver:* The received signal is split into two parts with power ratio ρ and $1-\rho$. The former is fed into the energy harvester and the latter is used for information decoding. The transmitter and RIS are jointly optimized for both purposes with the knowledge of splitting ratio, and the resulting R-E region may be non-convex.

- *Integrated receiver [80]:* The transmit signal is modulated in properties that can be well-preserved after rectification (e.g., pulse position) such that information can be decoded from the energy harvester output.

The most popular architectures in the literature are TS and PS due to their practicality and tractability. The R-E region of the former can be inferred from that of the latter, since the WIT-only and WPT-only vertices in TS correspond to $\rho = 1$ and $\rho = 0$ in PS,

respectively. Integrated receiver eliminates the need of RF chains and advanced architectures, but experiences information degradation and fits low-throughput applications.

2.4 Backscatter Communication (BackCom)

2.4.1 Introduction

The scattered waves from any object inherently contain some information about the object. This contributed to the great success of radar in the World War II, where the "objective" information about the target (e.g., size, speed, and position) can be extracted from the reflected signal. Soon after the war in 1948, Stockman demonstrated the concept of BackCom where the target is no longer a dumb wave scatterer but part of the communication system that is willing to modulates its "subjective" information over the reflected signal [81]. The communication society quickly realized its potential to separate the power-hungry RF carrier emitter with the low-power information modulator, which is essential for miniaturizing wireless devices and increasing the network scale. As shown in Figs. 2.9(c) and 2.9(d) on Page 47, the backscatter node (a.k.a. tag) is activated by an energy signal (also functions as carrier) in the downlink and modulates over the scattered signal in the uplink. The energy transmitter (a.k.a. carrier emitter) and information receiver (a.k.a. reader) can be either co-located or separated, known respectively as monostatic and bistatic BackCom.

One of the most well-known BackCom applications is RFID which made its debut in the 1970s [82]. RFID readers sends a query signal and exploit the reflected signal from nodes (attached to objects) to identify and track them. The nodes can be powered wirelessly by the impinging wave and does not have to be in the vicinity of the reader. It has been standardized in ISO/IEC 18000 and EPC Gen2 [83] and widely used in supply chain management, access control, and asset tracking. On the other hand, BackCom also plays an important role in emerging applications like IoT, WSN, and Machine-to-Machine (M2M) communications. Their main difference to RFID is that the message is no longer a static identifier but can be dynamically sensed from the environment or generated on demand. This enables a new paradigm of self-sustainable, intelligent, and pervasive sensing and communication, which is a key building block for our initial vision.

Nevertheless, low throughput and limited coverage are acknowledged as two critical problems for conventional BackCom systems. Those are inevitably inherited from the nature of wave scattering — the radiated signal has to travel a round trip (emitter-node-reader) with double pathloss, while the scatter response is frequency-dependent and usually results in a narrow bandwidth. Monostatic BackCom is also subject to a strong self-interference that

further degrades the error performance and achievable rate. Finally, the nodes are idle most of the time and only respond when externally inquired. This is in sharp contrast to RIS where the elements are contributing for channel enhancement all the time. To mitigate those issues, multi-antenna techniques and special modulation schemes are two promising solutions in the literature. For example, a multi-antenna carrier emitter can perform energy beamforming [84], a multi-antenna node can perform energy combining with spatial modulation [85, 86] or space-time coding [87], and a multi-antenna reader can perform coherent [88, 89] or non-coherent [90] detection. We will discuss some popular modulation and coding techniques for BackCom in the following subsection.

2.4.2 Modulation and Coding Schemes

BackCom and RIS share the same wave scattering model in Section 2.1.2.1, but the reflection coefficient Γ in (2.4) is exploited in different manners. The difference is two-fold:

- *Modulation requires variation:* BackCom relies on dynamically changing the reflection coefficient over time to encode information. This is different from RIS where the optimal configuration (and reflection coefficient) is fixed for a given channel realization.

- *Harvesting requires absorption:* Part of the impinging wave should be fed into the node to power its operation. This is different from RIS where a full reflection is desired to maximize its energy efficiency.

Denote the amplitude scattering ratio of the BackCom node as α that corresponds to a power absorption ratio $(1 - \alpha)^2$. Some popular modulation schemes are summarized below:

- *Quadrature Amplitude Modulation (QAM) [91]:* The reflection coefficient corresponding to the m-th symbol is

$$\Gamma_m = \alpha \frac{c_m}{\max_{m'}|c_{m'}|} \tag{2.18}$$

  where c_m is the corresponding constellation point. This scheme is simple but exhibits a low detection SNR especially when the constellation size is large.

- *Frequency-Shift Keying (FSK) [83]:* For 2-FSK, the reflection coefficient is

$$\Gamma(t) = \begin{cases} \alpha, & t \in \left[\frac{n}{\Delta f}, \frac{2n+1}{2\Delta f}\right) \\ -\alpha, & t \in \left[\frac{2n+1}{2\Delta f}, \frac{n+1}{\Delta f}\right) \end{cases} = \frac{\pi}{4} \sum_{m=1,\text{odd}}^{\infty} \frac{\alpha}{m} \sin\left(2\pi m \Delta f t\right), \tag{2.19}$$

where $n \in \mathbb{N}$. If the incident wave is a CW at frequency f_0, the reflected signal is dominated by its first harmonic

$$s_1(t) = \frac{\alpha\pi}{2}\Big(\sin\big(2\pi(f_0+\Delta f)t\big) - \sin\big(2\pi(f_0-\Delta f)t\big)\Big). \tag{2.20}$$

That is, periodically switching the reflection coefficient at rate Δf results in a frequency shift $\pm\Delta f$ on the reflected signal. Practical implementations have been demonstrated on a variety of license-free protocols (e.g., HitchHike [92], inter-technology [93], Passive Wi-Fi [94], BLE-Backscatter [95]) where the mirror copy can be suppressed.

- *Chirp Spread Spectrum (CSS) [96]:* A chirp is a signal whose frequency increases or decreases over time. CSS uses wideband linear-frequency modulated chirps to encode information, which is from Direct-Sequence Spread Spectrum (DSSS) and Frequency-Hopping Spread Spectrum (FHSS) with pseudo-random sequences and FSK with discrete frequencies. In particular, $N + 1$ reflection coefficients of the same envelope are sequentially selected at a regular rate Δf, given by

$$\Gamma_n = \alpha \exp(\jmath\phi_n), \quad n \in \{0, 1, \dots, N\}, \tag{2.21}$$

where $\phi_n = \frac{2\pi}{\Delta f}(An^2 + Bn)$ and A, B are constants. As the core modulation scheme in Long Range (LoRa), it is more robust to noise and interference (with a reception sensitivity of -149 dBm), harder to be detected by eavesdroppers, and can be used for ranging and localization [83].

Common BackCom channel coding schemes include unipolar Return-to-Zero (RZ) and Non-Return-to-Zero (NRZ), Manchester, differential, pulse-pause and FM0. They are not the focus of the thesis and the readers are referred to [97, Chapter 2.3] for details.

2.4.3 Applications

(a) Monostatic backscatter

(b) Bistatic backscatter

(c) Ambient backscatter

(d) Symbiotic radio
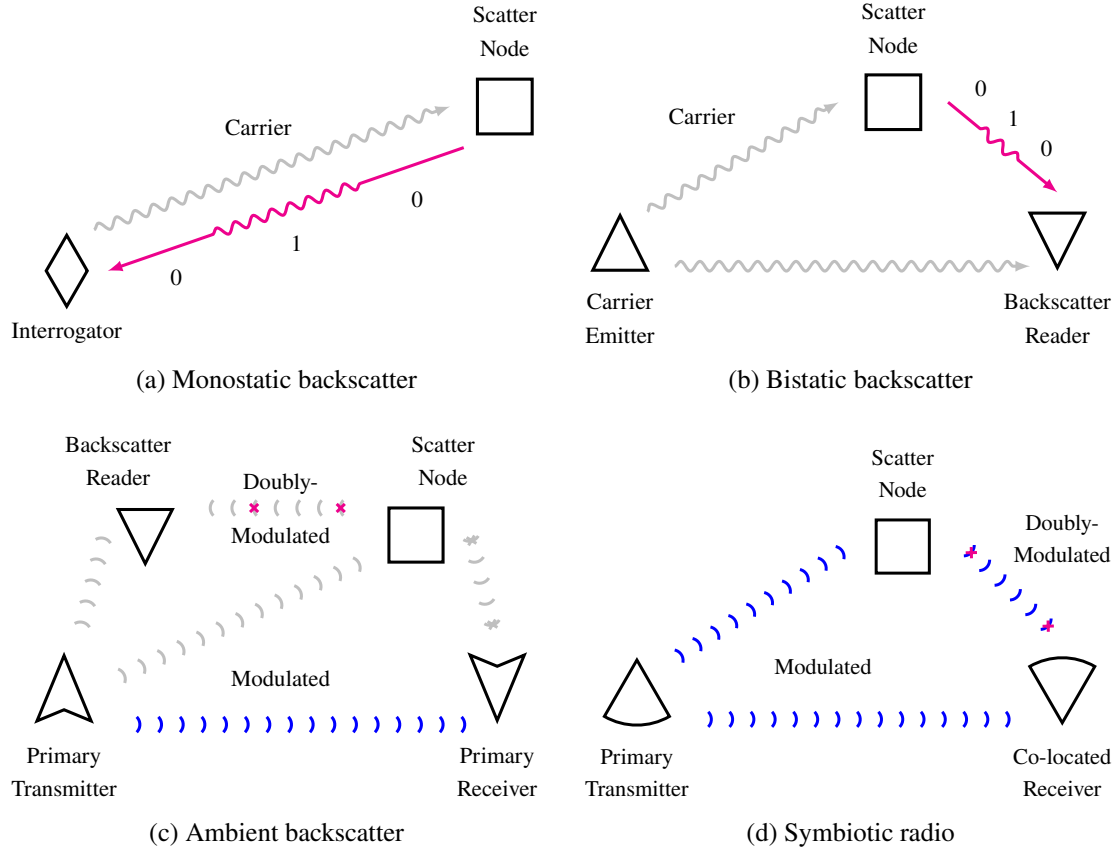
Fig. 2.11 Illustration of scattering applications. The blue flows denote the primary link while the magenta flows denote the backscatter link.

2.4.3.1 Monostatic Backscatter Communication (MBC)

Monostatic Backscatter Communication (MBC) is probably the most common BackCom scenario where the carrier emitter and reader are integrated into one device called interrogator. As shown in Figs. 2.9(c) and 2.11(a), the interrogator transmits a CW in the downlink and receives the reflected information-bearing signal in the uplink. The node varies its load impedance over time to switch between two states. Ideally, a full absorption (perfect matching, $\Gamma_0 = 0$) maps to bit "0" where energy is harvested, and a full reflection (perfect mismatch, $|\Gamma_1| = 1$) maps to bit "1" where SNR is determined. MBC is widely used in RFID systems. The integrated transceiver design reduces the hardware cost but suffers from strong self-interference and limited coverage.

2.4.3.2 Bistatic Backscatter Communication (BBC)

Bistatic Backscatter Communication (BBC) separates the carrier emitter and reader into two individual devices, as illustrated in Figs. 2.9(d) and 2.11(b). This helps to combat self-interference and extend the operation range, but the system involves three devices and requires more complex coordination and synchronization. It is more popular in more complicated scenarios like WSN and IoT with potentially moving nodes.

2.4.3.3 Ambient Backscatter Communication (AmBC)

Ambient Backscatter Communication (AmBC) has been recognized as a revolutionary technology since its debut in 2013 [98]. As shown in Fig. 2.11(c), it gets rid of dedicated RF sources and relies on ambient signals (e.g., TV, FM, and Wi-Fi) for both energy harvesting and information transfer. Compared with MBC and BBC, its carrier waveform is no longer a CW but a mixture of already modulated signals with different frequencies and amplitudes, which makes the detection more challenging. Therefore, it often employs FSK modulation that shifts the scattered signals to a different band for reduced interference on both coexisting systems. AmBC is a plug-and-play and environmental-friendly IoT solution, but its practical deployment is limited by the availability and quality of ambient signals.

2.4.3.4 Symbiotic Radio (SR)

Symbiotic Radio (SR) is a relatively new concept proposed in 2019 that introduced itself as "cooperative AmBC" [99]. As shown in Fig. 2.11(d), it shares not only the transmitter, RF source, but also the receiver with a primary transmission. This is different from traditional AmBC where the legacy system can be unaware of the backscatter link and the node wants to minimize its footprint. Such a symbiotic interaction can improve the reliability of the backscatter link as well as the energy efficiency of the primary link, but unavoidably challenges the system design. For example, the acquisition of backscatter CSI can be difficult due to its passive characteristic, the detection of node message may involve complicated signal processing like Successive Interference Cancellation (SIC), and the synchronization of both links can be nontrivial due to the load-switching constraints. If those issues can be mitigated, SR would be a win-win solution that supercharges resource-constrained devices by leveraging the existing network infrastructure.

Chapter 3

RIS-Aided SWIPT: Joint Waveform and Beamforming Design

3.1 Introduction

3.1.1 Simultaneous Wireless Information and Power Transfer

With the great advance in communication performance, a bottleneck of wireless networks has come to energy supply. SWIPT is a promising solution to connect and power mobile devices via RF waves. It provides low power at milliwatt level but broad coverage up to hundreds of meters in a sustainable and controllable manner, bringing more opportunities to the IoT and M2M networks. The upsurge in wireless devices, together with the decrease of electronics power consumption, calls for a re-thinking of future wireless networks based on WPT and SWIPT [74].

The concept of SWIPT was first cast in [72], where the authors investigated the R-E trade-off for a flat Gaussian channel and typical discrete channels. [100] proposed two practical co-located information and power receivers, i.e., TS and PS. Dedicated information and energy beamforming were then investigated in [101, 102] to characterize the R-E region for multi-antenna broadcast and interference channels. On the other hand, [76] pointed out that the RF-to-DC conversion efficiency of rectifiers depends on the input power and waveform shape. It implies that the modeling of the energy harvester, particularly its nonlinearity, has a crucial impact on the waveform preference, resource allocation, and system design of any wireless-powered systems [76, 103, 74]. Motivated by this, [64] derived a tractable nonlinear harvester model based on the Taylor expansion of diode I-V characteristics, and performed joint waveform and beamforming design for WPT. Simulation and experiments showed the benefit of modeling energy harvester nonlinearity in real system design [104, 105]

and demonstrated the joint waveform and beamforming strategy as a key technique to expand the operation range [106]. A low-complexity adaptive waveform design by Scaled Matched Filter (SMF) was proposed in [107] to exploit the rectifier nonlinearity, whose advantage was then demonstrated in a prototype with channel acquisition [108]. Beyond WPT, [73] uniquely showed that the rectifier nonlinearity brings radical changes to SWIPT design, namely:

- Modulated and unmodulated waveforms are not equally suitable for wireless power delivery;

- A multi-carrier unmodulated waveform superposed to a multi-carrier modulated waveform can enlarge the R-E region;

- A combination of PS and TS is generally the best strategy;

- The optimal input distribution is not the conventional Circularly Symmetric Complex Gaussian (CSCG);

- Modeling rectifier nonlinearity is beneficial to system performance and essential to efficient SWIPT design.

Those observations, validated experimentally in [104], led to the question: *What is the optimal input distribution for SWIPT under nonlinearity?* This question was answered in [109] for single-carrier SWIPT, and some attempts were further made in [110] for multi-carrier SWIPT. The answers shed new light to the fundamental limits of SWIPT and practical signaling (e.g., modulation and waveform) strategies. It is now well understood from [73, 109, 110] that, due to harvester nonlinearity, a combination of CSCG and on-off keying in single-carrier setting and non-zero mean asymmetric inputs in multi-carrier setting lead to significantly larger R-E region compared to conventional CSCG. Recently, [111] used machine learning techniques to design SWIPT signaling under nonlinearity to complement the information-theoretic results of [109], and new modulation schemes were subsequently invented.

3.1.2   Reconfigurable Intelligent Surface

RIS has recently emerged as a promising technique that adapts the propagation environment to enhance the spectrum and energy efficiency. In practice, a RIS consists of multiple individual sub-wavelength reflecting elements to adjust the amplitude and phase of the incoming signal (i.e., passive beamforming). Different from the relay, backscatter and frequency-selective surface [14], the RIS assists the primary transmission using passive components with negligible thermal noise but is limited to frequency-dependent reflection.

Inspired by the development of real-time reconfigurable metamaterials [38], the authors of [112] introduced a programmable metasurface that steers or polarizes the electromagnetic wave at a specific frequency to mitigate signal attenuation. [50] proposed a RIS-assisted Multiple-Input Single-Output (MISO) system and jointly optimized the precoder at the Access Point (AP) and the phase shifts at the RIS to minimize the transmit power. The active and passive beamforming problem was then extended to the discrete phase shift case [113] and the multi-user case [16]. In [49], the authors investigated the impact of non-zero resistance on the reflection pattern and emphasized the coupling between reflection amplitude and phase shift in practice. To estimate the cascaded AP-RIS-User Equipment (UE) link without RF-chains at the RIS, practical protocols were developed based on element-wise on/off switching [114], training sequence and reflection pattern design [115, 116], and compressed sensing [117]. The hardware architecture, design challenges, and application opportunities of practical RIS were covered in [1]. In [12], a prototype RIS with 256 2-bit elements based on PIN diodes was developed to support real-time video transmission at gigahertz and mmWave frequency.

3.1.3   RIS-Aided SWIPT

By integrating RIS with SWIPT, the constructive reflection can boost the end-to-end power efficiency and improve the R-E trade-off. In multi-user cases, dedicated energy beams were proved unnecessary for the weighted sum-power maximization [118] but essential when fairness issue is considered [119]. It was also claimed that LoS links could boost the power efficiency since rank-deficient channels require fewer energy beams [120]. However, [118–120] were based on a linear energy harvester model that is known in both the RF and the communication literature to be inefficient and inaccurate [74, 76, 103, 64, 104–108, 73, 109–111]. Based on practical RIS and harvester models, [121] introduced a scalable resource allocation framework for a large-scale tile-based RIS-assisted SWIPT system, where the optimization consists of a reflection design stage and a joint reflection selection and precoder design stage. The proposed framework provides a flexible trade-off between performance and complexity. To the best of our knowledge, all existing papers considered resource allocation and beamforming design for dedicated information and energy users in a single-carrier network. In this chapter, we instead build our design based on a proper nonlinear harvester model that captures the dependency of the output DC power on both the power and shape of the input waveform, and marry the benefits of joint multi-carrier waveform and active beamforming optimization for SWIPT with the passive beamforming capability of RIS, to investigate the R-E trade-off for one SWIPT user with co-located information decoder and energy harvester. We ask ourselves the important question: *How to jointly exploit the spatial domain and the frequency domain efficiently through joint waveform and beamforming*

design to enlarge the R-E region of RIS-aided SWIPT? The contributions of this chapter are summarized as follows.

First, we propose a novel RIS-aided SWIPT architecture based on joint waveform, active and passive beamforming design under the diode nonlinear model (2.15) [64]. Although this tractable harvester model accurately reveals how the input power level and waveform shape influence the output DC power, it also introduces design challenges such as frequency coupling (i.e., components of different frequencies compensate and produce DC), waveform coupling (i.e., different waveforms jointly contribute to DC), and high-order objective function. To make an efficient use of the rectifier nonlinearity, we superpose a multi-carrier unmodulated power waveform (deterministic multisine) to a multi-carrier modulated information waveform and evaluate the performance under the TS and PS receiving modes. The proposed joint waveform, active and passive beamforming architecture exploits the rectifier nonlinearity, the channel selectivity, and a beamforming gain across frequency and spatial domains to enlarge the achievable R-E region. This is the first work to propose a joint waveform, active and passive beamforming architecture for RIS-aided SWIPT.

Second, we characterize each R-E boundary point by energy maximization under a rate constraint. The problem is solved by a Block Coordinate Descent (BCD) algorithm based on the Channel State Information at the Transmitter (CSIT). For active beamforming, we prove that the global optimal active information and power precoders coincide at Maximum Ratio Transmission (MRT) even with rectifier nonlinearity. For passive beamforming, we propose a Successive Convex Approximation (SCA) algorithm and retrieve the RIS phase shift by eigen decomposition with optimality proof. Finally, the superposed waveform and the splitting ratio are optimized by the Geometric Programming (GP) technique. The RIS phase shift, active precoder, and waveform amplitude are updated iteratively until convergence. This is the first work to jointly optimize waveform and active/passive beamforming in RIS-aided SWIPT.

Third, we introduce two closed-form adaptive waveform schemes to avoid the exponential complexity of the GP algorithm. To facilitate practical SWIPT implementation, the Water-Filling (WF) strategy for modulated waveform and the SMF strategy for multisine waveform are combined in time and power domains, respectively. The passive beamforming design is also adapted to accommodate the low-complexity waveform schemes. The proposed low-complexity BCD algorithm achieves a good balance between performance and complexity.

Fourth, we provide numerical results to evaluate the proposed algorithms. It is concluded that:

- RIS enables constructive reflection and flexible subchannel design in the frequency domain that is essential for SWIPT systems;

- RIS mainly affects the effective channel instead of the waveform design;

- Multisine waveform is beneficial to energy transfer especially when the number of subbands is large;

- TS is preferred at low SNR while PS is preferred at high SNR;

- There exist two optimal RIS development locations, one close to the AP and one close to the UE;

- The output SNR scales linearly with the number of transmit antennas and quadratically with the number of RIS elements;

- Due to the rectifier nonlinearity, the output DC scales quadratically with the number of transmit antennas and quartically with the number of RIS elements;

- For narrowband SWIPT, the optimal active and passive beamforming for any R-E point are also optimal for the whole R-E region;

- For broadband SWIPT, the optimal active and passive beamforming depend on specific R-E point and require adaptive designs;

- The proposed algorithms are robust to practical impairments such as inaccurate cascaded CSIT and finite RIS reflection states.

3.2 System Model
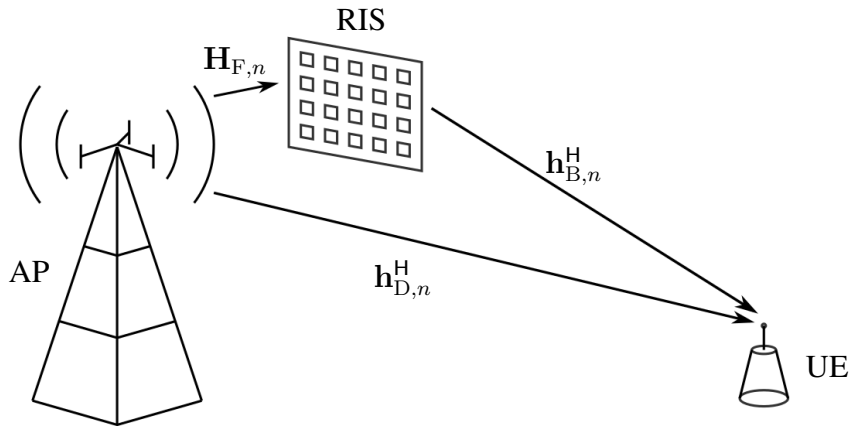
Fig. 3.1 A RIS-aided multi-carrier MISO SWIPT system.

As shown in Fig. 3.1, we propose a RIS-aided SWIPT system where an M-antenna AP delivers information and power simultaneously, through an L-element RIS, to a single-antenna

UE over N orthogonal evenly-spaced subbands. We consider a quasi-static block fading model and assume the CSIT of direct and cascaded channels (defined in Section 3.2.2) can be acquired. The signals reflected by two or more times are omitted, and the noise power is assumed too small to be harvested. We assume that the time difference of signal arrival via direct and reflected paths is negligible compared to the symbol period.

3.2.1 Transmitted Signal

Following [73], we superpose a multi-carrier modulated information-bearing waveform to an unmodulated power-dedicated multisine to boost the spectrum and energy efficiency. It is worth mentioning that the latter is beneficial for WPT due to its higher PAPR (as discussed in Section 2.2.3.2) and better high-order statistics on expectation (c.f. (3.9b) and (3.9d) in Section 3.2.6). The information signal transmitted over subband $n \in \mathcal{N} \triangleq \{1, \ldots, N\}$ at time t is

$$\mathbf{x}_{\mathrm{I},n}(t) = \Re \left\{ \mathbf{w}_{\mathrm{I},n} \tilde{x}_{\mathrm{I},n}(t) e^{j2\pi f_n t} \right\}, \tag{3.1}$$

where $\mathbf{w}_{\mathrm{I},n} \in \mathbb{C}^{M \times 1}$ is the information precoder at subband n, $\tilde{x}_{\mathrm{I},n} \sim \mathcal{CN}(0,1)$ is the information symbol at subband n, and f_n is the frequency of subband n. On the other hand, the power signal transmitted over subband n at time t is

$$\mathbf{x}_{\mathrm{P},n}(t) = \Re \left\{ \mathbf{w}_{\mathrm{P},n} e^{j2\pi f_n t} \right\}, \tag{3.2}$$

where $\mathbf{w}_{\mathrm{P},n} \in \mathbb{C}^{M \times 1}$ is the power precoder at subband n. Therefore, the superposed signal transmitted over all subbands at time t is

$$\mathbf{x}(t) = \Re \left\{ \sum_{n=1}^{N} (\mathbf{w}_{\mathrm{I},n} \tilde{x}_{\mathrm{I},n}(t) + \mathbf{w}_{\mathrm{P},n}) e^{j2\pi f_n t} \right\}. \tag{3.3}$$

We also define $\mathbf{w}_{\mathrm{I/P}} \triangleq [\mathbf{w}_{\mathrm{I/P},1}^{\mathsf{T}}, \ldots, \mathbf{w}_{\mathrm{I/P},N}^{\mathsf{T}}]^{\mathsf{T}} \in \mathbb{C}^{MN \times 1}$.

3.2.2 Reflection Pattern and Composite Channel

As discussed in Section 2.1.2.1, RIS element $l \in \mathcal{L} \triangleq \{1, \ldots, L\}$ varies its load impedance Z_l to manipulate the reflection coefficient θ_l (2.5). In the ideal scenario, this corresponds to a full reflection $|\theta_l| = 1$ with phase shift $\phi_l \in [0, 2\pi)$.

Remark 3.1. *Since the reactance X_l is a function of frequency, the reflection coefficient θ_l cannot be designed independently at different subbands. In this chapter, we assume the*

bandwidth is small compared to the operating frequency, such that the reflection coefficient at different subbands is approximately the same.

At subband n, we denote the AP-UE direct channel as $\mathbf{h}_{\mathrm{D},n}^{\mathsf{H}} \in \mathbb{C}^{1 \times M}$, the AP-RIS forward channel as $\mathbf{H}_{\mathrm{F},n} \in \mathbb{C}^{L \times M}$, and the RIS-UE backward channel as $\mathbf{h}_{\mathrm{B},n}^{\mathsf{H}} \in \mathbb{C}^{1 \times L}$. The auxiliary AP-RIS-UE link can be modeled as a concatenation of the backward channel, the RIS reflection, and the forward channel. Hence, the equivalent channel is given by

$$\mathbf{h}_n^{\mathsf{H}} = \mathbf{h}_{\mathrm{D},n}^{\mathsf{H}} + \mathbf{h}_{\mathrm{B},n}^{\mathsf{H}} \boldsymbol{\Theta} \mathbf{H}_{\mathrm{F},n} = \mathbf{h}_{\mathrm{D},n}^{\mathsf{H}} + \boldsymbol{\theta}^{\mathsf{H}} \mathbf{V}_n, \tag{3.4}$$

where $\boldsymbol{\theta} \triangleq [\theta_1, \ldots, \theta_L]^{\mathsf{H}} \in \mathbb{C}^{L \times 1}$ and $\mathbf{V}_n \triangleq \mathrm{diag}(\mathbf{h}_{\mathrm{B},n}^{\mathsf{H}}) \mathbf{H}_{\mathrm{F},n} \in \mathbb{C}^{L \times M}$ is the cascaded RIS channel.

Remark 3.2. *The cascaded channel $\mathbf{V}_n$ varies at different subbands and there exists a trade-off for passive beamforming design in the frequency domain. Therefore, the equivalent subchannels should be carefully designed to meet specific requirements of multi-carrier SWIPT. For example, one can design the reflection pattern to either enhance the strongest subband (e.g., $\max_{\boldsymbol{\theta},n} \|\mathbf{h}_n\|$), or improve the fairness among subbands (e.g., $\max_{\boldsymbol{\theta}} \min_n \|\mathbf{h}_n\|$). That is to say, RIS enables a flexible subchannel design in multi-carrier transmissions. A similar effect also exists in the spatial domain for multi-antenna scenarios. In total, each reflection coefficient is indeed shared by M antennas over N subbands.*

3.2.3 Received Signal

The received superposed signal at the single-antenna UE is

$$y(t) = \Re \left\{ \sum_{n=1}^{N} \left(\mathbf{h}_n^{\mathsf{H}} (\mathbf{w}_{\mathrm{I},n} \tilde{x}_{\mathrm{I},n}(t) + \mathbf{w}_{\mathrm{P},n}) + v_n(t) \right) e^{j2\pi f_n t} \right\}, \tag{3.5}$$

where $v_n(t)$ is the noise at RF band n. Please note that the modulated component can be used for energy harvesting if necessary, but the multisine component carries no information and cannot be used for information decoding.

3.2.4 Receiving Modes

Following the discussion in Section 2.3.3.2, we investigate the performance of TS and PS receivers in this work.[1] The TS receiver divides each transmission block into orthogonal data and energy sessions with duration $1 - \eta$ and η, respectively. During each session, the transmitter optimizes the waveform for either WIT or WPT, while the receiver activates the information decoder or the energy harvester correspondingly. The duration ratio η thus controls the R-E trade-off and is independent from the waveform and beamforming design. On the other hand, the PS receiver splits the incoming signal into individual data and energy streams with power ratio $1 - \rho$ and ρ, respectively. The data stream is fed into the information decoder while the energy stream is fed into the energy harvester. During each transmission block, the superposed waveform and splitting ratio are jointly designed to achieve different performance trade-offs. Since the R-E region of the TS receiver can be inferred from that of the PS receiver, we focus on the optimization with the PS receiver in the following context.

3.2.5 Information Decoder

A major benefit of the superposed waveform is that the multisine is deterministic and its impact on WIT can be completely eliminated by waveform cancellation or translated demodulation [73]. The former is achieved by subtracting the multisine from the received signal at additional signal processing cost, while the latter requires a demodulator with higher saturation power level. The achievable rate is thus

$$R(\boldsymbol{\theta}, \mathbf{w}_{\mathrm{I}}, \rho) = \sum_{n=1}^{N} \log_2 \left(1 + \frac{(1-\rho)|\mathbf{h}_n^{\mathsf{H}} \mathbf{w}_{\mathrm{I},n}|^2}{\sigma_n^2} \right), \tag{3.6}$$

where σ_n^2 is the variance of the total noise (at the RF-band and during the RF-to-baseband conversion) on tone n.

3.2.6 Energy Harvester

As discussed in Section 2.2.3.2, the output DC power of the energy harvester is a nonlinear function of the input power and waveform shape. When the diode is forward-biased and unsaturated, a truncated Taylor expansion of the diode I-V characteristic equation suggests

---

[1]It is worth mentioning that many other SWIPT transceiving strategies have been proposed in the literature. In particular, frequency selection is more practical where multisine is used over n subbands and information is carried over the remaining $N - n$ subbands, where n is a design parameter. This can be viewed as a special case of PS and its R-E region is strictly contained with that of the latter, such that we don't include a special study in this work.

that maximizing the average output DC is equivalent to maximizing a monotonic function [73]

$$z(\boldsymbol{\theta}, \mathbf{w}_{\mathrm{I}}, \mathbf{w}_{\mathrm{P}}, \rho) = \sum_{i=2,\text{even}}^{n_0} \beta_i \rho^{i/2} \mathbb{E}\left\{\mathbb{A}\left\{y^i(t)\right\}\right\}, \tag{3.7}$$

which is slightly different from (2.15) in that (i) only a power ratio ρ of the received signal is used for energy harvesting and (ii) part of the received waveform is modulated such that expectation has to be taken. With a slight abuse of notation, we refer to z as the average output DC in this chapter. It can be observed that the conventional linear harvester model, where the output DC power equals the sum of the power harvested on each frequency, is a special case of (3.7) with $n_0 = 2$. However, due to the coupling effect among different frequencies, some high-order frequency components compensate each other in frequency and further contribute to the output DC power. In other words, even-order terms with $i \geq 4$ account for the nonlinear diode behavior. For simplicity, we choose $n_0 = 4$ to investigate the fundamental rectifier nonlinearity. The average output DC power is then

$$z(\boldsymbol{\theta}, \mathbf{w}_{\mathrm{I}}, \mathbf{w}_{\mathrm{P}}, \rho) = \beta_2 \rho \Big(\mathbb{E}\left\{\mathbb{A}\left\{y_{\mathrm{I}}^2(t)\right\}\right\} + \mathbb{A}\left\{y_{\mathrm{P}}^2(t)\right\} \Big)$$
$$+ \beta_4 \rho^2 \Big(\mathbb{E}\left\{\mathbb{A}\left\{y_{\mathrm{I}}^4(t)\right\}\right\} + \mathbb{A}\left\{y_{\mathrm{P}}^4(t)\right\} + 6\mathbb{E}\left\{\mathbb{A}\left\{y_{\mathrm{I}}^2(t)\right\}\right\} \mathbb{A}\left\{y_{\mathrm{P}}^2(t)\right\} \Big), \tag{3.8}$$

and the components can be further rewritten as (note that $\mathbb{E}\left\{|\tilde{x}_{\mathrm{I},n}|^4\right\} = 2$ applies a modulation gain on the fourth-order DC terms)

$$\mathbb{E}\left\{\mathbb{A}\left\{y_{\mathrm{I}}^2(t)\right\}\right\} = \frac{1}{2}\sum_{n=1}^{N}(\mathbf{h}_n^{\mathsf{H}}\mathbf{w}_{\mathrm{I},n})(\mathbf{h}_n^{\mathsf{H}}\mathbf{w}_{\mathrm{I},n})^* = \frac{1}{2}\mathbf{h}^{\mathsf{H}}\mathbf{W}_{\mathrm{I},0}\mathbf{h}, \tag{3.9a}$$

$$\mathbb{E}\left\{\mathbb{A}\left\{y_{\mathrm{I}}^4(t)\right\}\right\} = \frac{3}{4}\left(\sum_{n=1}^{N}(\mathbf{h}_n^{\mathsf{H}}\mathbf{w}_{\mathrm{I},n})(\mathbf{h}_n^{\mathsf{H}}\mathbf{w}_{\mathrm{I},n})^*\right)^2 = \frac{3}{4}(\mathbf{h}^{\mathsf{H}}\mathbf{W}_{\mathrm{I},0}\mathbf{h})^2, \tag{3.9b}$$

$$\mathbb{A}\left\{y_{\mathrm{P}}^2(t)\right\} = \frac{1}{2}\sum_{n=1}^{N}(\mathbf{h}_n^{\mathsf{H}}\mathbf{w}_{\mathrm{P},n})(\mathbf{h}_n^{\mathsf{H}}\mathbf{w}_{\mathrm{P},n})^* = \frac{1}{2}\mathbf{h}^{\mathsf{H}}\mathbf{W}_{\mathrm{P},0}\mathbf{h}, \tag{3.9c}$$

$$\mathbb{A}\left\{y_{\mathrm{P}}^4(t)\right\} = \frac{3}{8}\sum_{\substack{n_1,n_2,n_3,n_4 \\ n_1+n_2=n_3+n_4}}(\mathbf{h}_{n_1}^{\mathsf{H}}\mathbf{w}_{\mathrm{P},n_1})(\mathbf{h}_{n_2}^{\mathsf{H}}\mathbf{w}_{\mathrm{P},n_2})(\mathbf{h}_{n_3}^{\mathsf{H}}\mathbf{w}_{\mathrm{P},n_3})^*(\mathbf{h}_{n_4}^{\mathsf{H}}\mathbf{w}_{\mathrm{P},n_4})^*$$
$$= \frac{3}{8}\sum_{k=-N+1}^{N-1}(\mathbf{h}^{\mathsf{H}}\mathbf{W}_{\mathrm{P},k}\mathbf{h})(\mathbf{h}^{\mathsf{H}}\mathbf{W}_{\mathrm{P},k}\mathbf{h})^*, \tag{3.9d}$$

where we define $\mathbf{h} \triangleq [\mathbf{h}_1^\mathsf{T}, \ldots, \mathbf{h}_N^\mathsf{T}]^\mathsf{T} \in \mathbb{C}^{MN \times 1}$ and $\mathbf{W}_{\mathrm{I/P}} \triangleq \mathbf{w}_{\mathrm{I/P}} \mathbf{w}_{\mathrm{I/P}}^\mathsf{H} \in \mathbb{H}_+^{MN \times MN}$. As illustrated by Fig. 3.2, $\mathbf{W}_{\mathrm{I/P}}$ can be divided into $N \times N$ blocks of size $M \times M$. Let $\mathbf{W}_{\mathrm{I/P},k}$ keep its block diagonal $k \in \{-N+1, \ldots, N-1\}$ and set all other blocks to $\mathbf{0}$.

Fig. 3.2 $\mathbf{W}_{\mathrm{I/P}}$ consists of $N \times N$ blocks of size $M \times M$. $\mathbf{W}_{\mathrm{I/P},k}$ keeps the k-th block diagonal of $\mathbf{W}_{\mathrm{I/P}}$ and nulls all remaining blocks. Solid, dashed and dotted blocks correspond to $k > 0$, $k = 0$ and $k < 0$, respectively. For $\mathbf{w}_{\mathrm{I/P},n_1} \mathbf{w}_{\mathrm{I/P},n_2}^\mathsf{H}$, the k-th block diagonal satisfies $k = n_2 - n_1$.

3.2.7 Rate-Energy Region

The achievable R-E region for the PS receiver is explicitly defined as

$$\mathcal{C}_{\mathrm{R-E}}(P) \triangleq \Big\{ (r, e) : 0 \le r \le R(\boldsymbol{\theta}, \mathbf{w}_{\mathrm{I}}, \rho), \ 0 \le e \le z(\boldsymbol{\theta}, \mathbf{w}_{\mathrm{I}}, \mathbf{w}_{\mathrm{P}}, \rho), \\ \left(\|\mathbf{w}_{\mathrm{I}}\|^2 + \|\mathbf{w}_{\mathrm{P}}\|^2 \right) / 2 \le P \Big\}, \tag{3.10}$$

where P is the average transmit power budget and the 1/2 converts the peak to average.

3.3 Problem Formulation

We characterize each R-E boundary point through a DC maximization problem subject to sum rate, transmit power, and reflection amplitude constraints as

$$\max_{\boldsymbol{\theta}, \mathbf{w}_\mathrm{I}, \mathbf{w}_\mathrm{P}, \rho} \quad z(\boldsymbol{\theta}, \mathbf{w}_\mathrm{I}, \mathbf{w}_\mathrm{P}, \rho) \tag{3.11a}$$

$$\mathrm{s.t.} \quad R(\boldsymbol{\theta}, \mathbf{w}_\mathrm{I}, \rho) \geq \bar{R}, \tag{3.11b}$$

$$\frac{1}{2} \left(\|\mathbf{w}_\mathrm{I}\|^2 + \|\mathbf{w}_\mathrm{P}\|^2 \right) \leq P, \tag{3.11c}$$

$$|\boldsymbol{\theta}| = \mathbf{1}, \tag{3.11d}$$

$$0 \leq \rho \leq 1. \tag{3.11e}$$

Problem (3.11) is intricate because of the coupled variables in (3.11a), (3.11b) and the non-convex constraint (3.11d). To obtain a feasible solution, we propose a BCD algorithm that iteratively updates (i) the RIS phase shift; (ii) the active precoder; (iii) the waveform amplitude and splitting ratio, until convergence.

3.3.1 Passive Beamforming

In this section, we optimize the RIS phase shift $\boldsymbol{\theta}$ for any given waveform $\mathbf{w}_\mathrm{I/P}$ and splitting ratio ρ. Note that

$$
\begin{aligned}
|\mathbf{h}_n^\mathsf{H} \mathbf{w}_{\mathrm{I},n}|^2 &= \mathbf{w}_{\mathrm{I},n}^\mathsf{H} \mathbf{h}_n \mathbf{h}_n^\mathsf{H} \mathbf{w}_{\mathrm{I},n} \\
&= \mathbf{w}_{\mathrm{I},n}^\mathsf{H} (\mathbf{h}_{\mathrm{D},n} + \mathbf{V}_n^\mathsf{H} \boldsymbol{\theta})(\mathbf{h}_{\mathrm{D},n}^\mathsf{H} + \boldsymbol{\theta}^\mathsf{H} \mathbf{V}_n) \mathbf{w}_{\mathrm{I},n} \\
&= \mathbf{w}_{\mathrm{I},n}^\mathsf{H} \mathbf{M}_n^\mathsf{H} \bar{\boldsymbol{\Theta}} \mathbf{M}_n \mathbf{w}_{\mathrm{I},n} \\
&= \mathrm{tr}(\mathbf{M}_n \mathbf{w}_{\mathrm{I},n} \mathbf{w}_{\mathrm{I},n}^\mathsf{H} \mathbf{M}_n^\mathsf{H} \bar{\boldsymbol{\Theta}}) \\
&= \mathrm{tr}(\mathbf{C}_n \bar{\boldsymbol{\Theta}}),
\end{aligned}
\tag{3.12}
$$

where $\mathbf{M}_n \triangleq [\mathbf{V}_n^\mathsf{H}, \mathbf{h}_{\mathrm{D},n}]^\mathsf{H} \in \mathbb{C}^{(L+1) \times M}$, t' is an auxiliary variable with unit modulus, $\bar{\boldsymbol{\theta}} \triangleq [\boldsymbol{\theta}^\mathsf{H}, t']^\mathsf{H} \in \mathbb{C}^{(L+1) \times 1}$, $\bar{\boldsymbol{\Theta}} \triangleq \bar{\boldsymbol{\theta}} \bar{\boldsymbol{\theta}}^\mathsf{H} \in \mathbb{H}_+^{(L+1) \times (L+1)}$, $\mathbf{C}_n \triangleq \mathbf{M}_n \mathbf{w}_{\mathrm{I},n} \mathbf{w}_{\mathrm{I},n}^\mathsf{H} \mathbf{M}_n^\mathsf{H} \in \mathbb{H}_+^{(L+1) \times (L+1)}$.

On the other hand, we define $t_{\mathrm{I/P},k}$ as

$$
\begin{aligned}
t_{\mathrm{I/P},k} &\triangleq \mathbf{h}^{\mathsf{H}}\mathbf{W}_{\mathrm{I/P},k}\mathbf{h} \\
&= \mathrm{tr}(\mathbf{h}\mathbf{h}^{\mathsf{H}}\mathbf{W}_{\mathrm{I/P},k}) \\
&= \mathrm{tr}\left((\mathbf{h}_D + \mathbf{V}^{\mathsf{H}}\boldsymbol{\theta})(\mathbf{h}_D^{\mathsf{H}} + \boldsymbol{\theta}^{\mathsf{H}}\mathbf{V})\mathbf{W}_{\mathrm{I/P},k}\right) \\
&= \mathrm{tr}(\mathbf{M}^{\mathsf{H}}\bar{\boldsymbol{\Theta}}\mathbf{M}\mathbf{W}_{\mathrm{I/P},k}) \\
&= \mathrm{tr}(\mathbf{M}\mathbf{W}_{\mathrm{I/P},k}\mathbf{M}^{\mathsf{H}}\bar{\boldsymbol{\Theta}}) \\
&= \mathrm{tr}(\mathbf{C}_{\mathrm{I/P},k}\bar{\boldsymbol{\Theta}}),
\end{aligned} \tag{3.13}
$$

where $\mathbf{V} \triangleq [\mathbf{V}_1, \ldots, \mathbf{V}_N] \in \mathbb{C}^{L \times MN}$, $\mathbf{M} \triangleq [\mathbf{V}^{\mathsf{H}}, \mathbf{h}_D]^{\mathsf{H}} \in \mathbb{C}^{(L+1) \times MN}$, $\mathbf{C}_{\mathrm{I/P},k} \triangleq \mathbf{M}\mathbf{W}_{\mathrm{I/P},k}\mathbf{M}^{\mathsf{H}} \in \mathbb{C}^{(L+1) \times (L+1)}$. On top of this, (3.6) and (3.8) reduce respectively to

$$
R(\bar{\boldsymbol{\Theta}}) = \sum_{n=1}^{N} \log_2 \left(1 + \frac{(1-\rho)\mathrm{tr}(\mathbf{C}_n\bar{\boldsymbol{\Theta}})}{\sigma_n^2} \right), \tag{3.14}
$$

$$
z(\bar{\boldsymbol{\Theta}}) = \frac{1}{2}\beta_2\rho(t_{\mathrm{I},0} + t_{\mathrm{P},0}) + \frac{3}{8}\beta_4\rho^2 \left(2t_{\mathrm{I},0}^2 + \sum_{k=-N+1}^{N-1} t_{\mathrm{P},k}t_{\mathrm{P},k}^* \right) + \frac{3}{2}\beta_4\rho^2 t_{\mathrm{I},0}t_{\mathrm{P},0}. \tag{3.15}
$$

To maximize the non-concave expression (3.15), we successively lower bound the second-order terms by their first-order Taylor expansions [122]. Based on the solution at iteration $r-1$, the approximations at iteration r are

$$
(t_{\mathrm{I},0}^{(r)})^2 \geq 2t_{\mathrm{I},0}^{(r)}t_{\mathrm{I},0}^{(r-1)} - (t_{\mathrm{I},0}^{(r-1)})^2, \tag{3.16}
$$

$$
t_{\mathrm{P},k}^{(r)}(t_{\mathrm{P},k}^{(r)})^* \geq 2\Re\left\{ t_{\mathrm{P},k}^{(r)}(t_{\mathrm{P},k}^{(r-1)})^* \right\} - t_{\mathrm{P},k}^{(r-1)}(t_{\mathrm{P},k}^{(r-1)})^*, \tag{3.17}
$$

$$
t_{\mathrm{I},0}^{(r)}t_{\mathrm{P},0}^{(r)} \geq t_{\mathrm{I},0}^{(r)}t_{\mathrm{P},0}^{(r-1)} + t_{\mathrm{P},0}^{(r)}t_{\mathrm{I},0}^{(r-1)} - t_{\mathrm{I},0}^{(r-1)}t_{\mathrm{P},0}^{(r-1)}. \tag{3.18}
$$

Note that $t_{\mathrm{I/P},0} = \mathrm{tr}(\mathbf{C}_{\mathrm{I/P},0}\bar{\boldsymbol{\Theta}})$ is real-valued because $\mathbf{C}_{\mathrm{I/P},0}$ and $\bar{\boldsymbol{\Theta}}$ are Hermitian matrices. Due to symmetry [123], we have

$$
\sum_{k=-N+1}^{N-1} \Re\left\{ t_{\mathrm{P},k}^{(r)}(t_{\mathrm{P},k}^{(r-1)})^* \right\} = \sum_{k=-N+1}^{N-1} t_{\mathrm{P},k}^{(r)}(t_{\mathrm{P},k}^{(r-1)})^*. \tag{3.19}
$$

Plugging (3.16)–(3.19) into (3.15), we obtain the DC approximation $\tilde{z}$ as

$$\tilde{z}(\bar{\boldsymbol{\Theta}}^{(r)}) = \frac{1}{2}\beta_2\rho(t_{\mathrm{I},0}^{(r)} + t_{\mathrm{P},0}^{(r)}) + \frac{3}{2}\beta_4\rho^2\left(t_{\mathrm{I},0}^{(r)}t_{\mathrm{P},0}^{(r-1)} + t_{\mathrm{P},0}^{(r)}t_{\mathrm{I},0}^{(r-1)} - t_{\mathrm{I},0}^{(r-1)}t_{\mathrm{P},0}^{(r-1)}\right)$$
$$+ \frac{3}{8}\beta_4\rho^2\left(4t_{\mathrm{I},0}^{(r)}t_{\mathrm{I},0}^{(r-1)} - 2(t_{\mathrm{I},0}^{(r-1)})^2 + \sum_{k=-N+1}^{N-1} 2t_{\mathrm{P},k}^{(r)}(t_{\mathrm{P},k}^{(r-1)})^* - t_{\mathrm{P},k}^{(r-1)}(t_{\mathrm{P},k}^{(r-1)})^*\right),$$
(3.20)

and transform problem (3.11) to

$$\max_{\bar{\boldsymbol{\Theta}}} \quad \tilde{z}(\bar{\boldsymbol{\Theta}}) \tag{3.21a}$$

$$\text{s.t.} \quad R(\bar{\boldsymbol{\Theta}}) \geq \bar{R}, \tag{3.21b}$$

$$\text{diag}^{-1}(\bar{\boldsymbol{\Theta}}) = \mathbf{1}, \tag{3.21c}$$

$$\bar{\boldsymbol{\Theta}} \succeq \mathbf{0}, \tag{3.21d}$$

$$\text{rank}(\bar{\boldsymbol{\Theta}}) = 1. \tag{3.21e}$$

The unit-rank constraint (3.21e) can be relaxed to formulate a Semi-Definite Programming (SDP) with approximation accuracy no greater than $\pi/4$ [124]. The resulting problem can be solved efficiently by `CVX toolbox` [125].

Proposition 3.1. *Any optimal solution $\bar{\boldsymbol{\Theta}}^\star$ to the relaxed passive beamforming problem (3.21a)–(3.21d) is strictly rank-1. That is to say, (3.21e) is redundant and no loss is introduced by Semi-Definite Relaxation (SDR).*

Proof. Please refer to Appendix 7.1.1. $\square$

In summary, we update $\bar{\boldsymbol{\Theta}}^{(r)}$ by iteratively solving (3.21a)–(3.21d) until convergence, extract $\hat{\boldsymbol{\theta}}^\star$ by eigen decomposition, and retrieve the RIS vector by $\boldsymbol{\theta}^\star = e^{j\arg([\hat{\boldsymbol{\theta}}^\star]_{(1:L)}/[\hat{\boldsymbol{\theta}}^\star]_{(L+1)})}$. The passive beamforming design is summarized in the SCA Algorithm 1, where the relaxed problem (3.21a)–(3.21d) involves a $(L+1)$-order positive semi-definite matrix variable and $(L+2)$ linear constraints. Given a solution accuracy ϵ_{IPM} for the interior-point method, the computational complexity of Algorithm 1 is $\mathcal{O}\left(I_{\mathrm{SCA}}(L+2)^4(L+1)^{0.5}\log(\epsilon_{\mathrm{IPM}}^{-1})\right)$, where I_{SCA} denotes the number of SCA iterations [124].

Proposition 3.2. *For any feasible initial point with given waveform and splitting ratio, the SCA Algorithm 1 is guaranteed to converge to local optimal points of the original problem (3.11).*

Proof. Please refer to Appendix 7.1.2. $\square$

Algorithm 1 SCA: RIS Phase Shift.

1: **Input** β_2, β_4, $\mathbf{h}_{\mathrm{D},n}$, $\mathbf{V}_n$, σ_n, $\mathbf{w}_{\mathrm{I/P},n}$, ρ, $\bar{R}$, ϵ, $\forall n$
2: Construct $\mathbf{V}$, $\mathbf{M}$, $\mathbf{M}_n$, $\mathbf{C}_n$, $\mathbf{C}_{\mathrm{I/P},k}$, $\forall n, k$
3: **Initialize** $i \leftarrow 0$, $\bar{\mathbf{\Theta}}^{(0)}$
4: Set $t_{\mathrm{I/P},k}^{(0)}$, $\forall k$ by (3.13)
5: Compute $z^{(0)}$ by (3.15)
6: **Repeat**
7:     $i \leftarrow i + 1$
8:     Get $\bar{\mathbf{\Theta}}^{(r)}$ by solving (3.21a)–(3.21d)
9:     Update $t_{\mathrm{I/P},k}^{(r)}$, $\forall k$ by (3.13)
10:     Compute $z^{(r)}$ by (3.15)
11: **Until** $\left| z^{(r)} - z^{(r-1)} \right| \leq \epsilon$
12: Set $\bar{\mathbf{\Theta}}^{\star} \leftarrow \bar{\mathbf{\Theta}}^{(r)}$
13: Get $\hat{\boldsymbol{\theta}}^{\star}$ by eigen decomposition, $\bar{\mathbf{\Theta}}^{\star} = \hat{\boldsymbol{\theta}}^{\star}(\hat{\boldsymbol{\theta}}^{\star})^{\mathsf{H}}$
14: Set $\boldsymbol{\theta}^{\star} \leftarrow e^{\jmath \arg\left([\hat{\boldsymbol{\theta}}^{\star}]_{(1:L)} / [\hat{\boldsymbol{\theta}}^{\star}]_{(L+1)}\right)}$
15: **Output** $\boldsymbol{\theta}^{\star}$

3.3.2 Active Beamforming

The original waveform and active beamforming problem (3.11) is over complex-valued vectors $\mathbf{w}_{\mathrm{I/P}}$ of size $MN \times 1$. The weight on subband n can be decomposed in spatial and frequency domains as

$$\mathbf{w}_{\mathrm{I/P},n} = s_{\mathrm{I/P},n}\mathbf{p}_{\mathrm{I/P},n}, \tag{3.22}$$

where $s_{\mathrm{I/P},n}$ denotes the amplitude of the modulated/multisine waveform at tone n, and $\mathbf{p}_{\mathrm{I/P},n}$ denotes the corresponding information/power precoder. This decoupling allows independent spatial and frequency optimizations, reducing the size of variables from $2MN$ to $2(M + N)$.

Proposition 3.3. *For single-user SWIPT, the global optimal information and power precoders coincide at the MRT*

$$\mathbf{p}_{\mathrm{I/P},n}^{\star} = \frac{\mathbf{h}_n}{\|\mathbf{h}_n\|}. \tag{3.23}$$

Proof. Please refer to Appendix 7.1.3. $\square$

3.3.3 Waveform and Splitting Ratio

Next, we jointly optimize the waveform amplitude $\mathbf{s}_{\mathrm{I/P}} \triangleq [s_{\mathrm{I/P},1}, \ldots, s_{\mathrm{I/P},N}]^{\mathsf{T}} \in \mathbb{R}_+^{N \times 1}$ and the splitting ratio $\rho \in \mathbb{I}$ for any given RIS phase shift $\boldsymbol{\theta}$ and active precoder $\mathbf{p}_{\mathrm{I/P},n}$, $\forall n$. With MRT precoder (3.23), the equivalent channel strength at subband n is $\|\mathbf{h}_n\|$, such that the

achievable rate (3.6) reduces to

$$R(\mathbf{s}_{\mathrm{I}}, \rho) = \log_2 \prod_{n=1}^{N} \left(1 + \frac{(1-\rho)\|\mathbf{h}_n\|^2 s_{\mathrm{I},n}^2}{\sigma_n^2} \right), \tag{3.24}$$

and the DC (3.8) rewrites as

$$z(\mathbf{s}_{\mathrm{I}}, \mathbf{s}_{\mathrm{P}}, \rho) = \frac{1}{2}\beta_2\rho \sum_{n=1}^{N} \|\mathbf{h}_n\|^2 (s_{\mathrm{I},n}^2 + s_{\mathrm{P},n}^2)$$

$$+ \frac{3}{8}\beta_4\rho^2 \left(2 \sum_{n_1,n_2} \prod_{j=1}^{2} \|\mathbf{h}_{n_j}\|^2 s_{\mathrm{I},n_j}^2 + \sum_{\substack{n_1,n_2,n_3,n_4 \\ n_1+n_2=n_3+n_4}} \prod_{j=1}^{4} \|\mathbf{h}_{n_j}\| s_{\mathrm{P},n_j} \right) \tag{3.25}$$

$$+ \frac{3}{2}\beta_4\rho^2 \left(\sum_{n_1,n_2} \|\mathbf{h}_{n_1}\|^2 \|\mathbf{h}_{n_2}\|^2 s_{\mathrm{I},n_1}^2 s_{\mathrm{P},n_2}^2 \right).$$

Problem (3.11) boils down to

$$\max_{\mathbf{s}_{\mathrm{I}},\mathbf{s}_{\mathrm{P}},\rho} \quad z(\mathbf{s}_{\mathrm{I}}, \mathbf{s}_{\mathrm{P}}, \rho) \tag{3.26a}$$

$$\text{s.t.} \quad R(\mathbf{s}_{\mathrm{I}}, \rho) \geq \bar{R}, \tag{3.26b}$$

$$\frac{1}{2} \left(\|\mathbf{s}_{\mathrm{I}}\|^2 + \|\mathbf{s}_{\mathrm{P}}\|^2 \right) \leq P. \tag{3.26c}$$

Following [73], we introduce auxiliary variables t'', $\bar{\rho}$ and transform problem (3.26) into a reversed GP

$$\min_{\mathbf{s}_{\mathrm{I}},\mathbf{s}_{\mathrm{P}},\rho,\bar{\rho},t''} \quad \frac{1}{t''} \tag{3.27a}$$

$$\text{s.t.} \quad \frac{t''}{z(\mathbf{s}_{\mathrm{I}}, \mathbf{s}_{\mathrm{P}}, \rho)} \leq 1, \tag{3.27b}$$

$$\frac{2^{\bar{R}}}{\prod_{n=1}^{N} \left(1 + \bar{\rho}\|\mathbf{h}_n\|^2 s_{\mathrm{I},n}^2 / \sigma_n^2 \right)} \leq 1, \tag{3.27c}$$

$$\frac{1}{2} \left(\|\mathbf{s}_{\mathrm{I}}\|^2 + \|\mathbf{s}_{\mathrm{P}}\|^2 \right) \leq P, \tag{3.27d}$$

$$\rho + \bar{\rho} \leq 1. \tag{3.27e}$$

Apparently, $\bar{\rho}^\star = 1 - \rho^\star$ as no power should be wasted at the receiver. The denominators of (3.27c) and (3.27b) consist of posynomials [126] that can be decomposed as sums of

monomials

$$1 + \frac{\bar{\rho}\|\mathbf{h}_n\|^2 s_{\mathrm{I},n}^2}{\sigma_n^2} \triangleq \sum_{m_{\mathrm{I},n}} g_{m_{\mathrm{I},n}}(s_{\mathrm{I},n}, \bar{\rho}), \tag{3.28}$$

$$z(\mathbf{s}_{\mathrm{I}}, \mathbf{s}_{\mathrm{P}}, \rho) \triangleq \sum_{m_{\mathrm{P}}} g_{m_{\mathrm{P}}}(\mathbf{s}_{\mathrm{I}}, \mathbf{s}_{\mathrm{P}}, \rho). \tag{3.29}$$

We upper bound (3.28) and (3.29) by the Geomtric Mean (GM)-Arithmetic Mean (AM) inequality [127] and transform problem (3.27) to

$$\min_{\mathbf{s}_{\mathrm{I}}, \mathbf{s}_{\mathrm{P}}, \rho, \bar{\rho}, t''} \quad \frac{1}{t''} \tag{3.30a}$$

$$\text{s.t.} \quad t'' \prod_{m_{\mathrm{P}}} \left(\frac{g_{m_{\mathrm{P}}}(\mathbf{s}_{\mathrm{I}}, \mathbf{s}_{\mathrm{P}}, \rho)}{\gamma_{m_{\mathrm{P}}}} \right)^{-\gamma_{m_{\mathrm{P}}}} \leq 1, \tag{3.30b}$$

$$2^{\bar{R}} \prod_n \prod_{m_{\mathrm{I},n}} \left(\frac{g_{m_{\mathrm{I},n}}(s_{\mathrm{I},n}, \bar{\rho})}{\gamma_{m_{\mathrm{I},n}}} \right)^{-\gamma_{m_{\mathrm{I},n}}} \leq 1, \tag{3.30c}$$

$$\frac{1}{2}\left(\|\mathbf{s}_{\mathrm{I}}\|^2 + \|\mathbf{s}_{\mathrm{P}}\|^2\right) \leq P, \tag{3.30d}$$

$$\rho + \bar{\rho} \leq 1, \tag{3.30e}$$

where $\gamma_{m_{\mathrm{I},n}}, \gamma_{m_{\mathrm{P}}} \geq 0$ and $\sum_{m_{\mathrm{I},n}} \gamma_{m_{\mathrm{I},n}} = \sum_{m_{\mathrm{P}}} \gamma_{m_{\mathrm{P}}} = 1$. The tightness of the AM-GM inequality depends on the selection of $\{\gamma_{m_{\mathrm{I},n}}, \gamma_{m_{\mathrm{P}}}\}$, and a feasible choice at iteration r is

$$\gamma_{m_{\mathrm{I},n}}^{(r)} = \frac{g_{m_{\mathrm{I},n}}(s_{\mathrm{I},n}^{(r-1)}, \bar{\rho}^{(r-1)})}{1 + \bar{\rho}^{(r-1)}\|\mathbf{h}_n\|^2 (s_{\mathrm{I},n}^{(r-1)})^2 / \sigma_n^2}, \tag{3.31}$$

$$\gamma_{m_{\mathrm{P}}}^{(r)} = \frac{g_{m_{\mathrm{P}}}(\mathbf{s}_{\mathrm{I}}^{(r-1)}, \mathbf{s}_{\mathrm{P}}^{(r-1)}, \rho^{(r-1)})}{z(\mathbf{s}_{\mathrm{I}}^{(r-1)}, \mathbf{s}_{\mathrm{P}}^{(r-1)}, \rho^{(r-1)})}. \tag{3.32}$$

With (3.31) and (3.32), problem (3.30) becomes convex and can be solved by `CVX toolbox` [125]. We update $\mathbf{s}_{\mathrm{I}}^{(r)}, \mathbf{s}_{\mathrm{P}}^{(r)}, \rho^{(r)}$ iteratively until convergence. The joint waveform amplitude and splitting ratio design is summarized in the GP Algorithm 2, which achieves local optimality at the cost of exponential computational complexity [127].

Proposition 3.4. *For any feasible initial point, the GP Algorithm 2 is guaranteed to converge to local optimal points of the waveform amplitude and splitting ratio design problem* (3.26).

Proof. The proof is similar to [64, 73] and is omitted here. □

Algorithm 2 GP: Waveform Amplitude and Splitting Ratio.

1: **Input** β_2, β_4, $\mathbf{h}_n$, P, σ_n, $\bar{R}$, ϵ, $\forall n$
2: **Initialize** $i \leftarrow 0$, $\mathbf{s}_{\mathrm{I/P}}^{(0)}$, $\rho^{(0)}$
3: Compute $R^{(0)}$, $z^{(0)}$ by (3.24), (3.25)
4: Set $g_{m_{\mathrm{I},n}}^{(0)}$, $g_{m_{\mathrm{P}}}^{(0)}$, $\forall n$ by (3.28), (3.29)
5: **Repeat**
6:      $i \leftarrow i + 1$
7:      Update $\gamma_{m_{\mathrm{I},n}}^{(r)}$, $\gamma_{m_{\mathrm{P}}}^{(r)}$, $\forall n$ by (3.31), (3.32)
8:      Get $\mathbf{s}_{\mathrm{I/P}}^{(r)}$, $\rho^{(r)}$ by solving problem (3.30)
9:      Compute $R^{(r)}$, $z^{(r)}$ by (3.24), (3.25)
10:      Update $g_{m_{\mathrm{I},n}}^{(r)}$, $g_{m_{\mathrm{P}}}^{(r)}$, $\forall n$ by (3.28), (3.29)
11: **Until** $|z^{(r)} - z^{(r-1)}| \leq \epsilon$
12: Set $\mathbf{s}_{\mathrm{I/P}}^{\star} \leftarrow \mathbf{s}_{\mathrm{I/P}}^{(r)}$, $\rho^{\star} \leftarrow \rho^{(r)}$
13: **Output** $\mathbf{s}_{\mathrm{I}}^{\star}$, $\mathbf{s}_{\mathrm{P}}^{\star}$, $\rho^{\star}$

3.3.4 Low-Complexity Adaptive Design

To facilitate practical SWIPT implementation, we propose two closed-form waveform schemes for TS and PS receivers, respectively.

- *TS:* As discussed Section 2.3.3.2, each time block is divided into orthogonal phases and there is no waveform superposition. For the WIT phase, the optimal modulated waveform amplitude is given by the WF strategy [128]

$$s_{\mathrm{I},n} = \sqrt{2 \left(\lambda - \frac{\sigma_n^2}{P \|\mathbf{h}_n\|^2} \right)^+}, \qquad (3.33)$$

where λ is chosen to satisfy the power constraint $\|\mathbf{s}_I\|^2 / 2 \leq P$ and can be obtained by iterative methods [129]. For the WPT phase, a reasonable multisine waveform amplitude is given by the SMF strategy [107]

$$s_{\mathrm{P},n} = \sqrt{\frac{2P}{\sum_{n=1}^N \|\mathbf{h}_n\|^{2\alpha}}} \|\mathbf{h}_n\|^\alpha, \qquad (3.34)$$

where the scaling ratio $\alpha \geq 1$ is a design parameter that exploits the rectifier nonlinearity and frequency selectivity.

- *PS:* When the receiver works in PS mode, the modulated and multisine components in the superposed waveform are respectively

$$s_{\text{I},n} = \sqrt{2(1-\delta)\left(\lambda - \frac{\sigma_n^2}{P\|\mathbf{h}_n\|^2}\right)^+}, \tag{3.35}$$

$$s_{\text{P},n} = \sqrt{\frac{2\delta P}{\sum_{n=1}^N \|\mathbf{h}_n\|^{2\alpha}}} \|\mathbf{h}_n\|^\alpha, \tag{3.36}$$

where the $\delta \in \mathbb{I}$ determines the power ratio of multisine waveform at the transmitter, and $\rho \in \mathbb{I}$ determines the power ratio of the energy harvester at the receiver.[2]

To accommodate the low-complexity waveform schemes, minor modifications should be made for the passive beamforming design. Specifically, the rate constraint (3.21b) should be dropped, since the achievable rate is controlled by η in TS or $\{\delta, \rho\}$ in PS. To achieve the WIT point, the rate (3.14) should be maximized and the DC expression (3.20) can be dropped. The Modified-SCA (M-SCA) Algorithm 3 summarizes the modified passive beamforming design when the receiver works in PS mode. Similar to propositions 3.1 and 3.2, no loss is introduced by SDR and local optimality is guaranteed. Since each SDP involves $(L+1)$ linear constraints, the computational complexity of Algorithm 3 is $\mathcal{O}\left(I_{\text{M−SCA}}(L+1)^{4.5}\log(\epsilon_{\text{IPM}}^{-1})\right)$, where $I_{\text{M−SCA}}$ denotes the number of M-SCA iterations [124].

3.3.5 Block Coordinate Descent

Based on the direct and cascaded CSIT, we iteratively update the passive beamforming $\boldsymbol{\theta}$ by Algorithm 1, the active precoder $\mathbf{p}_{\text{I/P},n}$, $\forall n$ by equation (3.23), and the waveform amplitude $\mathbf{s}_{\text{I/P}}$ and splitting ratio ρ by Algorithm 2, until convergence. The steps are summarized in the BCD Algorithm 4, whose computational complexity is exponential as inherited from Algorithm 2. It is guaranteed to converge, but may end up with a suboptimal solution because variables are coupled in constraint (3.11b) [130]. The R-E region is obtained by varying the rate constraint from 0 to C_{max}.

For the Low-Complexity (LC) design under PS mode, we obtain the phase shift by Algorithm 3, the active precoder $\mathbf{p}_{\text{I/P},n}$, $\forall n$ by equation (3.23), and the waveform amplitude by (3.35) and (3.36). The R-E region is obtained by performing a two-dimensional search over (δ, ρ) from $(0, 0)$ to $(1, 1)$. The steps are summarized in Algorithm 5. The computational complexity of Algorithm 5 is $\mathcal{O}\left(I_{\text{LC−BCD}}I_{\text{M−SCA}}(L+1)^{4.5}\log(\epsilon_{\text{IPM}}^{-1})\right)$, where $I_{\text{LC−BCD}}$ denotes the number of LC-BCD iterations [124].

---

[2]We notice that $\delta^\star = \rho^\star = 0$ at the WIT point and $\delta^\star = \rho^\star = 1$ at the WPT point. Intuitively, $\delta^\star$ and $\rho^\star$ should be positively correlated to improve the R-E trade-off.

Algorithm 3 M-SCA: RIS Phase Shift.

1: **Input** β_2, β_4, $\mathbf{h}_{\mathrm{D},n}$, $\mathbf{V}_n$, σ_n, $\mathbf{w}_{\mathrm{I/P},n}$, ρ, ϵ, $\forall n$
2: Construct $\mathbf{V}$, $\mathbf{M}$, $\mathbf{M}_n$, $\mathbf{C}_n$, $\mathbf{C}_{\mathrm{I/P},k}$, $\forall n, k$
3: **Initialize** $i \leftarrow 0$, $\bar{\boldsymbol{\Theta}}^{(0)}$
4: **If** $\rho = 0$
5:     Get $\bar{\boldsymbol{\Theta}}^\star$ by maximizing (3.14) s.t. (3.21c), (3.21d)
6: **Else**
7:     Set $t_{\mathrm{I/P},k}^{(0)}$, $\forall k$ by (3.13)
8:     Compute $z^{(0)}$ by (3.15)
9:     **Repeat**
10:         $i \leftarrow i + 1$
11:         Get $\bar{\boldsymbol{\Theta}}^{(r)}$ by maximizing (3.20) s.t. (3.21c), (3.21d)
12:         Update $t_{\mathrm{I/P},k}^{(r)}$, $\forall k$ by (3.13)
13:         Compute $z^{(r)}$ by (3.15)
14:     **Until** $|z^{(r)} - z^{(r-1)}| \leq \epsilon$
15:     Set $\bar{\boldsymbol{\Theta}}^\star \leftarrow \bar{\boldsymbol{\Theta}}^{(r)}$
16: **End If**
17: Get $\hat{\boldsymbol{\theta}}^\star$ by eigen decomposition, $\bar{\boldsymbol{\Theta}}^\star = \hat{\boldsymbol{\theta}}^\star (\hat{\boldsymbol{\theta}}^\star)^{\mathsf{H}}$
18: Set $\boldsymbol{\theta}^\star \leftarrow e^{j \arg\left([\hat{\boldsymbol{\theta}}^\star]_{(1:L)} / [\hat{\boldsymbol{\theta}}^\star]_{(L+1)}\right)}$
19: **Output** $\boldsymbol{\theta}^\star$

Algorithm 4 BCD: Waveform, Beamforming and Splitting Ratio.

1: **Input** β_2, β_4, $\mathbf{h}_{\mathrm{D},n}$, $\mathbf{V}_n$, P, σ_n, $\bar{R}$, ϵ, $\forall n$
2: **Initialize** $i \leftarrow 0$, $\boldsymbol{\theta}^{(0)}$, $\mathbf{p}_{\mathrm{I/P},n}^{(0)}$, $\mathbf{s}_{\mathrm{I/P}}^{(0)}$, $\rho^{(0)}$, $\forall n$
3: Set $\mathbf{w}_{\mathrm{I/P},n}^{(0)}$, $\forall n$ by (3.22)
4: Compute $z^{(0)}$ by (3.25)
5: **Repeat**
6:     $i \leftarrow i + 1$
7:     Get $\boldsymbol{\theta}^{(r)}$ based on $\mathbf{w}_{\mathrm{I/P}}^{(r-1)}$, $\rho^{(r-1)}$ by Algorithm 1
8:     Update $\mathbf{h}_n^{(r)}$, $\mathbf{p}_n^{(r)}$, $\forall n$ by (3.4), (3.23)
9:     Get $\mathbf{s}_{\mathrm{I/P}}^{(r)}$, $\rho^{(r)}$ by Algorithm 2
10:     Update $\mathbf{w}_{\mathrm{I/P},n}^{(r)}$, $\forall n$ by (3.22)
11:     Compute $z^{(r)}$ by (3.25)
12: **Until** $|z^{(r)} - z^{(r-1)}| \leq \epsilon$
13: Set $\boldsymbol{\theta}^\star \leftarrow \boldsymbol{\theta}^{(r)}$, $\mathbf{w}_{\mathrm{I/P}}^\star \leftarrow \mathbf{w}_{\mathrm{I/P}}^{(r)}$, $\rho^\star \leftarrow \rho^{(r)}$
14: **Output** $\boldsymbol{\theta}^\star$, $\mathbf{w}_{\mathrm{I}}^\star$, $\mathbf{w}_{\mathrm{P}}^\star$, $\rho^\star$

Algorithm 5 LC-BCD: Waveform and Beamforming.

1: **Input** β_2, β_4, $\mathbf{h}_{\mathrm{D},n}$, $\mathbf{V}_n$, P, σ_n, δ, ρ, ϵ, $\forall n$
2: **Initialize** $i \leftarrow 0$, $\boldsymbol{\theta}^{(0)}$, $\mathbf{p}_{\mathrm{I/P},n}^{(0)}$, $\mathbf{s}_{\mathrm{I/P}}^{(0)}$, $\forall n$
3: Set $\mathbf{w}_{\mathrm{I/P},n}^{(0)}$, $\forall n$ by (3.22)
4: Compute $R^{(0)}$, $z^{(0)}$ by (3.24), (3.25)
5: **Repeat**
6:     $i \leftarrow i + 1$
7:     Get $\boldsymbol{\theta}^{(r)}$ based on $\mathbf{w}_{\mathrm{I/P}}^{(r-1)}$ by Algorithm 3
8:     Update $\mathbf{h}_n^{(r)}$, $\mathbf{p}_n^{(r)}$, $\forall n$ by (3.4), (3.23)
9:     Update $\mathbf{s}_{\mathrm{I}}^{(r)}$, $\mathbf{s}_{\mathrm{P}}^{(r)}$ by (3.35), (3.36)
10:    Update $\mathbf{w}_{\mathrm{I/P},n}^{(r)}$, $\forall n$ by (3.22)
11:    Compute $R^{(r)}$, $z^{(r)}$ by (3.24), (3.25)
12:    **If** $\rho = 0$
13:       $\Delta \leftarrow R^{(r)} - R^{(r-1)}$
14:    **Else**
15:       $\Delta \leftarrow z^{(r)} - z^{(r-1)}$
16:    **End If**
17: **Until** $|\Delta| \leq \epsilon$
18: Set $\boldsymbol{\theta}^\star \leftarrow \boldsymbol{\theta}^{(r)}$, $\mathbf{w}_{\mathrm{I/P}}^\star \leftarrow \mathbf{w}_{\mathrm{I/P}}^{(r)}$
19: **Output** $\boldsymbol{\theta}^\star$, $\mathbf{w}_{\mathrm{I}}^\star$, $\mathbf{w}_{\mathrm{P}}^\star$

3.4 Performance Evaluations
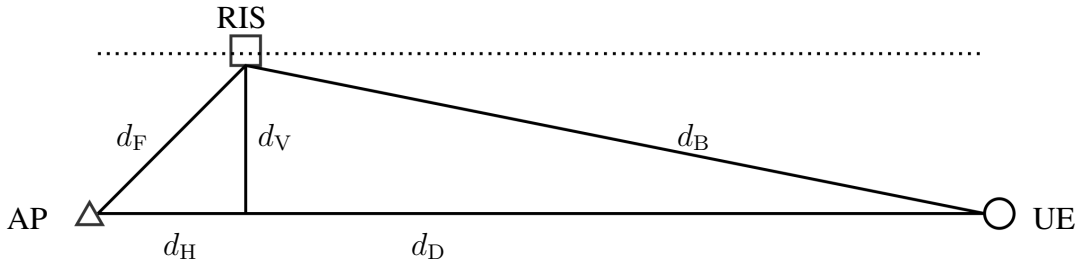
Fig. 3.3 System layout in simulation.

To evaluate the proposed RIS-aided SWIPT system, we consider the layout in Fig. 3.3 where the RIS moves along a line parallel to the AP-UE path. Let d_{H}, d_{V} be the horizontal and vertical distances from the AP to the RIS, and denote respectively d_{D}, $d_{\mathrm{F}} = \sqrt{d_{\mathrm{H}}^2 + d_{\mathrm{V}}^2}$, $d_{\mathrm{B}} = \sqrt{(d_{\mathrm{D}} - d_{\mathrm{H}})^2 + d_{\mathrm{V}}^2}$ as the distance of direct, forward and backward links. Set $d_{\mathrm{D}} = 12\,\mathrm{m}$ and $d_{\mathrm{H}} = d_{\mathrm{V}} = 2\,\mathrm{m}$ as reference. The path loss of direct, forward and backward links are denoted by Λ_{D}, Λ_{F} and Λ_{B}, respectively. We consider a Wi-Fi-like environment at center frequency $2.4\,\mathrm{GHz}$ where the channel follows IEEE TGn channel model D [131]. To

simulate an indoor environment where two rooms are separated by a wall and a RIS door, we set the path loss exponent to 2 up to $10\,\mathrm{m}$ and 3.5 onwards to penalize the penetration loss. All fadings are modeled as NLoS with tap delays and powers specified in model D, and the tap gains are modeled as i.i.d. CSCG variables. Rectenna parameters are set to $k_2 = 0.0034$, $k_4 = 0.3829$, $R_A = 50\,\Omega$ [64] such that $\beta_2 = 0.17$ and $\beta_4 = 957.25$. We also choose the average Effective Isotropic Radiated Power (EIRP) as $P = 40\,\mathrm{dBm}^3$, the receive antenna gain as $3\,\mathrm{dBi}$, the scaling ratio as $\alpha = 2$, and the tolerance as $\epsilon = 10^{-8}$. To further reduce the complexity, we assume $\delta = \rho$ and perform a one-dimensional search for the LC-BCD algorithm. Each R-E point is averaged over 200 channel realizations, and the x-axis is normalized to per-subband rate R/N.

3.4.1 Subchannel Manipulation
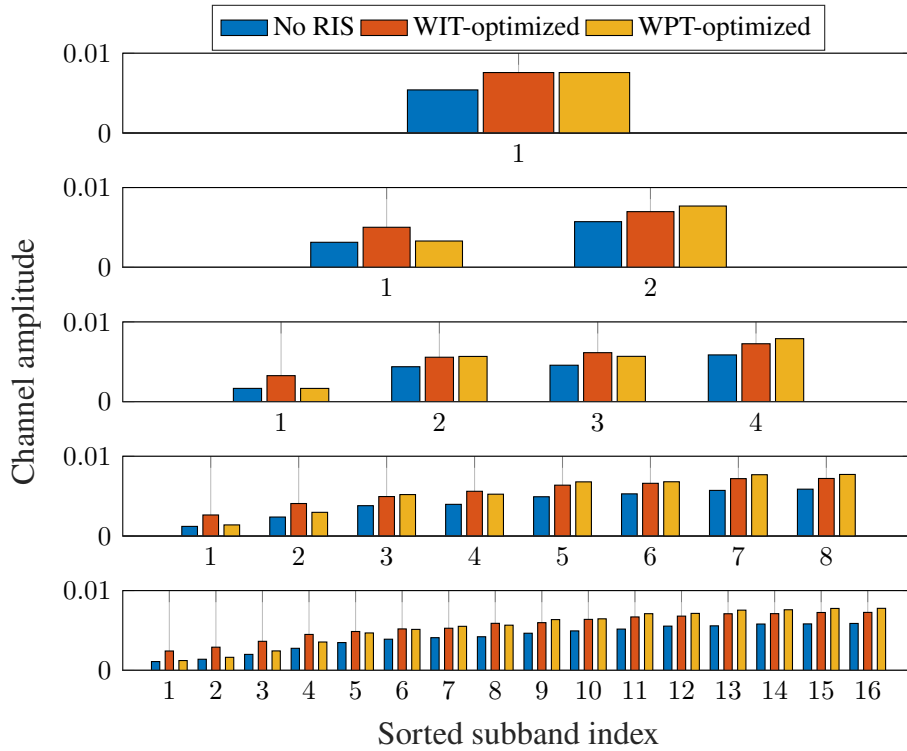
Fig. 3.4 Sorted equivalent subchannel amplitude with and without RIS versus N for $M = 1$, $L = 100$, $\sigma_n^2 = -40\,\mathrm{dBm}$, $B = 10\,\mathrm{MHz}$ and $d_\mathrm{H} = d_\mathrm{V} = 2\,\mathrm{m}$.

---

[3]One examiner has kindly pointed out that the regulation for EIRP is 36 dBm in the 2.4 GHz band. Unfortunately, re-running all the simulations is too time-consuming at this stage and reducing the EIRP by 4dB will only affect the scale of the simulation results without altering any conclusion. We have published the source code on this link for everyone to verify the results.

Fig. 3.4 reveals how RIS influences the sorted equivalent subchannel amplitude for one channel realization.[4] Due to the flexible subchannel design enabled by passive beamforming, the optimal amplitude distribution for WIT and WPT are dissimilar. Under the specified configuration, the WPT-optimized RIS aligns the strong subbands to exploit the rectifier nonlinearity. On the other hand, the WIT-optimized RIS provides a fair gain over all subchannels when L is sufficiently large. This is reminiscent of the WF scheme at high SNR, but is realized by channel alignment by RIS instead of resource allocation by transmitter.

3.4.2 R-E Region Characterization

3.4.2.1 Number of Subbands

(a) R-E region (b) WPT waveform amplitude
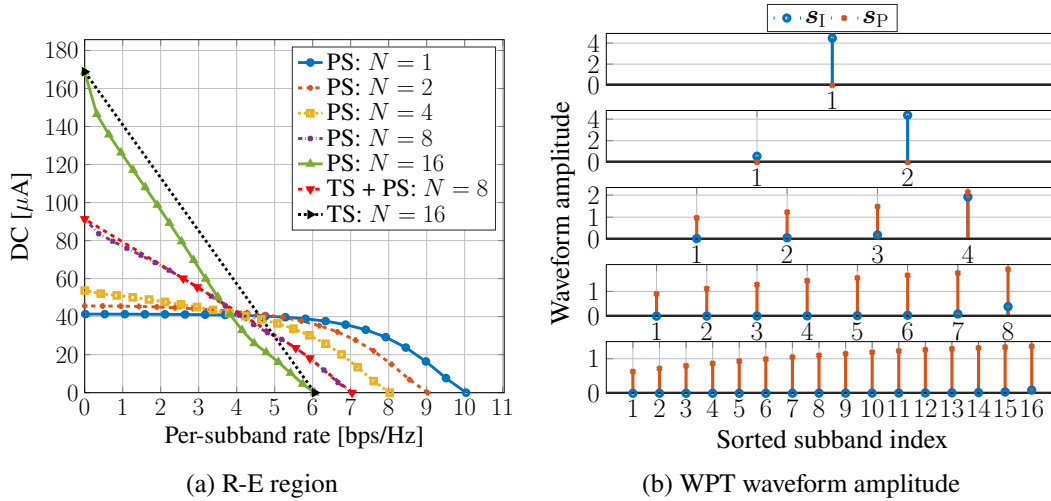
Fig. 3.5 Average R-E region and WPT waveform amplitude versus N for $M = 1$, $L = 20$, $\sigma_n^2 = -40\,\text{dBm}$, $B = 1\,\text{MHz}$ and $d_\text{H} = d_\text{V} = 2\,\text{m}$.

Fig. 3.5(a) illustrates the average R-E region versus the number of subband N. First, it is observed that increasing N reduces the per-subband rate but boosts the harvested energy. This is because less power is allocated to each subband but more balanced DC terms are introduced by frequency coupling to boost the harvested energy. On the other hand, Fig. 3.5(b) presents the sorted modulated/multisine amplitude $\text{s}_{\text{I}/P}$ for WPT. It demonstrates that a dedicated multisine waveform is unnecessary for a small N but is required for a large N. This observation origins from the rectifier nonlinearity. Although both waveforms have equivalent

---

[4]The results of RIS with random phase has not been included in Fig. 3.4, since its impact on subchannel amplitude gets averaged out and the result coincides with no RIS. This can be observed later in Figs. 3.10(a) and 3.10(b). In conclusion, the subchannel amplitude gain origins from the optimization of RIS rather than the extra propagation path.

second-order DC terms (3.9a) and (3.9c), for the fourth-order terms (3.9b) and (3.9d), the modulated waveform has N^2 monomials with a modulation gain of 2, while the multisine has $(2N^3 + N)/3$ monomials as the components of different frequencies compensate and produce DC. Second, the R-E region is convex for $N \in \{2, 4\}$ and concave-convex for $N \in \{8, 16\}$, such that PS outperforms TS for a small N and is outperformed for a large N. When N is in between, the optimal strategy is a combination of both, i.e., a time sharing between the WPT point and the saddle PS SWIPT point (as denoted by the red curve in Fig. 3.5(a)). When N is relatively small, only modulated waveform is used at both WIT and WPT points, and one can infer that no multisine waveform is needed for the entire R-E region. It aligns with the conclusion based on the conventional linear harvester model, namely the R-E region is convex, PS outperforms TS, and dedicated power waveform is unnecessary. As N becomes sufficiently large, the multisine waveform further boosts WPT and creates some concavity in the high-power region, which accounts for the superiority of TS under the nonlinear harvester model. Therefore, we conclude that the rectifier nonlinearity enlarges the R-E region by favoring a different waveform and receiving mode, both heavily depending on N.

3.4.2.2 Average Noise Power
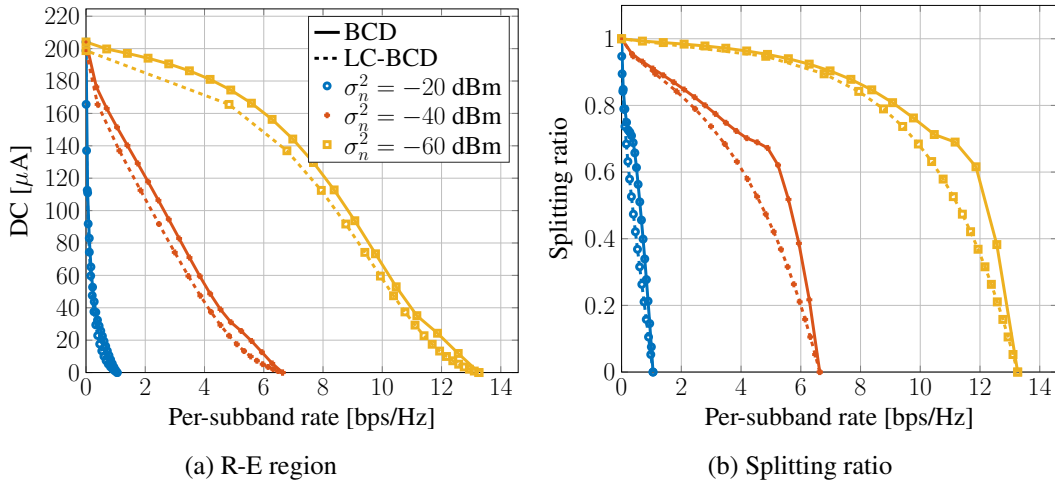
Fig. 3.6 Average R-E region and splitting ratio versus σ_n^2 for $M = 1$, $N = 16$, $L = 20$, $B = 1\,\mathrm{MHz}$ and $d_\mathrm{H} = d_\mathrm{V} = 2\,\mathrm{m}$.

The average noise power influences the R-E region as shown in Fig. 3.6(a). First, we note that the R-E region is roughly concave/convex at low/high SNR such that TS/PS are preferred correspondingly. At low SNR, the power is allocated to the modulated waveform on a few strongest subbands to achieve a high rate. As the rate constraint $\bar{R}$ decreases, Algorithm 2

activates more subbands that further boosts the harvested DC power because of frequency coupling and harvester nonlinearity. Second, there exists a turning point in the R-E region, especially for a low noise level ($\sigma_n^2 \leq -40\,\mathrm{dBm}$). The reason is that when $\bar{R}$ departs slightly from the maximum value, the algorithm tends to adjust the splitting ratio ρ rather than allocate more power to the multisine waveform, since a small amplitude multisine could be inefficient for energy purpose. As $\bar{R}$ further decreases, thanks to the advantage of multisine, a superposed waveform with a small ρ can outperform a modulated waveform with a large ρ. The result proves the benefit of superposed waveform and the necessity of joint waveform and splitting ratio optimization. Besides, the LC-BCD algorithm achieves a good balance between performance and complexity even if one-dimensional search is considered for $\delta = \rho$ from 0 to 1.

3.4.2.3 RIS Development

(a) R-E region   (b) Path loss product
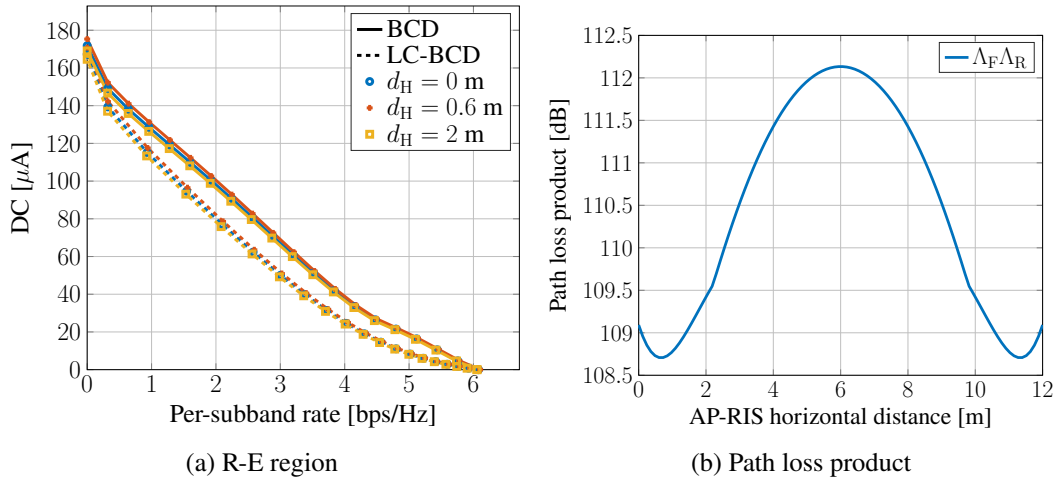
Fig. 3.7 Average R-E region and path loss versus d_H for $M = 1$, $N = 16$, $L = 20$, $\sigma_n^2 = -40\,\mathrm{dBm}$, $B = 1\,\mathrm{MHz}$ and $d_\mathrm{V} = 2\,\mathrm{m}$.

In Fig. 3.7(a), we compare the average R-E region achieved by different AP-RIS horizontal distance d_H. Different from the active AF relay that favors midpoint development [132], the RIS should be placed close to either the AP or the UE based on the product path loss model that applies to finite-size element reflection [47, 133]. Moreover, there exist two optimal RIS coordinates around $d_\mathrm{H} = 0.6$ and $11.4\,\mathrm{m}$ that minimize the path loss product $\Lambda_\mathrm{F}\Lambda_R$ and maximize the R-E trade-off. It suggests that equipping the AP with a RIS can potentially extend the operation range of SWIPT systems.

3.4.2.4   Number of Transmit Antennas and RIS Elements

(a) R-E region
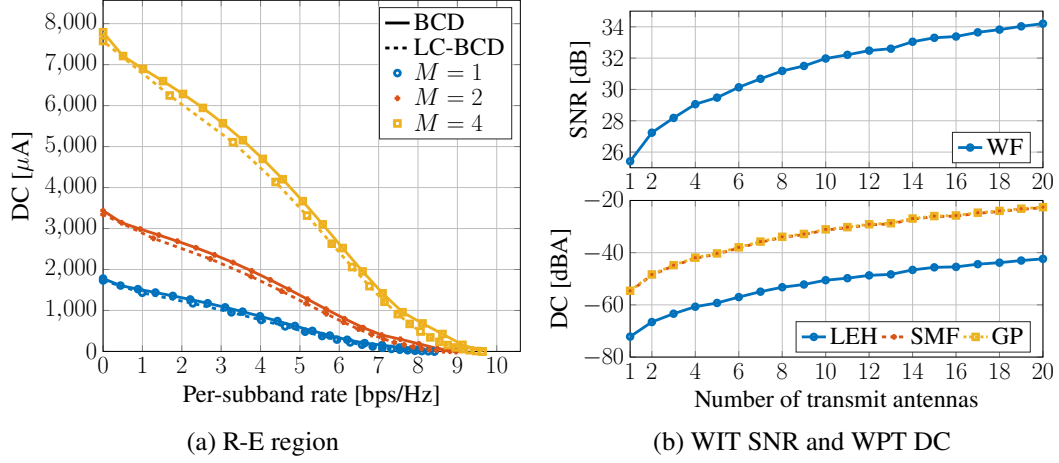
(b) WIT SNR and WPT DC

Fig. 3.8 Average R-E region, WIT SNR and WPT DC versus M for $N = 16$, $L = 20$, $\sigma_n^2 = -40\,\text{dBm}$, $B = 1\,\text{MHz}$, $d_\text{H} = d_\text{V} = 0.2\,\text{m}$.

(a) R-E region
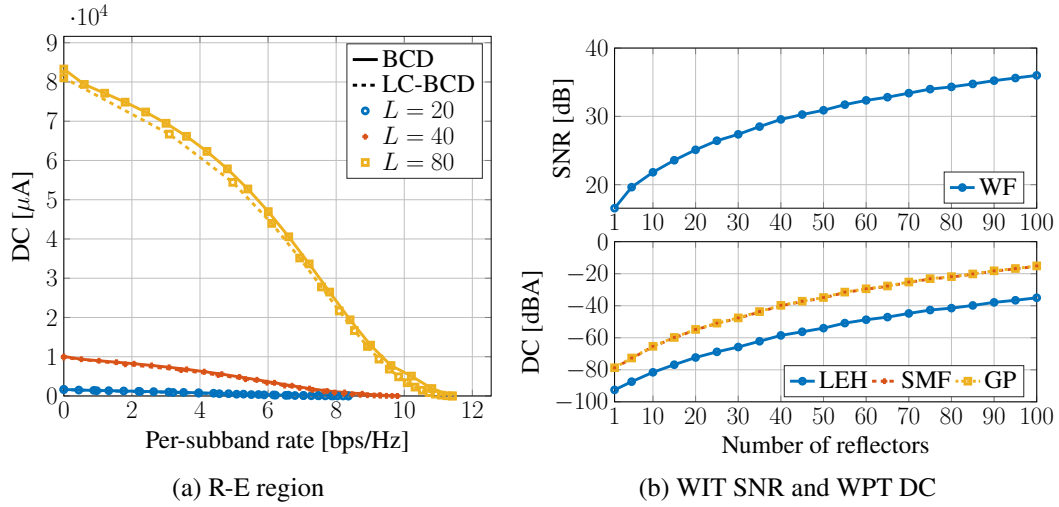
(b) WIT SNR and WPT DC

Fig. 3.9 Average R-E region, WIT SNR and WPT DC versus L for $M = 1$, $N = 16$, $\sigma_n^2 = -40\,\text{dBm}$, $B = 1\,\text{MHz}$ and $d_\text{H} = d_\text{V} = 0.2\,\text{m}$.

The impacts of the number of transmit antennas M and the RIS elements L on the R-E behavior are revealed in Figs. 3.8(a) and 3.9(a). First, it is observed that adding either active or passive elements can improve the equivalent SNR, which produces a nearly concave R-E region and favors the PS receiver. Second, the conventional Linear Energy Harvester (LEH) model leads to a power-inefficient design. To investigate the performance loss, we truncate the DC objective function (3.7) at $n_0 = 2$ such that (i) in the passive beamforming problem,

$z(\bar{\mathbf{\Theta}}) = \beta_2 \rho(t_{\mathrm{I},0} + t_{\mathrm{P},0})/2$ and no SCA is required; (ii) in the waveform design problem, the WPT-optimal strategy is the adaptive single sinewave that allocates all power to the multisine at the strongest subband [64]. As shown in Figs. 3.8(b) and 3.9(b), those conventional designs do not exploit the harvester nonlinearity and end up with a nearly $20\,\mathrm{dB}$ gap compared to the nonlinear model-based SMF and GP designs. Third, doubling M brings a $3\,\mathrm{dB}$ gain at the output SNR and a $12\,\mathrm{dB}$ increase at the harvested DC, which verified that active beamforming has an array gain of M [128] with power scaling order M^2 under the truncated nonlinear harvester model [64, 73]. Fourth, when the RIS is very close to the AP or UE, doubling L can bring a $6\,\mathrm{dB}$ gain at the output SNR and a $24\,\mathrm{dB}$ increase at the harvested DC. From the perspective of WIT, it suggests that passive beamforming can reach an array gain of L^2, as indicated by [16]. An interpretation is that the RIS coherently combines the incoming signal with a receive array gain L, then performs an equal gain reflection with a transmit array gain L. From the perspective of WPT, it suggests that passive beamforming comes with a power scaling order L^4 under the truncated nonlinear harvester model. We then verify this observation in a simplified case where the power is uniformly allocated over multisine, all channels are frequency-flat, and L is sufficiently large such that the direct channel becomes negligible. Let X be the cascaded small-scale fading coefficient. The DC in such case reduces to

$$z = \beta_2 \Lambda_{\mathrm{B}}^2 \Lambda_{\mathrm{F}}^2 |X|^2 L^2 P + \beta_4 \frac{2N^2 + 1}{2N} \Lambda_{\mathrm{B}}^4 \Lambda_{\mathrm{F}}^4 |X|^4 L^4 P^2, \tag{3.37}$$

which scales quartically with L. Compared with active antennas, RIS elements achieve higher array gain and power scaling order, but a very large L is required to compensate the double fading of the auxiliary link. These observations demonstrate the R-E benefit of passive beamforming and emphasize the importance of accounting for the harvester nonlinearity in the waveform and beamforming design.

3.4.2.5 Bandwidth

(a) $B = 1\,\mathrm{MHz}$
(b) $B = 10\,\mathrm{MHz}$
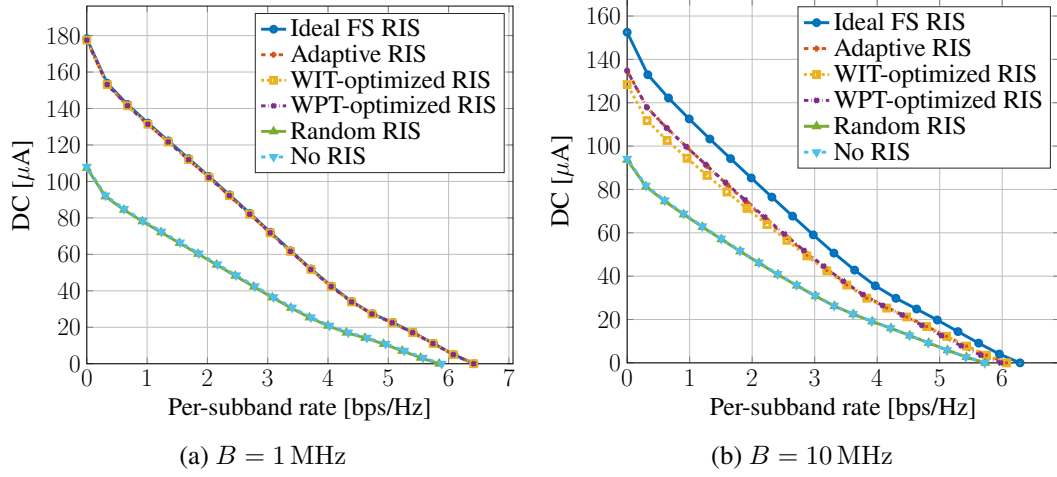
Fig. 3.10 Average R-E region for ideal, adaptive, fixed and no RIS versus B for $M = 1$, $N = 16$, $L = 20$, $\sigma_n^2 = -40\,\mathrm{dBm}$ and $d_\mathrm{H} = d_\mathrm{V} = 2\,\mathrm{m}$.

Figs. 3.10(a) and 3.10(b) explore the R-E region with different RIS strategies for narrowband and broadband SWIPT. The ideal Frequency-Selective (FS) RIS assumes the reflection coefficient of each element is independent and controllable at different frequencies. The adaptive RIS adjusts the passive beamforming for different R-E points by Algorithm 1. The WIT/WPT-optimized RIS is retrieved by Algorithm 3 then fixed for the whole R-E region. The random RIS models the phase shift of all elements as i.i.d. uniform random variables over $[0, 2\pi)$. First, random RIS and no RIS perform worse than other schemes since no passive beamforming is exploited. Their R-E boundaries coincide as the antenna mode reflection of the random RIS is canceled out after averaging. Second, when the bandwidth is small, the performance of ideal, adaptive, and WIT/WPT-optimized RIS are similar; when the bandwidth is large, the adaptive RIS outperforms the WIT/WPT-optimized RIS but is outperformed by the ideal FS RIS. In the former case, the subband responses are close to each other such that the trade-off in Remark 3.2 becomes insignificant, and the auxiliary link can be roughly maximized at all subbands. It suggests that for narrowband SWIPT, the optimal passive beamforming for any R-E point is optimal for the whole R-E region, and the corresponding equivalent channel and active precoder are also optimal for the whole R-E region. Hence, the achievable R-E region is obtained by optimizing the waveform amplitude and splitting ratio. On the other hand, since the channel frequency selectivity affects the performance of the information decoder and energy harvester differently, the optimal RIS reflection coefficient varies at different R-E trade-offs points for broadband SWIPT. As shown in Fig. 3.4, the subchannel amplification can be either spread evenly to improve the rate at

high SNR, or focused on a few strongest subbands to boost the output DC, thanks to adaptive passive beamforming.

3.4.2.6 Imperfect CSIT

(a) Imperfect cascaded CSIT
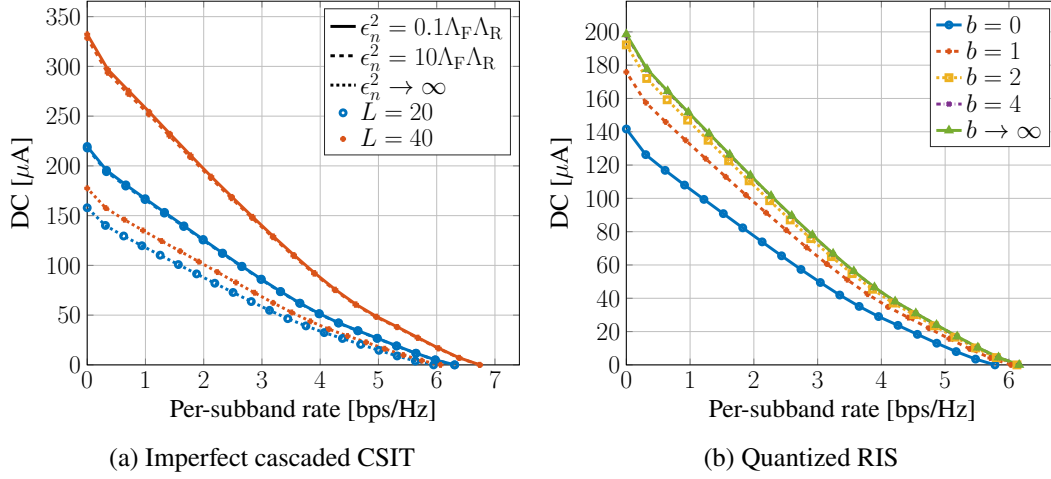
(b) Quantized RIS

Fig. 3.11 Average R-E region with imperfect cascaded CSIT and quantized RIS for $M = 1$, $N = 16$, $L = 20$, $\sigma_n^2 = -40\,\mathrm{dBm}$, $B = 10\,\mathrm{MHz}$ and $d_\mathrm{H} = d_\mathrm{V} = 2\,\mathrm{m}$. $\epsilon_n = 0$ and $\epsilon_n = \infty$ correspond respectively to perfect CSIT and no CSIT (and random RIS); $b = 0$ and $b \to \infty$ correspond respectively to no RIS and continuous RIS.

We then explore the impacts of imperfect cascaded CSIT and quantized RIS on the R-E performance. Due to the general lack of RF-chains at the RIS, it can be challenging to acquire accurate cascaded CSIT on a short-term basis. We assume the cascaded channel at subband n is

$$\mathbf{V}_n = \hat{\mathbf{V}}_n + \tilde{\mathbf{V}}_n, \tag{3.38}$$

where $\hat{\mathbf{V}}_n$ is the estimated cascaded CSIT and $\tilde{\mathbf{V}}_n$ is the estimation error with entries following i.i.d. CSCG distribution $\mathcal{CN}(0, \epsilon_n^2)$.[5] Figure 3.11(a) shows that the proposed passive beamforming Algorithm 1 is robust to cascaded CSIT inaccuracy for broadband SWIPT with different L. On the other hand, since the practical reflection coefficient depends on the available element impedances, we consider a discrete RIS codebook $\mathcal{C}_\phi = \{e^{j2\pi i/2^b} \mid i = 1, \dots, 2^b\}$ and uniformly quantize the continuous reflection coefficients obtained by Algorithm 4 to reduce the circuit complexity and control overhead. This relax-then-quantize approach can bring notable performance loss compared with direct optimization over the discrete phase shift set, especially for a small b (i.e., low-resolution RIS) [134]. Figure 3.11(b) suggests that

---

[5]Note that the subchannel responses are correlated but the estimations can be independent.

even $b = 1$ (i.e., two-state reflection) brings considerable R-E gain over the benchmark scheme without RIS, and the performance gap between $b = 4$ and continuous RIS is negligible. These observations demonstrate the advantage of the proposed joint waveform, active and passive beamforming design in practical RIS-aided SWIPT systems.

3.5 Conclusion and Future Works

This chapter investigated the R-E trade-off of a single user employing practical receiving strategies in a RIS-aided multi-carrier MISO SWIPT system. Uniquely, we considered the joint waveform, active and passive beamforming design under rectifier nonlinearity to maximize the achievable R-E region. A three-stage BCD algorithm was proposed to solve the problem. In the first stage, the RIS phase shift was obtained by the SCA technique and eigen decomposition. In the second and third stages, the active precoder was derived in closed form, and the waveform amplitude and splitting ratio were optimized by the GP method. We also proposed and combined closed-form adaptive waveform schemes with a modified passive beamforming strategy to formulate a low-complexity BCD algorithm that achieves a good balance between performance and complexity. Numerical results revealed significant R-E gains by modeling harvester nonlinearity in the RIS-aided SWIPT design. Unlike active antennas, RIS elements cannot be designed independently across frequencies, but can integrate coherent combining and equal gain transmission to enable constructive reflection and flexible subchannel design. Compared to the conventional no-RIS system, the RIS mainly affects the effective channel instead of the waveform design.

One particular unanswered question of this chapter is how to design waveform, active and passive beamforming in a multi-user multi-carrier RIS-aided SWIPT system. Also, harvester saturation effect and practical RIS models with amplitude-phase coupling [49], angle-dependent reflection [133], frequency-dependent reflection, and/or partially/fully-connected architecture [2] could be considered in future works.

Chapter 4

RIScatter: Unifying BackCom and RIS

4.1   Introduction

Future wireless network is envisioned to provide high throughput, uniform coverage, pervasive connectivity, heterogeneous control, and cognitive intelligence for trillions of low-power devices. BackCom separates a transmitter into a RF carrier emitter with power-hungry elements (e.g., synthesizer and amplifier) and an information-bearing node with power-efficient components (e.g., harvester and modulator) [46]. The receiver can be either co-located or separated with the carrier emitter, known as MBC and BBC in Fig. 4.1(a) and 4.1(b), respectively. Relevant applications such as RFID [135, 82] and passive sensor network [136, 137] have been extensively researched, standardized, and commercialized to embrace the IoE. However, conventional backscatter nodes only respond when externally inquired by a nearby reader. AmBC in Fig. 4.1(c) was proposed a decade ago where battery-free nodes recycle ambient signals (e.g., radio, television and Wi-Fi) to harvest energy and establish connections [98]. It does not require dedicated power source, carrier emitter, or frequency spectrum, but the backscatter decoding is subject to the strong interference from the primary (legacy) link. To tackle this, cooperative AmBC [138] employs a co-located receiver to decode both coexisting links, and the concept was further refined as SR in Fig. 4.1(d) [45]. Specifically, the active transmitter generates RF wave carrying primary information, the passive node creates a rich-scattering environment and superimposes its own information, and the co-located receiver cooperatively decodes both links. In those BackCom applications, the scatter node is considered as an *information source* and the reflection pattern depends exclusively on the information symbol. On the other hand, RIS in Fig. 4.1(e) is a smart signal reflector with numerous passive elements of adjustable phase shifts. It customizes the wireless environment for signal enhancement, interference suppression, scattering enrichment, and/or

non-line-of-sight bypassing [139]. Each RIS element is considered as a *channel shaper* and the reflection pattern depends exclusively on the CSI.

As a special case of Cognitive Radio (CR), active and passive transmissions coexist and interplay in AmBC and SR. Such a coexistence is classified into commensal (overlay), parasitic (underlay), and competitive (interfering) paradigms, and their achievable rate and outage performance were investigated in [99, 140]. The achievable rate and optimal input distribution for binary-input AmBC were investigated in [141], but its impact on the primary link was omitted. In [142], the authors analyzed the energy efficiency and achievable rate region for an AmBC-aided multi-user downlink Non-Orthogonal Multiple Access (NOMA) system. However, they assumed equal symbol duration and perfect synchronization for the coexisting links. Importantly, active-passive coexisting networks have three special and important properties:

1. Primary and backscatter symbols are superimposed by *double modulation* (i.e., multiplication coding);

2. Backscatter signal strength is much weaker than primary due to *double fading*;

3. The spreading factor (i.e., backscatter symbol duration over primary) is usually large[1].

The second property motivated [144, 45, 99, 140, 142, 145–148, 138, 149–151] to view SR as a multiplicative NOMA[2] and perform SIC from primary to backscatter link. During primary decoding, the backscatter signal can be modeled as channel uncertainty or multiplicative interference, when the spreading factor is large or small, respectively. Decoding each backscatter symbol also requires multiple SIC followed by a Maximal Ratio Combining (MRC) over primary blocks, which is operation-intensive and CSI-sensitive. Under those assumptions, the achievable rate region of cell-free SR was characterized in [151]. When the spreading factor is sufficiently large, the primary achievable rate under semi-coherent detection[3] asymptotically approaches its coherent counterpart such that both links are approximately interference-free [144]. However, this assumption severely limits the backscatter throughput.

---

[1]The load-switching interval of low-power backscatter modulators is usually 0.1 to 10 µs [143], accounting for a typical spreading factor between 10 and 10^3.

[2]As discussed in Section 2.4.2, a time-varying reflection pattern at rate Δf can shift the frequency of the scattered signal by $\pm \Delta f$. Therefore, the spreading ratio should be carefully chosen to balance backscatter rate and frequency offset.

[3]In this chapter, semi-coherent detection refers to the primary/backscatter decoding with known CSI and unknown backscatter/primary symbols.
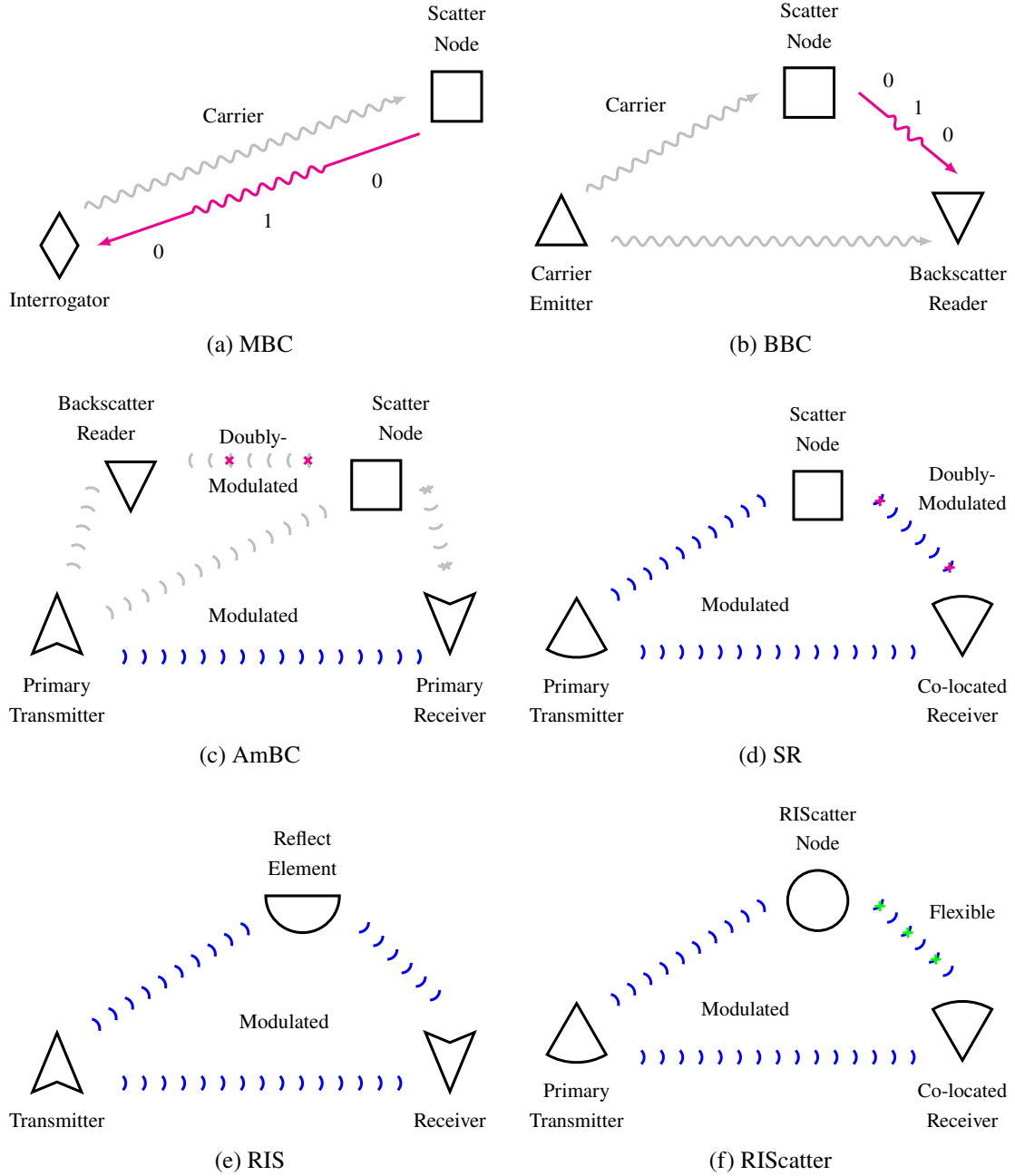
Fig. 4.1 Illustration of scattering applications. The blue flows denote the primary link while the magenta/green flows denote the backscatter link.

On the other hand, static RIS that employs fixed reflection pattern per channel block has been extensively studied in wireless communication, sensing, and power literature [50, 152–155, 30]. Dynamic RIS performs time sharing between different phase shifts and introduces artificial channel diversity within each channel block. The idea was first

Table 4.1 Comparison of Scattering Applications

Information link(s)	MBC/BBC	AmBC	SR (large spreading factor)	RIS	RIScatter
Information link(s)	Backscatter	Coexisting	Coexisting	Primary	Coexisting
Primary signal on backscatter decoding	Carrier	Multiplicative interference	Spreading code	—	Energy uncertainty
Backscatter signal on primary decoding	—	Multiplicative interference	CSI uncertainty	Passive beamforming	Dynamic passive beamforming
Cooperative devices	—	No	Primary transmitter and co-located receiver	—	Primary transmitter, scatter nodes, and co-located receiver
Sequential decoding	—	No	Primary-to-backscatter, SIC and MRC	—	Backscatter-to-primary, no SIC/MRC
Reflection pattern depends on	Information source	Information source	Information source	CSI	Information source, CSI, and QoS
Reflection state distribution	Equiprobable	Equiprobable	Equiprobable or Gaussian	Degenerate	Flexible
Load-switching speed	Fast	Slow	Slow	Quasi-static	Arbitrary

proposed to fine-tune the Orthogonal Frequency-Division Multiplexing (OFDM) resource blocks [156], then extended to the downlink power and uplink information phases of Wireless Powered Communication Network (WPCN) [15, 157, 158]. However, dynamic RIS carries no information because the reflection state at a specific time is known to the receiver. RIS can also be used as an information source, and prototypes have been developed for Phase Shift Keying (PSK) [159] and QAM [160]. From an information-theoretic perspective, the authors of [161] reported that joint transmitter-RIS encoding achieves the capacity of RIS-aided finite-input channel, and using RIS as a naive passive beamformer to maximize the receive SNR is generally rate-suboptimal. This inspired [162–171] to combine passive beamforming and backscatter modulation in the overall RIS design. In particular,

- *Symbol level precoding:* Maps the information symbols to the optimized RIS coefficient sets [162, 163];

- *Overlay modulation:* Superposes the information symbols over a common auxiliary matrix [164–167];

- *Spatial modulation:* Switches between the reflection coefficient sets that maximize SNR at different receive antennas [168–170];

- *Index modulation:* Employs dedicated reflection elements (resp. information elements) for passive beamforming (resp. backscatter modulation) [171].

Those RIS-based backscatter modulation schemes incur advanced hardware architecture and high optimization complexity. In contrast, [172] exploited commodity RFID tags, powered and controlled by a software-defined radio reader at a different frequency, to perform passive beamforming (but no backscatter modulation) towards a legacy user. Most relevant literature considered either Gaussian codebook [99, 140, 144–148, 166] that is impractical for low-power nodes, or finite equiprobable inputs [138, 45, 149, 150, 162–165, 167–171] that does not fully exploit the CSI and properties of active-passive coexisting networks. Those problems are addressed in this chapter and the contributions are summarized below.

First, we propose RIScatter as a novel protocol that unifies BackCom and RIS by adaptive reflection state (backscatter input) distribution design. The concept is shown in Fig. 4.1(f), where one or more RIScatter nodes ride over an active transmission to simultaneously modulate their information and engineer the wireless channel. A co-located receiver cooperatively decodes both coexisting links. Each reflection state is simultaneously a passive beamforming codeword and part of information codeword. The reflection pattern over time is semi-random and guided by the input probability assigned to each state. This probability distribution is carefully designed to incorporate the backscatter information, CSI, and Quality of Service

(QoS)[4]. Such an adaptive channel coding boils down to the degenerate distribution of RIS when the primary link is prioritized, and outperforms the uniform distribution of BackCom (by accounting the CSI) when the backscatter link is prioritized. Table 4.1 compares RIScatter to BackCom and RIS. However, two major challenges for RIScatter are the receiver design and input distribution design. This is the first work to unify BackCom and RIS from the perspective of input distribution.

Second, we address the first challenge and propose a low-complexity SIC-free receiver. It semi-coherently decodes the weak backscatter signal using an energy detector, re-encodes for the exact reflection pattern, then coherently decodes the primary link. Thanks to double modulation, backscatter detection can be viewed as part of channel training, and the impact of backscatter modulation can be modeled as dynamic passive beamforming afterwards. The proposed receiver may be built over legacy receivers with minor hardware upgrade, as it only requires one additional energy comparison and re-encoding per backscatter symbol (instead of primary symbol). The energy detector can also be tailored for arbitrary input distribution and spreading factor to increase backscatter throughput. This is the first work to propose a SIC-free cooperative receiver for active-passive coexisting networks.

Third, we address the second challenge in a single-user multi-node MISO scenario. We characterize the achievable primary-(total-)backscatter rate region by optimizing the input distribution at RIScatter nodes, the active beamforming at the AP, and the energy decision regions at the user under different QoS. A BCD algorithm is proposed where the Karush-Kuhn-Tucker (KKT) input distribution is numerically evaluated by the converging point of a sequence, the active beamforming is optimized by Projected Gradient Ascent (PGA), and the decision regions are refined by state-of-the-art sequential quantizer designs for Discrete Memoryless Thresholding Channel (DMTC). Uniquely, our optimization problem takes into account the CSI, QoS, and backscatter constellation, and the resulting input distribution is applicable to other detection schemes. This is also the first work to reveal the importance of backscatter input distribution and decision region designs in active-passive coexisting networks.

Fourth, we provide numerical results to demonstrate the benefits of RIScatter and proposed algorithms. The observations include:

- Adaptive reflection state distribution design can flexibly shift between backscatter modulation and passive beamforming;

- When the primary link is prioritized, input distribution becomes degenerate and RIScatter nodes coincide with discrete RIS;

---

[4]QoS refers to the relative priority of the primary link.

- When the backscatter link is prioritized, adaptive RIScatter encoding achieves higher backscatter rate than conventional line-coded BackCom with equiprobable inputs;

- Co-located RIScatter nodes can further leverage total backscatter rate by joint encoding;

- The proposed receiver maintains the passive beamforming benefit and provides comparable backscatter rate to SIC-based SR, with re-encoding costs reduced by N times (N is the spreading factor) and no re-precoding/cancellation;

- It also supports scatter nodes with faster load-switching speed for potentially higher throughput;

- PGA active beamformer effectively increases the primary (resp. backscatter) rate by boosting the receive SNR (resp. widening the energy gap under different reflection states), and can smoothly transition in between under different QoS;

- Distribution-aware backscatter detectors provide higher backscatter rate than the conventional Maximum-Likelihood (ML) detector.

4.2 RIScatter

4.2.1 Principles

Following the discussion on Section 2.1.2.1, we have the following conclusions:

- BackCom: The scatterer is an information source with random reflection pattern over time. The reflection coefficient is used merely as part of information codeword [91]

$$\Gamma_m = \alpha_m \frac{c_m}{\max_{m'}|c_{m'}|}, \tag{4.1}$$

where $\alpha_m \in \mathbb{I}$ is the amplitude scattering ratio at state m, and c_m is the corresponding constellation point.

- RIS: The scatterer is a channel shaper with deterministic reflection pattern over time. The reflection coefficient is used merely as a passive beamforming codeword [50]

$$\Gamma_m = \alpha_m \exp(\jmath\phi_m), \tag{4.2}$$

where ϕ_m is the phase shift at state m. Most papers assume $\alpha_m = \alpha$, with $\alpha \ll 1$ for BackCom and $\alpha = 1$ for RIS.

RIScatter generalizes BackCom and RIS from a probabilistic perspective. Each reflection coefficient simultaneously acts as a passive beamforming codeword and part of information codeword. As shown in Fig. 4.2(a), the reflection pattern of each RIScatter node over time is semi-random and guided by the input probability assigned to each state. This probability distribution is carefully designed to incorporate the backscatter information, CSI, and QoS, in order to strike a balance between backscatter modulation and passive beamforming. Fig. 4.2(b) illustrates the reflection pattern of a RIScatter node over time, where "PB", "BB", and "CB" refer to primary symbol block, backscatter symbol block, and channel block, respectively. We assume the coherent channel block is longer than backscatter symbol block, and the backscatter symbol block is longer than primary symbol block.
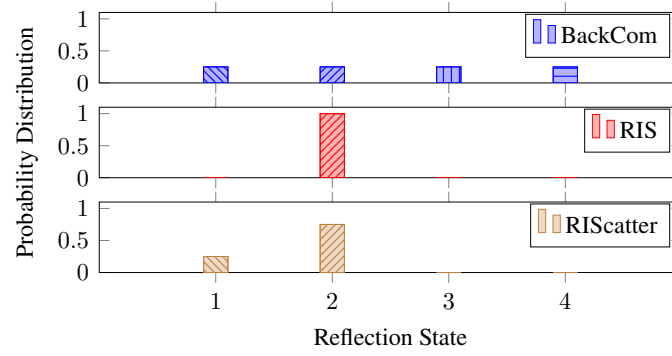
(a) Input Distribution
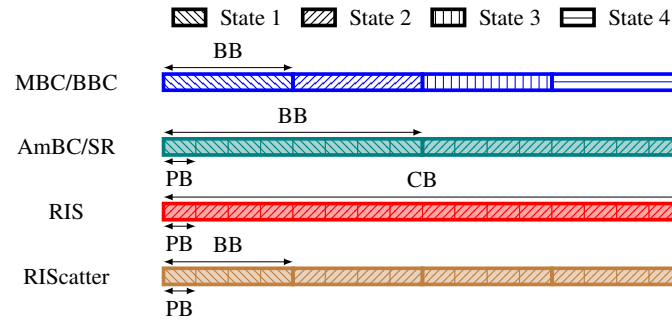
(b) Reflection Pattern

Fig. 4.2 Input distribution and reflection pattern of scattering applications. "PB", "BB", and "CB" refer to primary symbol block, backscatter symbol block, and channel block, respectively. Shadowing means presence of primary link. In this example, the optimal passive beamformer corresponds to state 2. The spreading factor is 4 for RIScatter and 8 for AmBC/SR. BackCom and RIS can be viewed as extreme cases of RIScatter, where the input distribution boils down to uniform and degenerate, respectively.

Remark 4.1. *Unlike dynamic RIS that simply performs a time sharing between reflection states, RIScatter conveys additional information by randomizing the reflection pattern over*

time while still guaranteeing the probability of occurrence of each state. Upon successful
backscatter detection, the impact of RIScatter nodes on the primary link can be modeled as
dynamic passive beamforming.

(a) Block Diagram

(b) Equivalent Circuit
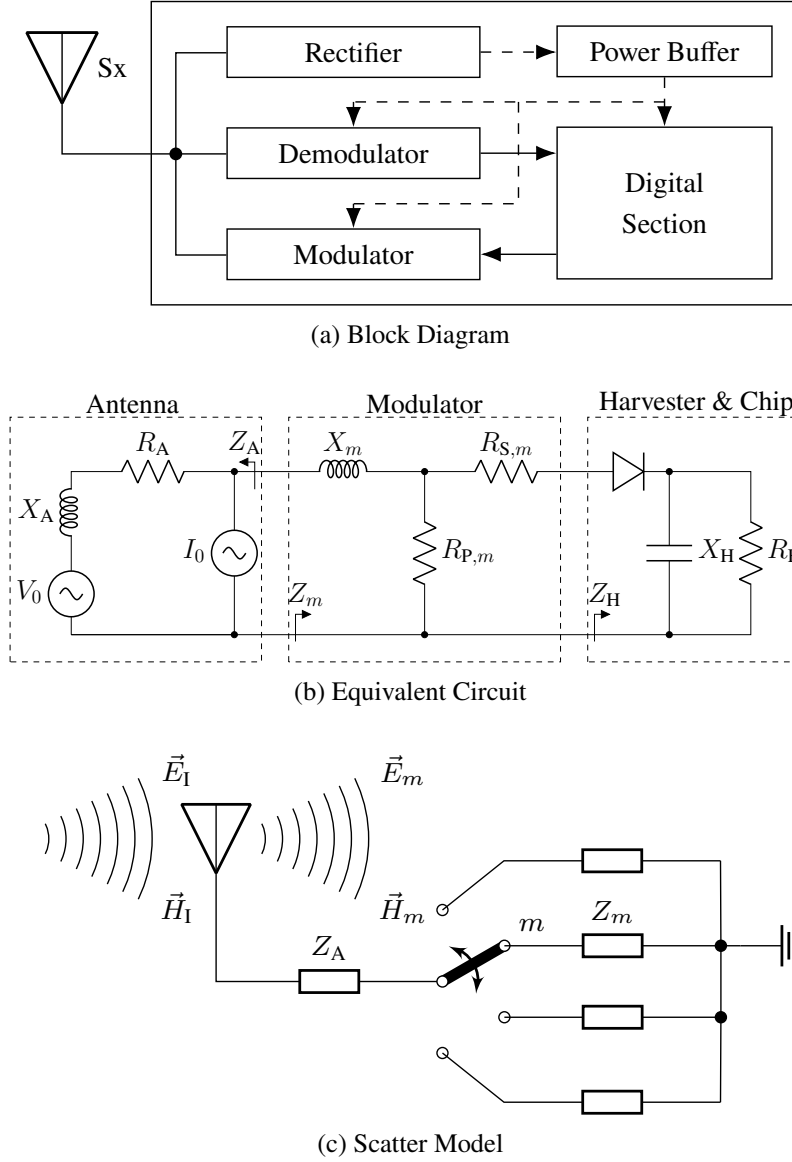
(c) Scatter Model

Fig. 4.3 Block diagram, equivalent circuit, and scatter model of a RIScatter node. The solid and dashed vectors represent signal and energy flows. The scatter antenna behaves as a constant power source, where the voltage V_0 and current I_0 are introduced by incident electric field $\vec{E}_I$ and magnetic field $\vec{H}_I$ [4].

RIScatter nodes can be implemented, for example, by adding an integrated receiver[5] [80] and adaptive encoder [173] to off-the-shelf passive RFID tags. The block diagram, equivalent circuit, and scatter model are illustrated in Fig. 4.3.

4.2.2 System Model
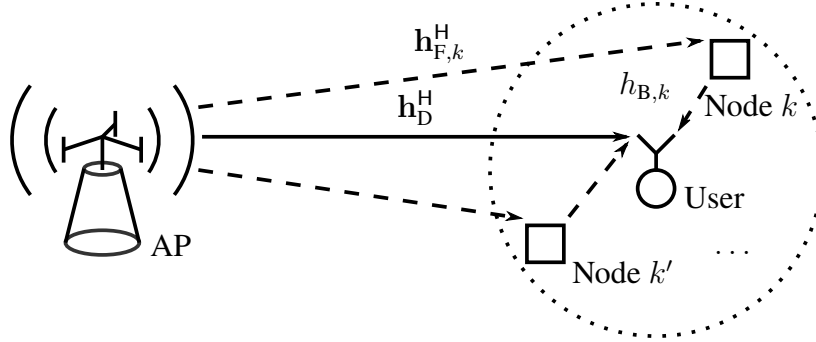
Fig. 4.4 A single-user multi-node RIScatter network.

As shown in Fig. 4.4, we consider a RIScatter network where a Q-antenna AP serves a single-antenna user and K nearby dispersed or co-located RIScatter nodes. Without loss of generality, we assume all nodes have M available reflection states. In the primary point-to-point system, the AP transmits information to the user over a multipath channel enhanced by RIScatter nodes. In the backscatter multiple access system, the AP acts as a carrier emitter, the RIScatter nodes modulate over the scattered signal, and the user jointly decodes all nodes. We assume the channel coherence time is longer than the backscatter symbol duration, the primary symbol duration is much longer than multipath delay spread (i.e., no inter-symbol interference), and the signal going through two or more RIScatter nodes is too weak to be received by the user. For simplicity, we consider a quasi-static block fading model and focus on a specific channel block where the CSI remains constant. Denote the AP-user direct channel as $\mathbf{h}_\mathrm{D}^\mathsf{H} \in \mathbb{C}^{1 \times Q}$, the AP-node $k \in \mathcal{K} \triangleq \{1, \ldots, K\}$ forward channel as $\mathbf{h}_{\mathrm{F},k}^\mathsf{H} \in \mathbb{C}^{1 \times Q}$, the node k-user backward channel as $h_{\mathrm{B},k}$, and the cascaded AP-node k-user channel as $\mathbf{h}_{\mathrm{C},k}^\mathsf{H} \triangleq h_{\mathrm{B},k}\mathbf{h}_{\mathrm{F},k}^\mathsf{H} \in \mathbb{C}^{1 \times Q}$. We assume the direct and cascaded CSI are available at the AP and the user. The cascaded CSI can be estimated by sequential [174, 84, 175] or parallel [176] approaches for dispersed nodes, or group-based [177] or hierarchical [115] approaches for co-located nodes. The impact of channel estimation error will be investigated in Section 4.4.

---

[5]The aim is to coordinate the node with the active source and to acquire the optimized input distribution, instead of decoding the primary information dedicated for the user. The node receiver can be implemented using simple circuits or even integrated with the rectifier [80] to reduce cost and complexity.

Let $\alpha_k \in \mathbb{I}$ be the amplitude scattering ratio of node k, $x_k \in \mathcal{X} \triangleq \{c_1, \ldots, c_M\}$ be the (coded) backscatter symbol of node k, and $x_\mathcal{K} \triangleq (x_1, \ldots, x_K)$ be the backscatter symbol tuple of all nodes. Due to double modulation, the composite channel is a function of backscatter symbol tuple[6]

$$\mathbf{h}^{\mathsf{H}}(x_\mathcal{K}) \triangleq \mathbf{h}_{\mathsf{D}}^{\mathsf{H}} + \sum_k \alpha_k \mathbf{h}_{\mathsf{C},k}^{\mathsf{H}} x_k \tag{4.3a}$$

$$= \mathbf{h}_{\mathsf{D}}^{\mathsf{H}} + \mathbf{x}^{\mathsf{H}} \mathrm{diag}(\alpha) \mathbf{H}_{\mathsf{C}}, \tag{4.3b}$$

where $\alpha \triangleq [\alpha_1, \ldots, \alpha_K]^{\mathsf{T}} \in \mathbb{I}^K$, $\mathbf{x} \triangleq [x_1, \ldots, x_K]^{\mathsf{H}} \in \mathcal{X}^K$, and $\mathbf{H}_{\mathsf{C}} \triangleq [\mathbf{h}_{\mathsf{C},1}, \ldots, \mathbf{h}_{\mathsf{C},K}]^{\mathsf{H}} \in \mathbb{C}^{K \times Q}$. Without loss of generality, we assume the spreading factor N is a positive integer. Within one backscatter block, the signal received by the user at primary block $n \in \mathcal{N} \triangleq \{1, \ldots, N\}$ is

$$y[n] = \mathbf{h}^{\mathsf{H}}(x_\mathcal{K})\mathbf{w}s[n] + v[n], \tag{4.4}$$

where $\mathbf{w} \in \mathbb{C}^Q$ is the active beamformer satisfying $\|\mathbf{w}\|^2 \leq P$, P is the maximum average transmit power, $s \sim \mathcal{CN}(0, 1)$ is the primary symbol, and $v \sim \mathcal{CN}(0, \sigma_v^2)$ is the Additive White Gaussian Noise (AWGN) with variance σ_v^2.

Let $m_k \in \mathcal{M} \triangleq \{1, \ldots, M\}$ be the reflection state index of node k, and $m_\mathcal{K} \triangleq (m_1, \ldots, m_K)$ be the state index tuple of all nodes. The backscatter symbol x_k (resp. symbol tuple $x_\mathcal{K}$) is a random variable that takes value x_{m_k} (resp. value tuple $x_{m_\mathcal{K}}$) with probability $p(x_{m_k})$ (resp. $p(x_{m_\mathcal{K}})$).

Remark 4.2. *Dispersed RIScatter nodes encode independently such that*

$$p(x_{m_\mathcal{K}}) = \prod_k p(x_{m_k}). \tag{4.5}$$

When multiple nodes are co-located, they can jointly encode by designing the joint probability $p(x_{m_\mathcal{K}})$ directly.

Let $z = \sum_n |y[n]|^2$ be the receive energy per backscatter block. When $x_{m_\mathcal{K}}$ is transmitted, the receive signal y follows CSCG distribution $\mathcal{CN}(0, \sigma_{m_\mathcal{K}}^2)$ with variance

$$\sigma_{m_\mathcal{K}}^2 = |\mathbf{h}^{\mathsf{H}}(x_{m_\mathcal{K}})\mathbf{w}|^2 + \sigma_v^2, \tag{4.6}$$

---

[6](4.3a) and (4.3b) are often used in BackCom and RIS literature, respectively.

and z follows Gamma distribution with conditional Probability Density Function (PDF)

$$f(z|x_{m_{\mathcal{K}}}) = \frac{z^{N-1} \exp(-z/\sigma_{m_{\mathcal{K}}}^2)}{\sigma_{m_{\mathcal{K}}}^{2N}(N-1)!}. \tag{4.7}$$

Remark 4.3. *We have assumed Gaussian codebook for the primary source and finite support for the backscatter nodes, since they are relatively practical and widely adopted in relevant literatures [141, 164, 165, 167, 171, 178]. The proposed framework is extendable to non-Gaussian primary source, and the conditional PDF (4.7) can be approximated using Central Limit Theorem (CLT) for large N.*

The user first jointly decodes the backscatter message of all nodes using a low-complexity energy detector.[7] The energy detector formulates a DMTC of size $M^K \times M^K$.

Remark 4.4. *The capacity-achieving decision region design for DMTC with non-binary inputs in arbitrary distribution remains an open issue. It was proved deterministic detectors can be rate-optimal, but non-convex regions (consist of non-adjacent partitions) are generally required and the optimal number of thresholds is unknown [180, 181]. Next, we restrict the energy detector to convex deterministic decision regions and consider sequential threshold design.*

Let $L = M^K$ be the number of decision regions. Sort $\{\sigma_{m_{\mathcal{K}}}^2\}$ in ascending order and denote the result sequence as $\sigma_1^2, \ldots, \sigma_L^2$. With sequential thresholding, the decision region of backscatter symbol tuple $l \in \mathcal{L} \triangleq \{1, \ldots, L\}$ is[8]

$$\mathcal{R}_l \triangleq [t_{l-1}, t_l), \quad 0 \le t_{l-1} \le t_l, \tag{4.8}$$

where t_l is the decision threshold between hypotheses x_l and x_{l+1}. An example is shown in Fig. 4.5.

---

[7]The reliability of the energy detector is improved by the adaptive input distribution and thresholding design. With high-order modulation or large number of scatter nodes, the reliability can be further enhanced by increasing the spreading factor or using error correction codes with low code-rate. In practice, users can decode backscatter nodes ranging from a few to hundreds of meters in the presence of noise and interference, and the backscatter throughput can reach few Kbps to tens of Mbps [179].

[8]$m_{\mathcal{K}}$ and l are one-to-one mapped. Both notations are used interchangeably in the following context.
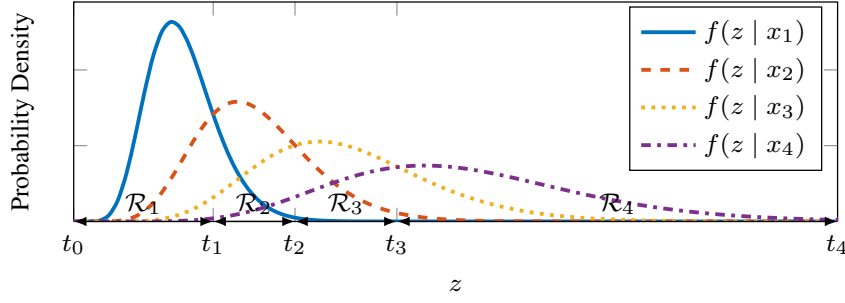
Fig. 4.5 PDF of the receive energy per backscatter block conditioned on different reflection state.

When the threshold vector $\mathbf{t} \triangleq [t_0, \ldots, t_L]^{\mathsf{T}} \in \mathbb{R}_+^{L+1}$ is given, we can formulate a Discrete Memoryless Multiple Access Channel (DMMAC) with transition probability from input $x_{m_{\mathcal{K}}}$ to output $\hat{x}_{m'_{\mathcal{K}}}$ as

$$q(\hat{x}_{m'_{\mathcal{K}}}|x_{m_{\mathcal{K}}}) = \int_{\mathcal{R}_{m'_{\mathcal{K}}}} f(z|x_{m_{\mathcal{K}}}) \, dz. \tag{4.9}$$

The backscatter mutual information is

$$I_{\mathrm{B}}(x_{\mathcal{K}}; \hat{x}_{\mathcal{K}}) = \sum_{m_{\mathcal{K}}} p(x_{m_{\mathcal{K}}}) I_{\mathrm{B}}(x_{m_{\mathcal{K}}}; \hat{x}_{\mathcal{K}}), \tag{4.10}$$

where $I_{\mathrm{B}}(x_{m_{\mathcal{K}}}; \hat{x}_{\mathcal{K}})$ is the backscatter information function

$$I_{\mathrm{B}}(x_{m_{\mathcal{K}}}; \hat{x}_{\mathcal{K}}) \triangleq \sum_{m'_{\mathcal{K}}} q(\hat{x}_{m'_{\mathcal{K}}}|x_{m_{\mathcal{K}}}) \log \frac{q(\hat{x}_{m'_{\mathcal{K}}}|x_{m_{\mathcal{K}}})}{p(\hat{x}_{m'_{\mathcal{K}}})}. \tag{4.11}$$

Once the backscatter information is successfully decoded, the user re-encodes to recover the reflection pattern, constructs the composite channel by (4.3), then coherently decodes the primary link. The primary mutual information is

$$I_{\mathrm{P}}(s; y|x_{\mathcal{K}}) = \sum_{m_{\mathcal{K}}} p(x_{m_{\mathcal{K}}}) I_{\mathrm{P}}(s; y|x_{m_{\mathcal{K}}}), \tag{4.12}$$

where $I_{\mathrm{P}}(s; y|x_{m_{\mathcal{K}}})$ is the primary information function

$$I_{\mathrm{P}}(s; y|x_{m_{\mathcal{K}}}) \triangleq \log\left(1 + \frac{|\mathbf{h}^{\mathsf{H}}(x_{m_{\mathcal{K}}})\mathbf{w}|^2}{\sigma_v^2}\right). \tag{4.13}$$

4.3   Rate-Region Characterization

With a slight abuse of notation, we define the weighed sum mutual information and information function as

$$I(x_{\mathcal{K}}) \triangleq \rho I_{\mathsf{P}}(s; y|x_{\mathcal{K}}) + (1 - \rho)I_{\mathsf{B}}(x_{\mathcal{K}}; \hat{x}_{\mathcal{K}}), \tag{4.14}$$

$$I(x_{m_{\mathcal{K}}}) \triangleq \rho I_{\mathsf{P}}(s; y|x_{m_{\mathcal{K}}}) + (1 - \rho)I_{\mathsf{B}}(x_{m_{\mathcal{K}}}; \hat{x}_{\mathcal{K}}), \tag{4.15}$$

where $\rho \in \mathbb{I}$ is the QoS. To obtain the achievable primary-(total-)backscatter rate region, we consider the weighted sum mutual information maximization problem with independent encoding at all nodes[9]

$$\max_{\{\mathbf{p}_k\}_{k \in \mathcal{K}}, \mathbf{w}, \mathbf{t}} \quad I(x_{\mathcal{K}}) \tag{4.16a}$$

$$\text{s.t.} \quad \mathbf{1}^{\mathsf{T}}\mathbf{p}_k = 1, \quad \forall k, \tag{4.16b}$$

$$\mathbf{p}_k \geq \mathbf{0}, \quad \forall k, \tag{4.16c}$$

$$\|\mathbf{w}\|^2 \leq P, \tag{4.16d}$$

$$t_{l-1} \leq t_l, \quad \forall l, \tag{4.16e}$$

$$\mathbf{t} \geq \mathbf{0}, \tag{4.16f}$$

where $\mathbf{p}_k = [p(x_{1_k}), \ldots, p(x_{M_k})]^{\mathsf{T}} \in \mathbb{I}^M$ is the input distribution of node k. Problem (4.16) generalizes BackCom by allowing CSI- and QoS-adaptive input distribution and decision region design. On the other hand, it also relaxes the feasible domain of discrete RIS phase shift selection problems from the vertices of M-dimensional probability simplex to the simplex itself. The original problem is highly non-convex and we propose a BCD algorithm that iteratively updates $\{\mathbf{p}_k\}_{k \in \mathcal{K}}$, $\mathbf{w}$ and $\mathbf{t}$.

4.3.1   Input Distribution

For any given $\mathbf{w}$ and $\mathbf{t}$, we can formulate a DMMAC by (4.9) and simplify (4.16) to

$$\max_{\{\mathbf{p}_k\}_{k \in \mathcal{K}}} \quad I(x_{\mathcal{K}}) \tag{4.17a}$$

$$\text{s.t.} \quad (4.16\text{b}), (4.16\text{c}), \tag{4.17b}$$

---

[9]Joint encoding over multiple nodes can be viewed as its special case with an augmented backscatter source.

which involves the product term (4.5) and is generally non-convex (unless $K = 1$). Following [182], we first recast the KKT conditions to their equivalent forms, then propose a numerical solution that guarantees those conditions on the converging point of a sequence.

Proposition 4.1. *The KKT optimality conditions for problem* (4.17) *are equivalent to,* $\forall k, m_k$,

$$I_k^\star(x_{m_k}) = I^\star(x_{\mathcal{K}}), \quad if\, p^\star(x_{m_k}) > 0, \tag{4.18a}$$

$$I_k^\star(x_{m_k}) \leq I^\star(x_{\mathcal{K}}), \quad if\, p^\star(x_{m_k}) = 0, \tag{4.18b}$$

where $I_k(x_{m_k})$ *is the weighted sum marginal information*

$$I_k(x_{m_k}) \triangleq \sum_{m_{\mathcal{K}\setminus\{k\}}} p(x_{m_{\mathcal{K}\setminus\{k\}}}) I(x_{m_{\mathcal{K}}}). \tag{4.19}$$

Proof. Please refer to Appendix 7.2.1. $\qquad\qquad\qquad\qquad\qquad\qquad\square$

For each RIScatter node, (4.18a) suggests each probable state should produce the same marginal information (averaged over all states of other nodes), while (4.18b) suggests any state with potentially less marginal information should not be used.

Proposition 4.2. *For any strictly positive initializer* $\{\mathbf{p}_k^{(0)}\}_{k\in\mathcal{K}}$, *the KKT input probability of node* k *at state* m_k *is given by the converging point of the sequence*

$$p^{(r+1)}(x_{m_k}) = \frac{p^{(r)}(x_{m_k}) \exp\left(\frac{\rho}{1-\rho} I_k^{(r)}(x_{m_k})\right)}{\sum_{m_k'} p^{(r)}(x_{m_k'}) \exp\left(\frac{\rho}{1-\rho} I_k^{(r)}(x_{m_k'})\right)}, \tag{4.20}$$

where r *is the iteration index.*

Proof. Please refer to Appendix 7.2.2. $\qquad\qquad\qquad\qquad\qquad\qquad\square$

At iteration $r+1$, the input distribution of node k is updated over $\left\{\{\mathbf{p}_q^{(r+1)}\}_{q=1}^{k-1}, \{\mathbf{p}_q^{(r)}\}_{q=k}^{K}\right\}$. The KKT input distribution design is summarized in Algorithm 6.

Remark 4.5. *The insufficiency of the KKT conditions for problem* (4.17) *implies that the proposed method may not converge to the global-optimal solution. However, simulation results in Section 4.4 will show that the average performance gap is indistinguishable at a moderate* K.

Algorithm 6 Input Distribution Evaluation by a Sequence

Input: K, N, $\mathbf{h}_\mathrm{D}^\mathsf{H}$, $\mathbf{H}_\mathrm{C}$, α, $\mathcal{X}$, σ_v^2, ρ, $\mathbf{w}$, $\mathbf{t}$, ϵ
Output: $\{\mathbf{p}_k^\star\}_{k\in\mathcal{K}}$
  1: Set $\mathbf{h}^\mathsf{H}(x_{m_\mathcal{K}})$, $\forall m_\mathcal{K}$ by (4.3)
  2:    $\sigma_{m_\mathcal{K}}^2$, $\forall m_\mathcal{K}$ by (4.6)
  3:    $f(z|x_{m_\mathcal{K}})$, $\forall m_\mathcal{K}$ by (4.7)
  4:    $q(\hat{x}_{m_\mathcal{K}'}|x_{m_\mathcal{K}})$, $\forall m_\mathcal{K}, m_\mathcal{K}'$ by (4.9)
  5: Initialize $r \leftarrow 0$
  6:        $\mathbf{p}_k^{(0)} > \mathbf{0}$, $\forall k$
  7: Get $p^{(r)}(x_{m_\mathcal{K}})$, $\forall m_\mathcal{K}$ by (4.5)
  8:    $I^{(r)}(x_{m_\mathcal{K}})$, $\forall m_\mathcal{K}$ by (4.11), (4.13), (4.15)
  9:    $I_k^{(r)}(x_{m_k})$, $\forall k, m_k$ by (4.19)
 10:    $I^{(r)}(x_\mathcal{K})$ by (4.10), (4.12), (4.14)
 11: **Repeat**
 12:        Update $r \leftarrow r + 1$
 13:            $\mathbf{p}_k^{(r)}$, $\forall k$ by (4.20)
 14:        Redo step 7–10
 15: **Until** $I^{(r)}(x_\mathcal{K}) - I^{(r-1)}(x_\mathcal{K}) \leq \epsilon$

4.3.2   Active Beamforming

For any given $\{\mathbf{p}_k\}_{k\in\mathcal{K}}$ and $\mathbf{t}$, problem (4.16) reduces to

$$\max_{\mathbf{w}} \quad I(x_\mathcal{K}) \tag{4.21a}$$

$$\text{s.t.} \quad (4.16\text{d}), \tag{4.21b}$$

which is still non-convex due to the integration and entropy terms. Note the DMMAC $q(x_l|x_{m_\mathcal{K}})$ depends on the variance of accumulated receive energy $\sigma_{m_\mathcal{K}}^2$, which is a function of $\mathbf{w}$. Plugging (4.7) into (4.9), we have

$$q(x_l|x_{m_\mathcal{K}}) = \frac{\int_{t_{l-1}/\sigma_{m_\mathcal{K}}^2}^{t_l/\sigma_{m_\mathcal{K}}^2} z^{N-1}\exp(-z)\,dz}{(N-1)!} \tag{4.22}$$

$$= Q\Big(N, \frac{t_{l-1}}{\sigma_{m_\mathcal{K}}^2}, \frac{t_l}{\sigma_{m_\mathcal{K}}^2}\Big), \tag{4.23}$$

where $Q(N, b_1, b_2) \triangleq \int_{b_1}^{b_2} z^{N-1} \exp(-z)/(N-1)!\, dz$ is the regularized incomplete Gamma function. Its series expansion is given by [183, Theorem 3]

$$Q\Big(N, \frac{t_{l-1}}{\sigma_{m_\mathcal{K}}^2}, \frac{t_l}{\sigma_{m_\mathcal{K}}^2}\Big) = \exp\Big(-\frac{t_{l-1}}{\sigma_{m_\mathcal{K}}^2}\Big) \sum_{n=0}^{N-1} \frac{\big(\frac{t_{l-1}}{\sigma_{m_\mathcal{K}}^2}\big)^n}{n!} - \exp\Big(-\frac{t_l}{\sigma_{m_\mathcal{K}}^2}\Big) \sum_{n=0}^{N-1} \frac{\big(\frac{t_l}{\sigma_{m_\mathcal{K}}^2}\big)^n}{n!}, \quad (4.24)$$

whose gradient with respect to $\mathbf{w}^*$ is

$$\nabla_{\mathbf{w}^*} Q\Big(N, \frac{t_{l-1}}{\sigma_{m_\mathcal{K}}^2}, \frac{t_l}{\sigma_{m_\mathcal{K}}^2}\Big) = \frac{\mathbf{h}(x_{m_\mathcal{K}})\mathbf{h}^\mathsf{H}(x_{m_\mathcal{K}})\mathbf{w}}{(\sigma_{m_\mathcal{K}}^2)^2}\Big(g_{m_\mathcal{K}}(t_l) - g_{m_\mathcal{K}}(t_{l-1})\Big), \quad (4.25)$$

where

$$g_{m_\mathcal{K}}(t_l) = t_l \exp\Big(-\frac{t_l}{\sigma_{m_\mathcal{K}}^2}\Big)\Big(-1 + \sum_{n=1}^{N-1} \frac{\big(n - \frac{t_l}{\sigma_{m_\mathcal{K}}^2}\big)\big(\frac{t_l}{\sigma_{m_\mathcal{K}}^2}\big)^{n-1}}{n!}\Big). \quad (4.26)$$

On top of (4.24) and (4.25), the mutual information (4.14) can be rewritten as

$$I(x_\mathcal{K}) = \sum_{m_\mathcal{K}} p(x_{m_\mathcal{K}})\Bigg(\rho \log\Big(1 + \frac{|\mathbf{h}^\mathsf{H}(x_{m_\mathcal{K}})\mathbf{w}|^2}{\sigma_v^2}\Big)$$

$$+ (1-\rho)\sum_l Q\Big(N, \frac{t_{l-1}}{\sigma_{m_\mathcal{K}}^2}, \frac{t_l}{\sigma_{m_\mathcal{K}}^2}\Big) \log \frac{Q\Big(N, \frac{t_{l-1}}{\sigma_{m_\mathcal{K}}^2}, \frac{t_l}{\sigma_{m_\mathcal{K}}^2}\Big)}{\sum_{m'_\mathcal{K}} p(x_{m'_\mathcal{K}})Q\Big(N, \frac{t_{l-1}}{\sigma_{m'_\mathcal{K}}^2}, \frac{t_l}{\sigma_{m'_\mathcal{K}}^2}\Big)} \Bigg) \quad (4.27)$$

and its gradient with respect to $\mathbf{w}^*$ is

$$\nabla_{\mathbf{w}^*} I(x_\mathcal{K}) = \sum_{m_\mathcal{K}} p(x_{m_\mathcal{K}})\Bigg(\rho \frac{\mathbf{h}(x_{m_\mathcal{K}})\mathbf{h}^\mathsf{H}(x_{m_\mathcal{K}})\mathbf{w}}{\sigma_{m_\mathcal{K}}^2}$$

$$+ (1-\rho)\sum_l \Big(\log \frac{Q\Big(N, \frac{t_{l-1}}{\sigma_{m_\mathcal{K}}^2}, \frac{t_l}{\sigma_{m_\mathcal{K}}^2}\Big)}{\sum_{m'_\mathcal{K}} p(x_{m'_\mathcal{K}})Q\Big(N, \frac{t_{l-1}}{\sigma_{m'_\mathcal{K}}^2}, \frac{t_l}{\sigma_{m'_\mathcal{K}}^2}\Big)} + 1\Big)\nabla_{\mathbf{w}^*} Q\Big(N, \frac{t_{l-1}}{\sigma_{m_\mathcal{K}}^2}, \frac{t_l}{\sigma_{m_\mathcal{K}}^2}\Big)$$

$$- \frac{Q\Big(N, \frac{t_{l-1}}{\sigma_{m_\mathcal{K}}^2}, \frac{t_l}{\sigma_{m_\mathcal{K}}^2}\Big) \sum_{m'_\mathcal{K}} p(x_{m'_\mathcal{K}})\nabla_{\mathbf{w}^*} Q\Big(N, \frac{t_{l-1}}{\sigma_{m'_\mathcal{K}}^2}, \frac{t_l}{\sigma_{m'_\mathcal{K}}^2}\Big)}{\sum_{m'_\mathcal{K}} p(x_{m'_\mathcal{K}})Q\Big(N, \frac{t_{l-1}}{\sigma_{m'_\mathcal{K}}^2}, \frac{t_l}{\sigma_{m'_\mathcal{K}}^2}\Big)} \Bigg)$$

$$(4.28)$$

Problem (4.21) can thus be solved by the PGA method. At iteration $r+1$, the unregulated active beamformer is updated by

$$\bar{\mathbf{w}}^{(r+1)} = \mathbf{w}^{(r)} + \gamma \nabla_{\mathbf{w}^*} I^{(r)}(x_\mathcal{K}), \quad (4.29)$$

Algorithm 7 Active Beamforming Optimization by PGA

Input: Q, N, $\mathbf{h}_{\mathrm{D}}^{\mathsf{H}}$, $\mathbf{H}_{\mathrm{C}}$, α, $\mathcal{X}$, P, σ_v^2, ρ, $\{\mathbf{p}_k\}_{k \in \mathcal{K}}$, $\mathbf{t}$, α, β, γ, ϵ
Output: $\mathbf{w}^\star$
 1: Set $\mathbf{h}^{\mathsf{H}}(x_{m_{\mathcal{K}}})$, $\forall m_{\mathcal{K}}$ by (4.3)
 2:      $p(x_{m_{\mathcal{K}}})$, $\forall m_{\mathcal{K}}$ by (4.5)
 3: Initialize $r \leftarrow 0$
 4:          $\mathbf{w}^{(0)}$, $\|\mathbf{w}^{(0)}\|^2 \leq P$
 5: Get $(\sigma_{m_{\mathcal{K}}}^{(r)})^2$, $\forall m_{\mathcal{K}}$ by (4.6)
 6:      $Q^{(r)}\big(N, \frac{t_{l-1}}{\sigma_{m_{\mathcal{K}}}^2}, \frac{t_l}{\sigma_{m_{\mathcal{K}}}^2}\big)$, $\forall m_{\mathcal{K}}, l$ by (4.24)
 7:      $I^{(r)}(x_{\mathcal{K}})$ by (4.27)
 8:      $\nabla_{\mathbf{w}^*} Q^{(r)}\big(N, \frac{t_{l-1}}{\sigma_{m_{\mathcal{K}}}^2}, \frac{t_l}{\sigma_{m_{\mathcal{K}}}^2}\big)$, $\forall m_{\mathcal{K}}, l$ by (4.25)
 9:      $\nabla_{\mathbf{w}^*} I^{(r)}(x_{\mathcal{K}})$ by (4.28)
10: **Repeat**
11:      Update $r \leftarrow r + 1$
12:          $\gamma^{(r)} \leftarrow \gamma$
13:          $\bar{\mathbf{w}}^{(r)}$ by (4.29)
14:          $\mathbf{w}^{(r)}$ by (4.30)
15:      Redo step 5–7
16:      **While** $I^{(r)}(x_{\mathcal{K}}) < I^{(r-1)}(x_{\mathcal{K}}) + \alpha\gamma\|\nabla_{\mathbf{w}^*} I^{(r-1)}(x_{\mathcal{K}})\|^2$
17:          Set $\gamma^{(r)} \leftarrow \beta\gamma^{(r)}$
18:          Redo step 13–15
19:      **End While**
20:      Redo step 8, 9
21: **Until** $\|\mathbf{w}^{(r)} - \mathbf{w}^{(r-1)}\| \leq \epsilon$

---

where γ is the step size (refinable by backtracking line search [184, Section 9.2]). Then, $\bar{\mathbf{w}}$ is projected onto the feasible domain (4.16d) to retrieve the active beamformer

$$\mathbf{w} = \frac{\sqrt{P}\bar{\mathbf{w}}}{\max\big(\sqrt{P}, \|\bar{\mathbf{w}}\|\big)}. \tag{4.30}$$

The PGA active beamforming design is summarized in Algorithm 7.

4.3.3 Decision Threshold

For any given $\{\mathbf{p}_k\}_{k \in \mathcal{K}}$ and $\mathbf{w}$, problem (4.16) reduces to

$$\max_{\mathbf{t}} \quad I(x_{\mathcal{K}}) \tag{4.31a}$$

$$\text{s.t.} \quad (4.16e), (4.16f), \tag{4.31b}$$

which is still non-convex since $\mathbf{t}$ appears on the limits of integration (4.9). Instead of solving it directly, we constrain the feasible domain from continuous space $\mathbb{R}_+^{L+1}$ to discrete candidates (i.e., fine-grained energy levels) $\mathcal{T}^{L+1}$. As shown in Fig. 4.6, the decision regions are formulated by grouping adjacent energy bins.
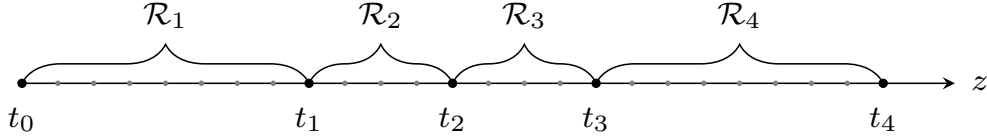
Fig. 4.6 The thresholds are chosen from fine-grained candidates instead of the continuous space. Each decision region consists of at least one bin.

Remark 4.6. *The design of the energy detector does not affect the primary achievable rate, since the composite channel* (4.3) *can always be determined after backscatter decoding and re-encoding. This implies that any thresholding maximizing the total backscatter rate is optimal for problem* (4.31)*.*

Remark 4.7. *In terms of total backscatter rate, the nodes can be viewed as an augmented source, and problem* (4.31) *becomes the rate-optimal quantizer design for DMTC.*

Thanks to Remark 4.6 and 4.7, problem (4.31) can be recast as

$$\max_{\mathbf{t} \in \mathcal{T}^{L+1}} \quad I_{\mathrm{B}}(x_{\mathcal{K}}; \hat{x}_{\mathcal{K}}) \tag{4.32a}$$

$$\text{s.t.} \quad (4.16e), \tag{4.32b}$$

whose global optimal solution has been obtained in recent works. [185] started from the quadrangle inequality and proposed a Dynamic Programming (DP) method accelerated by the Shor-Moran-Aggarwal-Wilber-Klawe (SMAWK) algorithm with computational complexity $\mathcal{O}\big(L^2(\mathrm{card}(\mathcal{T})-L)\big)$. On the other hand, [186] started from the optimality condition for three neighbor thresholds and presented a traverse-then-bisect algorithm with complexity $\mathcal{O}\big(\mathrm{card}(\mathcal{T})L\log(\mathrm{card}(\mathcal{T})L)\big)$. In Section 4.4, both schemes will be compared with the ML scheme [178]

$$t_l^{\mathrm{ML}} = N \frac{\sigma_{l-1}^2 \sigma_l^2}{\sigma_{l-1}^2 - \sigma_l^2} \log \frac{\sigma_{l-1}^2}{\sigma_l^2}, \quad l \in \mathcal{L} \setminus \{L\}, \tag{4.33}$$

which is suboptimal for problem (4.31) unless all nodes are with equiprobable inputs.

4.4   Simulation Results

In this section, we provide numerical results to evaluate the proposed algorithms. We assume the AP-user distance is $10\,\mathrm{m}$ and at least one RIScatter nodes are randomly dropped in a disk centered at the user with radius r. The AP is with maximum average transmit power $P = 36\,\mathrm{dBm}$ and all nodes employs M-QAM with $\alpha = 0.5$. For all channels involved, we consider a distance-dependent path loss model

$$L(d) = L_0 \left(\frac{d_0}{d} \right)^{\gamma}, \tag{4.34}$$

together with a Rician fading model

$$\mathbf{H} = \sqrt{\frac{\kappa}{1+\kappa}}\bar{\mathbf{H}} + \sqrt{\frac{1}{1+\kappa}}\tilde{\mathbf{H}}, \tag{4.35}$$

where d is the transmission distance, $L_0 = -30\,\mathrm{dB}$ is the reference path loss at $d_0 = 1\,\mathrm{m}$, κ is the Rician K-factor, $\bar{\mathbf{H}}$ is the deterministic line-of-sight component with unit-magnitude entries, and $\tilde{\mathbf{H}}$ is the Rayleigh fading component with standard independent and identically distributed (i.i.d.) CSCG entries. We choose $\gamma_{\mathrm{D}} = 2.6$, $\gamma_{\mathrm{F}} = 2.4$, $\gamma_{\mathrm{B}} = 2$, and $\kappa_{\mathrm{D}} = \kappa_{\mathrm{F}} = \kappa_{\mathrm{B}} = 5$ for direct, forward and backward links. The finite decision threshold domain $\mathcal{T}$ is obtained by b-bit uniform discretization over the critical interval defined by the $1 - \varepsilon$ confidence bounds of edge hypotheses (i.e., lower bound of x_1 and upper bound of x_L). We set $b = 9$ and $\varepsilon = 10^{-3}$. All achievable rate regions are averaged over 10^3 channel realizations.

4.4.1   Evaluation of Proposed Algorithms

4.4.1.1   Initialization

To characterize the achievable rate region, we progressively obtain all boundary points by successively increasing ρ and solving problem (4.16). For $\rho = 0$ where the backscatter link is prioritized, we initialize Algorithm 6 and 7 by uniform input distribution and MRT towards the sum cascaded channel $\sum_k \mathbf{h}_{\mathrm{C},k}^{\mathsf{H}}$, respectively. At the following points, both algorithms are initialized by the solutions at the previous point.

4.4.1.2   Convergence
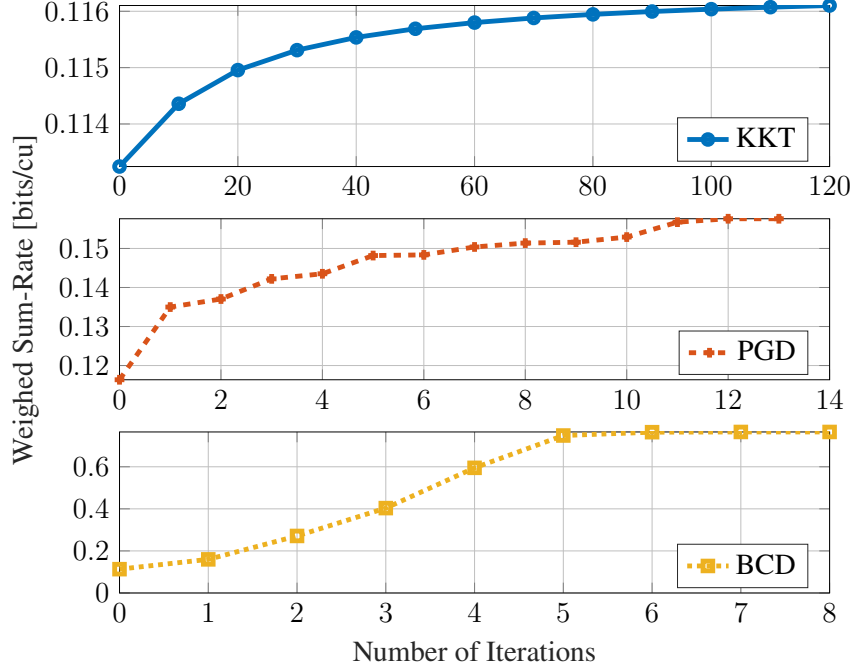
Fig. 4.7 Typical convergence curves at $\rho = 0$ for $Q = 4$, $K = 8$, $M = 2$, $N = 20$, $\sigma_v^2 = -40\,\mathrm{dBm}$ and $r = 2\,\mathrm{m}$.

The BCD algorithm is convergent for problem (4.16) since the input distribution and active beamforming subproblems converge and the thresholding subproblem attains global optimality. In company with BCD, we also plotted the convergence results of KKT and PGA algorithms in Fig. 4.7 to show how much performance is gained by solving each subproblem. It is observed that Algorithm 6 and 7 take around 100 and 10 iterations to converge, respectively. Overall, the BCD algorithm requires at most 5 iterations to converge. As ρ increases (not presented here), the convergence of all three algorithms are much faster thanks to the progressive initialization.

4.4.2   Comparison of Scattering Applications

On top of the setup in Fig. 4.4, we consider RIScatter and the following benchmark applications:

- *Legacy:* Legacy transmission without scatter nodes.

- *BBC:* The primary signal is CW and the receive signal is

$$y^{\text{BBC}}[n] = \Big(\mathbf{h}_{\text{D}}^{\mathsf{H}} + \sum_k \alpha_k \mathbf{h}_{\text{C},k}^{\mathsf{H}} x_k\Big)\mathbf{w} + v[n]. \tag{4.36}$$

The total backscatter rate approaches $K \log M$ when N is sufficiently large.

- *AmBC:* The user decodes each link independently and semi-coherently while treating the other as interference. The primary achievable rate is approximately[10]

$$I_{\text{P}}^{\text{AmBC}}(s;y) \approx \log\Big(1 + \frac{|\mathbf{h}_{\text{D}}^{\mathsf{H}}\mathbf{w}|^2}{\sum_k |\alpha_k \mathbf{h}_{\text{C},k}^{\mathsf{H}}\mathbf{w}|^2 + \sigma_v^2}\Big), \tag{4.37}$$

while the total backscatter rate follows (4.10) with uniform input distribution.

- *SR:* For a sufficiently large N, the average primary rate under semi-coherent detection asymptotically approaches (4.12) with uniform input distribution [144]. When $s[n]$ is successfully decoded and the direct interference $\mathbf{h}_{\text{D}}^{\mathsf{H}}\mathbf{w}s[n]$ is perfectly cancelled, the intermediate signal is

$$\hat{y}^{\text{SR}}[n] = \sum_k \alpha_k \mathbf{h}_{\text{C},k}^{\mathsf{H}} x_k \mathbf{w} s[n] + v[n]. \tag{4.38}$$

The total backscatter rate approaches $K \log M$.

- *RIS:* The reflection pattern is deterministic and the total backscatter rate is zero. The primary achievable rate is a special case of (4.12)

$$I_{\text{P}}^{\text{RIS}}(s;y|x_{\mathcal{K}}) = I_{\text{P}}(s;y|x_{m_{\mathcal{K}}^\star}) = \log\Big(1 + \frac{|\mathbf{h}^{\mathsf{H}}(x_{m_{\mathcal{K}}^\star})\mathbf{w}|^2}{\sigma_v^2}\Big), \tag{4.39}$$

where $m_{\mathcal{K}}^\star = \arg\max_{m_{\mathcal{K}}} I_{\text{P}}^{\text{RIS}}(s;y|x_{m_{\mathcal{K}}})$.

---

[10]The scattered component is treated as interference with average power $\mathbb{E}\{\sum_k \alpha_k \mathbf{h}_{\text{C},k}^{\mathsf{H}} x_k \mathbf{w} s[n]\} = \sum_k |\alpha_k \mathbf{h}_{\text{C},k}^{\mathsf{H}}\mathbf{w}|^2$ [144].
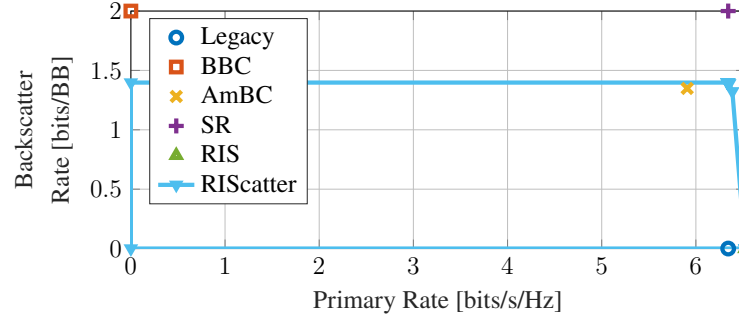
Fig. 4.8 Typical achievable rate region/points of scattering applications for $Q = 1$, $K = 1$, $M = 4$, $N = 10^3$, $\sigma_v^2 = -40\,\mathrm{dBm}$ and $r = 2\,\mathrm{m}$.

Fig. 4.8 compares the typical achievable rate region/points of RIScatter and those strategies. First, we observe BBC and SR achieve the best backscatter performance thanks to the coherent decoding. For SR, this comes with the cost of N re-encoding, precoding, subtraction together with a time-domain MRC per backscatter symbol. Since SR requires a very large N to guarantee the primary rate, the signal processing cost at the receiver can be prohibitive, and the backscatter *throughput* can be severely constrained. Second, the average primary rate slightly decreases/increases in the presence of a AmBC/RIS node, and the benefit of SR is not obvious. This is because the cascaded channel is around $25\,\mathrm{dB}$ weaker than the direct channel. Here, RIS ensures a constructive superposition of the direct and scattered components, while SR only creates a quasi-static rich-scattering environment that marginally enhances the average primary rate. When N is moderate, the randomly scattered signals should be modeled as interference rather than stable multipath, and the SR point should move vertically towards the AmBC point. Third, RIScatter enables a flexible primary-backscatter trade-off with adaptive input distribution design. In terms of maximum primary achievable rate, RIScatter coincides with RIS and outperforms the others by using the static reflection pattern that maximizes the primary SNR all the time. On the other hand, its maximum backscatter achievable rate is higher than that of AmBC. This is because the adaptive channel coding of RIScatter outperforms the equiprobable inputs of AmBC, especially at the low backscatter SNR caused by double fading. When multiple antenna is available at the AP, active beamforming can be optimized for RIScatter nodes and the advantage over AmBC should be more prominent.

4.4.3   Input Distribution under Different QoS
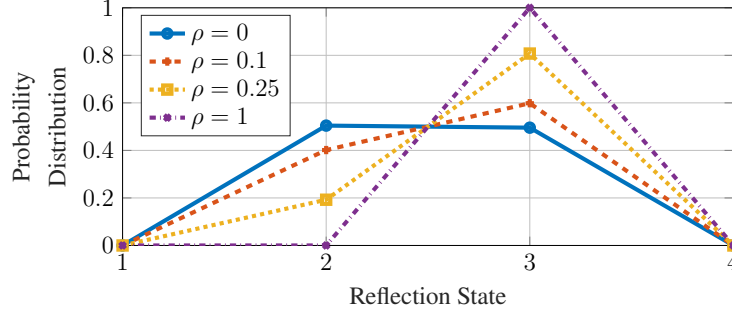
Fig. 4.9 Typical RIScatter reflection state distribution at different ρ for $Q = 1$, $K = 1$, $M = 4$, $N = 20$, $\sigma_v^2 = -40\,\mathrm{dBm}$ and $r = 2\,\mathrm{m}$.

The objective is to demonstrate that RIScatter nodes can leverage CSI- and QoS-adaptive input distribution design to balance backscatter modulation and passive beamforming. For one RIScatter node with $M = 4$, we evaluate the KKT input distribution at different QoS and present the result in Fig. 4.9. At $\rho = 0$ where the backscatter performance is prioritized, the optimal input distribution is 0 on two states and nearly uniform on the other two. This is inline with Shannon's observation that binary antipodal inputs is good enough for channel capacity at low SNR [5]. When the scattered signal is relatively weak, the conditional energy PDF under different hypotheses can be closely spaced as in Fig. 4.5. The extreme states producing the lowest/highest energy are always assigned with non-zero probability, while the middles cannot provide enough energy diversity and end up unused. At $\rho = 1$ where the primary link is prioritized, the optimal input distribution is $[0, 0, 1, 0]^\mathsf{T}$ since state 3 provides higher primary SNR than other states. That is, the reflection pattern becomes deterministic and the RIScatter node boils down to a static discrete RIS element. Increasing ρ from 0 to 1 creates a smooth transition from backscatter modulation to passive beamforming, suggesting RIScatter unifies BackCom and RIS from a probabilistic perspective.

4.4.4   Rate Region by Different Schemes
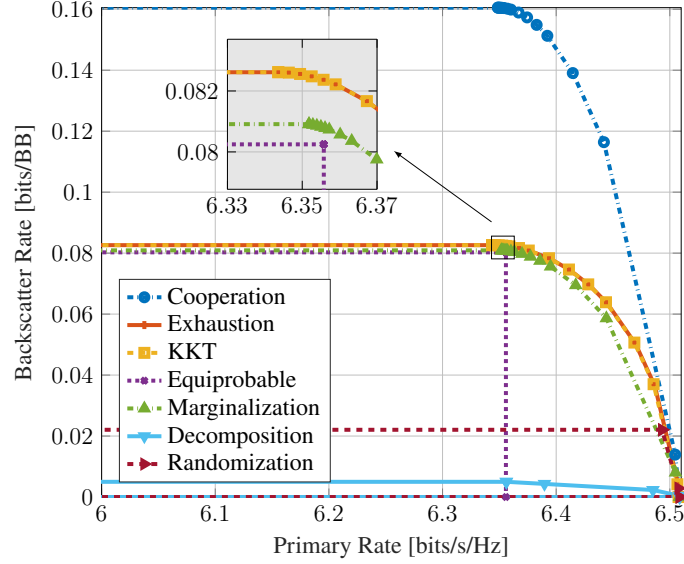
(a) Input Distribution, $Q = 1$
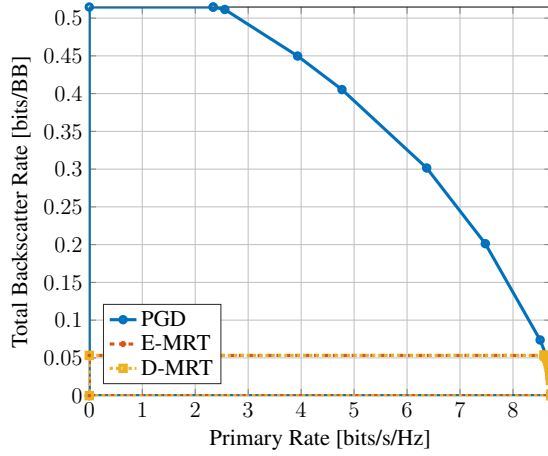
(b) Active Beamforming, $Q = 4$
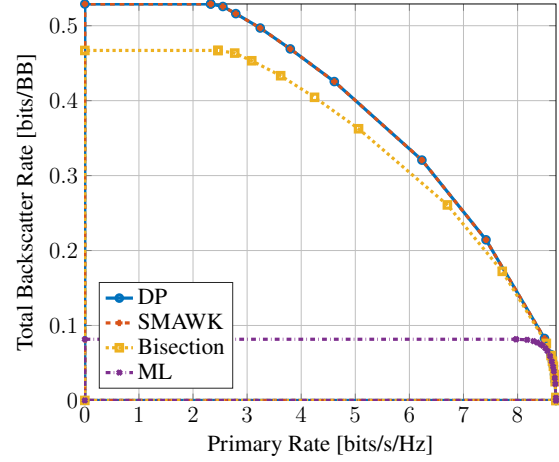
(c) Decision Threshold, $Q = 4$

Fig. 4.10 Average primary-total-backscatter rate regions by different input distribution, active beamforming, and decision threshold schemes for $K = 2$, $M = 4$, $N = 20$, $\sigma_v^2 = -40\,\mathrm{dBm}$ and $r = 2\,\mathrm{m}$.

4.4.4.1   Input Distribution

We compare these input distribution designs for problem (4.17):

- *Cooperation:* Joint encoding using a joint probability array $p(x_{m_\mathcal{K}})$ with M^K entries by Algorithm 6;

- *Exhaustion:* Exhaustive search over the M-dimensional probability simplex with resolution $\Delta p = 10^{-2}$;

- *KKT:* Solution by Algorithm 6;

- *Equiprobable:* Uniform input distribution.

We also consider these independent distribution recovery methods from the joint probability array:

- *Marginalization:* Marginal probability distributions;

- *Decomposition:* Normalized rank-1 Canonical Polyadic (CP) decomposed tensors by `Tensor Toolbox` [187];

- *Randomization:* Gaussian randomization with the guidance of correlation matrix [188].

Fig. 4.10(a) shows their average achievable rate regions. Cooperation achieves the outer bound of all schemes, but joint encoding over passive devices may incur additional hardware cost. Besides, the average rate performance of Exhaustion and KKT completely coincide with each other when $K = 2$. This confirms Remark 4.5 that the KKT input distribution can be good enough when K is moderate. Equiprobable experiences minor backscatter and major primary rate losses without exploiting CSI and QoS, and those gaps should be larger when M or K increases. Marginalization provides a close performance to KKT, but Randomization and Decomposition fail our expectations for most channel realizations. Those observations emphasize the importance of adaptive RIScatter encoding and demonstrate the advantage of the proposed KKT input distribution design.

4.4.4.2 Active Beamforming

We consider three typical active beamforming schemes for problem (4.21):

- *PGA:* Solution by Algorithm 7;

- *E-MRT:* MRT towards the ergodic composite channel $\sum_{m_{\mathcal{K}}} p(x_{m_{\mathcal{K}}}) \mathbf{h}^{\mathsf{H}}(x_{m_{\mathcal{K}}})$;

- *D-MRT:* MRT towards the direct channel $\mathbf{h}_{\mathrm{D}}^{\mathsf{H}}$.

Fig. 4.10(b) presents the average achievable rate regions for those schemes. In the low-ρ regime, the proposed PGA beamformer significantly outperforms both MRT schemes in terms of total backscatter rate. This is because the semi-coherent backscatter decoding relies on the relative energy difference under different backscatter symbol tuples. Such an energy diversity

is enhanced by PGA that effectively exploits backscatter constellation and input distribution knowledge rather than simply maximizes the channel strength. As ρ increases, the primary SNR outweighs the backscatter energy difference in (4.27), and PGA beamformer approaches E-MRT. At $\rho = 1$, both PGA and E-MRT boil down to MRT towards the strongest composite channel. The difference between E-MRT and D-MRT is insignificant when RIScatter nodes are dispersed. Those observations confirm that the proposed PGA active beamforming design can exploit the CSI, QoS, and backscatter constellation to enlarge the achievable rate region.

4.4.4.3   Decision Threshold

We evaluate the following decision threshold strategies for problem (4.32):

- *DP:* Benchmark DP method for sequential quantizer [185];

- *SMAWK: DP* accelerated by the SMAWK algorithm [185];

- *Bisection:* The traverse-then-bisect algorithm [186];

- *ML:* Maximum likelihood detector (4.33) [178].

Fig. 4.10(c) reveals the average achievable rate region for those strategies. The distribution-aware schemes DP, SMAWK and Bisection ensure higher total backscatter rate than ML. This is because the total backscatter rate (4.10) is a function of both input distribution and decision regions, and the rate-optimal thresholding depends heavily on the input distribution. For example, the backscatter symbol tuples with zero input probability should be assigned with empty decision regions, in order to increase the success detection rates of other hypotheses. It highlights the importance of joint input distribution and decision threshold design in rate maximization problems.

4.4.5   Rate Region under Different Configurations

(a) RIScatter Nodes

(b) Reflection States

(c) Transmit Antennas

(d) Spreading Factor
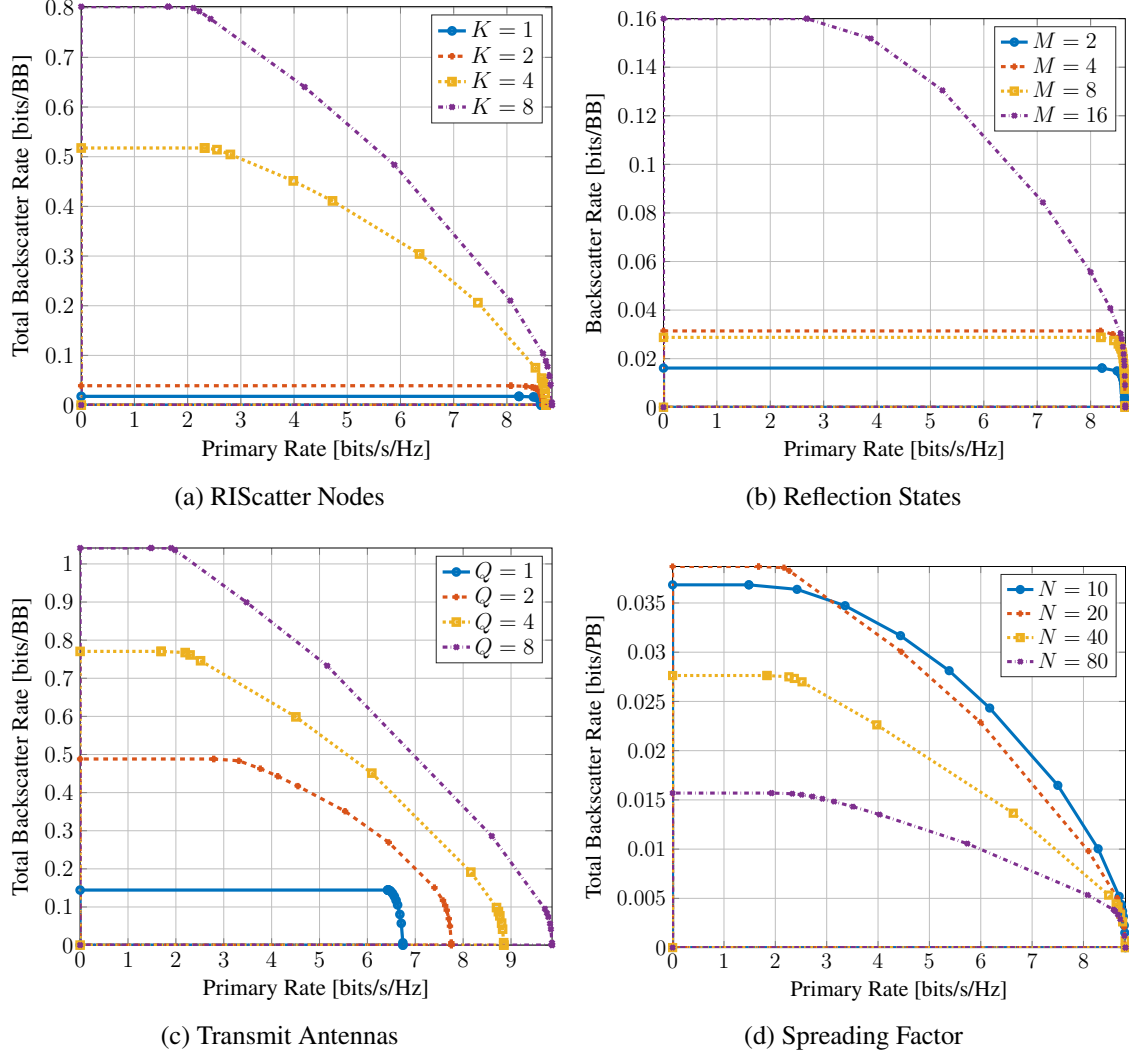
Fig. 4.11 Average primary-total-backscatter rate regions for different system configurations.

In this study, we choose $Q = 4$, $K = 8$, $M = 2$, $N = 20$, $\sigma_v^2 = -40\,\mathrm{dBm}$ and $r = 2\,\mathrm{m}$ as a reference, unless otherwise specified.

4.4.5.1   Number of Nodes

Fig. 4.11(a) reveals how the number RIScatter nodes K influences the primary-backscatter trade-off. Interestingly, we observe that increasing K has a larger benefit on the total backscatter rate than primary. This is because each RIScatter node not only affects the primary SNR but also influences the relative energy difference that other nodes can make. To

maximize the total backscatter rate, some nodes closer to the user may need to sacrifice their own rate and use the state that *minimizes* the composite channel strength, in order to increase the backscatter rate of other nodes. This accounts for the significant primary rate decrease in the low-ρ regime. On the other hand, when the primary link is prioritized, the RIScatter nodes boil down to RIS elements and enjoy a passive array gain of K^2.

4.4.5.2 Number of States

Fig. 4.11(b) shows the relationship between the available reflection states (i.e., QAM order) M and the achievable rate region when $K = 1$. We notice that increasing the reflection states has a marginal effect on the primary rate but significantly improves the backscatter rate. This is because the maximum amplitude normalized-QAM (4.1) involves more weak reflection points as M increases. It enhances the receive energy diversity but cannot provide enough phase shift resolution with maximum reflection.

4.4.5.3 Number of Transmit Antennas

Fig. 4.11(c) illustrates the impact of transmit antennas Q on the average performance. As Q increases, more scattered paths become available and the channel diversity can be better exploited to improve the primary-backscatter trade-off. It emphasizes the importance of multi-antenna RIScatter systems and demonstrate the effectiveness of the proposed PGA design.

4.4.5.4 Spreading factor

Fig. 4.11(d) shows how the spreading factor N affects the achievable rate region.[11] Using a very large N (as in the case of SR) can severely constrain the backscatter throughput, since the gain in energy certainty (by the law of large numbers) cannot withstand the loss in the gross rate. As $N \to \infty$, RIScatter nodes boil down to static RIS elements and the total backscatter rate approaches 0. On the other hand, when N is too small, the DMMAC (4.9) becomes unreliable and energy detection is error-prone. It explains the observation that $N = 10$ provides lower backscatter throughput than $N = 20$. Therefore, we conclude the spreading factor N should be carefully designed over multiple factors (e.g., primary and backscatter SNR, data rate requirements, load switching speed at the nodes, and signal processing capability at the user).

---

[11]Here, the unit of total backscatter rate is bits per primary block to show backscatter throughput.

(a) Average Noise Power

(b) Imperfect CSI

(c) Primary SNR
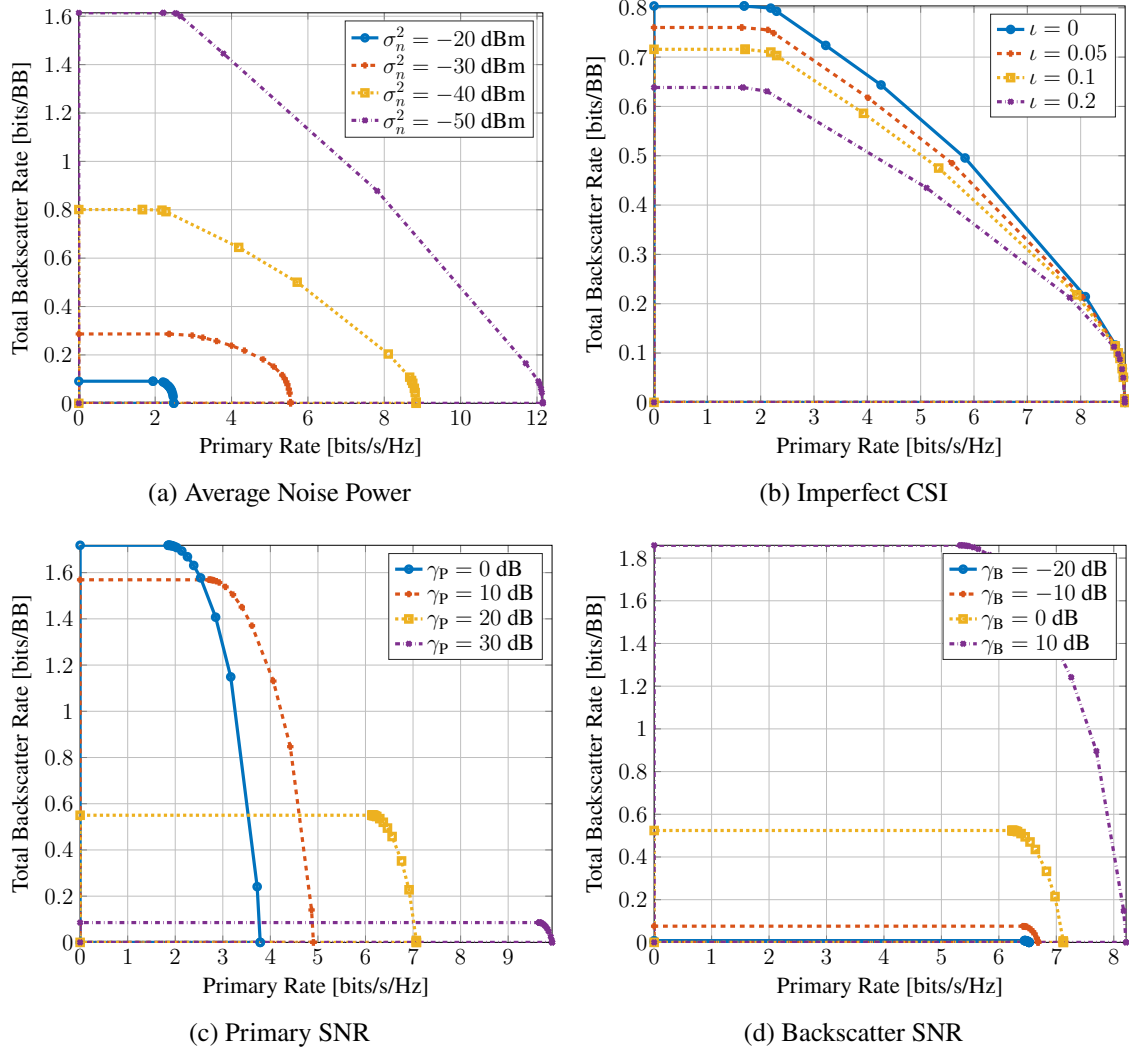
(d) Backscatter SNR

Fig. 4.12 Average primary-total-backscatter rate regions for different system configurations.

4.4.5.5 Average Noise Power

Fig. 4.12(a) depicts the impact of average noise power σ_v^2 on average rate regions. Note that the noise influences both primary and backscatter SNR. When σ_v^2 relatively high, one can choose a larger N to improve the SNR of energy detection.

4.4.5.6 Imperfect CSI

Due to the lack of RF chains at RIScatter nodes, fast and accurate acquisition of the cascaded CSI can be challenging, especially when the backscatter SNR is weak or the number of nodes is large. We consider an imperfect CSI model, where the cascaded channel of node k is

estimated as

$$\hat{\mathbf{h}}_{C,k} = \mathbf{h}_{C,k} + \tilde{\mathbf{h}}_{C,k}, \tag{4.40}$$

$\tilde{\mathbf{h}}_{C,k}$ is the estimation error with entries following i.i.d. CSCG distribution $\mathcal{CN}(0, \iota\Lambda_C)$, ι is the relative estimation error, and Λ_C is the cascaded path loss. In Fig. 4.12(b), it is observed that the channel estimation error mainly affects the backscatter rate. When ι increases from 0 to 0.2, the maximum total backscatter rate decreases by $20\,\%$. This is because the energy detector is sensitive to the DMMAC (4.9) and thus the estimation of the cascaded channel. On the other hand, a small estimation error may be insufficient to change the optimal passive beamforming state and the primary rate is almost unchanged.

4.4.5.7   Primary SNR

The backscatter SNR is fixed to $0\,\mathrm{dB}$ with $Q = 1$ in this study. Interestingly, Fig. 4.12(c) shows that increasing the primary SNR can improve the primary rate but degrade the backscatter rate. The reason is that the relative strength of the scattered signal compared to the direct signal is weakened, such that the nodes cannot make enough difference to the energy detector. It suggests that the nodes should be positioned in the proximity of the user to avoid SNR imbalance. This, together with Fig. 4.10(b) and 4.11(a), emphasizes the importance of balancing the primary and backscatter SNR in the design of active-passive coexisting networks.

4.4.5.8   Backscatter SNR

The primary SNR is fixed to $20\,\mathrm{dB}$ with $Q = 1$ in this study. Fig. 4.12(d) shows that the primary and backscatter rates are both improved when the backscatter SNR increases. This motivates one to use high-efficiency or semi-passive RIScatter nodes to improve the overall performance. In a multi-user RIScatter network, each node may be assigned to the nearest user to guarantee uniformly good performance for both links.

4.5   Conclusion

This chapter introduced RIScatter as a novel scatter protocol that bridges backscatter modulation and passive beamforming. Starting from scattering principles, we showed how RIScatter nodes generalize information nodes of BackCom and reflect elements of RIS, how they can be built over existing passive scatter devices, and how they simultaneously encode self information and assist legacy transmission. We also proposed a practical SIC-free receiver that exploits the properties of active-passive coexisting networks to benefit both

subsystems. The achievable primary-total-backscatter rate region was then studied for a single-user multi-node RIScatter network, where the input distribution, active beamforming, and decision thresholds are iteratively updated. Numerical results validated the proposed algorithms and emphasized the importance of adaptive input distribution and cooperative receiver design.

To support massive RIScatter networks with large number of nodes and states, one possible future direction is to consider backscatter detection over the received signal domain rather than energy domain, where multi-antenna [189] and learning-based approaches can be promising. Another interesting question is how to design RIScatter nodes and receivers in a multi-user system to fully exploit the dynamic passive beamforming that naturally origins from backscatter modulation.

Chapter 5

Channel Shaping using RIS: From Diagonal Model to Beyond

5.1   Introduction

Today we are witnessing a paradigm shift from connectivity to intelligence, where the wireless environment is no longer a chaotic medium but a conscious agent that can serve on demand. This is empowered by the recent advances in RIS, a programmable metasurface that recycles and redistributes ambient electromagnetic waves for improved wireless performance. A typical RIS consists of numerous low-power sub-wavelength non-resonant scattering elements, whose response can be engineered in real-time to manipulate the amplitude, phase, frequency, and polarization of the scattered waves [190]. It enables low-noise, full-duplex operation, and also features better flexibility than reflectarrays, lighter footprint than various relays, and greater scalability than conventional multi-antenna techniques. The most popular RIS research direction is *joint beamforming* design with transceivers for a specific performance measure, which has attracted significant attention in wireless communication [16, 191, 154], sensing [192–194], and power transfer literature [120, 155, 30]. While passive beamforming suffers severe attenuation from double fading, it usually offers a squared asymptotic behavior than active beamforming (e.g., second-order array gain and fourth-order harvested power [30]). On the other hand, RIS can also be used for *backscatter modulation* by periodically switching its reflection pattern within channel coherence time. This creates a free-ride message stream (similar to index modulation [195]) with dual benefits: integrating with the legacy transmitter for enhanced channel capacity [161, 168, 21] or serving as a dedicated source for low-power uplink communication [45, 32, 196]. Different from above directions, *channel shaping* exploits the RIS as a stand-alone device to modify the inherent properties

of the propagation environment. This provides a ubiquitous wave scattering benchmark for different wireless applications and helps to decouple the RIS-transceiver design. Relevant shaping metrics can be classified into two categories:

- *Singular value centric:* Closely related to the performance measures (e.g., achievable rate and harvested power [71]) but sensitive to numerical perturbations. The impact of RIS has been studied in terms of minimum singular value [197], effective rank [197, 198], condition number [199, 200], and degree of freedom [201–203].

- *Power centric:* The second-order statistics are less informative in MIMO but easier to analyze and optimize. The impact of RIS has been studied in terms of channel power gain [16, 2, 204, 52, 205] and leakage interference [206].

While those works offer initial glimpses into the channel shaping potential, one critical question remains unaddressed: *To what extent can a passive RIS reshape the MIMO channel in terms of singular values?* The answer depends heavily on the scattering model and hardware architecture. Most relevant works [197–203, 16, 206] assumed that each RIS element is tuned by a dedicated impedance and acts as an *individual* scatterer [1]. This ideally translates to a scattering matrix with unit-magnitude entries on the main diagonal and zeros elsewhere, applying merely a phase shift to the incoming signal. The concept was soon generalized to BD-RIS [2] that physically groups adjacent elements using passive reconfigurable components.[1] This allows *cooperative* scattering — wave impinging on one element can propagate within the circuit and depart partially from any element in the same group. It can thus redistribute both amplitude and phase of the scattered wave with zero power loss, generalizing the scattering matrix to block-diagonal with unitary blocks. Such a powerful model can be realized at reduced hardware cost using tree- and forest-connected architectures inspired by graph theory [52]. BD-RIS can also function in hybrid transmitting-and-reflecting mode [207] and multi-sector mode [55] to provide full-space coverage and multi-user support. Many practical design challenges have been addressed including channel estimation [208], mutual coupling [209], and wideband modelling [210]. Its beamforming superiority has been studied extensively in Single-Input Single-Output (SISO) and MISO systems, where the problems were cast as single-user SNR maximization [2, 204, 52, 205] and multi-user Weighted Sum-Rate (WSR) maximization [211, 212, 55, 213]. However, the interplay between BD-RIS and MIMO systems is still in the infancy stage. The authors of [214] investigated the rate-optimal joint beamforming design for a specific BD-RIS-aided MIMO system with blocked direct link and unitary (a.k.a. fully-connected) RIS. Similar constraints

---

[1]Those components can be either symmetric (e.g., capacitors and inductors) or asymmetric (e.g., ring hybrids and branch-line hybrids) [3], resulting in symmetric and asymmetric scattering matrices, respectively.

were also adopted in [215], which introduces a transmitter-side BD-RIS to massive MIMO that exploits statistical CSI for improved spectral efficiency. Received power maximization problem was studied over continuous-valued [204] and discrete-valued [216] BD-RIS, but the proposed single-stream transceiver is rate-suboptimal and the passive beamforming problem is equivalent to SISO. A practical frequency-dependent BD-RIS model has been recently proposed for multi-band multi-cell MIMO networks to facilitate practical deployments [217]. Although the results are promising, the channel shaping capability from off-diagonal entries deserves further investigation, and there lacks a universal yet efficient BD-RIS design framework. Furthermore, no previous work has attempted to characterize the singular value region of a MIMO channel manipulated by any type of RIS, and the BD-RIS-aided MIMO rate maximization problem remains unsolved. This paper aims for a comprehensive answer to the channel shaping question through theoretical analysis and numerical optimization. The contributions are summarized below.

First, we discuss the shaping potential from off-diagonal entries of BD-RIS in terms of subchannel rearrangement and subspace alignment. Subchannel rearrangement enables a flexible in-group permutation and combination of backward and forward channels by their strength. This unique feature of BD-RIS provides a higher shaping freedom and exploits spatial diversity more effectively than diagonal RIS. On the other hand, subspace alignment in MIMO generalizes phase matching in SISO and MISO to the high-dimensional singular vector space. The scattering matrix simultaneously affects the multiplicative intra-group alignment and additive inter-group alignment. However, both subspaces cannot be perfectly aligned at the same time and a balance needs to be struck in between. Increasing MIMO dimensions highlights the advantage of BD-RIS for subchannel rearrangement while exposing the limitation of diagonal RIS in subspace alignment. This is the first paper to study BD-RIS in general MIMO systems and discuss its shaping potential.

Second, we exploit the Riemannian geometry of the Stiefel manifold and propose an efficient BD-RIS design framework based on geodesic[2] Riemannian Conjugate Gradient (RCG). This method modified from [218, 219] not only provides better objective value and faster convergence than general non-geodesic approach [220, 221], but also works for arbitrary group size and any smooth optimization problem. Specifically, group-wise multiplicative rotational updates are performed along the geodesics of the Stiefel manifold and compactly evaluated as the exponential map [222]. By exploiting the inherent structure of unitary matrices, this method avoids retractions from the Euclidean space and facilitates the step size selection, which improves the computational efficiency and stability. This is the first work to tailor an efficient and universal optimization framework for BD-RIS.

---

[2]A geodesic refers to the shortest path between two points in a Riemannian manifold.

Third, we quantify the capability of a BD-RIS to redistribute the singular values of a MIMO Point-to-point Channel (PC) channel. The Pareto frontiers are characterized by optimizing the weighted sum of singular values, where the weights can be positive, zero, or negative. This problem is solved by the proposed geodesic RCG algorithm. The resulting singular value region generalizes most relevant metrics and provides an intuitive channel shaping benchmark. To explore the shaping limits of different RIS architectures, we also derive individual and collective singular value bounds for rank-deficient channels and unitary RIS via matrix analysis. Results validate those bounds and show that increasing BD-RIS group size significantly enlarges the singular value region, providing wider dynamic range and better trade-off. This is the first work to comprehensively answer the channel shaping capability question from both numerical and analytical perspectives in the most general BD-RIS setup.

Fourth, we tackle BD-RIS-aided MIMO achievable rate maximization problem with two beamforming solutions: a local-optimal approach via Alternating Optimization (AO) and a low-complexity approach over channel shaping. The former iteratively updates active beamforming by eigenmode transmission and passive beamforming by geodesic RCG until convergence. The latter suboptimally decouples the joint design into a channel power gain maximization subproblem and a conventional MIMO transmission subproblem, then propose a closed-form two-stage solution. We observe that BD-RIS yields higher channel power and achievable rate than diagonal RIS, while the relative gains scale with the group size and MIMO dimensions. Moreover, the rate difference between the optimal and shaping-inspired designs diminishes as the RIS evolves from diagonal to unitary. Those results emphasize the importance of using BD-RIS in large-scale MIMO systems and suggest channel shaping offers a promising path to decouple joint RIS-transceiver designs.

Fifth, we extend the aforementioned approaches to MIMO-Interference Channel (IC) where the BD-RIS is used for leakage interference minimization and WSR maximization. In the former case, we update the receive combiner, transmit precoder, and scattering matrix iteratively in closed forms with optimality proof. In the latter case, we alternatively updates the transmit precoder by bisection and the scattering matrix by RCG algorithm. We also compare the impact of RIS on PC and IC.

5.2 MIMO-PC

5.2.1 System Model

Consider a BD-RIS aided MIMO PC system with N_T, N_S, N_R transmit, scatter, and receive antennas, respectively. This configuration is denoted as $N_T \times N_S \times N_R$ in the following context. The BD-RIS can be modeled as an N_S-port network [51] that further divides into G individual groups, each containing $L \triangleq N_S/G$ elements interconnected by real-time reconfigurable components [2]. To simplify the analysis and explore the performance limits, we assume a lossless asymmetric network without mutual coupling between scattering elements, as previously considered in [207, 55, 214]. The overall scattering matrix of the BD-RIS is block-unitary

$$\boldsymbol{\Theta} = \mathrm{diag}(\boldsymbol{\Theta}_1, \dots, \boldsymbol{\Theta}_G), \tag{5.1}$$

where $\boldsymbol{\Theta}_g \in \mathbb{U}^{L \times L}$ is the g-th unitary block (i.e., $\boldsymbol{\Theta}_g^{\mathsf{H}} \boldsymbol{\Theta}_g = \mathbf{I}$) that describes the response of group $g \in \mathcal{G} \triangleq \{1, \dots, G\}$. Note that diagonal and unitary RIS can be regarded as its extreme cases with group size $L = 1$ and $L = N_S$, respectively. Some potential physical architectures of BD-RIS are illustrated in [2, Fig. 3], [55, Fig. 5], and [52, Fig. 2], where the radiation pattern and circuit topology need to be modeled in the scattering matrix.

Let $\mathbf{H}_D \in \mathbb{C}^{N_R \times N_T}$, $\mathbf{H}_B \in \mathbb{C}^{N_R \times N_S}$, $\mathbf{H}_F \in \mathbb{C}^{N_S \times N_T}$ denote the direct (transmitter-receiver), backward (RIS-receiver), and forward (transmitter-RIS) channels, respectively. The equivalent channel is a function of the scattering matrix

$$\mathbf{H} = \mathbf{H}_D + \mathbf{H}_B \boldsymbol{\Theta} \mathbf{H}_F = \mathbf{H}_D + \sum_g \underbrace{\mathbf{H}_{B,g} \boldsymbol{\Theta}_g \mathbf{H}_{F,g}}_{\triangleq \mathbf{H}_g}, \tag{5.2}$$

where $\mathbf{H}_{B,g} \in \mathbb{C}^{N_R \times L}$ and $\mathbf{H}_{F,g} \in \mathbb{C}^{L \times N_T}$ are the backward and forward subchannels for RIS group g, corresponding to the $(g-1)L$ to gL columns of $\mathbf{H}_B$ and rows of $\mathbf{H}_F$, respectively. Let $\mathbf{H}_g \triangleq \mathbf{H}_{B,g} \boldsymbol{\Theta}_g \mathbf{H}_{F,g}$ be the indirect channel via BD-RIS group g. Since unitary matrices constitute an algebraic group with respect to multiplication, the scattering matrix of group g can be decomposed as

$$\boldsymbol{\Theta}_g = \mathbf{L}_g \mathbf{R}_g^{\mathsf{H}}, \tag{5.3}$$

where $\mathbf{L}_g, \mathbf{R}_g \in \mathbb{U}^{L \times L}$ are two unitary factor matrices. Let $\mathbf{H}_{B,g} = \mathbf{U}_{B,g} \boldsymbol{\Sigma}_{B,g} \mathbf{V}_{B,g}^{\mathsf{H}}$ and $\mathbf{H}_{F,g} = \mathbf{U}_{F,g} \boldsymbol{\Sigma}_{F,g} \mathbf{V}_{F,g}^{\mathsf{H}}$ be the compact Singular Value Decomposition (SVD) of the backward

and forward channels, respectively. The equivalent channel can thus be rewritten as

$$
\mathbf{H} = \overbrace{\mathbf{H}_{\mathrm{D}} + \sum_g \mathbf{U}_{\mathrm{B},g}\boldsymbol{\Sigma}_{\mathrm{B},g}}^{\text{direct-indirect}} \underbrace{\mathbf{V}_{\mathrm{B},g}^{\mathsf{H}}\mathbf{L}_g\mathbf{R}_g^{\mathsf{H}}\mathbf{U}_{\mathrm{F},g}}_{\text{backward-forward}} \boldsymbol{\Sigma}_{\mathrm{F},g}\mathbf{V}_{\mathrm{F},g}^{\mathsf{H}}. \tag{5.4}
$$

By analyzing (5.4), we conclude that the off-diagonal entries of the BD-RIS scattering matrix provide two key potentials for MIMO channel shaping:

- *Subchannel rearrangement:* This unique feature of BD-RIS exploits the spatial diversity by rearranging and combining the backward and forward channel branches within each group. In SISO, diagonal RIS with perfect phase matching provides a maximum indirect channel amplitude of $\sum_{n=1}^{N_{\mathrm{S}}}|h_{\mathrm{B},n}||h_{\mathrm{F},n}|$ while BD-RIS can generalize it to $\sum_{g=1}^{G}\sum_{l=1}^{L}|h_{\mathrm{B},\pi_{\mathrm{B},g}(l)}||h_{\mathrm{F},\pi_{\mathrm{F},g}(l)}|$, where $\pi_{\mathrm{B},g}$ and $\pi_{\mathrm{F},g}$ are permutations of $\mathcal{L} \triangleq \{1,\ldots,L\}$. Note the first summation is over groups and the second summation is over permuted subchannels. By rearrangement inequality, the maximum channel gain is attained by pairing the l-th strongest backward and forward branches. Since the number of subchannels associated with each group is proportional to $N_{\mathrm{T}}N_{\mathrm{R}}$, we conclude the advantage of BD-RIS in subchannel rearrangement scales with MIMO dimensions,

- *Subspace alignment:* Each group can align the singular vectors of the associated backward-forward (intra-group, multiplicative) channels and direct-indirect (inter-group, additive) channels. In SISO, subspace alignment boils down to phase matching and the optimal scattering matrix of group g that maximizes the channel gain is

$$
\boldsymbol{\Theta}_g^{\star} = \exp\!\big(\jmath\arg(h_{\mathrm{D}})\big)\mathbf{V}_{\mathrm{B},g}\mathbf{U}_{\mathrm{F},g}^{\mathsf{H}}, \tag{5.5}
$$

where $\mathbf{V}_{\mathrm{B},g} = \big[\mathbf{h}_{\mathrm{B},g}/\|\mathbf{h}_{\mathrm{B},g}\|, \mathbf{N}_{\mathrm{B},g}\big] \in \mathbb{U}^{L\times L}$, $\mathbf{U}_{\mathrm{F},g} = \big[\mathbf{h}_{\mathrm{F},g}/\|\mathbf{h}_{\mathrm{F},g}\|, \mathbf{N}_{\mathrm{F},g}\big] \in \mathbb{U}^{L\times L}$, and $\mathbf{N}_{\mathrm{B},g}, \mathbf{N}_{\mathrm{F},g} \in \mathbb{C}^{L\times(L-1)}$ are the orthonormal bases of the null spaces of $\mathbf{h}_{\mathrm{B},g}$ and $\mathbf{h}_{\mathrm{F},g}$, respectively. Diagonal RIS ($L = 1$, empty null spaces) thus suffices for perfect phase matching in SISO. When it comes to MIMO, each individual scattering element can only apply a common phase shift to the "pinhole" indirect channel $\mathbf{H}_g \in \mathbb{C}^{N_{\mathrm{R}}\times N_{\mathrm{T}}}$ passing through itself. That is, the disadvantage of diagonal RIS in subspace alignment scales with MIMO dimensions. As will be shown later, even if the BD-RIS is unitary, there still exists a tradeoff between the alignment of direct-indirect and backward-forward subspaces.

5.2.2 Group-Wise Geodesic RCG

In this section, we first provide an overview on signal processing techniques for general BD-RIS design problems, then propose a novel group-wise geodesic RCG method that exploits the properties of unitary group to operate directly on the Stiefel manifold. We will later show that the proposed method not only provides better objective value and faster convergence than other approaches, but also works for arbitrary group size and any smooth optimization problem.

5.2.2.1 Conventional Techniques

General BD-RIS design techniques can be classified into two categories based on the optimization variable and hardware architecture:

- *Scattering matrix* $\boldsymbol{\Theta}$: This approach is often exploited for asymmetric architectures where the feasible domain of each group is a L-dimensional Stiefel manifold $\boldsymbol{\Theta}_g \in \mathbb{U}^{L \times L}$. Due to its non-convexity, relevant problems are usually solved by general non-geodesic manifold optimization [207, 55, 214] or relax-then-project methods [211]. The former will be discussed in the next subsection.

- *Reactance matrix* $\mathbf{X}$: This approach is often exploited for symmetric architectures where every pair of elements in the same group are connected by capacitors and inductors. According to network theory [223], it maps to the scattering matrix by $\boldsymbol{\Theta}_g = (\jmath \mathbf{X}_g + Z_0 \mathbf{I})^{-1} (\jmath \mathbf{X}_g - Z_0 \mathbf{I})$, which formulates an unconstrained optimization problem on the upper triangular entries of $\{\mathbf{X}_g\}_{g \in \mathcal{G}}$ that is solvable by quasi-Newton methods [2].

5.2.2.2 Geodesic vs Non-Geodesic RCG

We first revisit the general non-geodesic RCG method that is applicable to optimization problems over arbitrary manifolds [220, 221]. The main idea is to perform additive updates along the conjugate direction guided by the Riemannian gradient, then project the solution back onto the manifold. For maximization problem with smooth objective f and block-unitary constraint (5.1), the steps for BD-RIS group g at iteration r are summarized below:

1. *Compute the Euclidean gradient [224]:* The gradient of f with respect to $\boldsymbol{\Theta}_g^*$ in the Euclidean space is

$$\nabla_{\mathrm{E},g}^{(r)} = \frac{\partial f(\boldsymbol{\Theta}_g^{(r)})}{\partial \boldsymbol{\Theta}_g^*};\tag{5.6}$$

2. *Translate to the Riemannian gradient [220]:* At point $\mathbf{\Theta}^{(r)}$, the Riemannian gradient lies in the tangent space of the Stiefel manifold $\mathcal{T}_{\mathbf{\Theta}_g^{(r)}}\mathbb{U}^{L \times L} \triangleq \{\mathbf{M} \in \mathbb{C}^{L \times L} \mid \mathbf{M}^{\mathsf{H}}\mathbf{\Theta}_g^{(r)} + \mathbf{\Theta}_g^{(r)\mathsf{H}}\mathbf{M} = \mathbf{0}\}$. It gives the steepest ascent direction of the objective on the manifold can be obtained by projecting the Euclidean gradient onto the tangent space:

$$\nabla_{\mathrm{R},g}^{(r)} = \nabla_{\mathrm{E},g}^{(r)} - \mathbf{\Theta}_g^{(r)}\nabla_{\mathrm{E},g}^{(r)\mathsf{H}}\mathbf{\Theta}_g^{(r)}; \tag{5.7}$$

3. *Determine the conjugate direction [225]:* The conjugate direction is obtained over the Riemannian gradient and previous direction as

$$\mathbf{D}_g^{(r)} = \nabla_{\mathrm{R},g}^{(r)} + \gamma_g^{(r)}\mathbf{D}_g^{(r-1)}, \tag{5.8}$$

where $\gamma_g^{(r)}$ is the parameter that deviates the conjugate direction from the tangent space for accelerated convergence. A popular choice is the Polak-Ribière formula

$$\gamma_g^{(r)} = \frac{\mathrm{tr}\big((\nabla_{\mathrm{R},g}^{(r)} - \nabla_{\mathrm{R},g}^{(r-1)})\nabla_{\mathrm{R},g}^{(r)\mathsf{H}}\big)}{\mathrm{tr}\big(\nabla_{\mathrm{R},g}^{(r-1)}\nabla_{\mathrm{R},g}^{(r-1)\mathsf{H}}\big)}; \tag{5.9}$$

4. *Perform additive update [221]:* The point is updated by moving along a straight path in the conjugate direction

$$\bar{\mathbf{\Theta}}_g^{(r+1)} = \mathbf{\Theta}_g^{(r)} + \mu\mathbf{D}_g^{(r)}, \tag{5.10}$$

where μ is the step size refinable by the Armijo rule [226];

5. *Retract for feasibility [220, 207]:* The resulting point needs to be projected back onto the Stiefel manifold by

$$\mathbf{\Theta}_g^{(r+1)} = \bar{\mathbf{\Theta}}_g^{(r+1)}\big(\bar{\mathbf{\Theta}}_g^{(r+1)\mathsf{H}}\bar{\mathbf{\Theta}}_g^{(r+1)}\big)^{-1/2}. \tag{5.11}$$

One can also combine the addition (5.10) and retraction (5.11) in one step

$$\mathbf{\Theta}_g^{(r+1)} = \big(\mathbf{\Theta}_g^{(r)} + \mu\mathbf{D}_g^{(r)}\big)\big(\mathbf{I} + \mu^2\mathbf{D}_g^{(r)\mathsf{H}}\mathbf{D}_g^{(r)}\big)^{-1/2}, \tag{5.12}$$

and determine the step size therein.

A geodesic is a curve representing the shortest path between two points in a Riemannian manifold, whose tangent vectors remain parallel when transported along the curve. The above method is called non-geodesic since the points are updated in the linear embedding spaces of

the manifold by addition and retraction, instead of on the Stiefel manifold itself. Next, we revisit some concepts in differential geometry and introduce a group-wise geodesic RCG method on top of [218, 219].

A Lie group is simultaneously a continuous group and a differentiable manifold. Lie algebra refers to the tangent space of the Lie group at the identity element. The exponential map acts as a bridge between the Lie algebra and Lie group, which allows one to recapture the local group structure using linear algebra techniques. The set of unitary matrices $\mathbb{U}^{L \times L}$ forms a Lie group $U(L)$ under multiplication, and the corresponding Lie algebra $\mathfrak{u}(L) \triangleq \mathcal{T}_{\mathbf{I}} \mathbb{U}^{L \times L} = \{\mathbf{M} \in \mathbb{C}^{L \times L} \mid \mathbf{M}^{\mathsf{H}} + \mathbf{M} = \mathbf{0}\}$ consists of skew-Hermitian matrices. A geodesic emanating from the identity with velocity $\mathbf{D} \in \mathfrak{u}(L)$ can be described by [222]

$$\mathbf{G_I}(\mu) = \exp(\mu \mathbf{D}), \tag{5.13}$$

where $\exp(\mathbf{A}) = \sum_{k=0}^{\infty} (\mathbf{A}^k / k!)$ is the matrix exponential and μ is the step size (i.e., magnitude of the tangent vector). Note that the right translation is an isometry in $U(L)$. During the optimization of group g, the geodesic evaluated at the identity (5.13) should be translated to $\mathbf{\Theta}_g^{(r)}$ for successive updates [218]

$$\mathbf{G}_g^{(r)}(\mu) = \mathbf{G_I}(\mu)\mathbf{\Theta}_g^{(r)} = \exp(\mu \mathbf{D}_g^{(r)})\mathbf{\Theta}_g^{(r)}, \tag{5.14}$$

while the Riemannian gradient evaluated at $\mathbf{\Theta}_g^{(r)}$ (5.7) should be translated back to the identity for exploiting the Lie algebra [218]

$$\tilde{\nabla}_{\mathrm{R},g}^{(r)} = \nabla_{\mathrm{R},g}^{(r)} \mathbf{\Theta}_g^{(r)\mathsf{H}} = \nabla_{\mathrm{E},g}^{(r)} \mathbf{\Theta}_g^{(r)\mathsf{H}} - \mathbf{\Theta}_g^{(r)} \nabla_{\mathrm{E},g}^{(r)\mathsf{H}}. \tag{5.15}$$

After gradient translation, the deviation parameter and conjugate direction can be determined similarly to (5.9) and (5.8)

$$\tilde{\gamma}_g^{(r)} = \frac{\mathrm{tr}\big((\tilde{\nabla}_{\mathrm{R},g}^{(r)} - \tilde{\nabla}_{\mathrm{R},g}^{(r-1)})\tilde{\nabla}_{\mathrm{R},g}^{(r)\mathsf{H}}\big)}{\mathrm{tr}\big(\tilde{\nabla}_{\mathrm{R},g}^{(r-1)}\tilde{\nabla}_{\mathrm{R},g}^{(r-1)\mathsf{H}}\big)}. \tag{5.16}$$

$$\mathbf{D}_g^{(r)} = \tilde{\nabla}_{\mathrm{R},g}^{(r)} + \tilde{\gamma}_g^{(r)}\mathbf{D}_g^{(r-1)}, \tag{5.17}$$

The solution can thus be updated along the geodesic in a multiplicative rotational manner

$$\mathbf{\Theta}_g^{(r+1)} = \mathbf{G}_g^{(r)}(\mu) = \exp(\mu \mathbf{D}_g^{(r)})\mathbf{\Theta}_g^{(r)}, \tag{5.18}$$

Algorithm 8 Group-wise geodesic RCG for BD-RIS design

Input: $f(\boldsymbol{\Theta}), G$
Output: $\boldsymbol{\Theta}^\star$
1: **Initialize** $r \leftarrow 0, \boldsymbol{\Theta}^{(0)}$
2: **Repeat**
3:       **For** $g \leftarrow 1$ to G
4:             $\nabla_{\mathrm{E},g}^{(r)} \leftarrow (5.6)$
5:             $\tilde{\nabla}_{\mathrm{R},g}^{(r)} \leftarrow (5.15)$
6:             $\tilde{\gamma}_g^{(r)} \leftarrow (5.16)$
7:             $\mathbf{D}_g^{(r)} \leftarrow (5.17)$
8:             **If** $\Re\{\mathrm{tr}(\mathbf{D}_g^{(r)\mathsf{H}}\tilde{\nabla}_{\mathrm{R},g}^{(r)})\} < 0$ ▷ not an ascent direction
9:                   $\mathbf{D}_g^{(r)} \leftarrow \tilde{\nabla}_{\mathrm{R},g}^{(r)}$
10:             **End If**
11:             $\mu \leftarrow 1$
12:             $\mathbf{G}_g^{(r)}(\mu) \leftarrow (5.14)$
13:             **While** $f\big(\mathbf{G}_g^{(r)}(2\mu)\big) - f(\boldsymbol{\Theta}_g^{(r)}) \geq \mu \cdot \mathrm{tr}(\mathbf{D}_g^{(r)}\mathbf{D}_g^{(r)\mathsf{H}})/2$
14:                   $\mu \leftarrow 2\mu$
15:             **End While**
16:             **While** $f\big(\mathbf{G}_g^{(r)}(\mu)\big) - f(\boldsymbol{\Theta}_g^{(r)}) < \mu/2 \cdot \mathrm{tr}(\mathbf{D}_g^{(r)}\mathbf{D}_g^{(r)\mathsf{H}})/2$
17:                   $\mu \leftarrow \mu/2$
18:             **End While**
19:             $\boldsymbol{\Theta}_g^{(r+1)} \leftarrow (5.18)$
20:       **End For**
21:       $r \leftarrow r + 1$
22: **Until** $|f(\boldsymbol{\Theta}^{(r)}) - f(\boldsymbol{\Theta}^{(r-1)})|/f(\boldsymbol{\Theta}^{(r-1)}) \leq \epsilon$

---

where an appropriate μ may be obtained by the Armijo rule. To double the step size, one can simply square the rotation matrix instead of recomputing the matrix exponential, since $\exp^2(\mu\mathbf{D}_g^{(r)}) = \exp(2\mu\mathbf{D}_g^{(r)})$.

Algorithm 8 summarizes the proposed BD-RIS design framework based on group-wise geodesic RCG. Compared to the non-geodesic approach, it leverages the Lie group properties to replace the add-then-retract update (5.12) with a multiplicative rotational update (5.18) along the geodesic. This leads to faster convergence and simplifies the step size tuning thanks to appropriate parameter space. Convergence to a local optimum is still guaranteed if not initialized at a stationary point. Note that the group-wise updates can be performed in parallel to facilitate large-scale BD-RIS optimization problems. Since block-unitary matrices are also closed under multiplication, one can avoid group-wise updates by directly operating on $\boldsymbol{\Theta}$ and pinching (i.e., keeping the block diagonal and nulling the other entries) the Euclidean gradient (5.6), with potentially higher computational complexity and slower convergence.
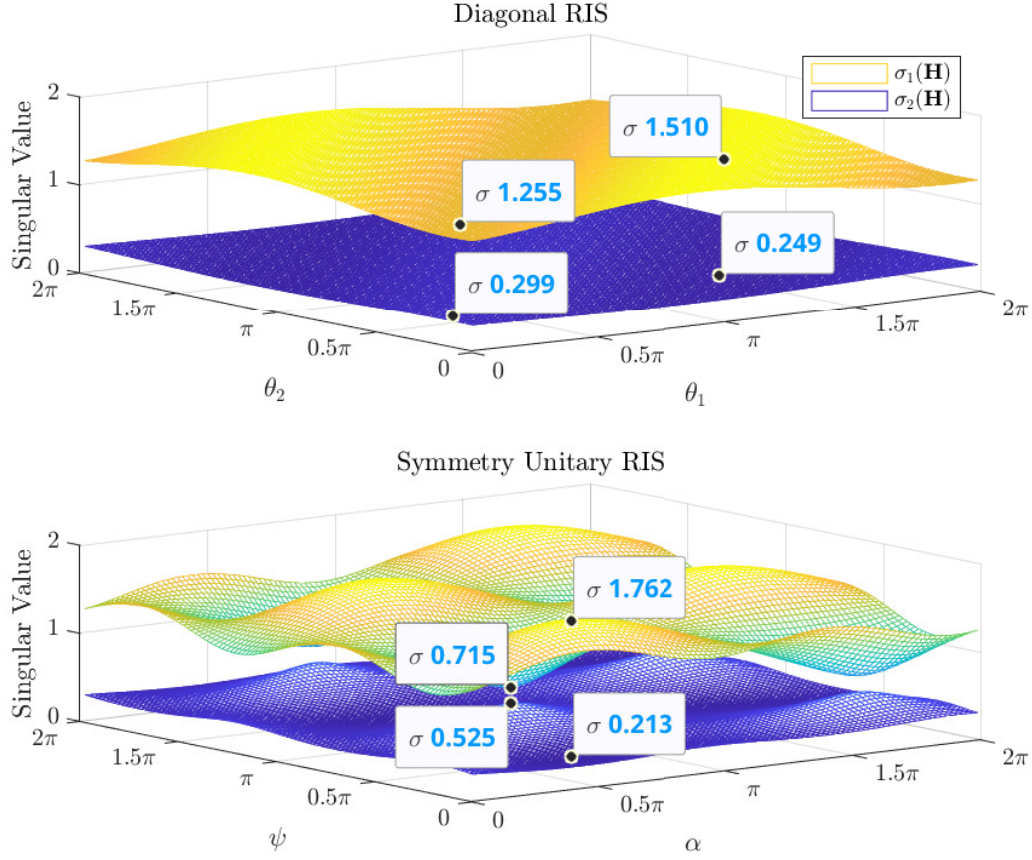
Fig. 5.1 $2 \times 2 \times 2$ (no direct) channel singular value shaping by diagonal and symmetry unitary RIS.

5.2.3 Channel Singular Values Redistribution

5.2.3.1 Toy Example

We first illustrate the channel shaping capabilities of different RIS models by a toy example. Consider a $2 \times 2 \times 2$ setup where the direct link is blocked. The diagonal RIS is modeled by $\boldsymbol{\Theta}_{\mathrm{D}} = \mathrm{diag}(e^{\jmath\theta_1}, e^{\jmath\theta_2})$ while the unitary BD-RIS has 4 independent angular parameters

$$\boldsymbol{\Theta}_{\mathrm{U}} = e^{\jmath\phi} \begin{bmatrix} e^{\jmath\alpha}\cos\psi & e^{\jmath\beta}\sin\psi \\ -e^{-\jmath\beta}\sin\psi & e^{-\jmath\alpha}\cos\psi \end{bmatrix}. \tag{5.19}$$

It is worth noting that ϕ has no impact on the singular value because $\mathrm{sv}(e^{\jmath\phi}\mathbf{A}) = \mathrm{sv}(\mathbf{A})$. For a fair comparison, we also enforce symmetry $\boldsymbol{\Theta}_{\mathrm{U}} = \boldsymbol{\Theta}_{\mathrm{U}}^{\mathsf{T}}$ by $\beta = \pi/2$ such that both architectures have the same number of angular parameters. Fig. 5.1 shows the channel singular values achieved by an exhaustive grid search over (θ_1, θ_2) for diagonal RIS and

(α, ψ) for symmetric unitary RIS. It is observed that both singular values can be manipulated up to 9% using diagonal RIS and 42% using symmetric BD-RIS, despite both architectures have the same number of scattering elements. A larger performance gap is expected when the symmetric constraint on (5.19) can be relaxed. This example shows BD-RIS can provide a wider dynamic range of channel singular values and motivates further studies on channel shaping.

5.2.3.2 Pareto Frontier Characterization

We then characterize the Pareto frontier of singular values of a general $N_{\mathrm{T}} \times N_{\mathrm{S}} \times N_{\mathrm{R}}$ channel (5.2) by maximizing their weighted sum

$$\max_{\boldsymbol{\Theta}} \quad \sum_n \rho_n \sigma_n(\mathbf{H}) \tag{5.20a}$$

$$\text{s.t.} \quad \boldsymbol{\Theta}_g^{\mathsf{H}} \boldsymbol{\Theta}_g = \mathbf{I}, \quad \forall g, \tag{5.20b}$$

where $n \in \mathcal{N} \triangleq \{1, \ldots, N\}$, $N \triangleq \min(N_{\mathrm{T}}, N_{\mathrm{R}})$ is the maximum channel rank, and ρ_n is the weight of the n-th singular value that can be positive, zero, or negative. Varying $\{\rho_n\}_{n \in \mathcal{N}}$ characterizes the Pareto frontier that encloses the entire singular value region. Thus, we claim problem (5.20) generalizes most singular value shaping problems. It can be solved optimally by Algorithm 8 with the Euclidean gradient given by Lemma 5.1.

Lemma 5.1. *The Euclidean gradient of* (5.20a) *with respect to BD-RIS group g is*

$$\frac{\partial \sum_n \rho_n \sigma_n(\mathbf{H})}{\partial \boldsymbol{\Theta}_g^*} = \mathbf{H}_{\mathrm{B},g}^{\mathsf{H}} \mathbf{U} \mathrm{diag}(\rho_1, \ldots, \rho_N) \mathbf{V}^{\mathsf{H}} \mathbf{H}_{\mathrm{F},g}^{\mathsf{H}}, \tag{5.21}$$

where $\mathbf{U}$ and $\mathbf{V}$ are the left and right compact singular matrices of $\mathbf{H}$, respectively.

Proof. Please refer to Appendix 7.3.1. $\qquad\square$

We then analyze the computational complexity of solving Pareto singular value problem (5.20) by Algorithm 8. To update each BD-RIS group, compact SVD of $\mathbf{H}$ requires $\mathcal{O}(N N_{\mathrm{T}} N_{\mathrm{R}})$, Euclidean gradient (5.21) requires $\mathcal{O}\big(LN(N_{\mathrm{T}} + N_{\mathrm{R}} + L + 1)\big)$, Riemannian gradient translation (5.15) requires $\mathcal{O}(L^3)$, deviation parameter (5.16) and conjugate direction (5.17) together require $\mathcal{O}(L^2)$, and matrix exponential (5.18) requires $\mathcal{O}(L^3)$ operations [227]. The overall complexity is thus $\mathcal{O}\big(I_{\mathrm{RCG}} G\big(N N_{\mathrm{T}} N_{\mathrm{R}} + LN(N_{\mathrm{T}} + N_{\mathrm{R}} + L + 1) + I_{\mathrm{BLS}} L^3\big)\big)$, where I_{RCG} and I_{BLS} are the number of iterations for geodesic RCG and backtracking line search (line 13–18 of Algorithm 8), respectively.

5.2.3.3 Some Analytical Bounds

We then discuss some analytical bounds related to channel singular values.

Proposition 5.1 (Degree of freedom). *In point-to-point MIMO, BD-RIS cannot achieve a higher Degree of Freedom (DoF) than diagonal RIS.*

Proof. Please refer to Appendix 7.3.2. □

Proposition 5.2 (Rank-deficient channel). *If the forward or backward channel is rank-k ($k \leq N$), then regardless of the passive RIS size and architecture, the n-th singular value of the equivalent channel is bounded by*

$$\sigma_n(\mathbf{H}) \leq \sigma_{n-k}(\mathbf{T}), \qquad\qquad if\, n > k, \qquad\qquad (5.22a)$$

$$\sigma_n(\mathbf{H}) \geq \sigma_n(\mathbf{T}), \qquad\qquad if\, n < N - k + 1, \qquad (5.22b)$$

where

$$\mathbf{T}\mathbf{T}^{\mathsf{H}} = \begin{cases} \mathbf{H}_{\mathrm{D}}(\mathbf{I} - \mathbf{V}_{\mathrm{F}}\mathbf{V}_{\mathrm{F}}^{\mathsf{H}})\mathbf{H}_{\mathrm{D}}^{\mathsf{H}}, & if\, \mathrm{rank}(\mathbf{H}_{\mathrm{F}}) = k, \\ \mathbf{H}_{\mathrm{D}}^{\mathsf{H}}(\mathbf{I} - \mathbf{U}_{\mathrm{B}}\mathbf{U}_{\mathrm{B}}^{\mathsf{H}})\mathbf{H}_{\mathrm{D}}, & if\, \mathrm{rank}(\mathbf{H}_{\mathrm{B}}) = k, \end{cases} \qquad (5.23)$$

and $\mathbf{V}_{\mathrm{F}}$ and $\mathbf{U}_{\mathrm{B}}$ are the right and left compact singular matrices of $\mathbf{H}_{\mathrm{F}}$ and $\mathbf{H}_{\mathrm{B}}$, respectively.

Proof. Please refer to Appendix 7.3.3. □

Corollary 5.2.1 (Extreme singular values). *With a sufficiently large passive RIS of arbitrary architecture, the first k channel singular values are unbounded above[3] while the last k channel singular values can be suppressed to zero.*

Proof. This is a direct result of (5.22). □

Corollary 5.2.2 (LoS channel[4]). *If the forward or backward channel is LoS, then a passive RIS of arbitrary architecture can at most enlarge the n-th ($n \geq 2$) channel singular value to the $(n-1)$-th singular value of $\mathbf{T}$, or suppress the n-th channel singular value to the n-th singular value of $\mathbf{T}$. That is,*

$$\sigma_1(\mathbf{H}) \geq \sigma_1(\mathbf{T}) \geq \sigma_2(\mathbf{H}) \geq \ldots \geq \sigma_{N-1}(\mathbf{T}) \geq \sigma_N(\mathbf{H}) \geq \sigma_N(\mathbf{T}). \qquad (5.24)$$

Proof. This is a direct result of (5.22) with $k = 1$. □

---

[3]The energy conservation law $\sum_n \sigma_n^2(\mathbf{H}) \leq 1$ still has to be respected. This constraint is omitted in the following context for brevity.

[4]A similar result has been derived for diagonal RIS [228].

In Section 5.4, we will show by simulation that a finite-size BD-RIS can better approach those bounds than diagonal RIS.

Proposition 5.3 (Unitary RIS without direct link). *If the BD-RIS is unitary and the direct link is absent, then the channel singular values can be manipulated up to*

$$\mathrm{sv}(\mathbf{H}) = \mathrm{sv}(\mathbf{BF}), \tag{5.25}$$

where $\mathbf{B}$ and $\mathbf{F}$ are arbitrary matrices with the same singular values as $\mathbf{H}_\mathrm{B}$ and $\mathbf{H}_\mathrm{F}$, respectively,

Proof. Please refer to Appendix 7.3.4. □

The problem now becomes, how the singular values of matrix product are bounded by the singular values of its individual factors. Let $\bar{N} = \max(N_\mathrm{T}, N_\mathrm{S}, N_\mathrm{R})$ and $\sigma_n(\mathbf{H}) = \sigma_n(\mathbf{H}_\mathrm{F}) = \sigma_n(\mathbf{H}_\mathrm{B}) = 0$ for $N < n \leq \bar{N}$. We have the following corollaries.

Corollary 5.3.1 (Generic singular value bounds).

$$\prod_{k \in K} \sigma_k(\mathbf{H}) \leq \prod_{i \in I} \sigma_i(\mathbf{H}_\mathrm{B}) \prod_{j \in J} \sigma_j(\mathbf{H}_\mathrm{F}), \tag{5.26}$$

for all admissible triples $(I, J, K) \in T_r^{\bar{N}}$ with $r < \bar{N}$, where

$$T_r^{\bar{N}} \triangleq \Big\{ (I, J, K) \in U_r^{\bar{N}} \mid \forall p < r, (F, G, H) \in T_p^r,$$
$$\sum_{f \in F} i_f + \sum_{g \in G} j_g \leq \sum_{h \in H} k_h + p(p+1)/2 \Big\},$$

$$U_r^{\bar{N}} \triangleq \Big\{ (I, J, K) \mid \sum_{i \in I} i + \sum_{j \in J} j = \sum_{k \in K} k + r(r+1)/2 \Big\}.$$

Proof. Please refer to [229, Theorem 8]. □

Corollary (5.3.1) is by far the most comprehensive singular value bound over Proposition 5.3, which is also recognized as a variation of Horn's inequality [230]. It is worth mentioning that the number of admissible triples (and bounds) grows exponentially with $\bar{N}$. For example, the number of inequalities described by (5.26) grows from 12 to 2062 when $\bar{N}$ increases from 3 to 7. This renders it computationally expensive for applications in large-scale MIMO systems. Next, we showcase some useful inequalities enclosed by (5.26). Readers are referred to [231, Chapter 16, 24] for more examples.

Corollary 5.3.2 (Upper bound on the largest singular value)**.**

$$\sigma_1(\mathbf{H}) \leq \sigma_1(\mathbf{H}_B)\sigma_1(\mathbf{H}_F). \tag{5.27}$$

Proof. This is a direct result of (5.26) with $r = 1$. $\qquad\square$

Corollary 5.3.3 (Lower bound on the smallest singular value)**.**

$$\sigma_{\bar{N}}(\mathbf{H}) \geq \sigma_{\bar{N}}(\mathbf{H}_B)\sigma_{\bar{N}}(\mathbf{H}_F). \tag{5.28}$$

Proof. This can be deducted from (5.26) with $r_1 = \bar{N}-1$ and $r_2 = \bar{N}$. $\qquad\square$

Corollary 5.3.4 (Upper bound on the product of first k singular values)**.**

$$\prod_{n=1}^{k} \sigma_n(\mathbf{H}) \leq \prod_{n=1}^{k} \sigma_n(\mathbf{H}_B) \prod_{n=1}^{k} \sigma_n(\mathbf{H}_F). \tag{5.29}$$

Proof. This is a direct result of (5.26) with $r = k$. $\qquad\square$

Corollary 5.3.5 (Lower bound on the product of last k singular values)**.**

$$\prod_{n=\bar{N}}^{\bar{N}-k+1} \sigma_n(\mathbf{H}) \geq \prod_{n=\bar{N}}^{\bar{N}-k+1} \sigma_n(\mathbf{H}_B) \prod_{n=\bar{N}}^{\bar{N}-k+1} \sigma_n(\mathbf{H}_F). \tag{5.30}$$

Proof. This can be deducted from (5.26) with $r_1 = \bar{N} - k$ and $r_2 = \bar{N}$. $\qquad\square$

Corollaries 5.3.3 and 5.3.5 are less informative when $\bar{N} \neq N$ (i.e., unequal number of transmit, scatter, and receive antennas) as the lower bounds would coincide at zero.

Corollary 5.3.6 (Upper bound on the channel power gain)**.** *The channel power gain is upper bounded by the sum of sorted element-wise product of squared singular values of backward and forward subchannels*

$$\|\mathbf{H}\|_F^2 = \sum_{n=1}^{N} \sigma_n^2(\mathbf{H}) \leq \sum_{n=1}^{N} \sigma_n^2(\mathbf{H}_B)\sigma_n^2(\mathbf{H}_F). \tag{5.31}$$

Proof. Please refer to [231, Inequality 24.4.7]. $\qquad\square$

To achieve the equalities in Corollaries (5.3.2) – (5.3.6), the RIS needs to completely align the subspaces of $\mathbf{H}_B$ and $\mathbf{H}_F$. The resulting scattering matrix is generally required to be unitary

$$\mathbf{\Theta}^\star = \mathbf{V}_B\mathbf{U}_F^H, \tag{5.32}$$

which can be concluded from (7.25) and (7.26) in Appendix 7.3.4. Interestingly, diagonal RIS can attain those equalities if and only if $\mathbf{H}_B$ and $\mathbf{H}_F$ are both rank-1. In such case, the equivalent channel reduces to $\mathbf{H} = \sigma_B \sigma_F \mathbf{u}_B \mathbf{v}_B^H \mathbf{\Theta} \mathbf{u}_F \mathbf{v}_F^H$ and the RIS only needs to align $\mathbf{v}_B^H$ and $\mathbf{u}_F$ by

$$\mathbf{\Theta}^\star = \mathbf{v}_B \mathbf{u}_F^H \odot \mathbf{I}, \tag{5.33}$$

which becomes a special case of (5.5). On the other hand, when $\mathbf{H}_B$ and $\mathbf{H}_F$ are both in Rayleigh fading, the expected maximum channel power gain $\mathbb{E}\{\|\mathbf{H}\|_F\}_{\max}$ can be evaluated as

$$\sum_{n=1}^{N} \int_0^\infty f_{\lambda_n^{\min(N_R, N_S)}}(x_n) dx_n \int_0^\infty f_{\lambda_n^{\min(N_S, N_T)}}(x_n) dx_n, \tag{5.34}$$

where λ_n^K is the n-th eigenvalue of the complex $K \times K$ Wishart matrix with probability density function $f_{\lambda_n^K}(x_n)$ given by [232, Equation 51]. We notice (5.34) is a generalization of [2, Equation 58] to MIMO.

Tighter bounds are generally inapplicable when the direct link is present or the BD-RIS is not unitary, since the direct-indirect channels and backward-forward channels cannot be completely aligned at the same time. In such case, we can exploit optimization approaches from a singular value perspective (Section 5.2.3.2) or a power gain perspective (Section 5.2.4.1).

5.2.4 Power Gain and Achievable Rate Maximization

5.2.4.1 Channel Power Gain

The MIMO channel power gain maximization problem is formulated with respect to the BD-RIS scattering matrix

$$\max_{\mathbf{\Theta}} \quad \|\mathbf{H}_D + \mathbf{H}_B \mathbf{\Theta} \mathbf{H}_F\|_F^2 \tag{5.35a}$$

$$\text{s.t.} \quad \mathbf{\Theta}_g^H \mathbf{\Theta}_g = \mathbf{I}, \quad \forall g, \tag{5.35b}$$

which generalizes the case of SISO [2], MISO [205, 211], single-stream MIMO [204, 216], and direct link-blocked MIMO with unitary RIS (5.32). The key of solving (5.35) is to balance the additive and multiplicative subspace alignments. Interestingly, in terms of maximizing the inner product $\langle \mathbf{H}_D, \mathbf{H}_B \mathbf{\Theta} \mathbf{H}_F \rangle$, (5.35) is reminiscent of the weighted orthogonal Procrustes problem [233]

$$\min_{\mathbf{\Theta}} \quad \|\mathbf{H}_D - \mathbf{H}_B \mathbf{\Theta} \mathbf{H}_F\|_F^2 \tag{5.36a}$$

$$\text{s.t.} \quad \mathbf{\Theta}^H \mathbf{\Theta} = \mathbf{I}, \tag{5.36b}$$

which relaxes the block-unitary constraint (5.36b) to unitary but still has no trivial solution. One lossy transformation exploits the Moore-Penrose inverse and moves $\boldsymbol{\Theta}$ to one side of the product [234], formulating two standard orthogonal Procrustes problems

$$\min_{\boldsymbol{\Theta}} \quad \|\mathbf{H}_{\mathrm{B}}^{\dagger}\mathbf{H}_{\mathrm{D}} - \boldsymbol{\Theta}\mathbf{H}_{\mathrm{F}}\|_{\mathrm{F}}^2 \text{ or } \|\mathbf{H}_{\mathrm{D}}\mathbf{H}_{\mathrm{F}}^{\dagger} - \mathbf{H}_{\mathrm{B}}\boldsymbol{\Theta}\|_{\mathrm{F}}^2 \tag{5.37a}$$

$$\text{s.t.} \quad \boldsymbol{\Theta}^{\mathsf{H}}\boldsymbol{\Theta} = \mathbf{I}, \tag{5.37b}$$

which have global optimal solutions

$$\boldsymbol{\Theta} = \mathbf{U}\mathbf{V}^{\mathsf{H}}, \tag{5.38}$$

where $\mathbf{U}$ and $\mathbf{V}$ are respectively the left and right compact singular matrices of $\mathbf{H}_{\mathrm{B}}^{\dagger}\mathbf{H}_{\mathrm{D}}\mathbf{H}_{\mathrm{F}}^{\mathsf{H}}$ or $\mathbf{H}_{\mathrm{B}}^{\mathsf{H}}\mathbf{H}_{\mathrm{D}}\mathbf{H}_{\mathrm{F}}^{\dagger}$ [123]. We emphasize that (5.32) and (5.38) are valid unitary RIS solutions to (5.35) when the direct link is absent and present, but the latter is neither optimal nor a generalization of the former due to the lossy transformation.

Inspired by [235], we propose an optimal solution to problem (5.35) with arbitrary group size. The idea is to successively approximate the quadratic objective (5.35a) by local Taylor expansions and solve each step in closed form by group-wise SVD.

Proposition 5.4. *Starting from any feasible* $\boldsymbol{\Theta}^{(0)}$*, the sequence*

$$\boldsymbol{\Theta}_g^{(r+1)} = \mathbf{U}_g^{(r)}\mathbf{V}_g^{(r)}, \quad \forall g. \tag{5.39}$$

converges to a stationary point of (5.35)*, where* $\mathbf{U}_g^{(r)}$ *and* $\mathbf{V}_g^{(r)}$ *are the left and right compact singular matrices of*

$$\mathbf{M}_g^{(r)} = \mathbf{H}_{\mathrm{B},g}^{\mathsf{H}}\left(\mathbf{H}_{\mathrm{D}} + \mathbf{H}_{\mathrm{B}}\mathrm{diag}\big(\boldsymbol{\Theta}_{[1:g-1]}^{(r+1)}, \boldsymbol{\Theta}_{[g:G]}^{(r)}\big)\mathbf{H}_{\mathrm{F}}\right)\mathbf{H}_{\mathrm{F},g}^{\mathsf{H}} \tag{5.40}$$

Proof. Please refer to Appendix 7.3.6. □

We then analyze the computational complexity of solving channel gain maximization problem (5.35) by Proposition 5.4. To update each BD-RIS group, matrix multiplication (5.40) requires $\mathcal{O}\big(N_{\mathrm{T}}N_{\mathrm{R}} + (G+1)(NL^2 + N_{\mathrm{T}}N_{\mathrm{R}}L)\big)$ operations and its compact SVD requires $\mathcal{O}(L^3)$ operations. The overall complexity is thus $\mathcal{O}\big(I_{\mathrm{SAA}}G\big(N_{\mathrm{T}}N_{\mathrm{R}} + (G+1)(NL^2 + N_{\mathrm{T}}N_{\mathrm{R}}L) + L^3\big)\big)$, where I_{SAA} is the number iterations for successive affine approximation.

5.2.4.2 Achievable Rate Maximization

We aim to maximize the achievable rate of the BD-RIS-aided MIMO system by jointly optimizing the active and passive beamforming

$$\max_{\mathbf{W},\boldsymbol{\Theta}} \quad R = \log \det \left(\mathbf{I} + \frac{\mathbf{W}^{\mathsf{H}}\mathbf{H}^{\mathsf{H}}\mathbf{H}\mathbf{W}}{\eta} \right) \tag{5.41a}$$

$$\text{s.t.} \quad \|\mathbf{W}\|_{\mathrm{F}}^2 \leq P, \tag{5.41b}$$

$$\boldsymbol{\Theta}_g^{\mathsf{H}}\boldsymbol{\Theta}_g = \mathbf{I}, \quad \forall g, \tag{5.41c}$$

where $\mathbf{W}$ is the transmit precoder, R is the achievable rate, η is the average noise power, and P is the transmit power constraint. Problem (5.41) is non-convex due to the block-unitary constraint (5.41c) and the coupling between variables. We propose a local-optimal approach via AO and a low-complexity approach based on channel shaping.

Alternating Optimization This approach updates $\boldsymbol{\Theta}$ and $\mathbf{W}$ iteratively until convergence. For a given $\mathbf{W}$, the passive beamforming subproblem is

$$\max_{\boldsymbol{\Theta}} \quad \log \det \left(\mathbf{I} + \frac{\mathbf{H}\mathbf{Q}\mathbf{H}^{\mathsf{H}}}{\eta} \right) \tag{5.42a}$$

$$\text{s.t.} \quad \boldsymbol{\Theta}_g^{\mathsf{H}}\boldsymbol{\Theta}_g = \mathbf{I}, \quad \forall g, \tag{5.42b}$$

where $\mathbf{Q} \triangleq \mathbf{W}\mathbf{W}^{\mathsf{H}}$ is the transmit covariance matrix. Problem (5.42) can be solved optimally by Algorithm 8 with the Euclidean gradient given by Lemma 5.2.

Lemma 5.2. *The Euclidean gradient of* (5.42a) *with respect to BD-RIS block g is*

$$\frac{\partial R}{\partial \boldsymbol{\Theta}_g^*} = \frac{1}{\eta}\mathbf{H}_{\mathrm{B},g}^{\mathsf{H}} \left(\mathbf{I} + \frac{\mathbf{H}\mathbf{Q}\mathbf{H}^{\mathsf{H}}}{\eta} \right)^{-1} \mathbf{H}\mathbf{Q}\mathbf{H}_{\mathrm{F},g}^{\mathsf{H}}. \tag{5.43}$$

Proof. Please refer to Appendix 7.3.5. $\qquad\square$

For a given $\boldsymbol{\Theta}$, the global optimal transmit precoder is given by eigenmode transmission [129]

$$\mathbf{W}^{\star} = \mathbf{V}\mathrm{diag}(\mathbf{s}^{\star})^{1/2}, \tag{5.44}$$

where $\mathbf{V}$ is the right singular matrix of the equivalent channel and $\mathbf{s}^{\star}$ is the optimal water-filling power allocation obtainable by the iterative method [128].

The AO algorithm is guaranteed to converge to local-optimal points of problem (5.41) since each subproblem is solved optimally and the objective is bounded above. Similar

to the analysis in Section 5.2.3.2, the computational complexity of solving subproblem (5.42) by geodesic RCG is $\mathcal{O}\big(I_{\mathrm{RCG}}G(NL^2 + LN_{\mathrm{T}}N_{\mathrm{R}} + N_{\mathrm{T}}^2 N_{\mathrm{R}} + N_{\mathrm{T}}N_{\mathrm{R}}^2 + N_{\mathrm{R}}^3 + I_{\mathrm{BLS}}L^3)\big)$. On the other hand, the complexity of solving active beamforming subproblem by (5.44) is $\mathcal{O}\big(NN_{\mathrm{T}}N_{\mathrm{R}}\big)$. The overall complexity is thus $\mathcal{O}\big(I_{\mathrm{AO}}\big(I_{\mathrm{RCG}}G(NL^2 + LN_{\mathrm{T}}N_{\mathrm{R}} + N_{\mathrm{T}}^2 N_{\mathrm{R}} + N_{\mathrm{T}}N_{\mathrm{R}}^2 + N_{\mathrm{R}}^3 + I_{\mathrm{BLS}}L^3) + NN_{\mathrm{T}}N_{\mathrm{R}}\big)\big)$, where I_{AO} is the number of iterations for AO.

Low-Complexity Solution   We then propose a suboptimal two-stage solution to problem (5.41) that decouples the joint RIS-transceiver design. The idea is to first consider channel shaping and replace the rate maximization subproblem (5.42) by channel power gain maximization problem (5.35), then proceed to conventional eigenmode transmission (5.44). Both steps are solved in closed form and the computational complexity is $\mathcal{O}\big(I_{\mathrm{SAA}}G\big(N_{\mathrm{T}}N_{\mathrm{R}} + (G+1)(NL^2 + N_{\mathrm{T}}N_{\mathrm{R}}L) + L^3\big) + NN_{\mathrm{T}}N_{\mathrm{R}}\big)$. While suboptimal, this shaping-inspired solution avoids outer iterations and implements inner iterations more efficiently.

5.3   MIMO-IC

5.3.1   System Model

We then shift the focus to an N_{S}-element BD-RIS-aided interference MIMO system of K transmitter-receiver pairs, where each transmitter is equipped with N_{T} antennas and each receiver is equipped with N_{R} antennas. Let $\mathbf{H}_{\mathrm{D}}^{[kj]} \in \mathbb{C}^{N_{\mathrm{R}} \times N_{\mathrm{T}}}$, $\mathbf{H}_{\mathrm{B}}^{[k]} \in \mathbb{C}^{N_{\mathrm{R}} \times N_{\mathrm{S}}}$, $\mathbf{H}_{\mathrm{F}}^{[j]} \in \mathbb{C}^{N_{\mathrm{S}} \times N_{\mathrm{T}}}$ denote respectively the direct channel from transmitter j to receiver k, backward channel of receiver k, and forward channel of transmitter j, where $j, k \in \{1, \ldots, K\} \triangleq \mathcal{K}$. It is assumed that all devices are at the same side of the RIS and share a common scattering matrix $\boldsymbol{\Theta}$. The equivalent channel from transmitter j to receiver k is

$$\mathbf{H}^{[kj]} = \mathbf{H}_{\mathrm{D}}^{[kj]} + \mathbf{H}_{\mathrm{B}}^{[k]}\boldsymbol{\Theta}\mathbf{H}_{\mathrm{F}}^{[j]} = \mathbf{H}_{\mathrm{D}}^{[kj]} + \sum_g \mathbf{H}_{\mathrm{B},g}^{[k]}\boldsymbol{\Theta}_g\mathbf{H}_{\mathrm{F},g}^{[j]}, \tag{5.45}$$

where $\mathbf{H}_{\mathrm{B},g}^{[k]} \in \mathbb{C}^{N_{\mathrm{R}} \times L}$ and $\mathbf{H}_{\mathrm{F},g}^{[j]} \in \mathbb{C}^{L \times N_{\mathrm{T}}}$ are associated with RIS group g.

5.3.2   Leakage Interference Minimization

Leakage interference refers to the sum of all interference terms in IC. Assume all transmitter sends $N_{\mathrm{E}} \leq N \triangleq \min(N_{\mathrm{T}}, N_{\mathrm{R}})$ data streams to its intended receiver. The leakage interference minimization problem is formulated with respect to all transmit precoders, all

receiver combiners, and the scattering matrix as

$$\min_{\boldsymbol{\Theta}, \{\mathbf{G}_k\}, \{\mathbf{W}_k\}} \quad \sum_{j \neq k} \sum \left\| \mathbf{G}_k (\mathbf{H}_{\mathrm{D}}^{[kj]} + \mathbf{H}_{\mathrm{B}}^{[k]} \boldsymbol{\Theta} \mathbf{H}_{\mathrm{F}}^{[j]}) \mathbf{W}_j \right\|_{\mathrm{F}}^2 \tag{5.46a}$$

$$\text{s.t.} \qquad \boldsymbol{\Theta}_g^{\mathsf{H}} \boldsymbol{\Theta}_g = \mathbf{I}, \quad \forall g \,, \tag{5.46b}$$

$$\mathbf{G}_k \mathbf{G}_k^{\mathsf{H}} = \mathbf{I}, \quad \forall k \,, \tag{5.46c}$$

$$\mathbf{W}_j^{\mathsf{H}} \mathbf{W}_j = \mathbf{I}, \quad \forall j, \tag{5.46d}$$

where $\mathbf{G}_k \in \mathbb{C}^{N_{\mathrm{D}} \times N_{\mathrm{R}}}$ is the combiner at receiver k and $\mathbf{W}_j \in \mathbb{C}^{N_{\mathrm{T}} \times N_{\mathrm{D}}}$ is the precoder at transmitter j. It is worth noting that $\boldsymbol{\Theta}_g$ is a square unitary matrix and $\boldsymbol{\Theta}_g^{\mathsf{H}} \boldsymbol{\Theta}_g = \mathbf{I}$ is equivalent to $\boldsymbol{\Theta}_g \boldsymbol{\Theta}_g^{\mathsf{H}} = \mathbf{I}$, while $\mathbf{G}_k$ and $\mathbf{W}_j$ may be respectively "fat" and "tall" rectangular semi-unitary matrices such that (5.46c) and (5.46d) are required. The non-convex problem can be solved iteratively by the BCD method detailed below.

5.3.2.1   Combiner and Precoder Design

For a given $\boldsymbol{\Theta}$, problem (5.46) reduces to conventional linear beamforming problem, for which an iterative algorithm alternating between the original and reciprocal networks is proposed in [236, 129]. At iteration r, the combiner at receiver k is updated as

$$\mathbf{G}_k^{(r)} = \mathbf{U}_{k,N}^{(r-1)^{\mathsf{H}}}, \tag{5.47}$$

where $\mathbf{U}_{k,N}^{(r-1)}$ is the eigenvectors corresponding to N smallest eigenvalues of the interference covariance matrix $\mathbf{Q}_k^{(r-1)} = \sum_{j \neq k} \mathbf{H}^{[kj]} \mathbf{W}_j^{(r-1)} \mathbf{W}_j^{(r-1)^{\mathsf{H}}} \mathbf{H}^{[kj]^{\mathsf{H}}}$. The precoder at transmitter j is updated as

$$\mathbf{W}_j^{(r)} = \bar{\mathbf{U}}_{j,N}^{(r)}, \tag{5.48}$$

where $\bar{\mathbf{U}}_{j,N}^{(r)}$ corresponds $\bar{\mathbf{Q}}_j^{(r)} = \sum_{k \neq j} \mathbf{H}^{[kj]^{\mathsf{H}}} \mathbf{G}_k^{(r)^{\mathsf{H}}} \mathbf{G}_k^{(r)} \mathbf{H}^{[kj]}$ in the reciprocal network.

5.3.2.2   Scattering Matrix Design

Once $\{\mathbf{G}_k\}$ and $\{\mathbf{W}_j\}$ are determined, we define $\bar{\mathbf{H}}_{\mathrm{D}}^{[kj]} \triangleq \mathbf{G}_k \mathbf{H}_{\mathrm{D}}^{[kj]} \mathbf{W}_j$, $\bar{\mathbf{H}}_{\mathrm{B}}^{[k]} \triangleq \mathbf{G}_k \mathbf{H}_{\mathrm{B}}^{[k]}$, and $\bar{\mathbf{H}}_{\mathrm{F}}^{[j]} \triangleq \mathbf{H}_{\mathrm{F}}^{[j]} \mathbf{W}_j$. The BD-RIS subproblem boils down to

$$\min_{\boldsymbol{\Theta}} \quad \sum_{j \neq k} \sum \left\| (\bar{\mathbf{H}}_{\mathrm{D}}^{[kj]} + \bar{\mathbf{H}}_{\mathrm{B}}^{[k]} \boldsymbol{\Theta} \bar{\mathbf{H}}_{\mathrm{F}}^{[j]}) \right\|_{\mathrm{F}}^2 \tag{5.49a}$$

$$\text{s.t.} \quad \boldsymbol{\Theta}_g^{\mathsf{H}} \boldsymbol{\Theta}_g = \mathbf{I}, \quad \forall g, \tag{5.49b}$$

which can be viewed as a channel shaping problem on $\bar{\mathbf{H}}_{\mathrm{D}}^{[kj]}$, $\bar{\mathbf{H}}_{\mathrm{B}}^{[k]}$, and $\bar{\mathbf{H}}_{\mathrm{F}}^{[j]}$.

Proposition 5.5. *Start from any $\boldsymbol{\Theta}^{(0)}$, the sequence*

$$\boldsymbol{\Theta}_g^{(r+1)} = \mathbf{U}_g^{(r)}\mathbf{V}_g^{(r)}, \quad \forall g \tag{5.50}$$

converges to a stationary point of (5.49), *where $\mathbf{U}_g^{(r)}$ and $\mathbf{V}_g^{(r)}$ are left and right singular matrix of*

$$\mathbf{M}_g^{(r)} = \sum_{j\neq k}\sum \big(\mathbf{B}_{k,g}\boldsymbol{\Theta}_g^{(r)}\mathbf{H}_{\mathrm{F},g}^{[j]} - \mathbf{H}_{\mathrm{B},g}^{[k]}{}^{\mathsf{H}}\mathbf{D}_g^{[kj]\,(r)}\big)\mathbf{H}_{\mathrm{F},g}^{[j]}{}^{\mathsf{H}}, \tag{5.51}$$

where $\mathbf{B}_{k,g} = \lambda_1\big(\mathbf{H}_{\mathrm{B},g}^{[k]}{}^{\mathsf{H}}\mathbf{H}_{\mathrm{B},g}^{[k]}\big)\mathbf{I} - \mathbf{H}_{\mathrm{B},g}^{[k]}{}^{\mathsf{H}}\mathbf{H}_{\mathrm{B},g}^{[k]}$ and

$$\mathbf{D}_g^{[kj]\,(r)} = \mathbf{H}_{\mathrm{D}}^{[jk]} + \sum_{g'<g}\mathbf{H}_{k,g'}^{\mathrm{B}}{}^{\mathsf{H}}\boldsymbol{\Theta}_{g'}^{(r+1)}\mathbf{H}_{k,g'}^{\mathrm{F}} + \sum_{g'>g}\mathbf{H}_{k,g'}^{\mathrm{B}}{}^{\mathsf{H}}\boldsymbol{\Theta}_{g'}^{(r)}\mathbf{H}_{k,g'}^{\mathrm{F}}. \tag{5.52}$$

Proof. The proof is similar to Appendix 7.3.6 and omitted here. $\qquad\square$

Problem (5.46) can be solved iteratively by (5.47), (5.48), and (5.50). Convergence to local-optimal points is guaranteed since each subproblem is solved optimally and the objective is bounded above.

5.3.3 Weighted Sum-Rate Maximization

Finally, we consider weighted sum-rate maximization in MIMO-IC by joint active beamforming design at the transmitters and passive beamforming design at the RIS. The achievable rate of transmission k is given by

$$R_k = \log\det\left(\mathbf{I} + \mathbf{W}_k\mathbf{H}^{[kj]}{}^{\mathsf{H}}\mathbf{Q}_k^{-1}\mathbf{H}^{[kj]}\mathbf{W}_k\right), \tag{5.53}$$

where $\mathbf{Q}_k$ is the interference-plus-noise covariance matrix at receiver k

$$\mathbf{Q}_k = \sum_{j\neq k}\mathbf{H}^{[kj]}\mathbf{W}_j\mathbf{W}_j{}^{\mathsf{H}}\mathbf{H}^{[kj]}{}^{\mathsf{H}} + \eta\mathbf{I}, \tag{5.54}$$

and η is the average noise power. The optimization problem is formulated as

$$\max_{\boldsymbol{\Theta},\{\mathbf{W}_k\}} \quad \sum_k \rho_k R_k \tag{5.55a}$$

$$\text{s.t.} \quad \boldsymbol{\Theta}_g^{\mathsf{H}}\boldsymbol{\Theta}_g = \mathbf{I}, \quad \forall g, \tag{5.55b}$$

$$\|\mathbf{W}_k\|_{\mathrm{F}}^2 \leq P_k. \quad \forall k \tag{5.55c}$$

where ρ_k is the weight that denotes the priority of transmission k. The problem is non-convex and can be solved by the AO method detailed below.

5.3.3.1 Precoder Design

For a given $\boldsymbol{\Theta}$, (5.55) reduces to conventional linear beamforming problem, for which a closed-form iterative solution has been proposed in [237] based on mutual information-Minimum Mean-Square-Error (MMSE) relationship [238]. We restate the steps as follows.

At iteration r, the MMSE combiner at receiver k is

$$\mathbf{G}_k^{(r)} = \mathbf{W}_k^{(r-1)\mathsf{H}}\mathbf{H}^{[kk]\mathsf{H}}\big(\mathbf{Q}_k^{(r-1)} + \mathbf{H}^{[kk]}\mathbf{W}_k^{(r-1)}\mathbf{W}_k^{(r-1)\mathsf{H}}\mathbf{H}^{[kk]\mathsf{H}}\big)^{-1}, \tag{5.56}$$

the corresponding error matrix is

$$\mathbf{E}_k^{(r)} = \big(\mathbf{I} + \mathbf{W}_k^{(r-1)\mathsf{H}}\mathbf{H}^{[kk]\mathsf{H}}\mathbf{Q}_k^{(r-1)}\mathbf{H}^{[kk]}\mathbf{W}_k^{(r-1)}\big)^{-1}, \tag{5.57}$$

the Mean-Square Error (MSE) weight is

$$\boldsymbol{\Omega}_k^{(r)} = \rho_k \mathbf{E}_k^{(r)-1}, \tag{5.58}$$

the Lagrange multiplier is

$$\lambda_k^{(r)} = \frac{\mathrm{tr}\big(\eta\boldsymbol{\Omega}_k^{(r)}\mathbf{G}_k^{(r)}\mathbf{G}_k^{(r)\mathsf{H}} + \sum_j \boldsymbol{\Omega}_k^{(r)}\mathbf{T}_{kj}^{(r)}\mathbf{T}_{kj}^{(r)\mathsf{H}} - \boldsymbol{\Omega}_j^{(r)}\mathbf{T}_{jk}^{(r)}\mathbf{T}_{jk}^{(r)\mathsf{H}}\big)}{P_k}, \tag{5.59}$$

where $\mathbf{T}_{kj}^{(r)} = \mathbf{G}_k^{(r)}\mathbf{H}^{[kj]}\mathbf{W}_j^{(r)}$. The optimal precoder at transmitter k is given by

$$\mathbf{W}_k^{(r)} = \Big(\sum_j \mathbf{H}^{[jk]\mathsf{H}}\mathbf{G}_j^{(r)\mathsf{H}}\boldsymbol{\Omega}_k^{(r)}\mathbf{G}_j^{(r)}\mathbf{H}^{[jk]} + \lambda_k^{(r)}\mathbf{I}\Big)^{-1}\mathbf{H}^{[kk]\mathsf{H}}\mathbf{G}_j^{(r)\mathsf{H}}\boldsymbol{\Omega}_k^{(r)}. \tag{5.60}$$

5.3.3.2   Scattering Matrix Design

Once $\{\mathbf{W}_k\}$ is determined, the complex derivative of (5.55a) with respect to RIS block g is

$$\frac{\partial \rho_k R_k}{\partial \mathbf{\Theta}_g^*} = \sum_k \rho_k \mathbf{H}_{\mathrm{B},g}^{[k]}{}^{\mathsf{H}} \mathbf{Q}_k^{-1} \mathbf{H}^{[kk]} \mathbf{W}_k \mathbf{E}_k \mathbf{W}_k^{\mathsf{H}} \left(\mathbf{H}_{k,g}^{\mathrm{F}}{}^{\mathsf{H}} - \mathbf{H}^{[kk]}{}^{\mathsf{H}} \mathbf{Q}_k^{-1} \sum_{j \neq k} \mathbf{H}^{[kj]} \mathbf{W}_j \mathbf{W}_j^{\mathsf{H}} \mathbf{H}_{\mathrm{F},g}^{[j]}{}^{\mathsf{H}} \right).$$

$$(5.61)$$

The RIS subproblem can be solved by RCG Algorithm 8 where line 4 uses (5.61) explicitly.

5.4   Simulation Results

In this section, we provide numerical results to evaluate the proposed BD-RIS designs. Consider a distance-dependent path loss model $\Lambda(d) = \Lambda_0 d^{-\gamma}$ where Λ_0 is the reference path loss at distance $1\,\mathrm{m}$, d is the propagation distance, and γ is the path loss exponent. The small-scale fading model is $\mathbf{H} = \sqrt{\kappa/(1+\kappa)}\mathbf{H}_{\mathrm{LoS}} + \sqrt{1/(1+\kappa)}\mathbf{H}_{\mathrm{NLoS}}$, where κ is the Rician K-factor, $\mathbf{H}_{\mathrm{LoS}}$ is the deterministic LoS component, and $\mathbf{H}_{\mathrm{NLoS}} \sim \mathcal{CN}(\mathbf{0}, \mathbf{I})$ is the Rayleigh component. We set $\Lambda_0 = -30\,\mathrm{dB}$, $d_{\mathrm{D}} = 14.7\,\mathrm{m}$, $d_{\mathrm{F}} = 10\,\mathrm{m}$, $d_{\mathrm{B}} = 6.3\,\mathrm{m}$, $\gamma_{\mathrm{D}} = 3$, $\gamma_{\mathrm{F}} = 2.4$ and $\gamma_{\mathrm{B}} = 2$ for reference, which corresponds to a typical indoor environment with $\Lambda_{\mathrm{D}} = -65\,\mathrm{dB}$, $\Lambda_{\mathrm{F}} = -54\,\mathrm{dB}$, $\Lambda_{\mathrm{B}} = -46\,\mathrm{dB}$. The indirect path via RIS is thus $35\,\mathrm{dB}$ weaker than the direct path. Rayleigh fading (i.e., $\kappa = 0$) is assumed for all channels unless otherwise specified.

5.4.1   Algorithm Evaluation

Table 5.1 Average Performance of Geodesic and Non-Geodesic RCG Algorithms on Problem (5.20)

RCG path	$N_{\mathrm{S}} = 16$			$N_{\mathrm{S}} = 256$		
	Objective	Iterations	Time [s]	Objective	Iterations	Time [s]
Geodesic	4.359×10^{-3}	11.59	1.839×10^{-2}	1.163×10^{-2}	25.58	3.461
Non-geodesic	4.329×10^{-3}	30.92	5.743×10^{-2}	1.116×10^{-2}	61.40	13.50

We first compare the geodesic and non-geodesic RCG algorithm on problem (5.20) in a 4T4R system with BD-RIS group size $L = 4$. The statistics are averaged over 100 independent runs. It is observed that the geodesic RCG method achieves a slightly higher objective value with significantly (up to $3\times$) lower number of iterations and shorter (up to $4\times$) computational time than the non-geodesic method. The results demonstrate the efficiency of the proposed geodesic RCG algorithm especially in large-scale BD-RIS design problems. If the scattering

matrix is constrained to be symmetric, one can project the solution to the feasible domain by
$\mathbf{\Theta} \leftarrow (\mathbf{\Theta} + \mathbf{\Theta}^{\mathsf{T}})/2$.

5.4.2   MIMO-PC

5.4.2.1   Pareto Frontier

(a) $2 \times 32 \times 2$ (no direct)

(b) $2 \times 32 \times 2$

(c) $2 \times 64 \times 2$

(d) $2 \times 128 \times 2$
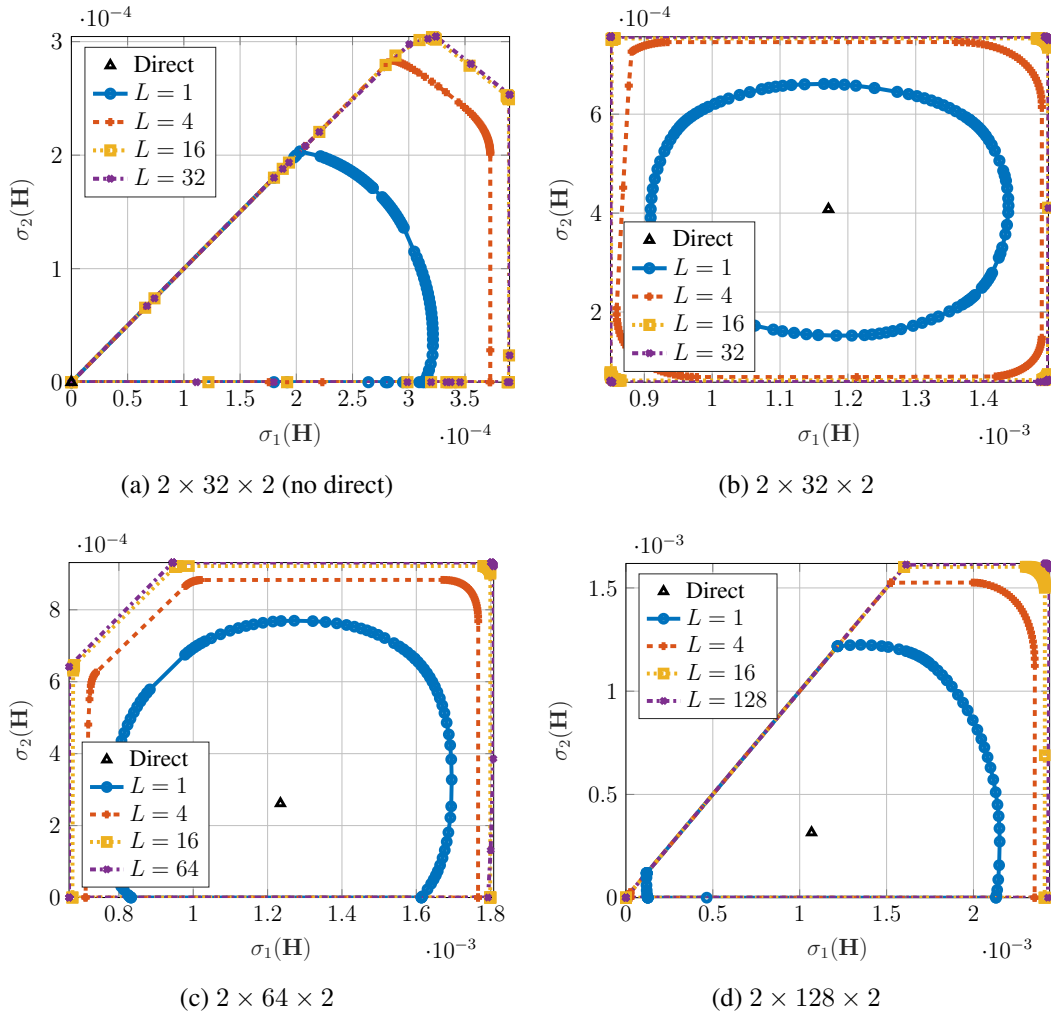
Fig. 5.2 Pareto frontiers of singular values of a 2T2R channel reshaped by a RIS.

Fig. 5.2 shows the Pareto singular values of a 2T2R MIMO reshaped by a RIS. When the direct link is absent, the achievable regions in Fig. 5.2(a) are shaped like pizza slices. This is because $\sigma_1(\mathbf{H}) \geq \sigma_2(\mathbf{H}) \geq 0$ and there exists a trade-off between the alignment of two subspaces. We observe that the smallest singular value can be enhanced up to 2×10^{-4} by diagonal RIS and 3×10^{-4} by unitary BD-RIS, corresponding to a $50\,\%$ gain. When the

direct link is present, the shape of the singular value region depends heavily on the relative strength of the indirect link. In Fig. 5.2(b), a 32-element RIS is insufficient to compensate the $35\,\mathrm{dB}$ path loss imbalance and results in a limited singular value region that is symmetric around the direct point. As the group size L increases, the shape of the region evolves from elliptical to square. This transformation not only improves the dynamic range of $\sigma_1(\mathbf{H})$ and $\sigma_2(\mathbf{H})$ by $22\,\%$ and $38\,\%$, but also provides a better trade-off in manipulating both singular values. It suggests the design freedom from larger group size allows better alignment of multiple subspaces simultaneously. The singular value region also enlarges as the number of scattering elements N_S increases. In particular, Fig. 5.2(d) shows that the equivalent channel can be completely nulled (corresponding to the origin) by a 128-element BD-RIS but not by a diagonal one. Those results demonstrate the superior channel shaping capability of BD-RIS and emphasizes the importance of cooperative wave scattering.

5.4.2.2 Analytical Bounds and Numerical Results

(a) $4 \times 32 \times 4$ (rank-1)

(b) $4 \times 64 \times 4$ (rank-1)

(c) $4 \times 128 \times 4$ (rank-2)

(d) $4 \times 256 \times 4$ (rank-4)
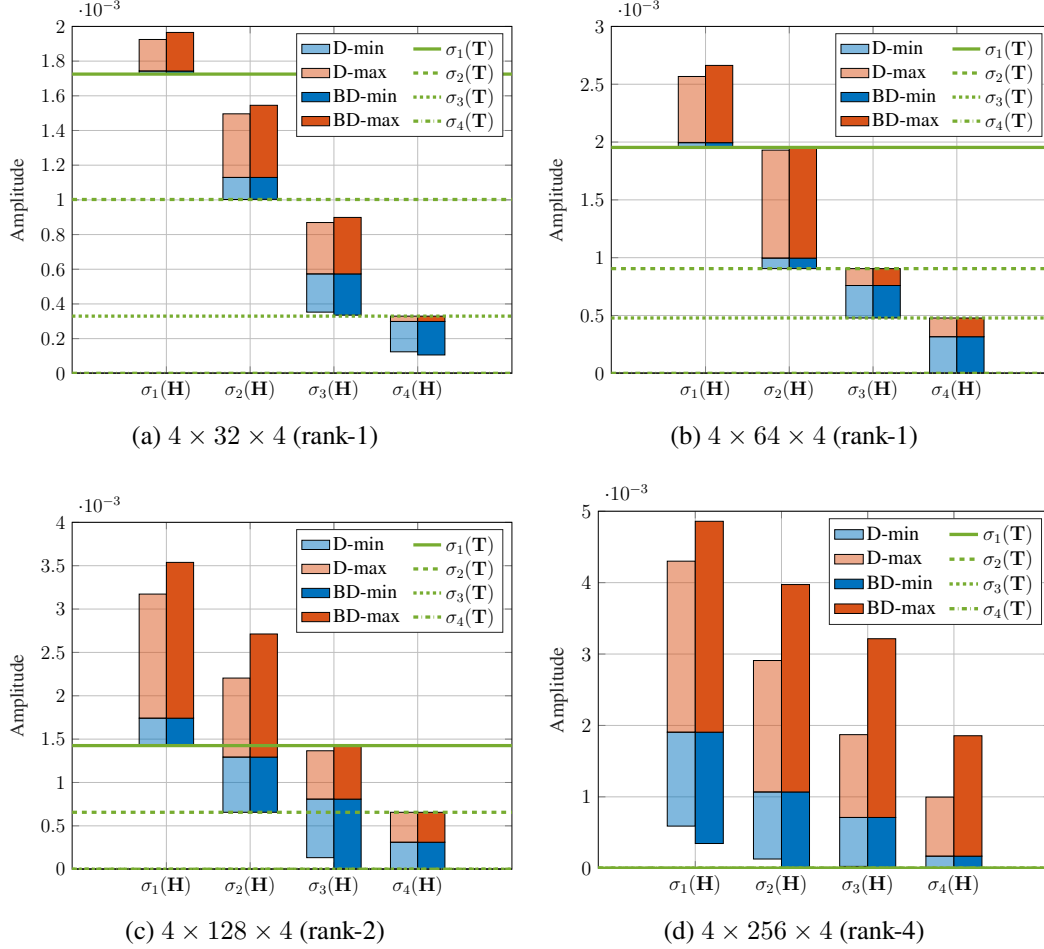
Fig. 5.3 Achievable channel singular values: analytical bounds (green lines) and numerical optimization results (blue and red bars). The intersections of the blue and red bars denote the singular values of the direct channel. The blue (resp. red) bars are obtained by solving problem (5.20) with $\rho_n = -1$ (resp. $+1$) and $\rho_{n'} = 0$, $\forall n' \neq n$. 'D' means diagonal RIS and 'BD' means fully-connected BD-RIS. 'rank-k' refers to the rank of the forward channel.

Fig. 5.3 illustrates the analytical singular value bounds in Proposition 5.2 and the numerical results obtained by solving problem (5.20) with $\rho_n = \pm 1$ and $\rho_{n'} = 0$, $\forall n' \neq n$. Here we assme a rank-k forward channel without loss of generality. When the RIS is in the vicinity of the transmitter, Figs. 5.3(a) and 5.3(b) show that the achievable channel singular values indeed satisfy Corollary 5.2.2, namely $\sigma_1(\mathbf{H}) \geq \sigma_1(\mathbf{T})$, $\sigma_2(\mathbf{T}) \leq \sigma_2(\mathbf{H}) \leq \sigma_1(\mathbf{T})$, etc. It is obvious that BD-RIS can approach those bounds better than diagonal RIS especially for a small N_{S}. Another example is given in Fig. 5.3(c) with rank-2 forward channel. The first two channel singular values are unbounded above and bounded below by the first two singular

values of $\mathbf{T}$, while the last two singular values can be suppressed to zero and bounded above by the first two singular values of $\mathbf{T}$. Those observations align with Proposition 5.2 and Corollary 5.2.1. Finally, Fig. 5.3(d) confirms there are no extra singular value bounds when both forward and backward channels are full-rank. This can be predicted from (5.23) where the compact singular matrix $\mathbf{V}_F$ becomes unitary and $\mathbf{T} = \mathbf{0}$. The numerical results are consistent with the analytical bounds, and we conclude that the channel shaping advantage of BD-RIS over diagonal RIS scales with forward and backward channel ranks.

(a) $1 \times 256 \times 1$ (no direct)   (b) $4 \times 256 \times 4$ (no direct)
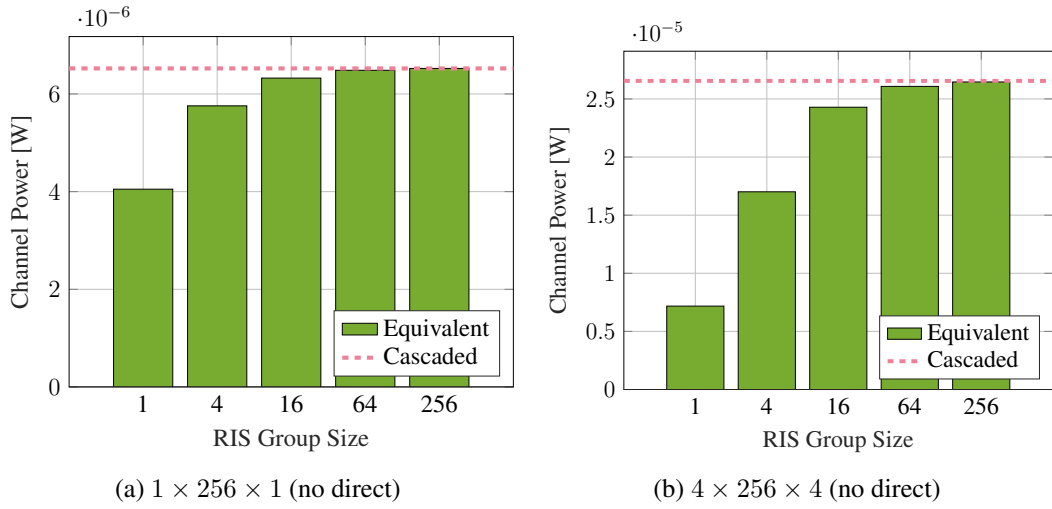
Fig. 5.4 Average maximum channel power versus BD-RIS group size and MIMO dimensions. 'Cascaded' refers to the available power of the cascaded channel, i.e., the sum of (sorted) element-wise power product of backward and forward subchannels.

Fig. 5.4 compares the analytical channel power bound in Corollary 5.3.6 and the numerical results obtained by solving problem (5.35) when the direct link is absent. Here, a fully-connected BD-RIS can attain the upper bound either in closed form (5.32) or via optimization approach (5.39). For the SISO case in Fig. 5.4(a), the maximum channel power is approximately 4×10^{-6} by diagonal RIS and 6.5×10^{-6} by fully-connected BD-RIS, corresponding to a $62.5\,\%$ gain. This aligns with the asymptotic BD-RIS scaling law derived for SISO in [2]. Interestingly, the gain surges to $270\,\%$ in 4T4R MIMO as shown in Fig. 5.4(b). This is because subspace alignment boils down to phase matching in SISO such that both triangular and Cauchy-Schwarz inequalities in [2, (50)] can be simultaneously tight regardless of the group size. That is, diagonal RIS is sufficient for subspace alignment in SISO while the $62.5\,\%$ gain from BD-RIS comes purely from subchannel rearrangement. Now consider a diagonal RIS in MIMO. Each element can only apply a common phase shift to the associated rank-1 $N_R \times N_T$ indirect channel. Therefore, perfect subspace alignment of indirect channels through different elements is generally impossible. It means the disadvantage of diagonal RIS

in subspace alignment and subchannel rearrangement scales with MIMO dimensions. We thus conclude that the power gain of BD-RIS scales with group size and MIMO dimensions.

5.4.2.3 Channel Power and Achievable Rate Maximization

(a) $16 \times N_\mathrm{S} \times 16$ (no direct)   (b) $16 \times N_\mathrm{S} \times 16$
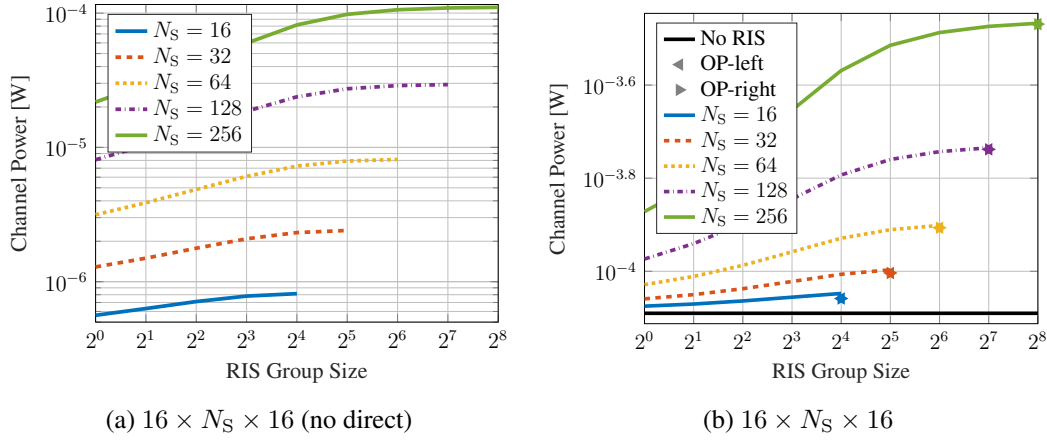
Fig. 5.5 Average maximum channel power versus RIS configuration. 'OP-left' and 'OP-right' refer to the suboptimal solutions to problem (5.35) by lossy transformation (5.37) where Θ is to the left and right of the product, respectively.

We first focus on channel power gain maximization problem (5.35). Fig. 5.5 shows the achievable channel power under different RIS configurations. An interesting observation is that the relative power gain of BD-RIS over diagonal RIS is even larger with direct link. For example, a 64-element fully BD-RIS can almost provide the same channel power as a 256-element diagonal RIS in Fig. 5.5b, but not in Fig. 5.5a. This is because the RIS needs to balance the multiplicative forward-backward combining and the additive direct-indirect combining, such that the subspace alignment advantage of BD-RIS becomes more pronounced. We also notice that the suboptimal solutions (5.38) for fully-connected BD-RIS by lossy transformation (5.37) are very close to optimal especially for a large N_S.

(a) $4 \times 128 \times 4$

(b) $N_{\mathrm{T}} \times 128 \times N_{\mathrm{R}}$

(c) $4 \times N_{\mathrm{S}} \times 4$

(d) $4 \times 128 \times 4$
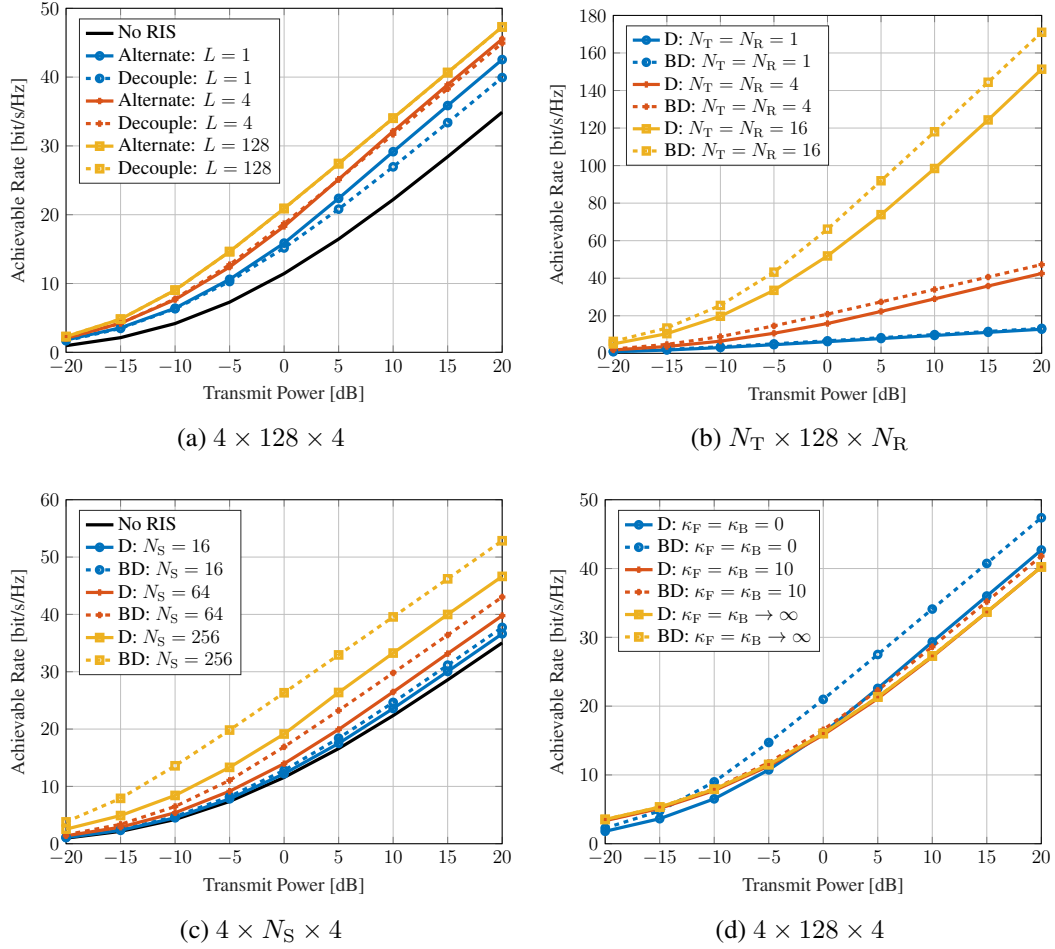
Fig. 5.6 Average achievable rate versus MIMO and RIS configurations. The noise power is $\eta = -75\,\mathrm{dB}$, corresponding to a direct SNR of -10 to $30\,\mathrm{dB}$. 'Alternate' refers to the alternating optimization and 'Decouple' refers to the low-complexity design. 'D' means diagonal RIS and 'BD' means fully-connected BD-RIS.

Fig. 5.6 presents the achievable rate under different MIMO and RIS configurations. At a transmit power of $10\,\mathrm{dB}$, Fig. 5.6(a) shows that introducing a 128-element diagonal RIS to 4T4R MIMO can improve the achievable rate from $22.2\,\mathrm{bps/Hz}$ to $29.2\,\mathrm{bps/Hz}$ ($+31.5\,\%$). In contrast, a BD-RIS of group size 4 and 128 can further improve the rate to $32.1\,\mathrm{bps/Hz}$ ($+44.6\,\%$) and $34\,\mathrm{bps/Hz}$ ($+53.2\,\%$), respectively. Interestingly, the gap between the optimal AO approach (5.42)–(5.44) and the low-complexity solution (5.39) and (5.44) narrows as the group size increases, and completely vanishes for a fully-connected BD-RIS. This implies that the RIS-transceiver design can often be decoupled via channel shaping with marginal performance loss. Figs. 5.6(b) and 5.6(c) also confirm the advantage of BD-RIS grows with the number of transmit, scatter, and receive antennas. In the low power regime (-20 to $-10\,\mathrm{dB}$), the slope of the achievable rate is significantly larger with BD-RIS, suggesting

that multiple streams can be activated at a much lower SNR. This is because BD-RIS not only spreads the channel singular values to a wider range, but also provides a better trade-off between subchannels (c.f. Fig. 5.2). Finally, Fig. 5.6(d) shows that the gap between diagonal and BD-RIS narrows as the Rician K-factor increases and becomes indistinguishable in LoS environment. The observation is expected from previous studies [2, 207, 204] and aligns with Corollary 5.2.2, which suggests that the BD-RIS should be deployed in rich-scattering environments to exploit its channel shaping potential.

5.4.3 MIMO-IC

5.4.3.1 Leakage Interference Minimization
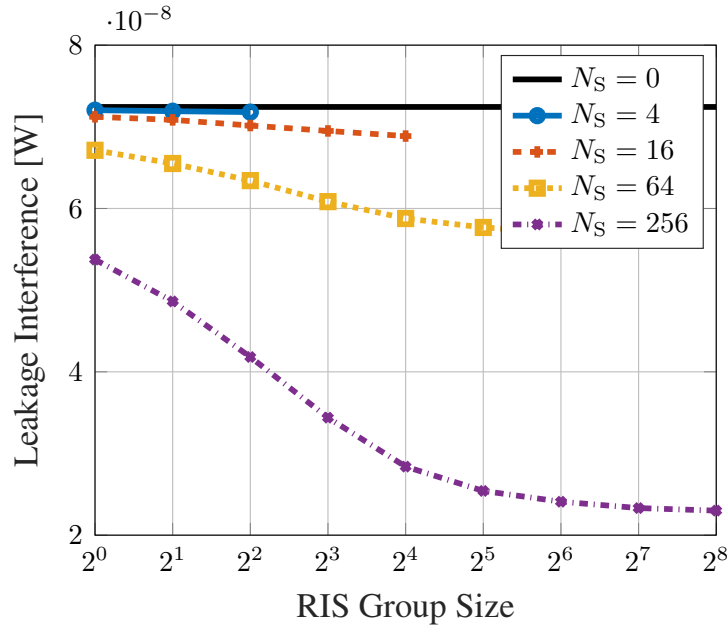
Fig. 5.7 Average leakage interference versus RIS elements N_{S} and group size L. Transmitters and receivers are randomly generated in a disk of radius 50 m centered at the RIS. $(N_{\mathrm{T}}, N_{\mathrm{R}}, N_{\mathrm{E}}, K) = (8, 4, 3, 5)$.

Fig. 5.7 illustrates how BD-RIS helps to reduce the leakage interference. In this case, a fully-connected 2^n-element BD-RIS is almost as good as a diagonal 2^{n+2}-element RIS in terms of leakage interference. Interestingly, the result suggests that BD-RIS can achieve a higher DoF than diagonal RIS in MIMO-IC, which is not the case in MIMO-PC as discussed in 5.1. This demonstrates the potential of BD-RIS in interference alignment or cancellation.

5.4.3.2   Weighted Sum-Rate Maximization
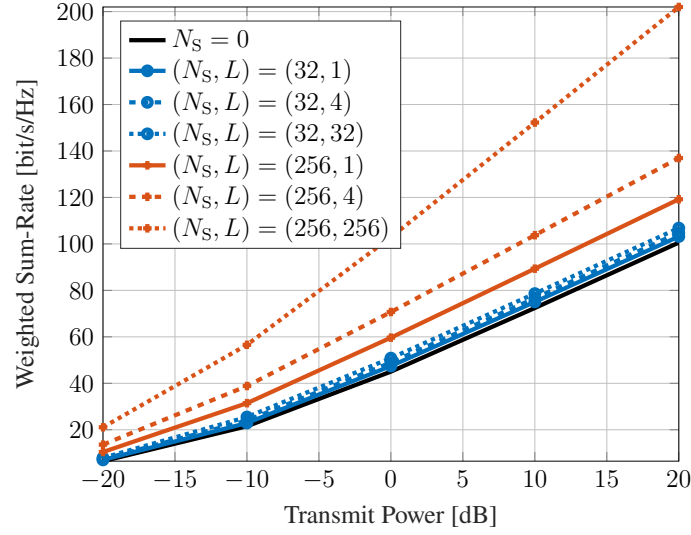
Fig. 5.8 Average weighted sum-rate versus average transmit power, RIS elements N_S, and group size L. $(N_T, N_R, N_E, K) = (8, 4, 3, 5)$.

Fig. 5.8 shows the average weighted sum-rate versus average transmit power and RIS configuration. We observe that the advantage of BD-RIS over diagonal RIS becomes more pronounced when the number of reflecting elements increases. This is because the total number of subchannels in the system grows linearly with N_S such that the gain from subchannel rearrangement capability of BD-RIS is amplified. It suggests cooperative scattering among elements is particularly important for large-scale RIS deployments in MIMO-IC systems, where the performance-complexity trade-off is more favorable than SISO and single-user scenarios.
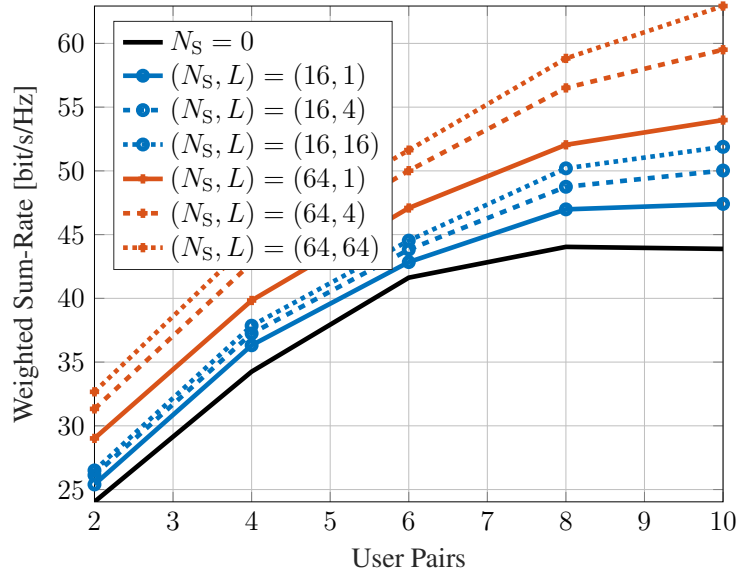
Fig. 5.9 Average weighted sum-rate versus transmitter-receiver pairs K, RIS elements N_S, and group size L. $(N_\mathrm{T}, N_\mathrm{R}, N_\mathrm{E}) = (4, 4, 3)$, $P = 25\,\mathrm{dB}$, and $\rho_k = 1$, $\forall k$.

Fig. 5.9 shows the average weighted sum-rate versus the number of transmitter-receiver pairs and RIS configuration. We observe that introducing a RIS to IC systems is helpful to mitigate the rate saturation effect as the number of users increases. In the overloaded regime ($K \geq 8$), BD-RIS provides a larger slope of the achievable rate than diagonal RIS. This is because the BD-RIS can better align the interference subspaces of different users. At $K = 10$, adding a 64-element diagonal and BD-RIS can improve the weighted sum-rate by $23\,\%$ and $43\,\%$, respectively. These results provide valuable insights for practical RIS design in dense connection scenarios, where BD configurations can significantly enhance the network capacity.

5.5   Conclusion

This chapter studied the channel shaping capability of RIS in MIMO-PC and IC. We considered a general BD architecture that allows elements within the same group to cooperate, enabling advanced wave manipulation than conventional RIS. An efficient RCG algorithm was proposed for smooth BD-RIS optimization problems, which offers lower computation complexity and faster convergence than existing methods. For PC, we characterized the Pareto frontiers of channel singular values via optimization approach and provided analytical bounds in rank-deficient and fully-connected scenarios. Two joint beamforming designs were proposed for rate maximization problem, one based on AO for optimal performance and one

based on channel shaping for lower complexity. For IC, we highlighted that BD-RIS can reduce the leakage interference and improve the weighted sum-rate. Extensive simulation results and theoretical analysis showed that the advantage of BD-RIS scales with the number of elements, group size, MIMO dimensions, and channel diversity, thanks to its superior subspace alignment and subchannel rearrangement capability.

One future direction is incorporating one RIS at transmitter and one at receiver for stronger channel manipulation, which may fully align both direct-indirect and forward-backward subspaces simultaneously.

Chapter 6

Conclusions and Future Works

6.1 Conclusions

This thesis explored the versatile potential of RIS for augmenting future wireless networks from a physical-layer perspective. After introducing the necessary background, we focused on three most promising directions (passive beamforming, backscatter modulation, channel shaping) and investigated those in different application scenarios:

- In the domain of SWIPT, we unveiled new trade-offs and design insights by introducing RIS into multi-antenna, multi-carrier systems. Considering harvester nonlinearity, we characterized the achievable R-E region through a joint optimization of waveform, active and passive beamforming based on the CSIT. This problem was solved by BCD, where we obtained the active precoder in closed form, the passive beamforming by SCA, and the waveform amplitude by GP. To facilitate practical implementation, we also proposed two low-complexity designs based on closed-form adaptive waveform schemes. Simulation results highlighted a second-order array gain and a fourth-order power scaling order with respect to RIS elements, while being robust to CSI inaccuracy and RIS resolution.

- The proposed RIScatter concept demonstrated the synergy between active and passive transmissions. RIScatter is a batteryless cognitive radio that recycles ambient signal in an adaptive and customizable manner, where dispersed or co-located scatter nodes partially modulate their information and partially engineer the wireless channel. The key is to render the probability distribution of reflection states as a joint function of the information source, CSI, and relative priority of coexisting links. This enables RIScatter to softly bridge BackCom and RIS; reduce to either in special cases; or evolve in a mixed form for heterogeneous traffic control and universal hardware design.

We also proposed a low-complexity SIC-free receiver that exploits the properties of RIScatter. For a single-user multi-node network, we characterized the achievable primary-(total-)backscatter rate region by optimizing the input distribution at scatter nodes, the active beamforming at the AP, and the energy decision regions at the user. Simulation results demonstrated that the received signal can be exploited for dual purposes and the nodes can shift smoothly between backscatter modulation and passive beamforming via input distribution control.

- Finally, we investigated the fundamental limits of RIS for reshaping MIMO PC and IC. We departed from the widely-adopted diagonal phase shift model to a general BD architecture with superior subspace alignment and subchannel rearrangement capabilities. An efficient geodesic RCG algorithm was tailored for smooth BD-RIS optimization problems, which features lower complexity and faster convergence. For MIMO-PC, we characterized the achievable channel singular value region through numerical and analytical approaches, then tackled the rate maximization problem by a local-optimal AO approach and a low-complexity shaping-inspired approach. For MIMO-IC, we extended the proposed algorithms to solve leakage interference minimization and WSR maximization problems. Simulation results suggested channel shaping offers a promising path to decouple the joint RIS-transceiver design with minor performance degradation and much lower computational complexity.

6.2 Future Works

Many interesting problems are countered during the research but not fully addressed due to time constraints, to name a few:

- *RIS-aided multi-user SWIPT:* Extension to multi-user scenario is non-trivial because (i) the waveform and passive beamforming are shared among users while the active beamforming and power splitting ratios are user-specific; (ii) the interference can be harvested for power purpose such that dedicated information and power precoders are desired; (iii) due to harvester nonlinearity, the optimal design is highly non-convex and depends heavily on the multiple access scheme; (iv) a proper criterion is needed to cover the R-E trade-off and fairness among users.

- *Capacity region of RIScatter:* The current work considers a decoding order from backscatter to primary, corresponding to a primary-optimal point (but not a corner due to energy detector) in the capacity region. If the primary message can be decoded first, it can be modeled as a spreading sequence that enhances the backscatter SNR by N times

(where N is the symbol period ratio) [144], corresponding to a backscatter-optimal point. Besides, the backscatter detection can be performed coherently in the signal domain to further improve the achievable rate.

- *RIScatter, index modulation, and rate splitting:* In RIScatter, the primary and backscatter symbols are superimposed by multiplicative coding, and the nodes usually have a finite number of reflection states. Instead of acting as a pure channel controller or individual information source, a RIS can be integrated into the RF transmitter as an additional index modulator to enhance the spectral efficiency [168]. The transmitted message is thus split into an amplitude-phase modulated component and an index-modulated component, which can be decoded separately at the receiver [239]. This could further improve the capacity of RIS-aided MIMO systems [21], or make a low-complexity realization of Rate-Splitting Multiple Access (RSMA) [240] in a multi-user system where the reflection pattern conveys the common message.

- *RIScatter and sensing:* The proposed RIScatter concept can be extended to sensing applications, where the scatter nodes are equipped with sensors to monitor the environment and report the information to the AP. The challenge is to design the input distribution and reflection states to stabilize the environment for improved sensing performance while guaranteeing the communication quality.

- *BD-RIS and frequency shifting:* Similar to AmBC, the different groups of BD-RIS can be used to shift the incident wave to different frequencies. This phenomenon can be exploited to mitigate the self and inter-operator interference [241], generate a multi-frequency signal out of a CW, or manipulate the response of frequency-selective channels. However, it could be challenging to design and implement the time-varying scattering matrices at a low power consumption.

- *Multi-sector BD-RIS and interference alignment:* The current work solves leakage interference minimization and WSR maximization problems in RIS-aided IC. It remains unknown how many scattering elements are required to completely eliminate the interference, and what is the DoF in a K-user $N_T \times N_S \times N_R$ IC. Besides, there exists a multi-sector model [55] that provides full-space coverage and highly directional beams. It would be interesting to see how those sector-specific (instead of being shared by all users) scattering matrices can help to align the interference and improve the fairness issue.

Chapter 7

Appendix

7.1 Proofs for Chapter 3

7.1.1 Proof of Proposition 3.1

For any feasible $\bar{\boldsymbol{\Theta}}$ to problem (3.21), $\mathrm{tr}(\bar{\boldsymbol{\Theta}}) = L + 1$ always holds because of the modulus constraint (3.21c). Therefore, problem (3.21) can be recast as

$$\max_{\bar{\boldsymbol{\Theta}}} \quad \tilde{z}(\bar{\boldsymbol{\Theta}}) - \mathrm{tr}(\bar{\boldsymbol{\Theta}}) \tag{7.1a}$$

$$\text{s.t.} \quad R(\bar{\boldsymbol{\Theta}}) \geq \bar{R}, \tag{7.1b}$$

$$\mathrm{diag}^{-1}(\bar{\boldsymbol{\Theta}}) = \mathbf{1}, \tag{7.1c}$$

$$\bar{\boldsymbol{\Theta}} \succeq \mathbf{0}, \tag{7.1d}$$

$$\mathrm{rank}(\bar{\boldsymbol{\Theta}}) = 1. \tag{7.1e}$$

It is straightforward to verify the convex problem (7.1a)–(7.1d) satisfies the Slater's condition and strong duality holds [184]. The corresponding Lagrangian function at iteration r is

$$
\begin{aligned}
\mathcal{L} = {}& \mathrm{tr}\left(\bar{\mathbf{\Theta}}^{(r)}\right) - \frac{1}{2}\beta_2\rho\,\mathrm{tr}\left((\mathbf{C}_{\mathrm{I},0} + \mathbf{C}_{\mathrm{P},0})\bar{\mathbf{\Theta}}^{(r)}\right) \\
& - \frac{3}{4}\beta_4\rho^2\Bigg(2t_{\mathrm{I},0}^{(r-1)}\mathrm{tr}\left(\mathbf{C}_{\mathrm{I},0}\bar{\mathbf{\Theta}}^{(r)}\right) + \sum_{k=-N+1}^{N-1}(t_{\mathrm{P},k}^{(r-1)})^*\mathrm{tr}\left(\mathbf{C}_{\mathrm{P},k}\bar{\mathbf{\Theta}}^{(r)}\right) \\
& \qquad + 2t_{\mathrm{P},0}^{(r-1)}\mathrm{tr}\left(\mathbf{C}_{\mathrm{I},0}\bar{\mathbf{\Theta}}^{(r)}\right) + 2t_{\mathrm{I},0}^{(r-1)}\mathrm{tr}\left(\mathbf{C}_{\mathrm{P},0}\bar{\mathbf{\Theta}}^{(r)}\right) \Bigg) \\
& + \mu\left(2^{\bar{R}} - \prod_{n=1}^{N}\left(1 + \frac{(1-\rho)\mathrm{tr}\left(\mathbf{C}_n\bar{\mathbf{\Theta}}^{(r)}\right)}{\sigma_n^2}\right) \right) \\
& + \mathrm{tr}\left(\mathrm{diag}(\nu) \odot \left(\bar{\mathbf{\Theta}}^{(r)} \odot \mathbf{I} - \mathbf{I}\right)\right) - \mathrm{tr}\left(\mathbf{\Upsilon}\bar{\mathbf{\Theta}}^{(r)}\right) + \zeta,
\end{aligned}
\tag{7.2}
$$

where μ, ν, $\mathbf{\Upsilon}$ denote respectively the scalar, vector and matrix Lagrange multiplier associated with constraint (7.1b), (7.1c) and (7.1d), and ζ collects all terms irrelevant to $\bar{\mathbf{\Theta}}^{(r)}$. The KKT conditions on the primal and dual solutions are

$$
\mu^\star \geq 0, \mathbf{\Upsilon}^\star \succeq \mathbf{0},
\tag{7.3a}
$$

$$
\nu^\star \odot \mathrm{diag}^{-1}(\bar{\mathbf{\Theta}}^\star) = \mathbf{0}, \mathbf{\Upsilon}^\star\bar{\mathbf{\Theta}}^\star = \mathbf{0},
\tag{7.3b}
$$

$$
\nabla_{\bar{\mathbf{\Theta}}^\star}\mathcal{L} = 0.
\tag{7.3c}
$$

We then express (7.3c) explicitly as $\mathbf{\Upsilon}^\star = \mathbf{I} - \mathbf{\Delta}^\star$, where

$$
\begin{aligned}
\mathbf{\Delta}^\star = {}& \frac{1}{2}\beta_2\rho(\mathbf{C}_{\mathrm{I},0} + \mathbf{C}_{\mathrm{P},0}) \\
& + \frac{3}{4}\beta_4\rho^2\Bigg(2t_{\mathrm{I},0}^{(r-1)}\mathbf{C}_{\mathrm{I},0} + \sum_{k=-N+1}^{N-1}(t_{\mathrm{P},k}^{(r-1)})^*\mathbf{C}_{\mathrm{P},k} + 2t_{\mathrm{P},0}^{(r-1)}\mathbf{C}_{\mathrm{I},0} + 2t_{\mathrm{I},0}^{(r-1)}\mathbf{C}_{\mathrm{P},0} \Bigg) \\
& + \mu^\star\sum_{n=1}^{N}\frac{(1-\rho)\mathbf{C}_n}{\sigma_n^2}\prod_{n'=1,n'\neq n}^{N}\left(1 + \frac{(1-\rho)\mathrm{tr}\left(\mathbf{C}_{n'}\bar{\mathbf{\Theta}}^\star\right)}{\sigma_{n'}^2}\right) - \mathrm{diag}(\nu^\star).
\end{aligned}
\tag{7.4}
$$

Note that (7.3b) suggests $\mathrm{rank}(\mathbf{\Upsilon}^\star) + \mathrm{rank}(\bar{\mathbf{\Theta}}^\star) \leq L + 1$. By reusing the proof in [242, Appendix A], we conclude $\mathrm{rank}(\mathbf{\Upsilon}^\star) \geq L$. On the other hand, $\bar{\mathbf{\Theta}}^\star$ cannot be $\mathbf{0}$ and $\mathrm{rank}(\bar{\mathbf{\Theta}}^\star) \geq 1$. Therefore, any optimal solution $\bar{\mathbf{\Theta}}^\star$ to the relaxed problem (7.1) must be rank-1. Due to the equivalence between (3.21a) and (7.1a), $\bar{\mathbf{\Theta}}^\star$ is also optimal to the relaxed problem (3.21). The proof is completed.

7.1.2 Proof of Proposition 3.2

The objective function (3.21a) is non-decreasing over iterations because the solution to (3.21a)–(3.21d) at iteration $r-1$ is still feasible at iteration r. As $r \to \infty$, $\tilde{z}(\bar{\boldsymbol{\Theta}}^{(r)})$ is bounded above because of the unit-modulus constraint (3.21c). Thus, Algorithm 1 is guaranteed to converge. Besides, we notice that Algorithm 1 is an inner approximation algorithm [243], because $\tilde{z}(\bar{\boldsymbol{\Theta}}) \leq z(\bar{\boldsymbol{\Theta}})$, $\partial \tilde{z}(\bar{\boldsymbol{\Theta}}^{(r)})/\partial \bar{\boldsymbol{\Theta}} = \partial z(\bar{\boldsymbol{\Theta}}^{(r)})/\partial \bar{\boldsymbol{\Theta}}$ and the approximation (3.16)–(3.18) are asymptotically tight as $r \to \infty$ [244]. Therefore, it is guaranteed to provide a local optimal $\bar{\boldsymbol{\Theta}}^\star$ to the relaxed passive beamforming problem. According to Proposition 3.1, $\bar{\boldsymbol{\Theta}}^\star$ is rank-1 such that $\boldsymbol{\theta}^\star$ can be extracted without performance loss and the local optimality inherits to the original problem (3.11).

7.1.3 Proof of Proposition 3.3

From the perspective of WIT, the MRT precoder (3.23) maximizes $|\mathbf{h}_n^{\mathsf{H}} \mathbf{w}_{\mathrm{I},n}| = \|\mathbf{h}_n\| s_{\mathrm{I},n}$ and thus the rate (3.6). From the perspective of WPT, the MRT precoder (3.23) maximizes $(\mathbf{h}_n^{\mathsf{H}} \mathbf{w}_{\mathrm{I/P},n})(\mathbf{h}_n^{\mathsf{H}} \mathbf{w}_{\mathrm{I/P},n})^* = \|\mathbf{h}_n\|^2 s_{\mathrm{I/P},n}^2$ and thus the second and fourth order DC terms (3.9a)–(3.9d). Therefore, the global optimal information and power precoders coincide at MRT.

7.2 Proofs for Chapter 4

7.2.1 Proof of Proposition 4.1

Denote the Lagrange multipliers associated with (4.16b) and (4.16c) as $\{\nu_k\}_{k \in \mathcal{K}}$ and $\{\lambda_{m_k}\}_{k \in \mathcal{K}, m_k \in \mathcal{M}}$, respectively. The Lagrangian function of problem (4.17) is

$$L(p, \nu, \lambda) = I(x_{\mathcal{K}}) + \sum_k \nu_k \Big(\sum_{m_k} p(x_{m_k}) - 1 \Big) + \sum_{k,m_k} \lambda_{m_k} p(x_{m_k}), \tag{7.5}$$

and the KKT conditions are, $\forall k, m_k$,

$$I_k^\star(x_{m_k}) - (1-\rho) + \nu_k^\star + \lambda_{m_k}^\star = 0, \tag{7.6a}$$

$$\lambda_{m_k}^\star = 0, \quad \text{if } p^\star(x_{m_k}) > 0, \tag{7.6b}$$

$$\lambda_{m_k}^\star \geq 0, \quad \text{if } p^\star(x_{m_k}) = 0. \tag{7.6c}$$

Plugging (7.6b) and (7.6c) into (7.6a) yields

$$I_k^\star(x_{m_k}) = 1 - \rho - \nu_k^\star, \quad \text{if } p^\star(x_{m_k}) > 0, \tag{7.7a}$$

$$I_k^\star(x_{m_k}) \leq 1 - \rho - \nu_k^\star, \quad \text{if } p^\star(x_{m_k}) = 0, \tag{7.7b}$$

such that

$$\sum_{m_k} p^\star(x_{m_k}) I_k^\star(x_{m_k}) = 1 - \rho - \nu_k^\star. \tag{7.8}$$

On the other hand, by definition (4.19) we have

$$\sum_{m_k} p^\star(x_{m_k}) I_k^\star(x_{m_k}) = I^\star(x_\mathcal{K}), \tag{7.9}$$

where the right-hand side is irrelevant to k. (7.7), (7.8), and (7.9) together complete the proof.

7.2.2   Proof of Proposition 4.2

We first prove sequence (4.20) is non-decreasing in weighted sum mutual information. Let $p(x_{m_\mathcal{K}}) = \prod_{q \in \mathcal{K}} p(x_{m_q})$ and $p'(x_{m_\mathcal{K}}) = p'(x_{m_k}) \prod_{q \in \mathcal{K} \setminus \{k\}} p(x_{m_q})$ be two distributions potentially different at x_{m_k}, and $J\big(p(x_{m_\mathcal{K}}), p'(x_{m_\mathcal{K}})\big)$ be a joint function defined as

$$
\begin{aligned}
J\big(p(x_{m_\mathcal{K}}), p'(x_{m_\mathcal{K}})\big) \triangleq \sum_{m_\mathcal{K}} p(x_{m_\mathcal{K}}) &\left(\rho \log\left(1 + \frac{|\mathbf{h}^\mathsf{H}(x_{m_\mathcal{K}})\mathbf{w}|^2}{\sigma_v^2} \right) \right. \\
&\left. + (1 - \rho) \sum_{m'_\mathcal{K}} q(\hat{x}_{m'_\mathcal{K}} | x_{m_\mathcal{K}}) \log \frac{q(\hat{x}_{m'_\mathcal{K}} | x_{m_\mathcal{K}}) p'(x_{m_\mathcal{K}})}{p'(\hat{x}_{m'_\mathcal{K}}) p(x_{m_\mathcal{K}})} \right).
\end{aligned}
\tag{7.10}
$$

It is straightforward to verify $J\big(p(x_{m_\mathcal{K}}), p(x_{m_\mathcal{K}})\big) = I(x_\mathcal{K})$ and $J\big(p(x_{m_\mathcal{K}}), p'(x_{m_\mathcal{K}})\big)$ is a concave function for a given $p'(x_{m_\mathcal{K}})$. Setting $\nabla_{p(x_{m_k})} J\big(p(x_{m_\mathcal{K}}), p'(x_{m_\mathcal{K}})\big) = 0$ yields

$$S_k'(x_{m_k}) - S_k'(x_{i_k}) + (1 - \rho) \log \frac{p(x_{i_k})}{p^\star(x_{m_k})} = 0, \tag{7.11}$$

where $i_k \neq m_k$ is the reference state and

$$S_k'(x_{m_k}) \triangleq I_k'(x_{m_k}) + (1 - \rho) \sum_{m_{\mathcal{K} \setminus \{k\}}} p(x_{m_{\mathcal{K} \setminus \{k\}}}) \sum_{m'_\mathcal{K}} q(\hat{x}_{m'_\mathcal{K}} | x_{m_\mathcal{K}}) \log p'(x_{m_\mathcal{K}}). \tag{7.12}$$

Evidently, $\forall m_k \neq i_k$, (7.11) boils down to

$$p^\star(x_{m_k}) = \frac{p'(x_{m_k}) \exp\left(\frac{\rho}{1-\rho} I'_k(x_{m_k})\right)}{\sum_{m'_k} p'(x_{m'_k}) \exp\left(\frac{\rho}{1-\rho} I'_k(x_{m'_k})\right)}. \tag{7.13}$$

Since $p(x_{i_k}) = 1 - \sum_{m_k \neq i_k} p^\star(x_{m_k})$ has exactly the same form as (7.13), the choice of reference does not matter and (7.13) is optimal $\forall m_k \in \mathcal{M}$. That is, for a fixed $p'(x_{m_\mathcal{K}})$, (7.13) ensures

$$J\big(p(x_{m_\mathcal{K}}), p'(x_{m_\mathcal{K}})\big) \geq I'(x_\mathcal{K}). \tag{7.14}$$

On the other hand, we notice

$$I(x_\mathcal{K}) - J\big(p(x_{m_\mathcal{K}}), p'(x_{m_\mathcal{K}})\big)$$

$$= (1-\rho) \sum_{m_k} \frac{p'(x_{m_k}) f'_k(x_{m_k})}{\sum_{m'_k} p'(x_{m'_k}) f'_k(x_{m'_k})} \sum_{m''_\mathcal{K}} q(\hat{x}_{m''_\mathcal{K}} | x_{m_k}) \log \frac{\sum_{m'_k} p'(x_{m'_k}) q(\hat{x}_{m''_\mathcal{K}} | x_{m'_k}) f'_k(x_{m_k})}{\sum_{m'_k} p'(x_{m'_k}) q(\hat{x}_{m''_\mathcal{K}} | x_{m'_k}) f'_k(x_{m'_k})} \tag{7.15a}$$

$$\geq (1-\rho) \sum_{m_k} \frac{p'(x_{m_k}) f'_k(x_{m_k})}{\sum_{m'_k} p'(x_{m'_k}) f'_k(x_{m'_k})} \sum_{m''_\mathcal{K}} q(\hat{x}_{m''_\mathcal{K}} | x_{m_k}) \left(1 - \frac{\sum_{m'_k} p'(x_{m'_k}) q(\hat{x}_{m''_\mathcal{K}} | x_{m'_k}) f'_k(x_{m'_k})}{\sum_{m'_k} p'(x_{m'_k}) q(\hat{x}_{m''_\mathcal{K}} | x_{m'_k}) f'_k(x_{m_k})}\right) \tag{7.15b}$$

$$= (1-\rho) \left(1 - \sum_{m_k} \frac{p'(x_{m_k}) \cancel{f'_k(x_{m_k})}}{\sum_{m'_k} p'(x_{m'_k}) f'_k(x_{m'_k})} \sum_{m''_\mathcal{K}} q(\hat{x}_{m''_\mathcal{K}} | x_{m_k}) \frac{\sum_{m'_k} p'(x_{m'_k}) q(\hat{x}_{m''_\mathcal{K}} | x_{m'_k}) f'_k(x_{m'_k})}{\sum_{m'_k} p'(x_{m'_k}) q(\hat{x}_{m''_\mathcal{K}} | x_{m'_k}) \cancel{f'_k(x_{m_k})}}\right) \tag{7.15c}$$

$$= (1-\rho) \left(1 - \sum_{m''_\mathcal{K}} \frac{\sum_{m_k} p'(x_{m_k}) q(\cancel{\hat{x}_{m''_\mathcal{K}} | x_{m_k}})}{\sum_{m'_k} p'(x_{m'_k}) f'_k(x_{m'_k})} \frac{\sum_{m'_k} p'(x_{m'_k}) q(\hat{x}_{m''_\mathcal{K}} | x_{m'_k}) f'_k(x_{m'_k})}{\cancel{\sum_{m'_k} p'(x_{m'_k}) q(\hat{x}_{m''_\mathcal{K}} | x_{m'_k})}}\right) \tag{7.15d}$$

$$= (1-\rho) \left(1 - \frac{\sum_{m'_k} p'(x_{m'_k}) f'_k(x_{m'_k}) \sum_{m''_\mathcal{K}} q(\hat{x}_{m''_\mathcal{K}} | x_{m'_k})}{\sum_{m'_k} p'(x_{m'_k}) f'_k(x_{m'_k})}\right)$$

$$= 0, \tag{7.15e}$$

where $f'_k(x_{m_k}) \triangleq \exp\left(\frac{\rho}{1-\rho} I'_k(x_{m_k})\right)$ and the equality holds if and only if $p(x_{m_\mathcal{K}})$ and $p'(x_{m_\mathcal{K}})$ equals (i.e., (7.13) converges). (7.14) and (7.15) together imply $I(x_\mathcal{K}) \geq I'(x_\mathcal{K})$. Since mutual information is bounded above, we conclude the sequence (4.20) is non-decreasing and convergent.

Next, we prove any converging point of sequence (4.20), denoted as $p^\star(x_{m_k})$, fulfills the KKT conditions (4.18). Let

$$D^{(r)}(x_{m_k}) \triangleq \frac{p^{(r+1)}(x_{m_k})}{p^{(r)}(x_{m_k})} = \frac{f_k^{(r)}(x_{m_k})}{\sum_{m_k'} p^{(r)}(x_{m_k'}) f_k^{(r)}(x_{m_k'})}. \tag{7.16}$$

As sequence (4.20) is convergent, any state with $p^\star(x_{m_k}) > 0$ need to satisfy $D^\star(x_{m_k}) \triangleq \lim_{r \to \infty} D^{(r)}(x_{m_k}) = 1$, namely

$$I_k^\star(x_{m_k}) = \frac{1-\rho}{\rho} \log \sum_{m_k'} p^\star(x_{m_k'}) \exp\Big(\frac{\rho}{1-\rho} I_k^\star(x_{m_k'})\Big). \tag{7.17}$$

The right-hand side is a constant for node k and implies (7.7a). That is, any converging point with nonzero probability must satisfy (4.18a). On the other hand, we assume $p^\star(x_{m_k}) = 0$ does not satisfy (4.18b), namely

$$I_k^\star(x_{m_k}) > I^\star(x_{\mathcal{K}}) = \sum_{m_k'} p^\star(x_{m_k'}) I_k^\star(x_{m_k'}), \tag{7.18}$$

Since the exponential function is monotonically increasing, (7.18) implies $f_k^\star(x_{m_k}) > \sum_{m_k'} p^\star(x_{m_k'}) f_k^\star(x_{m_k'})$ and $D^\star(x_{m_k}) > 1$. It contradicts with

$$p^{(r)}(x_{m_k}) = p^{(0)}(x_{m_k}) \prod_{n=1}^{r} D^{(n)}(x_{m_k}), \tag{7.19}$$

since the left-hand side is zero while all terms on the right-hand side are strictly positive. The proof is completed.

7.3 Proofs for Chapter 5

7.3.1 Proof of Lemma 5.1

Let $\mathbf{H} = \sum_n \mathbf{u}_n \sigma_n \mathbf{v}_n^{\mathsf{H}}$ be the compact SVD of the equivalent channel. Since the singular vectors are orthonormal, the n-th singular value can be expressed as

$$\sigma_n = \mathbf{u}_n^{\mathsf{H}} \mathbf{H} \mathbf{v}_n = \mathbf{u}_n^{\mathsf{T}} \mathbf{H}^* \mathbf{v}_n^*, \tag{7.20}$$

whose differential with respect to $\boldsymbol{\Theta}_g^*$ is

$$
\begin{aligned}
\partial\sigma_n &= \partial\mathbf{u}_n^{\mathsf{T}}\underbrace{\mathbf{H}^*\mathbf{v}_n^*}_{\sum_m \mathbf{u}_m^*\sigma_m\mathbf{v}_m^{\mathsf{T}}\mathbf{v}_n} + \mathbf{u}_n^{\mathsf{T}}\cdot\partial\mathbf{H}^*\cdot\mathbf{v}_n^* + \underbrace{\mathbf{u}_n^{\mathsf{T}}\mathbf{H}^*}_{\mathbf{u}_n^{\mathsf{T}}\sum_m \mathbf{u}_m^*\sigma_m\mathbf{v}_m^{\mathsf{T}}}\partial\mathbf{v}_n^* \\
&= \underbrace{\partial\mathbf{u}_n^{\mathsf{T}}\mathbf{u}_n^*}_{\partial 1=0}\cdot\sigma_n + \mathbf{u}_n^{\mathsf{T}}\cdot\partial\mathbf{H}^*\cdot\mathbf{v}_n^* + \sigma_n\cdot\underbrace{\mathbf{v}_n^{\mathsf{T}}\partial\mathbf{v}_n^*}_{\partial 1=0} \\
&= \mathbf{u}_n^{\mathsf{T}}\mathbf{H}_{\mathrm{B},g}^*\cdot\partial\boldsymbol{\Theta}_g^*\cdot\mathbf{H}_{\mathrm{F},g}^*\mathbf{v}_n^* \\
&= \mathrm{tr}(\mathbf{H}_{\mathrm{F},g}^*\mathbf{v}_n^*\mathbf{u}_n^{\mathsf{T}}\mathbf{H}_{\mathrm{B},g}^*\cdot\partial\boldsymbol{\Theta}_g^*).
\end{aligned}
$$

According to [224], the corresponding complex derivative is

$$
\frac{\partial\sigma_n}{\partial\boldsymbol{\Theta}_g^*} = \mathbf{H}_{\mathrm{B},g}^{\mathsf{H}}\mathbf{u}_n\mathbf{v}_n^{\mathsf{H}}\mathbf{H}_{\mathrm{F},g}^{\mathsf{H}}. \tag{7.21}
$$

A linear combination of (7.21) yields (5.21).

7.3.2 Proof of Proposition 5.1

The scattering matrix of BD-RIS can be decomposed as[1]

$$
\boldsymbol{\Theta} = \mathbf{L}\boldsymbol{\Theta}_{\mathrm{D}}\mathbf{R}^{\mathsf{H}}, \tag{7.22}
$$

where $\boldsymbol{\Theta}_{\mathrm{D}} \in \mathbb{U}^{N_{\mathrm{S}}\times N_{\mathrm{S}}}$ corresponds to diagonal RIS and $\mathbf{L},\mathbf{R} \in \mathbb{U}^{N_{\mathrm{S}}\times N_{\mathrm{S}}}$ are block diagonal matrices of $L\times L$ unitary blocks. Manipulating $\mathbf{L}$ and $\mathbf{R}$ rotates the linear spans of $\bar{\mathbf{H}}_{\mathrm{B}} \triangleq \mathbf{H}_{\mathrm{B}}\mathbf{L}$ and $\bar{\mathbf{H}}_{\mathrm{F}} \triangleq \mathbf{R}^{\mathsf{H}}\mathbf{H}_{\mathrm{F}}$ and maintains their rank. On the other hand, there exists a $\boldsymbol{\Theta}_{\mathrm{D}}$ such that

$$
\begin{aligned}
\mathrm{rank}(\mathbf{H}_{\mathrm{B}}\boldsymbol{\Theta}_{\mathrm{D}}\mathbf{H}_{\mathrm{F}}) &= \min\big(\mathrm{rank}(\mathbf{H}_{\mathrm{B}}),\mathrm{rank}(\boldsymbol{\Theta}_{\mathrm{D}}),\mathrm{rank}(\mathbf{H}_{\mathrm{F}})\big) \\
&= \min\big(\mathrm{rank}(\bar{\mathbf{H}}_{\mathrm{B}}),N_{\mathrm{S}},\mathrm{rank}(\bar{\mathbf{H}}_{\mathrm{F}})\big) \\
&= \max_{\boldsymbol{\Theta}}\ \mathrm{rank}(\mathbf{H}_{\mathrm{B}}\boldsymbol{\Theta}\mathbf{H}_{\mathrm{F}})
\end{aligned}
$$

The same result holds if the direct link is present.

7.3.3 Proof of Proposition 5.2

We consider rank-k forward channel and the proof follows similarly for rank-k backward channel. Let $\mathbf{H}_{\mathrm{F}} = \mathbf{U}_{\mathrm{F}}\boldsymbol{\Sigma}_{\mathrm{F}}\mathbf{V}_{\mathrm{F}}^{\mathsf{H}}$ be the compact SVD of the forward channel. The channel

---

[1]This is because (block) unitary matrices are closed under multiplication.

Gram matrix $\mathbf{G} \triangleq \mathbf{H}\mathbf{H}^{\mathsf{H}}$ can be written as

$$
\begin{aligned}
\mathbf{G} &= \mathbf{H}_{\mathrm{D}}\mathbf{H}_{\mathrm{D}}^{\mathsf{H}} + \mathbf{H}_{\mathrm{B}}\boldsymbol{\Theta}\mathbf{U}_{\mathrm{F}}\boldsymbol{\Sigma}_{\mathrm{F}}\boldsymbol{\Sigma}_{\mathrm{F}}^{\mathsf{H}}\mathbf{U}_{\mathrm{F}}^{\mathsf{H}}\boldsymbol{\Theta}^{\mathsf{H}}\mathbf{H}_{\mathrm{B}}^{\mathsf{H}} + \mathbf{H}_{\mathrm{B}}\boldsymbol{\Theta}\mathbf{U}_{\mathrm{F}}\boldsymbol{\Sigma}_{\mathrm{F}}\mathbf{V}_{\mathrm{F}}^{\mathsf{H}}\mathbf{H}_{\mathrm{D}}^{\mathsf{H}} + \mathbf{H}_{\mathrm{D}}\mathbf{V}_{\mathrm{F}}\boldsymbol{\Sigma}_{\mathrm{F}}\mathbf{U}_{\mathrm{F}}^{\mathsf{H}}\boldsymbol{\Theta}^{\mathsf{H}}\mathbf{H}_{\mathrm{B}}^{\mathsf{H}} \\
&= \mathbf{H}_{\mathrm{D}}(\mathbf{I} - \mathbf{V}_{\mathrm{F}}\mathbf{V}_{\mathrm{F}}^{\mathsf{H}})\mathbf{H}_{\mathrm{D}}^{\mathsf{H}} + (\mathbf{H}_{\mathrm{B}}\boldsymbol{\Theta}\mathbf{U}_{\mathrm{F}}\boldsymbol{\Sigma}_{\mathrm{F}} + \mathbf{H}_{\mathrm{D}}\mathbf{V}_{\mathrm{F}})(\boldsymbol{\Sigma}_{\mathrm{F}}\mathbf{U}_{\mathrm{F}}^{\mathsf{H}}\boldsymbol{\Theta}^{\mathsf{H}}\mathbf{H}_{\mathrm{B}}^{\mathsf{H}} + \mathbf{V}_{\mathrm{F}}^{\mathsf{H}}\mathbf{H}_{\mathrm{D}}^{\mathsf{H}}) \\
&= \mathbf{Y} + \mathbf{Z}\mathbf{Z}^{\mathsf{H}},
\end{aligned}
$$

where we define $\mathbf{Y} \triangleq \mathbf{H}_{\mathrm{D}}(\mathbf{I} - \mathbf{V}_{\mathrm{F}}\mathbf{V}_{\mathrm{F}}^{\mathsf{H}})\mathbf{H}_{\mathrm{D}}^{\mathsf{H}} \in \mathbb{H}^{N_{\mathrm{R}} \times N_{\mathrm{R}}}$ and $\mathbf{Z} \triangleq \mathbf{H}_{\mathrm{B}}\boldsymbol{\Theta}\mathbf{U}_{\mathrm{F}}\boldsymbol{\Sigma}_{\mathrm{F}} + \mathbf{H}_{\mathrm{D}}\mathbf{V}_{\mathrm{F}} \in \mathbb{C}^{N_{\mathrm{R}} \times k}$. That is to say, $\mathbf{G}$ can be expressed as a Hermitian matrix plus k rank-1 perturbations. According to the Cauchy interlacing formula [123], the n-th eigenvalue of $\mathbf{G}$ is bounded by

$$
\lambda_n(\mathbf{G}) \leq \lambda_{n-k}(\mathbf{Y}), \qquad\qquad \text{if } n > k, \tag{7.23}
$$

$$
\lambda_n(\mathbf{G}) \geq \lambda_n(\mathbf{Y}), \qquad\qquad \text{if } n < N - k + 1. \tag{7.24}
$$

Since $\mathbf{Y} = \mathbf{T}\mathbf{T}^{\mathsf{H}}$ is positive semi-definite, taking the square roots of (7.23) and (7.24) gives (5.22a) and (5.22b).

7.3.4 Proof of Proposition 5.3

Let $\mathbf{H}_{\mathrm{B}} = \mathbf{U}_{\mathrm{B}}\boldsymbol{\Sigma}_{\mathrm{B}}\mathbf{V}_{\mathrm{B}}^{\mathsf{H}}$ and $\mathbf{H}_{\mathrm{F}} = \mathbf{U}_{\mathrm{F}}\boldsymbol{\Sigma}_{\mathrm{F}}\mathbf{V}_{\mathrm{F}}^{\mathsf{H}}$ be the SVD of the backward and forward channels, respectively. The scattering matrix of fully-connected RIS can be decomposed as

$$
\boldsymbol{\Theta} = \mathbf{V}_{\mathrm{B}}\mathbf{X}\mathbf{U}_{\mathrm{F}}^{\mathsf{H}}, \tag{7.25}
$$

where $\mathbf{X} \in \mathbb{U}^{N_{\mathrm{S}} \times N_{\mathrm{S}}}$ is a unitary matrix to be designed. The equivalent channel is thus a function of $\mathbf{X}$

$$
\mathbf{H} = \mathbf{H}_{\mathrm{B}}\boldsymbol{\Theta}\mathbf{H}_{\mathrm{F}} = \mathbf{U}_{\mathrm{B}}\boldsymbol{\Sigma}_{\mathrm{B}}\mathbf{X}\boldsymbol{\Sigma}_{\mathrm{F}}\mathbf{V}_{\mathrm{F}}^{\mathsf{H}}. \tag{7.26}
$$

Since $\mathrm{sv}(\mathbf{U}\mathbf{A}\mathbf{V}^{\mathsf{H}}) = \mathrm{sv}(\mathbf{A})$ for unitary $\mathbf{U}$ and $\mathbf{V}$, we have

$$
\begin{aligned}
\mathrm{sv}(\mathbf{H}) &= \mathrm{sv}(\mathbf{U}_{\mathrm{B}}\boldsymbol{\Sigma}_{\mathrm{B}}\mathbf{X}\boldsymbol{\Sigma}_{\mathrm{F}}\mathbf{V}_{\mathrm{F}}^{\mathsf{H}}) \\
&= \mathrm{sv}(\boldsymbol{\Sigma}_{\mathrm{B}}\mathbf{X}\boldsymbol{\Sigma}_{\mathrm{F}}) \\
&= \mathrm{sv}(\bar{\mathbf{U}}_{\mathrm{B}}\boldsymbol{\Sigma}_{\mathrm{B}}\bar{\mathbf{V}}_{\mathrm{B}}^{\mathsf{H}}\bar{\mathbf{U}}_{\mathrm{F}}\boldsymbol{\Sigma}_{\mathrm{F}}\bar{\mathbf{V}}_{\mathrm{F}}^{\mathsf{H}}) \\
&= \mathrm{sv}(\mathbf{B}\mathbf{F}),
\end{aligned}
$$

where $\bar{\mathbf{U}}_{\mathrm{B/F}}$ and $\bar{\mathbf{V}}_{\mathrm{B/F}}$ are arbitrary unitary matrices.

7.3.5 Proof of Lemma 5.2

The differential of R with respect to $\boldsymbol{\Theta}_g^*$ is [224]

$$
\begin{aligned}
\partial R &= \frac{1}{\eta} \mathrm{tr}\bigg\{ \partial \mathbf{H}^* \cdot \mathbf{Q}^\mathsf{T} \mathbf{H}^\mathsf{T} \Big(\mathbf{I} + \frac{\mathbf{H}^* \mathbf{Q}^\mathsf{T} \mathbf{H}^\mathsf{T}}{\eta} \Big)^{-1} \bigg\} \\
&= \frac{1}{\eta} \mathrm{tr}\bigg\{ \mathbf{H}_{\mathrm{B},g}^* \cdot \partial \boldsymbol{\Theta}_g^* \cdot \mathbf{H}_{\mathrm{F},g}^* \mathbf{Q}^\mathsf{T} \mathbf{H}^\mathsf{T} \Big(\mathbf{I} + \frac{\mathbf{H}^* \mathbf{Q}^\mathsf{T} \mathbf{H}^\mathsf{T}}{\eta} \Big)^{-1} \bigg\} \\
&= \frac{1}{\eta} \mathrm{tr}\bigg\{ \mathbf{H}_{\mathrm{F},g}^* \mathbf{Q}^\mathsf{T} \mathbf{H}^\mathsf{T} \Big(\mathbf{I} + \frac{\mathbf{H}^* \mathbf{Q}^\mathsf{T} \mathbf{H}^\mathsf{T}}{\eta} \Big)^{-1} \mathbf{H}_{\mathrm{B},g}^* \cdot \partial \boldsymbol{\Theta}_g^* \bigg\},
\end{aligned}
$$

and the corresponding complex derivative is (5.43).

7.3.6 Proof of Proposition 5.4

The differential of (5.35a) with respect to $\boldsymbol{\Theta}_g^*$ is

$$
\begin{aligned}
\partial \|\mathbf{H}\|_{\mathrm{F}}^2 &= \mathrm{tr}\big(\mathbf{H}_{\mathrm{B},g}^* \cdot \partial \boldsymbol{\Theta}_g^* \cdot \mathbf{H}_{\mathrm{F},g}^* (\mathbf{H}_{\mathrm{D}}^\mathsf{T} + \mathbf{H}_{\mathrm{F}}^\mathsf{T} \boldsymbol{\Theta}^\mathsf{T} \mathbf{H}_{\mathrm{B}}^\mathsf{T}) \big) \\
&= \mathrm{tr}\big(\mathbf{H}_{\mathrm{F},g}^* (\mathbf{H}_{\mathrm{D}}^\mathsf{T} + \mathbf{H}_{\mathrm{F}}^\mathsf{T} \boldsymbol{\Theta}^\mathsf{T} \mathbf{H}_{\mathrm{B}}^\mathsf{T}) \mathbf{H}_{\mathrm{B},g}^* \cdot \partial \boldsymbol{\Theta}_g^* \big)
\end{aligned}
$$

and the corresponding complex derivative is

$$
\frac{\partial \|\mathbf{H}\|_{\mathrm{F}}^2}{\partial \boldsymbol{\Theta}_g^*} = \mathbf{H}_{\mathrm{B},g}^\mathsf{H} (\mathbf{H}_{\mathrm{D}} + \mathbf{H}_{\mathrm{B}} \boldsymbol{\Theta} \mathbf{H}_{\mathrm{F}}) \mathbf{H}_{\mathrm{F},g}^\mathsf{H} = \mathbf{M}_g. \tag{7.27}
$$

First, we approximate the quadratic objective (5.35a) by its local Taylor expansion

$$
\max_{\boldsymbol{\Theta}} \quad \sum_g 2\Re\big\{ \mathrm{tr}(\boldsymbol{\Theta}_g^\mathsf{H} \mathbf{M}_g) \big\} \tag{7.28a}
$$

$$
\text{s.t.} \quad \boldsymbol{\Theta}_g^\mathsf{H} \boldsymbol{\Theta}_g = \mathbf{I}, \quad \forall g. \tag{7.28b}
$$

Let $\mathbf{M}_g = \mathbf{U}_g \boldsymbol{\Sigma}_g \mathbf{V}_g^\mathsf{H}$ be the compact SVD of $\mathbf{M}_g$. We have

$$
\Re\big\{ \mathrm{tr}(\boldsymbol{\Theta}_g^\mathsf{H} \mathbf{M}_g) \big\} = \Re\big\{ \mathrm{tr}(\boldsymbol{\Sigma}_g \mathbf{V}_g^\mathsf{H} \boldsymbol{\Theta}_g^\mathsf{H} \mathbf{U}_g) \big\} \le \mathrm{tr}(\boldsymbol{\Sigma}_g). \tag{7.29}
$$

The upper bound is tight when $\mathbf{V}_g^\mathsf{H} \boldsymbol{\Theta}_g^\mathsf{H} \mathbf{U}_g = \mathbf{I}$, which implies the optimal solution of (7.28) is $\tilde{\boldsymbol{\Theta}}_g = \mathbf{U}_g \mathbf{V}_g^\mathsf{H}, \forall g$.

Next, we prove that solving (7.28) successively does not decrease (5.35a). Since $\tilde{\boldsymbol{\Theta}}$ optimal for problem (7.28), we have $\sum_g 2\Re\big\{ \mathrm{tr}(\tilde{\boldsymbol{\Theta}}_g^\mathsf{H} \mathbf{M}_g) \big\} \ge \sum_g 2\Re\big\{ \mathrm{tr}(\boldsymbol{\Theta}_g^\mathsf{H} \mathbf{M}_g) \big\}$ which is

explicitly expressed by

$$2\Re\Big\{\sum_g \mathrm{tr}(\tilde{\boldsymbol{\Theta}}_g^\mathsf{H}\mathbf{H}_{\mathrm{B},g}^\mathsf{H}\mathbf{H}_{\mathrm{D}}\mathbf{H}_{\mathrm{F},g}^\mathsf{H}) + \sum_{g_1,g_2} \mathrm{tr}(\tilde{\boldsymbol{\Theta}}_{g_1}^\mathsf{H}\mathbf{H}_{\mathrm{B},g_1}^\mathsf{H}\mathbf{H}_{\mathrm{B},g_2}\boldsymbol{\Theta}_{g_2}\mathbf{H}_{\mathrm{F},g_2}\mathbf{H}_{\mathrm{F},g_1}^\mathsf{H})\Big\}$$

$$\geq 2\Re\Big\{\sum_g \mathrm{tr}(\boldsymbol{\Theta}_g^\mathsf{H}\mathbf{H}_{\mathrm{B},g}^\mathsf{H}\mathbf{H}_{\mathrm{D}}\mathbf{H}_{\mathrm{F},g}^\mathsf{H}) + \sum_{g_1,g_2} \mathrm{tr}(\boldsymbol{\Theta}_{g_1}^\mathsf{H}\mathbf{H}_{\mathrm{B},g_1}^\mathsf{H}\mathbf{H}_{\mathrm{B},g_2}\boldsymbol{\Theta}_{g_2}\mathbf{H}_{\mathrm{F},g_2}\mathbf{H}_{\mathrm{F},g_1}^\mathsf{H})\Big\}. \quad (7.30)$$

On the other hand, expanding $\|\sum_g \mathbf{H}_{\mathrm{B},g}\tilde{\boldsymbol{\Theta}}_g\mathbf{H}_{\mathrm{F},g} - \sum_g \mathbf{H}_{\mathrm{B},g}\boldsymbol{\Theta}_g\mathbf{H}_{\mathrm{F},g}\|_\mathrm{F}^2 \geq 0$ gives

$$\sum_{g_1,g_2} \mathrm{tr}(\mathbf{H}_{\mathrm{F},g_1}^\mathsf{H}\tilde{\boldsymbol{\Theta}}_{g_1}^\mathsf{H}\mathbf{H}_{\mathrm{B},g_1}^\mathsf{H}\mathbf{H}_{\mathrm{B},g_2}\tilde{\boldsymbol{\Theta}}_{g_2}\mathbf{H}_{\mathrm{F},g_2}) - 2\Re\Big\{\sum_{g_1,g_2} \mathrm{tr}(\mathbf{H}_{\mathrm{F},g_1}^\mathsf{H}\tilde{\boldsymbol{\Theta}}_{g_1}^\mathsf{H}\mathbf{H}_{\mathrm{B},g_1}^\mathsf{H}\mathbf{H}_{\mathrm{B},g_2}\boldsymbol{\Theta}_{g_2}\mathbf{H}_{\mathrm{F},g_2})\Big\}$$

$$+ \sum_{g_1,g_2} \mathrm{tr}(\mathbf{H}_{\mathrm{F},g_1}^\mathsf{H}\boldsymbol{\Theta}_{g_1}^\mathsf{H}\mathbf{H}_{\mathrm{B},g_1}^\mathsf{H}\mathbf{H}_{\mathrm{B},g_2}\boldsymbol{\Theta}_{g_2}\mathbf{H}_{\mathrm{F},g_2}) \geq 0. \quad (7.31)$$

Adding (7.30) and (7.31), we have

$$2\Re\Big\{\mathrm{tr}(\tilde{\boldsymbol{\Theta}}^\mathsf{H}\mathbf{H}_{\mathrm{B}}^\mathsf{H}\mathbf{H}_{\mathrm{D}}\mathbf{H}_{\mathrm{F}}^\mathsf{H})\Big\} + \mathrm{tr}(\mathbf{H}_{\mathrm{F}}^\mathsf{H}\tilde{\boldsymbol{\Theta}}^\mathsf{H}\mathbf{H}_{\mathrm{B}}^\mathsf{H}\mathbf{H}_{\mathrm{B}}\tilde{\boldsymbol{\Theta}}\mathbf{H}_{\mathrm{F}})$$

$$\geq 2\Re\Big\{\mathrm{tr}(\boldsymbol{\Theta}^\mathsf{H}\mathbf{H}_{\mathrm{B}}^\mathsf{H}\mathbf{H}_{\mathrm{D}}\mathbf{H}_{\mathrm{F}}^\mathsf{H})\Big\} + \mathrm{tr}(\mathbf{H}_{\mathrm{F}}^\mathsf{H}\boldsymbol{\Theta}^\mathsf{H}\mathbf{H}_{\mathrm{B}}^\mathsf{H}\mathbf{H}_{\mathrm{B}}\boldsymbol{\Theta}\mathbf{H}_{\mathrm{F}}), \quad (7.32)$$

which suggests that updating $\tilde{\boldsymbol{\Theta}}$ does not decrease (5.35a).

Finally, we prove that the converging point of (7.28), denoted by $\tilde{\boldsymbol{\Theta}}^?$, is a stationary point of (5.35). The KKT conditions of (5.35) and (7.28) are equivalent in terms of primal/dual feasibility and complementary slackness, while the stationary conditions are respectively, $\forall g$,

$$\mathbf{H}_{\mathrm{B},g}^\mathsf{H}(\mathbf{H}_{\mathrm{D}} + \mathbf{H}_{\mathrm{B}}\boldsymbol{\Theta}^\star\mathbf{H}_{\mathrm{F}})\mathbf{H}_{\mathrm{F},g}^\mathsf{H} - \boldsymbol{\Theta}_g^\star\boldsymbol{\Lambda}_g^\mathsf{H} = 0, \quad (7.33)$$

$$\mathbf{M}_g - \boldsymbol{\Theta}_g^\star\boldsymbol{\Lambda}_g^\mathsf{H} = 0. \quad (7.34)$$

On convergence, (7.34) becomes $\mathbf{H}_{\mathrm{B},g}^\mathsf{H}(\mathbf{H}_{\mathrm{D}} + \mathbf{H}_{\mathrm{B}}\boldsymbol{\Theta}^?\mathbf{H}_{\mathrm{F}})\mathbf{H}_{\mathrm{F},g}^\mathsf{H} - \boldsymbol{\Theta}_g^?\boldsymbol{\Lambda}_g^\mathsf{H} = 0$ and reduces to (7.33). The proof is thus completed.

References

[1] Q. Wu and R. Zhang, "Towards smart and reconfigurable environment: Intelligent reflecting surface aided wireless network," *IEEE Communications Magazine*, vol. 58, pp. 106–112, Jan 2020.

[2] S. Shen, B. Clerckx, and R. Murch, "Modeling and architecture design of reconfigurable intelligent surfaces using scattering parameter network analysis," *IEEE Transactions on Wireless Communications*, vol. 21, pp. 1229–1243, Feb 2022.

[3] H.-R. Ahn, *Asymmetric Passive Components in Microwave Integrated Circuits*. Hoboken, NJ, USA: Wiley, 2006.

[4] Y. Huang, A. Alieldin, and C. Song, "Equivalent circuits and analysis of a generalized antenna system," *IEEE Antennas and Propagation Magazine*, vol. 63, pp. 53–62, Apr 2021.

[5] C. E. Shannon, "A mathematical theory of communication," *Bell System Technical Journal*, vol. 27, pp. 379–423, Jul 1948.

[6] F. Tariq, M. R. A. Khandaker, K.-K. Wong, M. A. Imran, M. Bennis, and M. Debbah, "A speculative study on 6G," *IEEE Wireless Communications*, vol. 27, pp. 118–125, Aug 2020.

[7] D. Georgiev, "Internet of things statistics, facts & predictions [2024's update]," https://review42.com/resources/internet-of-things-stats/, accessed: 2024-03-13.

[8] M. Shafi, A. F. Molisch, P. J. Smith, T. Haustein, P. Zhu, P. D. Silva, F. Tufvesson, A. Benjebbour, and G. Wunder, "5G: A tutorial overview of standards, trials, challenges, deployment, and practice," *IEEE Journal on Selected Areas in Communications*, vol. 35, pp. 1201–1221, Jun 2017.

[9] H. Tataria, M. Shafi, A. F. Molisch, M. Dohler, H. Sjoland, and F. Tufvesson, "6G wireless systems: Vision, requirements, challenges, insights, and opportunities," *Proceedings of the IEEE*, vol. 109, pp. 1166–1199, Jul 2021.

[10] M. Alsabah, M. A. Naser, B. M. Mahmmod, S. H. Abdulhussain, M. R. Eissa, A. Al-Baidhani, N. K. Noordin, S. M. Sait, K. A. Al-Utaibi, and F. Hashim, "6G wireless communications networks: A comprehensive survey," *IEEE Access*, vol. 9, pp. 148 191–148 243, 2021.

[11] W. Jiang, B. Han, M. A. Habibi, and H. D. Schotten, "The road towards 6G: A comprehensive survey," *IEEE Open Journal of the Communications Society*, vol. 2, pp. 334–366, 2021.

[12] L. Dai, B. Wang, M. Wang, X. Yang, J. Tan, S. Bi, S. Xu, F. Yang, Z. Chen, M. D. Renzo, C.-B. Chae, and L. Hanzo, "Reconfigurable intelligent surface-based wireless communications: Antenna design, prototyping, and experimental results," *IEEE Access*, vol. 8, pp. 45 913–45 923, 2020.

[13] P. Nayeri, F. Yang, and A. Z. Elsherbeni, *Reflectarray Antennas: Theory, Designs, and Applications*. Chichester, UK: Wiley, Feb 2018.

[14] R. Anwar, L. Mao, and H. Ning, "Frequency selective surfaces: A review," *Applied Sciences*, vol. 8, no. 9, p. 1689, Sep 2018.

[15] Q. Wu, X. Zhou, and R. Schober, "IRS-assisted wireless powered NOMA: Do we really need different phase shifts in DL and UL?" *IEEE Wireless Communications Letters*, vol. 10, pp. 1493–1497, Jul 2021.

[16] Q. Wu and R. Zhang, "Intelligent reflecting surface enhanced wireless network via joint active and passive beamforming," *IEEE Transactions on Wireless Communications*, vol. 18, pp. 5394–5409, Nov 2019.

[17] T. Jiang and W. Yu, "Interference nulling using reconfigurable intelligent surface," *IEEE Journal on Selected Areas in Communications*, vol. 40, pp. 1392–1406, May 2022.

[18] G. Ghatak, V. Malik, S. S. Kalamkar, and A. K. Gupta, "Where to deploy reconfigurable intelligent surfaces in the presence of blockages?" in *2021 IEEE 32nd Annual International Symposium on Personal, Indoor and Mobile Radio Communications (PIMRC)*, Sep 2021, pp. 1419–1424.

[19] S. Zeng, H. Zhang, B. Di, Z. Han, and L. Song, "Reconfigurable intelligent surface (RIS) assisted wireless coverage extension: RIS orientation and location optimization," *IEEE Communications Letters*, vol. 25, pp. 269–273, Jan 2021.

[20] A. Almohamad, A. M. Tahir, A. Al-Kababji, H. M. Furqan, T. Khattab, M. O. Hasna, and H. Arslan, "Smart and secure wireless communications via reflecting intelligent surfaces: A short survey," *IEEE Open Journal of the Communications Society*, vol. 1, pp. 1442–1456, 2020.

[21] J. Ye, S. Guo, S. Dang, B. Shihada, and M.-S. Alouini, "On the capacity of reconfigurable intelligent surface assisted MIMO symbiotic communications," *IEEE Transactions on Wireless Communications*, vol. 21, pp. 1943–1959, Mar 2022.

[22] E. Basar, "Reconfigurable intelligent surfaces for doppler effect and multipath fading mitigation," *Frontiers in Communications and Networks*, vol. 2, May 2021.

[23] E. Arslan, I. Yildirim, F. Kilinc, and E. Basar, "Over-the-air equalization with reconfigurable intelligent surfaces," *IET Communications*, vol. 16, pp. 1486–1497, Aug 2022.

[24] O. Ozdogan, E. Bjornson, and E. G. Larsson, "Using intelligent reflecting surfaces for rank improvement in MIMO communications," in *ICASSP 2020 - 2020 IEEE International Conference on Acoustics, Speech and Signal Processing (ICASSP)*, May 2020, pp. 9160–9164.

[25] Y. Yang, B. Zheng, S. Zhang, and R. Zhang, "Intelligent reflecting surface meets OFDM: Protocol design and rate maximization," *IEEE Transactions on Communications*, vol. 68, pp. 4522–4535, Jul 2020.

[26] G. Chen and Q. Wu, "Fundamental limits of intelligent reflecting surface aided multiuser broadcast channel," *IEEE Transactions on Communications*, vol. 71, pp. 5904–5919, Oct 2023.

[27] R. Liu, Q. Wu, M. D. Renzo, and Y. Yuan, "A path to smart radio environments: An industrial viewpoint on reconfigurable intelligent surfaces," *IEEE Wireless Communications*, vol. 29, pp. 202–208, Feb 2022.

[28] R. Alliance, "Reconfigurable intelligent surface technology white paper," 2023.

[29] ITU-R, "Future technology trends of terrestrial international mobile telecommunications systems towards 2030 and beyond," International Telecommunication Union, Report ITU-R M.2516-0, 2022.

[30] Y. Zhao, B. Clerckx, and Z. Feng, "IRS-aided SWIPT: Joint waveform, active and passive beamforming design under nonlinear harvester model," *IEEE Transactions on Communications*, vol. 70, pp. 1345–1359, 2022.

[31] Y. Zhao and B. Clerckx, *RIS in Wireless Information and Power Transfer*. Hoboken, NJ, USA: Wiley, 2023, pp. 271–295.

[32] ——, "RIScatter: Unifying backscatter communication and reconfigurable intelligent surface," *IEEE Journal on Selected Areas in Communications*, pp. 1–1, Dec 2024.

[33] Y. Zhao, H. Li, M. Franceschetti, and B. Clerckx, "Channel shaping using reconfigurable intelligent surfaces: From diagonal model to beyond," *To be submitted to IEEE Transactions on Wireless Communications*.

[34] V. G. Veselago, "The electrodynamics of substances with negative ϵ and μ," *Soviet Physics Uspekhi*, vol. 10, pp. 509–514, Apr 1968.

[35] J. Pendry, A. Holden, D. Robbins, and W. Stewart, "Magnetism from conductors and enhanced nonlinear phenomena," *IEEE Transactions on Microwave Theory and Techniques*, vol. 47, pp. 2075–2084, 1999.

[36] N. Yu, P. Genevet, M. A. Kats, F. Aieta, J.-P. Tetienne, F. Capasso, and Z. Gaburro, "Light propagation with phase discontinuities: Generalized laws of reflection and refraction," *Science*, vol. 334, pp. 333–337, Oct 2011.

[37] J. Pendry, "Negative refraction," *Contemporary Physics*, vol. 45, pp. 191–202, May 2004.

[38] T. J. Cui, M. Q. Qi, X. Wan, J. Zhao, and Q. Cheng, "Coding metamaterials, digital metamaterials and programmable metamaterials," *Light: Science & Applications*, vol. 3, no. 10, pp. e218–e218, Oct 2014.

[39] Q. Ma, G. D. Bai, H. B. Jing, C. Yang, L. Li, and T. J. Cui, "Smart metasurface with self-adaptively reprogrammable functions," *Light: Science & Applications*, vol. 8, p. 98, Oct 2019.

[40] W. J. Padilla, D. N. Basov, and D. R. Smith, "Negative refractive index metamaterials," *Materials Today*, vol. 9, pp. 28–35, Jul 2006.

[41] M. Poulakis, "6G's metamaterials solution: There's plenty of bandwidth available if we use reconfigurable intelligent surfaces," *IEEE Spectrum*, vol. 59, pp. 40–45, Nov 2022.

[42] Y. C. Liang, Q. Zhang, J. Wang, R. Long, H. Zhou, and G. Yang, "Backscatter communication assisted by reconfigurable intelligent surfaces," *Proceedings of the IEEE*, 2022.

[43] R. Hansen, "Relationships between antennas as scatterers and as radiators," *Proceedings of the IEEE*, vol. 77, pp. 659–662, May 1989.

[44] S. J. Thomas and M. S. Reynolds, "A 96 Mbit/sec, 15.5 pJ/bit 16-QAM modulator for UHF backscatter communication," in *2012 IEEE International Conference on RFID (RFID)*, Apr 2012, pp. 185–190.

[45] Y.-C. Liang, Q. Zhang, E. G. Larsson, and G. Y. Li, "Symbiotic radio: Cognitive backscattering communications for future wireless networks," *IEEE Transactions on Cognitive Communications and Networking*, vol. 6, pp. 1242–1255, Dec 2020.

[46] C. Boyer and S. Roy, "Backscatter communication and RFID: Coding, energy, and MIMO analysis," *IEEE Transactions on Communications*, vol. 62, pp. 770–785, Mar 2014.

[47] O. Ozdogan, E. Bjornson, and E. G. Larsson, "Intelligent reflecting surfaces: Physics, propagation, and pathloss modeling," *IEEE Wireless Communications Letters*, vol. 9, no. 5, pp. 581–585, May 2020.

[48] M. Najafi, V. Jamali, R. Schober, and H. V. Poor, "Physics-based modeling and scalable optimization of large intelligent reflecting surfaces," *IEEE Transactions on Communications*, vol. 69, pp. 2673–2691, Apr 2021.

[49] S. Abeywickrama, R. Zhang, Q. Wu, and C. Yuen, "Intelligent reflecting surface: Practical phase shift model and beamforming optimization," *IEEE Transactions on Communications*, vol. 68, pp. 5849–5863, Sep 2020.

[50] Q. Wu and R. Zhang, "Intelligent reflecting surface enhanced wireless network: Joint active and passive beamforming design," in *2018 IEEE Global Communications Conference (GLOBECOM)*, vol. 18, Dec 2018, pp. 1–6.

[51] M. T. Ivrlac and J. A. Nossek, "Toward a circuit theory of communication," *IEEE Transactions on Circuits and Systems I: Regular Papers*, vol. 57, pp. 1663–1683, Jul 2010.

[52] M. Nerini, S. Shen, H. Li, and B. Clerckx, "Beyond diagonal reconfigurable intelligent surfaces utilizing graph theory: Modeling, architecture design, and optimization," *IEEE Transactions on Wireless Communications*, pp. 1–1, May 2024.

[53] X. Mu, Y. Liu, L. Guo, J. Lin, and R. Schober, "Simultaneously transmitting and reflecting (STAR) RIS aided wireless communications," *IEEE Transactions on Wireless Communications*, vol. 21, pp. 3083–3098, May 2022.

[54] Y. Liu, X. Mu, J. Xu, R. Schober, Y. Hao, H. V. Poor, and L. Hanzo, "STAR: Simultaneous transmission and reflection for 360° coverage by intelligent surfaces," *IEEE Wireless Communications*, vol. 28, pp. 102–109, Dec 2021.

[55] H. Li, S. Shen, and B. Clerckx, "Beyond diagonal reconfigurable intelligent surfaces: A multi-sector mode enabling highly directional full-space wireless coverage," *IEEE Journal on Selected Areas in Communications*, vol. 41, pp. 2446–2460, Aug 2023.

[56] J. Koomey, S. Berard, M. Sanchez, and H. Wong, "Implications of historical trends in the electrical efficiency of computing," *IEEE Annals of the History of Computing*, vol. 33, pp. 46–54, Mar 2011.

[57] J. Huang, Y. Zhou, Z. Ning, and H. Gharavi, "Wireless power transfer and energy harvesting: Current status and future prospects," *IEEE Wireless Communications*, vol. 26, pp. 163–169, Aug 2019.

[58] X. Hao, H. Zhang, Z. Shen, Z. Liu, L. Zhang, H. Jiang, J. Liu, and H. Liao, "A 43.2 μW 2.4 GHz 64-QAM pseudo-backscatter modulator based on integrated directional coupler," in *2018 IEEE International Symposium on Circuits and Systems (ISCAS)*, May 2018, pp. 1–5.

[59] R. Correia and N. B. Carvalho, "Ultrafast backscatter modulator with low-power consumption and wireless power transmission capabilities," *IEEE Microwave and Wireless Components Letters*, vol. 27, pp. 1152–1154, Dec 2017.

[60] J. Zhou, P. Zhang, J. Han, L. Li, and Y. Huang, "Metamaterials and metasurfaces for wireless power transfer and energy harvesting," *Proceedings of the IEEE*, vol. 110, pp. 31–55, Jan 2022.

[61] J. Joung, C. K. Ho, K. Adachi, and S. Sun, "A survey on power-amplifier-centric techniques for spectrum- and energy-efficient wireless communications," *IEEE Communications Surveys & Tutorials*, vol. 17, pp. 315–333, Jan 2015.

[62] A. Alizadeh, S. Hassanzadehyamchi, A. Medi, and S. Kiaei, "An X-band class-J power amplifier with active load modulation to boost drain efficiency," *IEEE Transactions on Circuits and Systems I: Regular Papers*, vol. 67, pp. 3364–3377, Oct 2020.

[63] N. M. L. Tan, T. Abe, and H. Akagi, "Design and performance of a bidirectional isolated DC-DC converter for a battery energy storage system," *IEEE Transactions on Power Electronics*, vol. 27, pp. 1237–1248, Mar 2012.

[64] B. Clerckx and E. Bayguzina, "Waveform design for wireless power transfer," *IEEE Transactions on Signal Processing*, vol. 64, no. 23, pp. 6313–6328, Dec 2016.

[65] C. R. Valenta and G. D. Durgin, "Harvesting wireless power: Survey of energy-harvester conversion efficiency in far-field, wireless power transfer systems," *IEEE Microwave Magazine*, vol. 15, pp. 108–120, Jun 2014.

[66] S. A. Rotenberg, S. K. Podilchak, P. D. H. Re, C. Mateo-Segura, G. Goussetis, and J. Lee, "Efficient rectifier for wireless power transmission systems," *IEEE Transactions on Microwave Theory and Techniques*, vol. 68, pp. 1921–1932, May 2020.

[67] E. Boshkovska, D. W. K. Ng, N. Zlatanov, and R. Schober, "Practical non-linear energy harvesting model and resource allocation for swipt systems," *IEEE Communications Letters*, vol. 19, pp. 2082–2085, Dec 2015.

[68] Y. Zeng, B. Clerckx, and R. Zhang, "Communications and signals design for wireless power transmission," *IEEE Transactions on Communications*, vol. 65, pp. 2264–2290, May 2017.

[69] M. D. Prete, A. Costanzo, M. Magno, D. Masotti, and L. Benini, "Optimum excitations for a dual-band microwatt wake-up radio," *IEEE Transactions on Microwave Theory and Techniques*, vol. 64, pp. 4731–4739, Dec 2016.

[70] Y. Huang and B. Clerckx, "Large-scale multiantenna multisine wireless power transfer," *IEEE Transactions on Signal Processing*, vol. 65, pp. 5812–5827, Nov 2017.

[71] S. Shen and B. Clerckx, "Beamforming optimization for MIMO wireless power transfer with nonlinear energy harvesting: RF combining versus DC combining," *IEEE Transactions on Wireless Communications*, vol. 20, pp. 199–213, Jan 2021.

[72] L. R. Varshney, "Transporting information and energy simultaneously," in *2008 IEEE International Symposium on Information Theory*, Jul 2008, pp. 1612–1616.

[73] B. Clerckx, "Wireless information and power transfer: Nonlinearity, waveform design, and rate-energy tradeoff," *IEEE Transactions on Signal Processing*, vol. 66, no. 4, pp. 847–862, Feb 2018.

[74] B. Clerckx, R. Zhang, R. Schober, D. W. K. Ng, D. I. Kim, and H. V. Poor, "Fundamentals of wireless information and power transfer: From RF energy harvester models to signal and system designs," *IEEE Journal on Selected Areas in Communications*, vol. 37, no. 1, pp. 4–33, Jan 2019.

[75] T. M. Cover and J. A. Thomas, *Elements of Information Theory*. Hoboken, NJ, USA: Wiley, Sep 2005.

[76] M. Trotter, J. Griffin, and G. Durgin, "Power-optimized waveforms for improving the range and reliability of RFID systems," in *2009 IEEE International Conference on RFID*, Apr 2009, pp. 80–87.

[77] Q. Wu, X. Guan, and R. Zhang, "Intelligent reflecting surface-aided wireless energy and information transmission: An overview," *Proceedings of the IEEE*, vol. 110, pp. 150–170, Jan 2022.

[78] X. Lu, P. Wang, D. Niyato, D. I. Kim, and Z. Han, "Wireless networks with RF energy harvesting: A contemporary survey," *IEEE Communications Surveys & Tutorials*, vol. 17, pp. 757–789, 2015.

[79] B. Clerckx, J. Kim, K. W. Choi, and D. I. Kim, "Foundations of wireless information and power transfer: Theory, prototypes, and experiments," *Proceedings of the IEEE*, vol. 110, pp. 8–30, Jan 2022.

[80] J. Kim and B. Clerckx, "Wireless information and power transfer for IoT: Pulse position modulation, integrated receiver, and experimental validation," *IEEE Internet of Things Journal*, vol. 9, pp. 12 378–12 394, Jul 2022.

[81] H. Stockman, "Communication by means of reflected power," *Proceedings of the IRE*, vol. 36, pp. 1196–1204, Oct 1948.

[82] J. Landt, "The history of RFID," *IEEE Potentials*, vol. 24, pp. 8–11, Oct 2005.

[83] Q. H. Abbasi, H. T. Abbas, A. Alomainy, and M. A. Imran, Eds., *Backscattering and RF Sensing for Future Wireless Communication*. Hoboken, NJ, USA: Wiley, Jun 2021.

[84] G. Yang, C. K. Ho, and Y. L. Guan, "Multi-antenna wireless energy transfer for backscatter communication systems," *IEEE Journal on Selected Areas in Communications*, vol. 33, pp. 2974–2987, Dec 2015.

[85] C. Chen, G. Wang, H. Guan, Y.-C. Liang, and C. Tellambura, "Transceiver design and signal detection in backscatter communication systems with multiple-antenna tags," *IEEE Transactions on Wireless Communications*, vol. 19, pp. 3273–3288, May 2020.

[86] E. Goudeli, C. Psomas, and I. Krikidis, "Spatial-modulation-based techniques for backscatter communication systems," *IEEE Internet of Things Journal*, vol. 7, pp. 10 623–10 634, Oct 2020.

[87] W. Liu, S. Shen, D. H. K. Tsang, and R. Murch, "Enhancing ambient backscatter communication utilizing coherent and non-coherent space-time codes," *IEEE Transactions on Wireless Communications*, vol. 20, pp. 6884–6897, Oct 2021.

[88] C. He, S. Chen, H. Luan, X. Chen, and Z. J. Wang, "Monostatic MIMO backscatter communications," *IEEE Journal on Selected Areas in Communications*, vol. 38, pp. 1896–1909, Aug 2020.

[89] X. Wang, H. Yigitler, R. Duan, E. Y. Menta, and R. Jantti, "Coherent multi-antenna receiver for BPSK-modulated ambient backscatter tags," *IEEE Internet of Things Journal*, vol. 4662, pp. 1–1, 2021.

[90] J. K. Devineni and H. S. Dhillon, "Non-coherent detection and bit error rate for an ambient backscatter link in time-selective fading," *IEEE Transactions on Communications*, vol. 69, pp. 602–618, Jan 2021.

[91] S. J. Thomas, E. Wheeler, J. Teizer, and M. S. Reynolds, "Quadrature amplitude modulated backscatter in passive and semipassive UHF RFID systems," *IEEE Transactions on Microwave Theory and Techniques*, vol. 60, pp. 1175–1182, Apr 2012.

[92] P. Zhang, D. Bharadia, K. Joshi, and S. Katti, "HitchHike: Practical backscatter using commodity wi-fi," in *Proceedings of the 14th ACM Conference on Embedded Network Sensor Systems CD-ROM*, Nov 2016, pp. 259–271.

[93] V. Iyer, V. Talla, B. Kellogg, S. Gollakota, and J. Smith, "Inter-technology backscatter: Towards internet connectivity for implanted devices vikram," in *Proceedings of the 2016 ACM SIGCOMM Conference*, Aug 2016, pp. 356–369.

[94] B. Kellogg, V. Talla, J. R. Smith, and S. Gollakot, "Passive Wi-Fi: Bringing low power to Wi-Fi transmissions," *GetMobile: Mobile Computing and Communications*, vol. 20, pp. 38–41, Jan 2017.

[95] J. F. Ensworth and M. S. Reynolds, "BLE-backscatter: Ultralow-power IoT nodes compatible with Bluetooth 4.0 low energy (BLE) smartphones and tablets," *IEEE Transactions on Microwave Theory and Techniques*, vol. 65, pp. 3360–3368, Sep 2017.

[96] V. Talla, M. Hessar, B. Kellogg, A. Najafi, J. R. Smith, and S. Gollakota, "LoRa backscatter: Enabling the vision of ubiquitous connectivity," *Proceedings of the ACM on Interactive, Mobile, Wearable and Ubiquitous Technologies*, vol. 1, pp. 1–24, Sep 2017.

[97] D. T. Hoang, D. Niyato, D. I. Kim, N. V. Huynh, and S. Gong, Eds., *Ambient Backscatter Communication Networks*.   Cambridge, UK: Cambridge University Press, 2020.

[98] V. Liu, A. Parks, V. Talla, S. Gollakota, D. Wetherall, and J. R. Smith, "Ambient backscatter: Wireless communication out of thin air," *ACM SIGCOMM Computer Communication Review*, vol. 43, pp. 39–50, Sep 2013.

[99] H. Guo, Y.-C. Liang, R. Long, and Q. Zhang, "Cooperative ambient backscatter system: A symbiotic radio paradigm for passive IoT," *IEEE Wireless Communications Letters*, vol. 8, pp. 1191–1194, Aug 2019.

[100] X. Zhou, R. Zhang, and C. K. Ho, "Wireless information and power transfer: Architecture design and rate-energy tradeoff," *IEEE Transactions on Communications*, vol. 61, no. 11, pp. 4754–4767, Nov 2013.

[101] R. Zhang and C. K. Ho, "MIMO broadcasting for simultaneous wireless information and power transfer," *IEEE Transactions on Wireless Communications*, vol. 12, no. 5, pp. 1989–2001, May 2013.

[102] J. Park and B. Clerckx, "Joint wireless information and energy transfer in a K-user MIMO interference channel," *IEEE Transactions on Wireless Communications*, vol. 13, no. 10, pp. 5781–5796, Oct 2014.

[103] B. Clerckx and J. Kim, "On the beneficial roles of fading and transmit diversity in wireless power transfer with nonlinear energy harvesting," *IEEE Transactions on Wireless Communications*, vol. 17, no. 11, pp. 7731–7743, Nov 2018.

[104] J. Kim, B. Clerckx, and P. D. Mitcheson, "Experimental analysis of harvested energy and throughput trade-off in a realistic SWIPT system," in *2019 IEEE Wireless Power Transfer Conference (WPTC)*, Jun 2019, pp. 1–5.

[105] ——, "Signal and system design for wireless power transfer: Prototype, experiment and validation," *IEEE Transactions on Wireless Communications*, vol. 19, no. 11, pp. 7453–7469, Nov 2020.

[106] J. Kim and B. Clerckx, "Range expansion for wireless power transfer using joint beam-forming and waveform architecture: An experimental study in indoor environment," *IEEE Wireless Communications Letters*, vol. 10, no. 6, pp. 1237–1241, Jun 2021.

[107] B. Clerckx and E. Bayguzina, "Low-complexity adaptive multisine waveform design for wireless power transfer," *IEEE Antennas and Wireless Propagation Letters*, vol. 16, no. 1, pp. 2207–2210, 2017.

[108] J. Kim, B. Clerckx, and P. D. Mitcheson, "Prototyping and experimentation of a closed-loop wireless power transmission with channel acquisition and waveform optimization," in *2017 IEEE Wireless Power Transfer Conference (WPTC)*, May 2017, pp. 1–4.

[109] M. Varasteh, B. Rassouli, and B. Clerckx, "On capacity-achieving distributions for complex AWGN channels under nonlinear power constraints and their applications to SWIPT," *IEEE Transactions on Information Theory*, vol. 66, no. 10, pp. 6488–6508, Oct 2020.

[110] ——, "SWIPT signaling over frequency-selective channels with a nonlinear energy harvester: Non-zero mean and asymmetric inputs," *IEEE Transactions on Communications*, vol. 67, no. 10, pp. 7195–7210, Oct 2019.

[111] M. Varasteh, J. Hoydis, and B. Clerckx, "Learning to communicate and energize: Modulation, coding, and multiple access designs for wireless information-power transmission," *IEEE Transactions on Communications*, vol. 68, no. 11, pp. 6822–6839, Nov 2020.

[112] C. Liaskos, S. Nie, A. Tsioliaridou, A. Pitsillides, S. Ioannidis, and I. Akyildiz, "Real-izing wireless communication through software-defined hypersurface environments," in *2018 IEEE 19th International Symposium on "A World of Wireless, Mobile and Multimedia Networks" (WoWMoM)*, Jun 2018, pp. 14–15.

[113] Q. Wu and R. Zhang, "Beamforming optimization for intelligent reflecting surface with discrete phase shifts," in *ICASSP 2019 - 2019 IEEE International Conference on Acoustics, Speech and Signal Processing (ICASSP)*, May 2019, pp. 7830–7833.

[114] Q.-U.-A. Nadeem, A. Kammoun, A. Chaaban, M. Debbah, and M.-S. Alouini, "Intelligent reflecting surface assisted wireless communication: Modeling and channel estimation," *arXiv:1906.02360*, pp. 1–7, Jun 2019.

[115] C. You, B. Zheng, and R. Zhang, "Intelligent reflecting surface with discrete phase shifts: Channel estimation and passive beamforming," in *ICC 2020 - 2020 IEEE International Conference on Communications (ICC)*, Jun 2020, pp. 1–6.

[116] J.-M. Kang, "Intelligent reflecting surface: Joint optimal training sequence and refection pattern," *IEEE Communications Letters*, vol. 24, no. 8, pp. 1784–1788, Aug 2020.

[117] P. Wang, J. Fang, H. Duan, and H. Li, "Compressed channel estimation for intelligent reflecting surface-assisted millimeter wave systems," *IEEE Signal Processing Letters*, vol. 27, pp. 905–909, 2020.

[118] Q. Wu and R. Zhang, "Weighted sum power maximization for intelligent reflecting surface aided SWIPT," *IEEE Wireless Communications Letters*, vol. 9, no. 5, pp. 586–590, May 2020.

[119] Y. Tang, G. Ma, H. Xie, J. Xu, and X. Han, "Joint transmit and reflective beamforming design for IRS-assisted multiuser MISO SWIPT systems," in *ICC 2020 - 2020 IEEE International Conference on Communications (ICC)*, Jun 2020, pp. 1–6.

[120] Q. Wu and R. Zhang, "Joint active and passive beamforming optimization for intelligent reflecting surface assisted SWIPT under QoS constraints," *IEEE Journal on Selected Areas in Communications*, vol. 38, no. 8, pp. 1735–1748, Aug 2020.

[121] D. Xu, X. Yu, V. Jamali, D. W. K. Ng, and R. Schober, "Resource allocation for large IRS-assisted SWIPT systems with non-linear energy harvesting model," in *2021 IEEE Wireless Communications and Networking Conference (WCNC)*, Mar 2021, pp. 1–7.

[122] T. Adali and S. Haykin, Eds., *Adaptive Signal Processing: Next Generation Solutions*. Hoboken, NJ, USA: Wiley, Mar 2010.

[123] G. H. Golub and C. F. V. Loan, *Matrix Computations*. Baltimore, MD, USA: Johns Hopkins University Press, 2013.

[124] Z. Luo, W. Ma, A. So, Y. Ye, and S. Zhang, "Semidefinite relaxation of quadratic optimization problems," *IEEE Signal Processing Magazine*, vol. 27, no. 3, pp. 20–34, May 2010.

[125] M. Grant, S. Boyd, and Y. Ye, "CVX: MATLAB software for disciplined convex programming," 2016.

[126] S. Boyd, S.-J. Kim, L. Vandenberghe, and A. Hassibi, "A tutorial on geometric programming," *Optimization and Engineering*, vol. 8, no. 1, pp. 67–127, May 2007.

[127] M. Chiang, *Geometric Programming for Communication Systems*. Boston, MA, USA: Now, 2005.

[128] D. Tse and P. Viswanath, *Fundamentals of Wireless Communication*. Cambridge, UK: Cambridge University Press, May 2005.

[129] B. Clerckx and C. Oestges, *MIMO Wireless Networks: Channels, Techniques and Standards for Multi-Antenna, Multi-User and Multi-Cell Systems*. Waltham, MA, USA: Academic Press, 2013.

[130] L. Grippo and M. Sciandrone, "On the convergence of the block nonlinear gauss-seidel method under convex constraints," *Operations Research Letters*, vol. 26, no. 3, pp. 127–136, Apr 2000.

[131] V. Erceg, "IEEE P802.11 wireless LANs TGn channel models," *IEEE 802.11-03/940r4*, 2004.

[132] S. Li, K. Yang, M. Zhou, J. Wu, L. Song, Y. Li, and H. Li, "Full-duplex amplify-and-forward relaying: Power and location optimization," *IEEE Transactions on Vehicular Technology*, vol. 66, no. 9, pp. 8458–8468, Sep 2017.

[133] W. Tang, M. Z. Chen, X. Chen, J. Y. Dai, Y. Han, M. Di Renzo, Y. Zeng, S. Jin, Q. Cheng, and T. J. Cui, "Wireless communications with reconfigurable intelligent surface: Path loss modeling and experimental measurement," *IEEE Transactions on Wireless Communications*, vol. 20, no. 1, pp. 421–439, Jan 2021.

[134] Q. Wu and R. Zhang, "Beamforming optimization for wireless network aided by intelligent reflecting surface with discrete phase shifts," *IEEE Transactions on Communications*, vol. 68, no. 3, pp. 1838–1851, Mar 2020.

[135] D. Dobkin, *The RF in RFID: Passive UHF RFID in Practice*. London, UK: Newnes, Nov 2012.

[136] G. Vannucci, A. Bletsas, and D. Leigh, "A software-defined radio system for backscatter sensor networks," *IEEE Transactions on Wireless Communications*, vol. 7, pp. 2170–2179, Jun 2008.

[137] S. D. Assimonis, S. N. Daskalakis, and A. Bletsas, "Sensitive and efficient RF harvesting supply for batteryless backscatter sensor networks," *IEEE Transactions on Microwave Theory and Techniques*, vol. 64, pp. 1327–1338, Apr 2016.

[138] G. Yang, Q. Zhang, and Y.-C. Liang, "Cooperative ambient backscatter communications for green internet-of-things," *IEEE Internet of Things Journal*, vol. 5, pp. 1116–1130, Apr 2018.

[139] Q. Wu, S. Zhang, B. Zheng, C. You, and R. Zhang, "Intelligent reflecting surface-aided wireless communications: A tutorial," *IEEE Transactions on Communications*, vol. 69, pp. 3313–3351, May 2021.

[140] H. Ding, D. B. da Costa, and J. Ge, "Outage analysis for cooperative ambient backscatter systems," *IEEE Wireless Communications Letters*, vol. 9, pp. 601–605, May 2020.

[141] J. Qian, Y. Zhu, C. He, F. Gao, and S. Jin, "Achievable rate and capacity analysis for ambient backscatter communications," *IEEE Transactions on Communications*, vol. 67, pp. 6299–6310, Sep 2019.

[142] H. E. Hassani, A. Savard, E. V. Belmega, and R. C. de Lamare, "Multi-user downlink NOMA systems aided by ambient backscattering: Achievable rate regions and energy-efficiency maximization," *IEEE Transactions on Green Communications and Networking*, pp. 1–1, 2023.

[143] R. Torres, R. Correia, N. Carvalho, S. N. Daskalakis, G. Goussetis, Y. Ding, A. Georgiadis, A. Eid, J. Hester, and M. M. Tentzeris, "Backscatter communications," *IEEE Journal of Microwaves*, vol. 1, pp. 864–878, Oct 2021.

[144] R. Long, Y.-C. Liang, H. Guo, G. Yang, and R. Zhang, "Symbiotic radio: A new communication paradigm for passive internet of things," *IEEE Internet of Things Journal*, vol. 7, pp. 1350–1363, Feb 2020.

[145] S. Zhou, W. Xu, K. Wang, C. Pan, M.-S. Alouini, and A. Nallanathan, "Ergodic rate analysis of cooperative ambient backscatter communication," *IEEE Wireless Communications Letters*, vol. 8, pp. 1679–1682, Dec 2019.

[146] T. Wu, M. Jiang, Q. Zhang, Q. Li, and J. Qin, "Beamforming design in multiple-input-multiple-output symbiotic radio backscatter systems," *IEEE Communications Letters*, vol. 25, pp. 1949–1953, Jun 2021.

[147] J. Xu, Z. Dai, and Y. Zeng, "Enabling full mutualism for symbiotic radio with massive backscatter devices," in *2021 IEEE Global Communications Conference (GLOBECOM)*, Dec 2021, pp. 1–6.

[148] Z. Yang and Y. Zhang, "Optimal SWIPT in RIS-aided MIMO networks," *IEEE Access*, vol. 9, pp. 112 552–112 560, 2021.

[149] S. Han, Y.-C. Liang, and G. Sun, "The design and optimization of random code assisted multi-BD symbiotic radio system," *IEEE Transactions on Wireless Communications*, vol. 20, pp. 5159–5170, Aug 2021.

[150] Q. Zhang, Y.-C. Liang, H.-C. Yang, and H. V. Poor, "Mutualistic mechanism in symbiotic radios: When can the primary and secondary transmissions be mutually beneficial?" *IEEE Transactions on Wireless Communications*, vol. 1276, pp. 1–1, 2022.

[151] Z. Dai, R. Li, J. Xu, Y. Zeng, and S. Jin, "Rate-region characterization and channel estimation for cell-free symbiotic radio communications," *IEEE Transactions on Communications*, vol. 71, pp. 674–687, Feb 2023.

[152] S. Zhang and R. Zhang, "Capacity characterization for intelligent reflecting surface aided MIMO communication," *IEEE Journal on Selected Areas in Communications*, vol. 38, pp. 1823–1838, Aug 2020.

[153] S. Lin, B. Zheng, F. Chen, and R. Zhang, "Intelligent reflecting surface-aided spectrum sensing for cognitive radio," *IEEE Wireless Communications Letters*, vol. 11, pp. 928–932, May 2022.

[154] Y. Liu, Y. Zhang, X. Zhao, S. Geng, P. Qin, and Z. Zhou, "Dynamic-controlled RIS assisted multi-user MISO downlink system: Joint beamforming design," *IEEE Transactions on Green Communications and Networking*, vol. 6, pp. 1069–1081, Jun 2022.

[155] Z. Feng, B. Clerckx, and Y. Zhao, "Waveform and beamforming design for intelligent reflecting surface aided wireless power transfer: Single-user and multi-user solutions," *IEEE Transactions on Wireless Communications*, 2022.

[156] Y. Yang, S. Zhang, and R. Zhang, "IRS-enhanced OFDMA: Joint resource allocation and passive beamforming optimization," *IEEE Wireless Communications Letters*, vol. 9, pp. 760–764, Jun 2020.

[157] Q. Wu, X. Zhou, W. Chen, J. Li, and X. Zhang, "IRS-aided WPCNs: A new optimization framework for dynamic IRS beamforming," *IEEE Transactions on Wireless Communications*, pp. 1–1, Dec 2021.

[158] M. Hua and Q. Wu, "Joint dynamic passive beamforming and resource allocation for IRS-aided full-duplex WPCN," *IEEE Transactions on Wireless Communications*, pp. 1–1, Dec 2021.

[159] W. Tang, J. Y. Dai, M. Chen, X. Li, Q. Cheng, S. Jin, K.-K. Wong, and T. J. Cui, "Programmable metasurface-based RF chain-free 8PSK wireless transmitter," *Electronics Letters*, vol. 55, pp. 417–420, Apr 2019.

[160] J. Y. Dai, W. Tang, L. X. Yang, X. Li, M. Z. Chen, J. C. Ke, Q. Cheng, S. Jin, and T. J. Cui, "Realization of multi-modulation schemes for wireless communication by time-domain digital coding metasurface," *IEEE Transactions on Antennas and Propagation*, vol. 68, pp. 1618–1627, Mar 2020.

[161] R. Karasik, O. Simeone, M. D. Renzo, and S. S. Shitz, "Beyond max-SNR: Joint encoding for reconfigurable intelligent surfaces," in *2020 IEEE International Symposium on Information Theory (ISIT)*, Jun 2020, pp. 2965–2970.

[162] R. Liu, H. Li, M. Li, and Q. Liu, "Symbol-level precoding design for intelligent reflecting surface assisted multi-user MIMO systems," in *2019 11th International Conference on Wireless Communications and Signal Processing (WCSP)*, Oct 2019, pp. 1–6.

[163] A. Bereyhi, V. Jamali, R. R. Muller, A. M. Tulino, G. Fischer, and R. Schober, "A single-RF architecture for multiuser massive MIMO via reflecting surfaces," in *ICASSP 2020 - 2020 IEEE International Conference on Acoustics, Speech and Signal Processing (ICASSP)*, May 2020, pp. 8688–8692.

[164] X. Xu, Y.-C. Liang, G. Yang, and L. Zhao, "Reconfigurable intelligent surface empowered symbiotic radio over broadcasting signals," in *GLOBECOM 2020 - 2020 IEEE Global Communications Conference*, Dec 2020, pp. 1–6.

[165] Q. Zhang, Y.-C. Liang, and H. V. Poor, "Reconfigurable intelligent surface assisted MIMO symbiotic radio networks," *IEEE Transactions on Communications*, vol. 69, pp. 4832–4846, Jul 2021.

[166] J. Hu, Y. C. Liang, and Y. Pei, "Reconfigurable intelligent surface enhanced multi-user MISO symbiotic radio system," *IEEE Transactions on Communications*, vol. 69, pp. 2359–2371, Apr 2021.

[167] M. Hua, Q. Wu, L. Yang, R. Schober, and H. V. Poor, "A novel wireless communication paradigm for intelligent reflecting surface based symbiotic radio systems," *IEEE Transactions on Signal Processing*, vol. 70, pp. 550–565, Apr 2022.

[168] E. Basar, "Reconfigurable intelligent surface-based index modulation: A new beyond MIMO paradigm for 6G," *IEEE Transactions on Communications*, vol. 68, pp. 3187–3196, May 2020.

[169] T. Ma, Y. Xiao, X. Lei, P. Yang, X. Lei, and O. A. Dobre, "Large intelligent surface assisted wireless communications with spatial modulation and antenna selection," *IEEE Journal on Selected Areas in Communications*, vol. 38, pp. 2562–2574, Nov 2020.

[170] J. Yuan, M. Wen, Q. Li, E. Basar, G. C. Alexandropoulos, and G. Chen, "Receive quadrature reflecting modulation for RIS-empowered wireless communications," *IEEE Transactions on Vehicular Technology*, vol. 70, pp. 5121–5125, May 2021.

[171] S. Hu, C. Liu, Z. Wei, Y. Cai, D. W. K. Ng, and J. Yuan, "Beamforming design for intelligent reflecting surface-enhanced symbiotic radio systems," in *ICC 2022 - IEEE International Conference on Communications*, May 2022, pp. 2651–2657.

[172] I. Vardakis, G. Kotridis, S. Peppas, K. Skyvalakis, G. Vougioukas, and A. Bletsas, "Intelligently wireless batteryless RF-powered reconfigurable surface: Theory, implementation & limitations," *IEEE Transactions on Wireless Communications*, vol. 22, pp. 3942–3954, Jun 2023.

[173] X. He, W. Jiang, M. Cheng, X. Zhou, P. Yang, and B. Kurkoski, "GuardRider: Reliable Wi-Fi backscatter using reed-solomon codes with QoS guarantee," in *2020 IEEE/ACM 28th International Symposium on Quality of Service (IWQoS)*, Jun 2020, pp. 1–10.

[174] D. Bharadia, K. R. Joshi, M. Kotaru, and S. Katti, "BackFi: High throughput Wi-Fi backscatter," in *Proceedings of the 2015 ACM Conference on Special Interest Group on Data Communication*, vol. 45, Aug 2015, pp. 283–296.

[175] H. Guo, Q. Zhang, S. Xiao, and Y.-C. Liang, "Exploiting multiple antennas for cognitive ambient backscatter communication," *IEEE Internet of Things Journal*, vol. 6, pp. 765–775, Feb 2019.

[176] M. Jin, Y. He, C. Jiang, and Y. Liu, "Parallel backscatter: Channel estimation and beyond," *IEEE/ACM Transactions on Networking*, vol. 29, pp. 1128–1140, Jun 2021.

[177] B. Zheng and R. Zhang, "Intelligent reflecting surface-enhanced OFDM: Channel estimation and reflection optimization," *IEEE Wireless Communications Letters*, vol. 9, pp. 518–522, Apr 2020.

[178] J. Qian, A. N. Parks, J. R. Smith, F. Gao, and S. Jin, "IoT communications with M-PSK modulated ambient backscatter: Algorithm, analysis, and implementation," *IEEE Internet of Things Journal*, vol. 6, pp. 844–855, Feb 2019.

[179] W. Wu, X. Wang, A. Hawbani, L. Yuan, and W. Gong, "A survey on ambient backscatter communications: Principles, systems, applications, and challenges," *Computer Networks*, vol. 216, Oct 2022.

[180] T. Nguyen, Y.-J. Chu, and T. Nguyen, "On the capacities of discrete memoryless thresholding channels," in *2018 IEEE 87th Vehicular Technology Conference (VTC Spring)*, Jun 2018, pp. 1–5.

[181] T. Nguyen and T. Nguyen, "Optimal quantizer structure for maximizing mutual information under constraints," *IEEE Transactions on Communications*, vol. 69, pp. 7406–7413, Nov 2021.

[182] M. Rezaeian and A. Grant, "Computation of total capacity for discrete memoryless multiple-access channels," *IEEE Transactions on Information Theory*, vol. 50, pp. 2779–2784, Nov 2004.

[183] G. J. O. Jameson, "The incomplete gamma functions," *The Mathematical Gazette*, vol. 100, pp. 298–306, Jul 2016.

[184] S. Boyd and L. Vandenberghe, *Convex Optimization*. Cambridge, UK: Cambridge University Press, Mar 2004.

[185] X. He, K. Cai, W. Song, and Z. Mei, "Dynamic programming for sequential deterministic quantization of discrete memoryless channels," *IEEE Transactions on Communications*, vol. 69, pp. 3638–3651, Jun 2021.

[186] T. Nguyen and T. Nguyen, "On thresholding quantizer design for mutual information maximization: Optimal structures and algorithms," in *2020 IEEE 91st Vehicular Technology Conference (VTC2020-Spring)*, May 2020, pp. 1–5.

[187] B. W. Bader and T. G. Kolda, "Tensor toolbox for MATLAB," Sep 2022.

[188] E. Calvo, D. P. Palomar, J. R. Fonollosa, and J. Vidal, "On the computation of the capacity region of the discrete MAC," *IEEE Transactions on Communications*, vol. 58, pp. 3512–3525, Dec 2010.

[189] W. Liu, S. Shen, D. H. K. Tsang, R. K. Mallik, and R. Murch, "An efficient ratio detector for ambient backscatter communication," *IEEE Transactions on Wireless Communications*, pp. 1–1, Oct 2024.

[190] E. Basar, M. D. Renzo, J. D. Rosny, M. Debbah, M.-S. Alouini, and R. Zhang, "Wireless communications through reconfigurable intelligent surfaces," *IEEE Access*, vol. 7, pp. 116 753–116 773, 2019.

[191] H. Guo, Y.-C. Liang, J. Chen, and E. G. Larsson, "Weighted sum-rate maximization for reconfigurable intelligent surface aided wireless networks," *IEEE Transactions on Wireless Communications*, vol. 19, pp. 3064–3076, May 2020.

[192] Y. He, Y. Cai, H. Mao, and G. Yu, "RIS-assisted communication radar coexistence: Joint beamforming design and analysis," *IEEE Journal on Selected Areas in Communications*, vol. 40, pp. 2131–2145, Jul 2022.

[193] H. Luo, R. Liu, M. Li, Y. Liu, and Q. Liu, "Joint beamforming design for RIS-assisted integrated sensing and communication systems," *IEEE Transactions on Vehicular Technology*, vol. 71, pp. 13 393–13 397, Dec 2022.

[194] M. Hua, Q. Wu, C. He, S. Ma, and W. Chen, "Joint active and passive beamforming design for IRS-aided radar-communication," *IEEE Transactions on Wireless Communications*, vol. 22, pp. 2278–2294, Apr 2023.

[195] E. Basar, M. Wen, R. Mesleh, M. D. Renzo, Y. Xiao, and H. Haas, "Index modulation techniques for next-generation wireless networks," *IEEE Access*, vol. 5, pp. 16 693–16 746, Aug 2017.

[196] H. Yang, H. Ding, K. Cao, M. Elkashlan, H. Li, and K. Xin, "A RIS-segmented symbiotic ambient backscatter communication system," *IEEE Transactions on Vehicular Technology*, vol. 73, pp. 812–825, Jan 2024.

[197] M. A. ElMossallamy, H. Zhang, R. Sultan, K. G. Seddik, L. Song, G. Y. Li, and Z. Han, "On spatial multiplexing using reconfigurable intelligent surfaces," *IEEE Wireless Communications Letters*, vol. 10, pp. 226–230, Feb 2021.

[198] S. Meng, W. Tang, W. Chen, J. Lan, Q. Y. Zhou, Y. Han, X. Li, and S. Jin, "Rank optimization for MIMO channel with RIS: Simulation and measurement," *IEEE Wireless Communications Letters*, vol. 13, pp. 437–441, Feb 2024.

[199] Y. Zheng, T. Lin, and Y. Zhu, "Passive beamforming for IRS-assisted MU-MIMO systems with one-bit ADCs: An SER minimization design approach," *IEEE Communications Letters*, vol. 26, pp. 1101–1105, May 2022.

[200] W. Huang, B. Lei, S. He, C. Kai, and C. Li, "Condition number improvement of IRS-aided near-field MIMO channels," in *2023 IEEE International Conference on Communications Workshops (ICC Workshops)*, May 2023, pp. 1210–1215.

[201] A. H. Bafghi, V. Jamali, M. Nasiri-Kenari, and R. Schober, "Degrees of freedom of the K-user interference channel assisted by active and passive IRSs," *IEEE Transactions on Communications*, vol. 70, pp. 3063–3080, May 2022.

[202] S. Zheng, B. Lv, T. Zhang, Y. Xu, G. Chen, R. Wang, and P. C. Ching, "On DoF of active RIS-assisted MIMO interference channel with arbitrary antenna configurations: When will RIS help?" *IEEE Transactions on Vehicular Technology*, Dec 2023.

[203] S. H. Chae and K. Lee, "Cooperative communication for the rank-deficient MIMO interference channel with a reconfigurable intelligent surface," *IEEE Transactions on Wireless Communications*, vol. 22, pp. 2099–2112, Mar 2023.

[204] M. Nerini, S. Shen, and B. Clerckx, "Closed-form global optimization of beyond diagonal reconfigurable intelligent surfaces," *IEEE Transactions on Wireless Communications*, vol. 23, pp. 1037–1051, Feb 2024.

[205] I. Santamaria, M. Soleymani, E. Jorswieck, and J. Gutiérrez, "SNR maximization in beyond diagonal RIS-assisted single and multiple antenna links," *IEEE Signal Processing Letters*, vol. 30, pp. 923–926, 2023.

[206] ——, "Interference leakage minimization in RIS-assisted MIMO interference channels," in *ICASSP 2023 - 2023 IEEE International Conference on Acoustics, Speech and Signal Processing (ICASSP)*, vol. 39, Jun 2023, pp. 1–5.

[207] H. Li, S. Shen, and B. Clerckx, "Beyond diagonal reconfigurable intelligent surfaces: From transmitting and reflecting modes to single-, group-, and fully-connected architectures," *IEEE Transactions on Wireless Communications*, vol. 22, pp. 2311–2324, Apr 2023.

[208] H. Li, S. Shen, Y. Zhang, and B. Clerckx, "Channel estimation and beamforming for beyond diagonal reconfigurable intelligent surfaces," *arXiv:2403.18087*, 2024.

[209] H. Li, S. Shen, M. Nerini, M. D. Renzo, and B. Clerckx, "Beyond diagonal reconfigurable intelligent surfaces with mutual coupling: Modeling and optimization," *IEEE Communications Letters*, pp. 1–1, Oct 2024.

[210] H. Li, M. Nerini, S. Shen, and B. Clerckx, "Wideband modeling and beamforming for beyond diagonal reconfigurable intelligent surfaces," *arXiv:2403.12893*, 2024.

[211] T. Fang and Y. Mao, "A low-complexity beamforming design for beyond-diagonal RIS aided multi-user networks," *IEEE Communications Letters*, pp. 1–1, Jul 2023.

[212] Y. Zhou, Y. Liu, H. Li, Q. Wu, S. Shen, and B. Clerckx, "Optimizing power consumption, energy efficiency and sum-rate using beyond diagonal RIS — a unified approach," *IEEE Transactions on Wireless Communications*, pp. 1–1, 2023.

[213] M. Soleymani, I. Santamaria, E. Jorswieck, and B. Clerckx, "Optimization of rate-splitting multiple access in beyond diagonal RIS-assisted URLLC systems," *IEEE Transactions on Wireless Communications*, pp. 1–1, Jul 2024.

[214] G. Bartoli, A. Abrardo, N. Decarli, D. Dardari, and M. D. Renzo, "Spatial multiplexing in near field MIMO channels with reconfigurable intelligent surfaces," *IET Signal Processing*, vol. 17, Mar 2023.

[215] A. Mishra, Y. Mao, C. D'Andrea, S. Buzzi, and B. Clerckx, "Transmitter side beyond-diagonal reconfigurable intelligent surface for massive MIMO networks," *IEEE Wireless Communications Letters*, vol. 13, pp. 352–356, Feb 2024.

[216] M. Nerini, S. Shen, and B. Clerckx, "Discrete-value group and fully connected architectures for beyond diagonal reconfigurable intelligent surfaces," *IEEE Transactions on Vehicular Technology*, vol. 72, pp. 16 354–16 368, Dec 2023.

[217] A. S. de Sena, M. Rasti, N. H. Mahmood, and M. Latva-aho, "Beyond diagonal RIS for multi-band multi-cell MIMO networks: A practical frequency-dependent model and performance analysis," *arXiv:2401.06475*, 2024.

[218] T. E. Abrudan, J. Eriksson, and V. Koivunen, "Steepest descent algorithms for optimization under unitary matrix constraint," *IEEE Transactions on Signal Processing*, vol. 56, pp. 1134–1147, Mar 2008.

[219] T. Abrudan, J. Eriksson, and V. Koivunen, "Conjugate gradient algorithm for optimization under unitary matrix constraint," *Signal Processing*, vol. 89, pp. 1704–1714, Sep 2009.

[220] P.-A. Absil, R. Mahony, and R. Sepulchre, *Optimization Algorithms on Matrix Manifolds*. Princeton, NJ, USA: Princeton University Press, 2009.

[221] C. Pan, G. Zhou, K. Zhi, S. Hong, T. Wu, Y. Pan, H. Ren, M. D. Renzo, A. L. Swindlehurst, R. Zhang, and A. Y. Zhang, "An overview of signal processing techniques for RIS/IRS-aided wireless systems," *IEEE Journal of Selected Topics in Signal Processing*, vol. 16, pp. 883–917, Aug 2022.

[222] A. Edelman, T. A. Arias, and S. T. Smith, "The geometry of algorithms with orthogonality constraints," *SIAM Journal on Matrix Analysis and Applications*, vol. 20, pp. 303–353, Jan 1998.

[223] D. M. Pozar, *Microwave Engineering*. Wiley, Dec 2011.

[224] A. Hjorungnes and D. Gesbert, "Complex-valued matrix differentiation: Techniques and key results," *IEEE Transactions on Signal Processing*, vol. 55, pp. 2740–2746, Jun 2007.

[225] J. Nocedal and S. J. Wright, *Numerical Optimization*. Springer, Sep 2006.

[226] L. Armijo, "Minimization of functions having lipschitz continuous first partial derivatives," *Pacific Journal of Mathematics*, vol. 16, pp. 1–3, Jan 1966.

[227] C. Moler and C. V. Loan, "Nineteen dubious ways to compute the exponential of a matrix, twenty-five years later," *SIAM Review*, vol. 45, pp. 3–49, Jan 2003.

[228] D. Semmler, M. Joham, and W. Utschick, "High SNR analysis of RIS-aided MIMO broadcast channels," in *2023 IEEE 24th International Workshop on Signal Processing Advances in Wireless Communications (SPAWC)*, Sep 2023, pp. 221–225.

[229] W. Fulton, "Eigenvalues, invariant factors, highest weights, and schubert calculus," *Bulletin of the American Mathematical Society*, vol. 37, pp. 209–249, Apr 2000.

[230] R. Bhatia, "Linear algebra to quantum cohomology: The story of alfred horn's inequalities," *The American Mathematical Monthly*, vol. 108, pp. 289–318, Apr 2001.

[231] L. Hogben, Ed., *Handbook of Linear Algebra*. Boca Raton, FL, USA: CRC press, 2013.

[232] A. Zanella, M. Chiani, and M. Win, "On the marginal distribution of the eigenvalues of wishart matrices," *IEEE Transactions on Communications*, vol. 57, pp. 1050–1060, Apr 2009.

[233] J. C. Gower and G. B. Dijksterhuis, *Procrustes Problems*. Oxford, UK: Oxford University Press, 2004.

[234] T. Bell, "Global positioning system-based attitude determination and the orthogonal procrustes problem," *Journal of Guidance, Control, and Dynamics*, vol. 26, pp. 820–822, Sep 2003.

[235] F. Nie, R. Zhang, and X. Li, "A generalized power iteration method for solving quadratic problem on the Stiefel manifold," *Science China Information Sciences*, vol. 60, p. 112101, Nov 2017.

[236] K. Gomadam, V. R. Cadambe, and S. A. Jafar, "A distributed numerical approach to interference alignment and applications to wireless interference networks," *IEEE Transactions on Information Theory*, vol. 57, pp. 3309–3322, Jun 2011.

[237] F. Negro, S. P. Shenoy, I. Ghauri, and D. T. Slock, "Weighted sum rate maximization in the MIMO interference channel," in *21st Annual IEEE International Symposium on Personal, Indoor and Mobile Radio Communications*, Sep 2010, pp. 684–689.

[238] D. Guo, S. Shamai, and S. Verdu, "Mutual information and minimum mean-square error in gaussian channels," *IEEE Transactions on Information Theory*, vol. 51, pp. 1261–1282, Apr 2005.

[239] C. Zhong, X. Hu, X. Chen, D. W. K. Ng, and Z. Zhang, "Spatial modulation assisted multi-antenna non-orthogonal multiple access," *IEEE Wireless Communications*, vol. 25, pp. 61–67, Apr 2018.

[240] Y. Mao, B. Clerckx, and V. O. K. Li, "Rate-splitting multiple access for downlink communication systems: Bridging, generalizing, and outperforming SDMA and NOMA," *EURASIP Journal on Wireless Communications and Networking*, vol. 2018, p. 133, Dec 2018.

[241] N. I. Miridakis, T. A. Tsiftsis, P. A. Karkazis, H. C. Leligou, P. Popovski, N. I. Miridakis, P. A. Karkazis, T. A. Tsiftsis, H. C. Leligou, and P. Popovski, "Impact of inter-operator interference via reconfigurable intelligent surfaces," *arXiv:2403.00349*, 2024.

[242] D. Xu, X. Yu, Y. Sun, D. W. K. Ng, and R. Schober, "Resource allocation for IRS-assisted full-duplex cognitive radio systems," *IEEE Transactions on Communications*, vol. 68, no. 12, pp. 7376–7394, Dec 2020.

[243] B. R. Marks and G. P. Wright, "A general inner approximation algorithm for nonconvex mathematical programs," *Operations Research*, vol. 26, no. 4, pp. 681–683, Aug 1978.

[244] W.-C. Li, T.-H. Chang, C. Lin, and C.-Y. Chi, "Coordinated beamforming for multiuser MISO interference channel under rate outage constraints," *IEEE Transactions on Signal Processing*, vol. 61, no. 5, pp. 1087–1103, Mar 2013.